Universitat Politècnica de València

Departamento de Comunicaciones

A Novel Approach to Label-Free Biosensors Based on Photonic Bandgap Structures

Javier García Castelló

Supervisor: Dr. Jaime García Rupérez

Thesis submitted to the Univesitat Politècnica de València in partial fulfillment of the requirements for the degree of Doctor of Philosophy in Telecommunications engineering.

Acknowledgements

Writing this PhD dissertation would have been impossible without considerable assistance from all the people who have always been by my side these last four years. Especially, I am deeply indebted to my research advisor Dr. Jaime García Rupérez who gave me the opportunity to discover a new nanoworld of biosensing devices on silicon. Jaime has always been very enthusiastic with our work and has provided valuable inputs to the research. In addition, Jaime has been accessible and friendly, which made my research life enjoyable. Thank you. I would also like to show my gratitude to Dr. Veronica Toccafondo, who has been my colleague in the lab where we performed uncountable experiments. I was always glad to listen to her advice and new ideas concerning the problems we encountered each day. Moreover, I would like to express my acknowledgement to Prof. Javier Martí, for all the effort he has put into the Nanophotonics Technology Center (NTC), which has become a prestigious research institute reference in Spain.

I would like to thank all my colleagues from NTC during these fantastic four years. They have been not only my teammates, but also my friends, with whom I have spent many moments of endless conversations and discussions - professional and personal - accompanied by litres upon litres of coffee or beer. My deepest gratitude to each of them. Thanks to Jose María Escalante, Jesús Palací, Jordi Peiró, Mercé LLopis, David Zurita, Raffaele Caroselli, Paco Rodríguez, Carlos G. Meca, Rubén Ortuño, Alexander Bockelt, Christian Chaverri, Guillermo Villanueva, Maria Lorente, Joaquín Matres, Antoine Brimont, Sara Mas, Ana Mª Gutiérrez, Mariam Aamer and Pere Pérez. I would also like to thank the running team: Carlos G. Suárez, Luis Collado, Antonio Abanades, Gianni Preve, José A. Ayúcar, Daniel Puerto and Satur. I give further thanks to the management and administration team for simplifying our lives with the travels and purchase orders, and furthermore to the fabrication team who were in charge of making our dreams come true at nanoscale dimensions.

Special gratitude is owed to our chemist colleagues in the "Centro de Reconocimiento Molecular y Desarrollo Tecnológico" in Universitat Politècnica de València, namely Dr. María José

Bañuls, Dr. Jorge Escorihuela, Dr. Sergio Peransí and Prof. Ángel Maquieira. Their expertise in the field of bioconjugation chemistry made me understand the interaction of the molecules on the surface of our sensors.

I wish to thank Prof. Peter Bienstman, for giving me the chance to take part in his sensors and biosensor group at Photonic Research Group in University of Gent. The support of Tom Claes and Cristina Lerma who contributed to the great time I had improving my knowledge and spending one of the most unforgettable periods of my life in Belgium.

To the "Red Rosita's crew": Jose María, Julian, Miguel Ángel, Toni and Óscar. They encouraged me during my weakest moments and it is an honour to have shared the same passion for the sea.

My deepest gratitude to my FFF (fools, friends and family). My Fools: Blasco, Amahl, Jose Carlos, Francesc and Mora, because without them Campanar wouldn't be the same. Friends: Marcos, Javier, Laura, Jorge, Carlos, Maider, Berta, Marta, Carla, Asenov, Àngela, Juan, Álvaro, David, Lorena, Ismael… To all of you, thanks for share a little piece of your time with me. And to my family, who showed me unlimited support. They gave me life, made me who I am and provided me what I needed. I will be always in debt to them. Lastly, I can't forget my "best awesomest" brother Marcos, I know that you will be much better than me in everything. Sincerely, thanks.

In the case that I have forgotten someone, to you I say: thank you too.

Abstract

The necessity of using extremely high sensitivity biosensors in certain research areas has remarkably increased during the last two decades. Optical structures, where light is used to transduce biochemical interactions into optical signals, are a very interesting approach for the development of this type of biosensors. Within optical sensors, photonic integrated architectures are probably the most promising platform to develop novel lab-on-a-chip devices. Such planar structures exhibit an extremely high sensitivity, a significantly reduced footprint and a high multiplexing potential for sensing applications. Furthermore, their compatibility with CMOS processes and materials, such as silicon, opens the route to mass production, thus reducing drastically the cost of the final devices. Optical sensors achieve their specificity and label-free operation by means of a proper chemical functionalization of their surfaces. The selective attachment of the receptors allows the detection of the target analytes within a complex matrix.

This PhD Thesis is focused on the development of label-free photonic integrated sensors in which the detection is based on the interaction of the target analytes with the evanescent field that travels along the structures. Herein, we studied several photonic structures for sensing purposes, such as photonic crystals and ring resonators. Photonic crystals, where their periodicity provokes the appearance of multiple back and forth reflections, exhibits the so-called slow-light phenomenon that allows an increase of the interaction between the light and the target matter. On the other hand, the circulating nature of the resonant modes in a ring resonator offers a multiple interaction with the matter near the structure, providing a longer effective length.

We have also proposed a novel approach for the interrogation of photonic bandgap sensing structures where simply the output power needs to measured, contrary to current approaches based on the spectral interrogation of the photonic structures. This novel technique consists on measuring the overlap between a broadband source and the band edge from a SOI-based corrugated waveguide, so that we can determine indirectly its spectral position in real-time. Since there is no need to employ tunable equipment, we obtain a lighter, simpler and a cost-effective platform, as well as a real-time observation of the molecular interactions. The experimental demonstration with antibody detection measurements has shown the potential of this technique for sensing purposes.

Resumen

La necesidad de usar biosensores extremadamente sensibles en ciertas áreas se ha incrementado notablemente durante las dos últimas décadas. Las estructuras ópticas, donde la luz es usada para transformar interacciones bioquímicas en señales ópticas, son una interesante solución para el desarrollo de este tipo de biosensores. Dentro de los sensores ópticos, las arquitecturas integradas son probablemente la plataforma más prometedora para desarrollar novedosos dispositivos lab-on-a-chip. Estas estructuras planares basadas en silicio muestran una alta sensibilidad, reducido tamaño y un elevado nivel de multiplexación para aplicaciones de sensado. Además, su compatibilidad con los materiales y procesos CMOS abre la puerta a la fabricación en masa reduciendo drásticamente el coste del dispositivo final. Los sensores ópticos obtienen su especifidad y el sensado sin el empleo de marcadores a través de una correcta funcionalización de sus superficies. La unión selectiva de los receptores permite la detección de los analItos objetivos dentro de una muestra compleja.

Esta tesis está centrada en el desarrollo de un sensor fotónico integrado sin el empleo de marcadores en el cual la detección está basada en la interacción de los analitos objetivo con el campo evanescente que viaja por la superficie de las estructuras. Hemos estudiado varias estructuras como cristales fotónicos y anillos resonantes para aplicaciones de sensado. Los cristales fotónicos, cuya periodicidad provoca la aparición de multiples reflexiones, muestran el fenómeno de luz lenta que permite un incremento de la interacción entre la luz y la materia. Por otra parte, la naturaleza circular del modo en el anillo resonante ofrece numerosas interacciones con la materia cerca de la estructura proporcionando una longitud efectiva mayor.

Nosotros, además, proponemos un nuevo método de interrogación del *band gap* fotónico de las estructuras de sensado donde simplemente es necesario medir la potencia de salida, al contrario que las técnicas actuales basadas en la medida del espectro. Esta nueva técnica consiste en medir el solape entre la fuente de banda ancha y el borde de la banda de una guía corrugada fabricada en SOI, por lo que podemos determinar indirectamente su posición espectral en tiempo real. Como no hay necesidad de emplear equipos sintonizables, obtenemos una plataforma más ligera, simple y económica además de la observación en tiempo real de las interacciones moleculares. La demostración experimental con anticuerpos muestra el potencial de esta técnica para propósitos de sensado.

Resum

La necessitat d'usar biosensors extremadament sensibles en certes àrees s'ha incrementat notablement durant les dos últimes dècades. Les estructures òptiques, on la llum s'utilitza per a transformar interaccions bioquímiques en senyals òptiques, són una interessant solució per al desenvolupament d'este tipus de biosensors. Dins dels sensors òptics, les arquitectures integrades són probablement la plataforma més prometedora per a desenvolupar els nous dispositius lab-on-a-chip. Aquestes estructures planars basades en silici mostren una alta sensibilitat, reduida grandària i un elevat nivell de multiplexació per a aplicacions de sensat. A més, la seua compatibilitat amb els materials i processos CMOS obri la porta a la fabricació en massa reduint dràsticament el cost del dispositiu final. Els sensors òptics obtenen el seu especifidad i el sensat sense l'ús de marcadors a través d'una correcta funcionalització de les seues superfícies. La unió selectiva dels receptors permet la detecció dels analits objectius dins d'una mostra complexa.

Esta tesi està centrada en el desenvolupament d'un sensor fotónic integrat sense l'ús de marcadors en el qual la detecció està basada en la interacció dels analits objectiu amb el camp evanescent que viatja per la superfície de les estructures. Hem estudiat diverses estructures com a cristalls fotónics i anells ressonants per a aplicacions de sensat. Els cristalls fotónics, la periodicitat dels quals provoca l'aparició de múltiples reflexions, mostren el fenomen de la llum lenta que permet un increment de la interacció entre la llum i la matèria. D'altra banda, la naturalesa circular del mode en l'anell ressonant oferix nombroses interaccions amb la matèria prop de l'estructura proporcionant una longitud efectiva major.

Nosaltres, a més, proposem un nou mètode d'interrogació del band gap fotónic de les estructures de sensat on simplement és necessari mesurar la potència d'eixida, al contrari que les tècniques actuals basades en la mesura de l'espectre. Aquesta nova tècnica consisteix a mesurar el solapament entre la font de banda ampla i el bord de la banda d'una guia corrugada fabricada en SOI, per la qual cosa podem determinar indirectament la seua posició espectral en temps real. Com no hi ha necessitat d'emprar equips sintonitzables, obtenim una plataforma més lleugera, simple i econòmica, a més de l'observació en temps real de les interaccions moleculars. La demostració experimental amb anticossos mostra el potencial d'esta tècnica per a propòsits de sensat.

Table of contents

1

Introduction to biosensors: transducers, applications and technologies

1.1 Introduction

The definition of a biosensing device can be slightly different according to the area of application, due to the use of diverse technologies, methods or terminologies. However, the basic concept is always similar. For instance, M. Cooper simply defines a biosensor as "a device that uses biological or chemical receptors to detect analytes (molecules) in a sample" [COO09]. On the other hand, S.P.J. Higson introduced the concept biosensor as "a chemical sensing device in which a biologically derived recognition entity is coupled to a transducer, to allow the quantitative development of some complex biochemical parameter" [HIG94]. These descriptions, as well as

most of the definitions about biosensors, have the same point in common: a biosensor is a system that recognizes biochemical molecules, known as analytes, by means of their binding on a biochemical layer; then the system is able to convert the recognition information into a measurable signal to be analysed.

Some authors consider that biosensors comprise two parts: the biological layer, which is in charge of the specific recognition of the target analyte(s); and the transducer, which has the ability to transform the chemical information provided by the biological layer into a quantified signal, e.g. mechanical, optical or electrical [MOH06]. However, most researchers also agree on that a biosensor also comprises a third basic component: the read-out system that allows the visualization and interpretation of the sensing information by the user. Finally, in small-sized biosensors, where the sensing area is significantly reduced (e.g., below hundreds of microns), the delivery of the target analyte(s) is another key issue that must be taken into account. For that reason, we can even consider the sample delivery system as a basic part of a photonic biosensing system. Fig. 1.1 shows a simplified schematic representation of a biosensor with the four parts mentioned above: biological layer (or recognition layer), transducer, sample delivery system and read-out system.

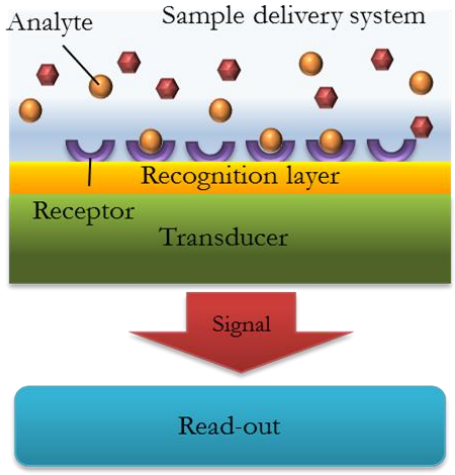

Fig. 1.1: *Schematic representation of a biosensor comprising four basic parts: sample delivery system, biological layer, transducer and read-out of the output signal.*

In this chapter, we will first introduce in section 1.2 the properties and the role of the recognition layer. Then, in section 1.3, some of the most common transduction mechanisms used for biomolecular and biochemical sensing will be reviewed. In section 1.4, we will list the most important requirements of a biosensor. Afterwards, in sections 1.5 and 1.6, we will introduce the lab-on-a-chip (LOC) technology as well as some of its main application fields. In section 1.7, we will briefly introduce the silicon photonics technology platform, which has been used for the development of the photonic sensors used in this work. Finally, once all these concepts related with biosensors technology have been introduced, we will present in sections 1.8 and 1.9 the objectives and the framework of this Thesis as well as the framework in which it has been carried out..

1.2 Recognition layer

The recognition layer provides to the sensing devices the ability to the selectively detect the presence of the target analytes. Generally, it consists on a specific coating of proper receptors that recognize the target molecules among all the background particles present in the sample. This specificity is determined by the affinity between the receptor and each target analyte, thus provoking that only the targeted analyte is the responsible of the chemical/physical changes to be detected. Then the transduction element transforms such chemical/physical signal into a measurable signal that is possible to be quantified using the read-out system.

In order to obtain a high sensitivity sensor, many sensing techniques require labelling the target molecules in order to make their detection feasible. However, such labelling procedure can be very complex and time consuming. Moreover, labels may interfere with the detection signal, giving rise to unreliable results. Contrary to these label-based techniques, label-free methods allow significantly simplifying the sample preparation procedure as well as avoiding any interference of the labels on the final detection result, since the recognition procedure is directly based in the presence of the target molecule itself even when it is contained in complex buffers.

The creation of the recognition layer comprising the molecular receptors is achieved by means of the biochemical functionalization (or bio-functionalization) of the sensing structure. This process is one of the most critical steps to obtain a biosensor with acceptable performance since several intrinsic parameters such as sensitivity, detection limit, long-term stability, or uniformity, are determined by the quality of the biochemical coating. Many different mechanisms can be used to attach the receptors to the sensing structure, such as physical attachment, chemical attachment or molecular recognition. In chapter 2, we will introduce some of the most common immobilization techniques currently used for silicon substrates. In that chapter, we will also introduce the different surface modification approaches that we have employed in the course of this PhD work for the bio-functionalization of our photonic sensing structures.

Concerning the receptors comprising the recognition layer, several types of molecules can be used, such as enzymes, antibodies, proteins, oligonucleotides, DNA, cells or aminoacids among others. Table 1.1 lists the receptors mostly used for the development of affinity biosensors, which will be mainly determined by the final application of the biosensor. For example, in an immunoassay a certain antibody will be attached to the sensing structure in order to detect specifically the presence of its antigen couple within the target sample.

Bioreceptor component	Recognition mechanism
Enzymes, proteins	They can catalyze specific chemical reactions. In can be measured by conversion of the analyte into a detectable signal. The detection of the analyte can act as a inhibitor or activator of the reaction.
Antibodies and antigens	The antigen triggers the immune response of the organism to produce antibodies. Therefore, the antibody specifically recognizes the antigen in the sample.
DNA strands	The recognition process is based in the hybridization of complementary DNA strands through double helix.
Cellular structures	A whole microorganism can be used as a recognition element such as non catalitic receptor.
Biomimetic	The recognition is achieved using genetically engineered molecules: for instance, artificial membrane and molecularly imprinted polymers (MIP) imitate the shape of the bioreceptor molecules in order to attract the target molecules.

Table 1.1: *Specific biomolecules widely employed for the functionalization of biosensing devices and their recognition mechanism [WAN11].*

1.3 Transduction mechanisms

The transducer is the core element of any sensing device. It transforms the information provided by the physical or chemical interaction between the receptor and the target analyte, into a quantifiable signal. This signal can be electrical, mechanical or optical among others. This conversion permits to the read-out equipment perform several functions to the signal such as amplifying, recording or analysing to extract the main information of the interaction event.

Currently, there are several transduction elements with different physical conversion methods. The choice of each of them, as occurs for the recognition layer, will also depend of the application and the affinity mechanism between the target analyte and receptor. In this section, we briefly introduce several types of transduction methods for the label-free detection of the molecular interactions using affinity biosensors. Although a wide range of transduction methods exist, in this section we will mainly focus on electrochemical, mechanical, acoustic and optical transducers.

1.3.1 Electrochemical transducers

Electrochemical transducers employ the variation of their electroanalitical properties such as voltage, current, conductance or impedance due to the interaction between the analyte and the attached receptor. As a sensing result, it provides a signal that can be measured using currently available electrical equipment. The firsts electrochemical sensors dated from the 50's [CLA56]. The basic configuration of these sensors consists of a sensing electrode and a reference electrode, where between them the sample is placed. When the sensing electrode is exposed to the target sample, the electrical properties of the sensor changes, thus monitoring the electrical parameter through the

electrodes it is possible to perform the detection of the target substance. This transduction technology has attracted a great interest due to its simplicity, maturity, low power consumption and potential multiplexing capability [ROY09]. Since its discover, there have been many kinds of electrochemical transducers from simple voltammetry sensors [GOS94] to recent developments in field effect transistor (FET) based on silicon nanowires (SiNWs) [FAN12], carbon nanotubes (CNTs) [TAN12] and electrochemical impedance spectroscopy (EIS) [ISM12]. A thorough revision of sensing devices based on electrochemical methods is provided in these review articles [GRI08, CHE13]

Cyclic voltammetry [DEY12] is a method widely employed for the development of electrochemical biosensors. It is useful to obtain information about the redox potential and electrochemical reaction rates. The voltage and intensity of the sample is measured between the reference electrode and the working electrode and the signal is plotted in a voltammogram. The I-V curve of the sensor for a given reaction will depend on the catalyst concentration of the recognition.

In electrochemical biosensors based on FET transistors, the conductivity between the source and drain electrodes is modified due to the binding of target analytes on the channel that connects them (instead of using a third gate electrode as for usual FET transistors), thus producing a change in the measured FET current. Fig. 1.2a shows an implementation of FET-based biosensor where a SiNW is used to connect the source and the drain. Such nanowire is functionalized with specific receptors, so binding events with the target molecules will provoke a change in the measured current. The reduced size of the nanowire provides an extraordinary high sensitivity due to the higher interaction of the particles with the transmitted current, as shown in Fig. 1.2b. One example of its potential using this configuration is the detection of streptavidin with a concentration below the pM range which was demonstrated by using biotin-functionalized SiNW. Furthermore, a reversible antibody binding dependence of the concentration was also shown [CUI01].

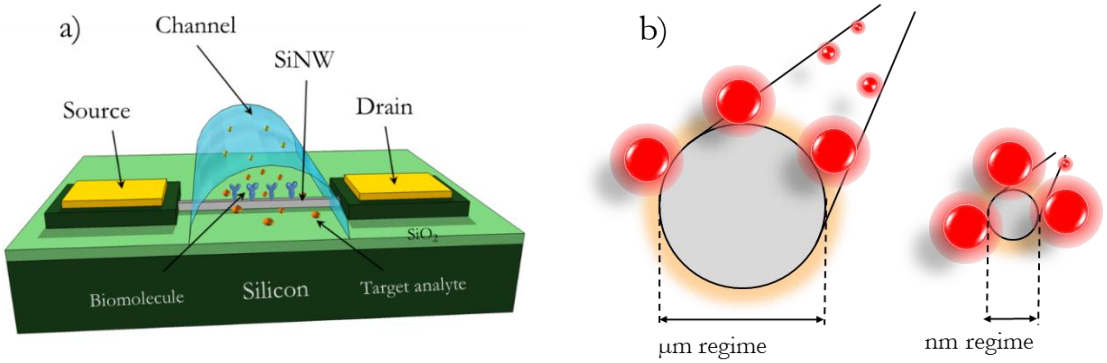

Fig. 1.2: *a) Schematic diagram of a SiNW FET sensing device. The conductivity of the SiNW will depend on the molecules bound to its surface. b) Illustration showing the influence of SiNW size on the effect of the target analytes bound to it.*

The recent application of CNTs to the development of biosensing devices is also currently under an exhaustive investigation due to their extraordinary and very promising electrical and mechanical properties, which can be tuned depending the tube diameter. Regarding their use for sensing, the most common method to implement electrochemical transducers based on CNTs is by coating FET transistors and chemiresistors with them in order to control the reactivity towards the target analytes. Due to the reduced dimensions of the CNTs, which is comparable to the dimension of target analytes, scientists expect a significant improvement in the sensitivity of the sensing devices. The application of CNTs has been demonstrated in electrochemical transducers for the detection of several analytes such enzymes, antibodies or nucleic acids [WAN04].

The last kind of electrochemical transduction mechanism presented here is EIS, which is another potential method for the analysis of biological samples [LIS08]. The presence of the target molecules on top of the electrodes will affect the local environment of the sensing device that will be translated into a variation of the electrical resistance/impedance/capacitance/conductance of the system as a function of the frequency as shown in Fig. 1.3 [MAN10].

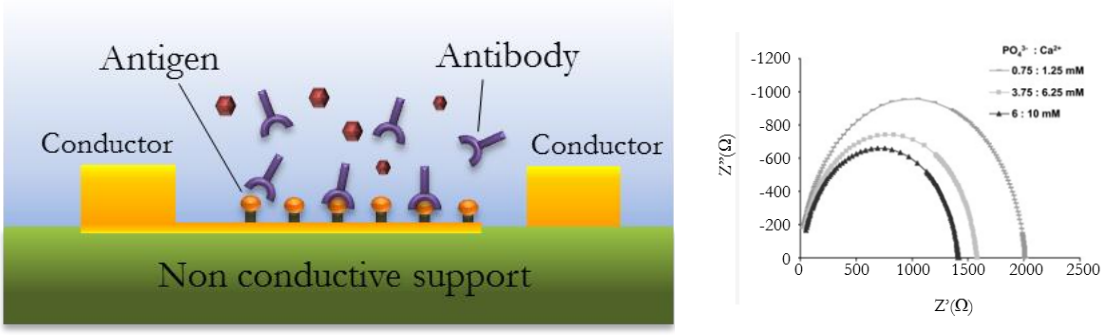

Fig. 1.3:*Cross section of an EIS device. The frequency response of the measured parameter will depend on the binding events between the probes and the target analytes. Plot of a measurement of the imaginary part as a function of the real part of the impedance varying the analyte concentration.*

Therefore, electrochemical transduction methods for label-free detection have become a very mature detection platform. Furthermore, its compatibility with CMOS fabrication processes permits the development of compact and low-cost biosensing devices with high production volume and, in many cases, suitable for multi-parametric detection (despite the multiplexing level is usually very limited). Currently, as result of many investigations, several systems based on electrochemical transduction have become commercially available for different application fields. For example, ACEA Bioscience [ACE13] and Applied Biophysics [BIO13a] have developed analysis systems with application in the field of cell screening, which are shown in Fig. 1.4. These systems are based on measuring the impedance of the cells on small top electrodes.

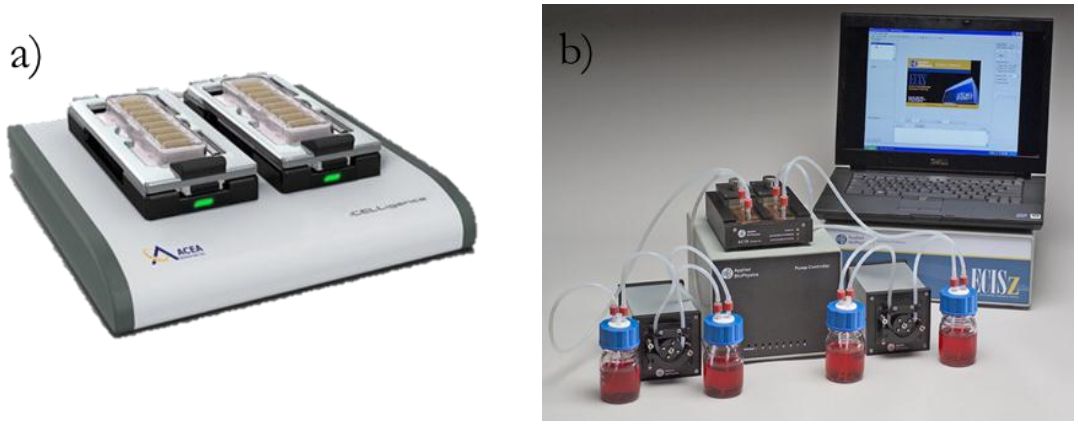

Fig. 1.4: *Commercial equipment: a) iCELLigence from ACEA Bioscience, and b) ECIS Z from Applied Biophysics.*

1.3.2 Mechanical transducers

Another transduction mechanism for the detection of the interaction between the receptor and the target analytes is that based on the use of mechanical variations such strain or resonance frequency [TAM13]. Identically to most sensing techniques, the selectivity and the sensitivity of the sensor towards the target analytes are determined by a proper functionalization of the biological layer. Among mechanical transducers, we will focus here on two well-differentiated groups: quartz crystal microbalances (QCM) and cantilevers. A complete review of mechanical transducers technology can be found in [CAR06, BUC11].

The principle of operation of QCM devices, which are shown in Fig. 1.5a, relies on the measurement of the oscillation frequency of the system by connecting an external oscillator to the piezoelectric quartz crystal [FRI08]. The oscillation resonance of the system will undergo a frequency change due to the mass change provoked by the binding of the target molecules to the receptors [ZAM08, ZAN04]. For that reason, QCM sensing devices are widely employed for the motorization of the deposition of thin film on surfaces. The main drawback of this technology is the appearance of nonlinearities in the frequency oscillation due to the viscoelasticity and hydration of the piezoelectric device when the target analyte is contained in aqueous solution [SHO12]. It has been demonstrated that QCM sensors are an excellent tool for a rapid and sensitive detection of analytes, for example, staphylococcal enterotoxin has been detected with a detection limit of 6.1 ng/ml using a fast assay [LIU12]. Among the companies that commercialize sensing equipment based on QCM technology, we can find Q-sense with its equipment Omega Auto in Fig. 1.5b which is able to measure the mass of the structure and the thickness of the molecular layers.

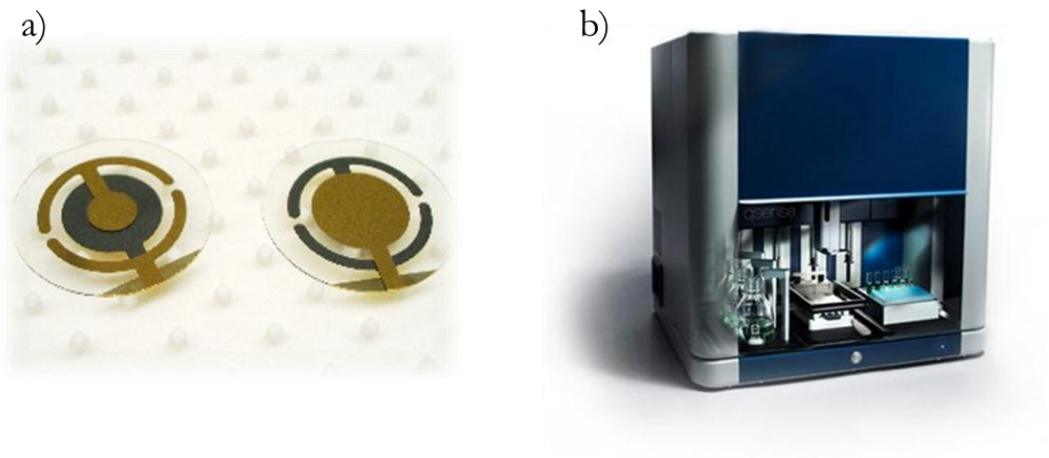

Fig. 1.5: *a) Top and back parts of a common QCM with gold electrodes and b) Omega Auto from Q-sense, based on QCM technology for the analysis of molecular interactions.*

On the other hand, microcantilevers are an interesting approach due to their mature development using integrated technology. Its integration allows multiplexed detection in label-free format being able to measure multitude of sensing devices in parallel. Two basic operation modes for microcantilevers are mainly used: static and dynamic. The first one is based in the measurement of the deflection of the cantilever when the target molecules are bound to the receptors [KOS13], as shown in Fig. 1.6. For this approach, usually the variation of the cantilever deflection is measured using the reflected signal from a laser beam in the cantilever.

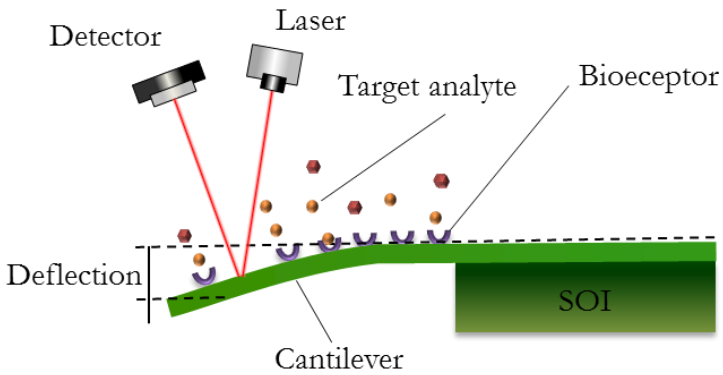

Fig. 1.6: *Representation of the operation principle in a deflection-based cantilever.*

The dynamic measurement of the cantilever variations is another mode for detecting the presence of the target analytes. In cantilever-based sensors, it is possible to measure the change of its resonance frequency, which is oscillated using a piezoelectric actuator [LAV04]. The binding of the target molecules leads to a change in the resonant frequency of the cantilever that is measured using a laser as well, similar to the previous configuration. The advantage of this scheme is that the

sensor can be coated on its upper and lower surfaces giving rise an enhancement of the detection. This scheme is more complex than the deflection-based approach since it requires maintaining the cantilever in resonant mode. A recent work based on an array of gold-coated microcantilevers functionalized with thiolated ssDNA probes working in dynamic mode proved the successful hybridization of the complementary target ssDNA with a concentration down to 4 fM and with a sensitivity range of up to 6 orders of magnitude [JOH12].

Concluding, mechanical sensors have demonstrated to be an alternative to implement multiplexed label-free biosensors for the detection of several analytes, being the performance of these devices comparable to other high performance techniques. Some commercial solutions based on microcantilevers sensors that have been released into the market by Cantion (a) [CAN13], Bioscale (b) [BIO13b] or Concentris (c) [CON13] are shown in Fig. 1.7.

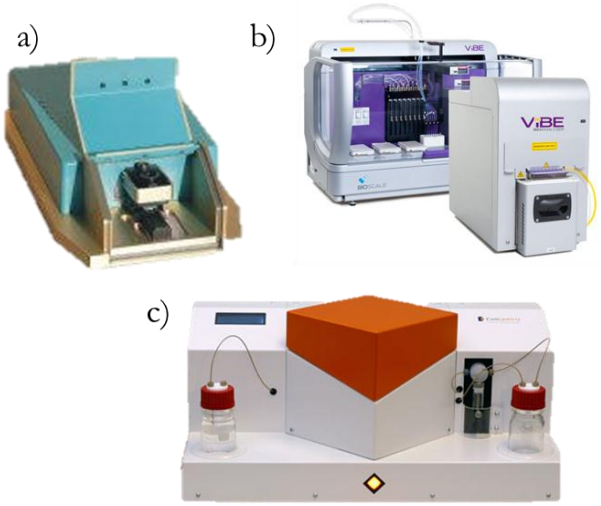

Fig. 1.7: *Commercial equipment based on microcantilever sensors: a) CantiLab3D from Cantion, b) ViBE from Bioscale and c) CantiSens CSR-801 from Concentris.*

1.3.3 Acoustic transducers

Acoustic waves can also be used to develop biosensing devices. In fact, there are numerous applications where this kind of sensors can be used, which are reviewed in [ION11]. This transduction technology is based in the ability of acoustic waves for analysing biochemical reactions in liquid and gas environments due to the possibility of such waves to travel across the sample. These sensors exhibit valuable performances such as high sensitivity, portability, robustness and compatibility with standard microfabrication processes.

The conversion of the biochemical information into a measurable signal is achieved by using different types of acoustic waves. These waves can be either generated or received by means

of different mechanisms including piezoelectric, magnetostrictive, optical and thermal. Similar to the cantilever sensors, acoustic biosensors are designed to work using an oscillator in the resonance regime. The surface of the acoustic biosensor can be functionalized using standard techniques and the binding of the target analyte will induce a change in the frequency of the acoustic wave [MAT13]. By measuring this variation of the resonance frequency and its subsequent analysis, it is possible to determine the correlation between the acoustic signal and the interaction of the molecules.

The classification of acoustic sensors can be performed according to the nature of the acoustic waves used for the detection: bulk waves [ZHA10] and surface acoustic waves (SAW) [LAN08]. The former method employs a common bulk piezoelectric crystal as a source and detector of the acoustic wave, which travels through the target liquid or gas. For the second method, the surface acoustic waves can be excited using an interdigital system of metallic electrodes (IDT) on the surface. The principle of operation of this approach is schematically depicted in Fig. 1.8 where a surface acoustic wave travels between the two IDTs (one to generate the signal and the other to receive it) interacting with the target sample. We can find several published results of SAW sensing devices for example for the detection of rabbit IgG with a detection limit below 1 μg/ml using a device functionalized with anti-rabbit antibodies [MAT13].

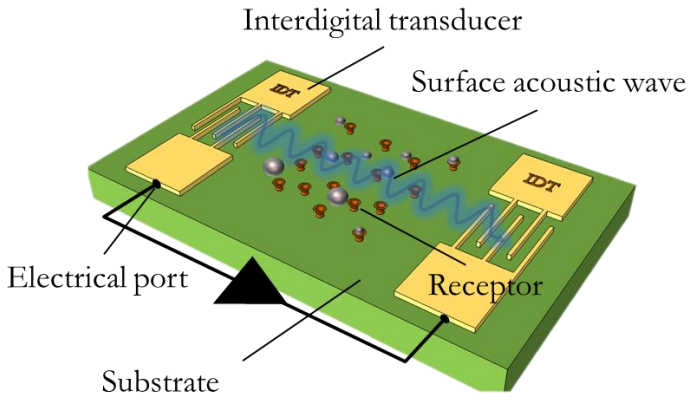

Fig. 1.8: *Illustration of a SAW biosensor where IDTs are used for excitation and detection of the surface acoustic wave.*

One of the main benefits of acoustic sensors is its possibility to operate using wireless excitation, thus being able to work in extremely hazardous conditions such as high temperatures. In addition, the compatibility with integrated circuit technology permits a high efficiency in the fabrication. However, the main drawback of this technique is that any vibration induced on the system would produce a negative effect to the sensing signal of the sensor. In order to compensate vibration noise, a complex analysis should be performed to differentiate between true biosensing signal and vibrations. Recently a new company, SAW Instruments [SAW13], has released a

commercial device for label-free biosensing based on SAW technology, the SAM-X (see Fig. 1.9), with the ability to measure protein-ligand interactions.

Fig. 1.9: *Commercial SAM-X system based on surface acoustic waves technology manufactured by the German company SAW-Instruments.*

1.3.4 Optical transducers

Optical transducers employ the interaction of the light with the target analytes to convert the biological information into a measurable signal. In the majority of optical sensors, the sensing mechanism relies in the variation of the effective index of the propagating mode that occurs when a variation of the chemical or physical parameters is produced on the surface of the structure, as shown in Fig. 1.10. When an optical wave is traveling through the core of an optical waveguide, a fraction of its energy, known as evanescent field, extends to the surrounding medium decreasing its intensity exponentially from the surface. This evanescent field will be the responsible of the changes in the effective index of the propagating mode when the sensing events are produced.

It is obvious to think that the more amount of evanescent wave on the surface, the more interaction of the field with the target analytes. However, in order to develop an evanescent field sensor it is necessary to reach a compromise between the portion of the evanescent field that travels on the surface and the portion that is confined on the waveguide core. An excessive amount of evanescent field would provoke a significant degradation of the performance of the guiding structure itself making the signal very weak. Therefore, the design parameters will play a crucial role in determining the performance of the sensor.

In order to convert the effective index variations into a measurable signal such as intensity or frequency variations, different configurations of photonic structures can be used (e.g., Mach Zehnder interferometer (MZI), ring resonators (RR), photonic crystals (PhC)). Some of the most typical configurations of photonic sensors are introduced below.

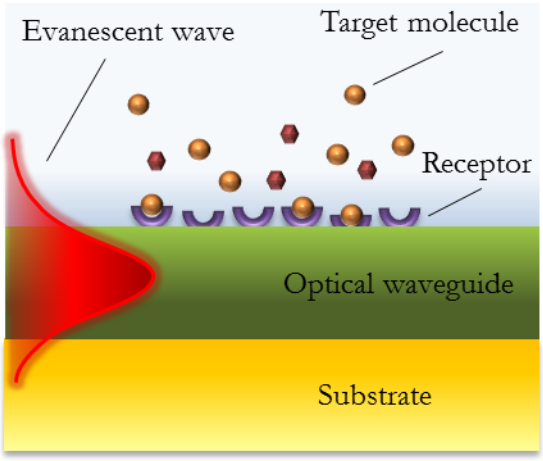

Fig. 1.10: *Schematic illustration of a label-free optical biosensor based on the evanescent wave interaction. Due to the interaction of the light with the analytes bound to the probes, the optical wave undergoes a change in its propagation constant due to the variation of the effective refractive index.*

Optical fiber sensors

Due to their inexpensive cost and their physical properties, optical fibers have been historically employed as mechanical sensors for the detection of strain, temperature or vibration variations in several structures to monitor the forces acting over them [UDD11]. However, fibers can be also chemically modified to be used for biosensing purposes [LEE03]. A recent review about last trends in chemical and biochemical sensors based on optical fibers can be found in [WAN13].

One of the most employed approach is the use of fiber Bragg gratings (FBG), which are fabricated by inscribing a periodic modulation of the refractive index in the core of a standard fiber. The configuration of a typical FBG is shown Fig. 1.11a. This modulation provokes the appearance of a range of reflected wavelengths that depends on the period, the refractive index of the structure, and the refractive index on the surroundings of the structure. The fact that fibers are typically employed for data transmission makes that their core is extremely protected to prevent losses, what is a limitation for biosensing purposes. In order to overcome this drawback, the cladding of the fiber must be removed (either chemically or by polishing) in order to expose the core and allocate the target sample close to the optical wave used to perform the sensing.

Long period gratings (LPG), in Fig. 1.11b, are similar to FBGs but in this case, the modulation pattern is in the order of a fraction of millimeters [CHI12]. In the LPG, guided light also couples to the cladding, so there is no need to carry out additional processing steps to remove the coating. Other configuration implemented in optical fibers for biological detection is achieved by using Fabry-Perot (FP) cavities [WEI08], as shown in Fig. 1.11c. The cavity can be created by different methods including tapering the fiber or inserting a hollow fiber between two standard

fibers. The characteristic spectrum of these FP-based sensors can be monitored in order to relate the measured spectral shift with the refractive index variation due to the molecular bindings.

In addition, a singular approach are photonic crystal fibers (PCF) that exhibit a cross section comprising an array of microscopic holes as shown in Fig. 1.11d. These fibers have unique light guiding properties and their holes can be filled with the target sample, thus enhancing its interaction with the optical wave compared to standard fibers. Using a combination of PCF and LPG, the monitorization of the thickness of a poly-Lysine monolayer and the detection of double-strand DNA (dsDNA) has been reported [RIN06].

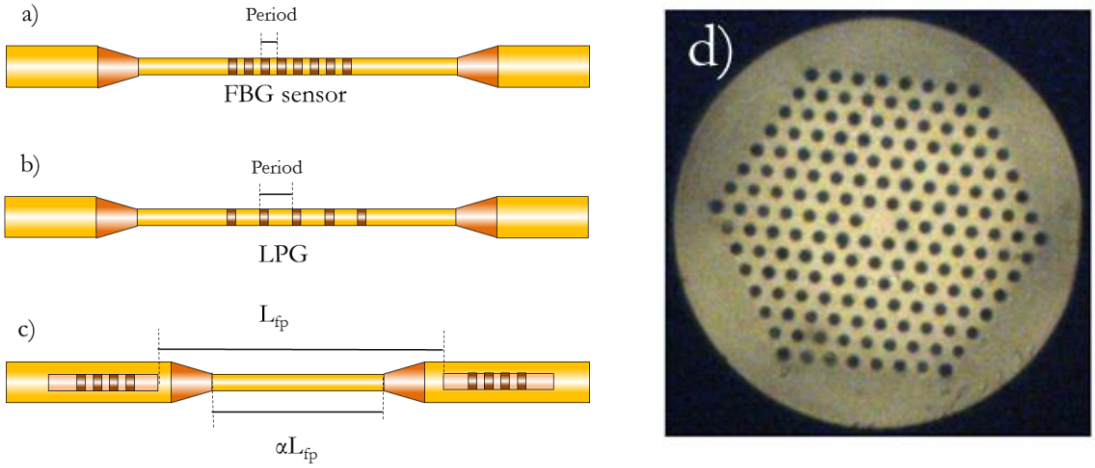

Fig. 1.11: *Schematic illustration of a) FBG inscribed in a fiber, b) LPG structure, c) Fabry-Perot cavity based on two FBGs and d) cross section of a PCF.*

Interferometric sensors

There are a wide variety of optical biosensors based on interferometric methods, such as Mach-Zehnder interferometers (MZI) [ZOU08], Young interferometers, Hartman interferometers, Bimodal waveguide interferometer [ZIN11] (this structure will be further explained in chapter 5, where its properties will be compared with other low-cost sensing platforms), or dual polarization interferometer (DPI, commercialized by Farfield [FAR13]). Generally, the fundamental working principle of these structures for sensing purposes is simple: the optical path is divided in two and each route will undergo a different phase change due to the interaction (or not) with the target analyte; then these two paths are recombined and a given interference signal will be exhibited. Fig. 1.12 schematically depicts a MZI-based sensor, where we can see that the access waveguide is split in two and only one of them will be in contact with the target analytes. Then, both waveguides are recombined at the output and the output signal, which will be determined by the phase difference between the two paths, will be governed by the equation:

$$I_{out} = \frac{I_{in}}{2}(1 + \cos(\Delta\varphi(\alpha))), \tag{1.1}$$

where I_{in} and I_{out} are the input and the output power intensities respectively, and $\Delta\varphi(\alpha)$ is the phase difference between both propagation paths due to variations in the optical length, which include the variation in the effective refractive index for the sensing arm when the detection is performed.

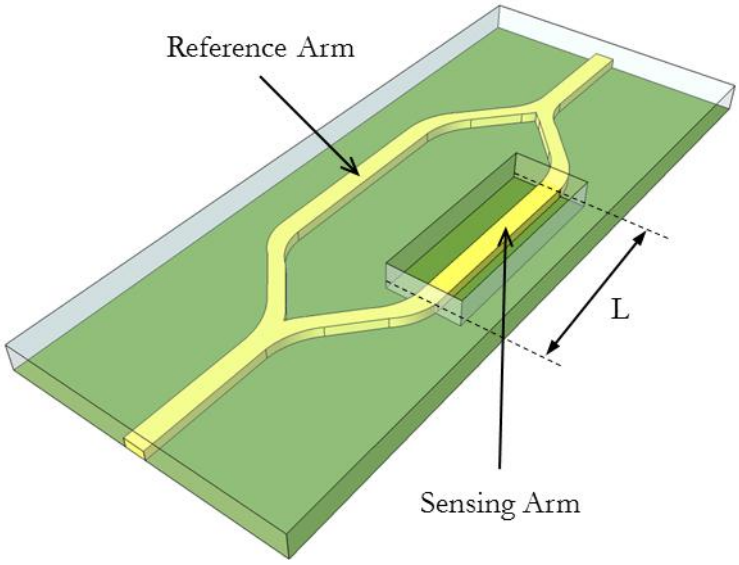

Fig. 1.12: *Mach-Zehnder interferometer sensor.*

MZI-based biosensors are one of the more widely used interferometric sensing structures in the context of planar integrated photonic technology. Integrated MZI sensing devices have been demonstrated in a wide variety of materials, ranging from silicon oxide [CRE10], silicon nitride [SEP06], silicon on insulator [DEN11] and even polymers [BRU11]. Many groups have reported different applications using integrated MZI-based biosensors, such as peptides detection [CRE10], antigen/antibody detection [DEN09] and label free detection of ssDNA [ESI05]. Moreover, multiplexed measurements have been demonstrated by employing up to 16 sensors in parallel implemented in works reported by the National Research Council of Canada [DEN11].

Plasmonic sensors

Plasmonic methods are based on the use of Surface Plasmon Waves (SPW) [SIP13], which are a charge density oscillation that occurs at the interface of two media with opposite dielectric constants, e.g. a metal and a dielectric. In order to excite this electromagnetic surface wave it is necessary to insert photons in the interface, generally by using a prism-coupling configuration as shown in Fig. 1.13. At determined angle and wavelength, the optical evanescent wave matches with the SPW producing the coupling of the photons to it. The wavelength and the angle of the coupled optical beam are highly dependent on the refractive index of the vicinity on the metal layer and therefore any change in the surface produced by a binding event or a refractive index alteration will provoke a variation on the resonant angle and/or wavelength. Different aspects related to the SPR sensors are described in several review articles along the years [SCA10, PET11, SIP13]. It is worth

noting that, strictly speaking, plasmonic biosensors are not evanescent field biosensors; however, the interaction of the SPW with the target analytes can be considered analogous to that type of sensing structures.

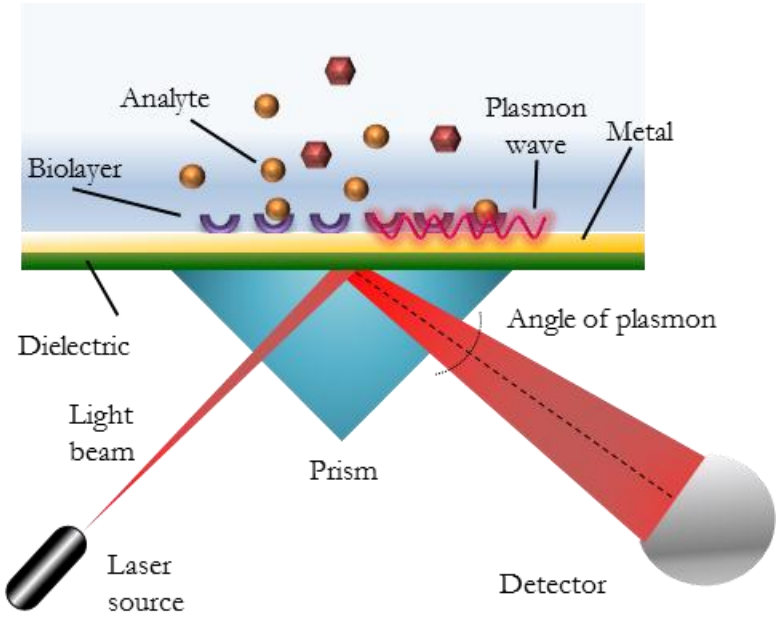

Fig. 1.13: *Schematic representation of a SPR sensor based on prism coupled configuration.*

The fact that a prism is required in the basic configuration for coupling to the SPW is a big limitation of this system, since this element is bulky and difficult to integrate [ZHA11]. For this reason, different configurations for the excitation of the SPWs have been proposed in the last years such as waveguide coupling [AKO12] or fiber polished coupling.

The basic SPR sensing technique is limited by its low integration level due to the elements required for the coupling. In order to increase the multiplexing level of the technique we can find the SPR imaging (SPRi) technique [STE04]. This technique is based on the same fundamental principles of SPR but a CCD detector is employed to monitor simultaneously several binding events on the same surface instead a simple power detector. A broad-beam monochromatic polarized light from a laser source is used to illuminate the functionalized surface and a CCD camera provides the assay information measuring the power of each spot. However, the implementation of the SPRi technique for multiplexed detection of different biological substances causes a reduction of the limit of detection because the optical spot must be larger in order to illuminate the whole sensing area.

Another approaches related to plasmonic sensors are those based on localized surface plasmon resonances (LSPR) [SEP09]. LSPR are collective electron oscillations confined in the edge of metal nanoparticles introduced in the surface of the sensor. The metal nanoparticle exhibits a spectral resonance of the LSPR dependent on the size, shape, and local dielectric environment

when an optical excitation incides. Therefore, the nanoparticle scattering provides valuable information of the surroundings of the nanoparticles, leading to an enhancement of the sensitivity of the device.

In conclusion, plasmonic-based sensors (i.e., SPR, SPRi and LSPR) have demonstrated to be a robust platform for the label-free detection of a wide range of molecules. This technology is characterized by its maturity, high sensitivity and good reliability, what has led to the production of several commercial equipment based on it, such as those by Biacore [BIA13] or the Spanish company Sensia [SEN13], whose systems are shown in Fig. 1.14.

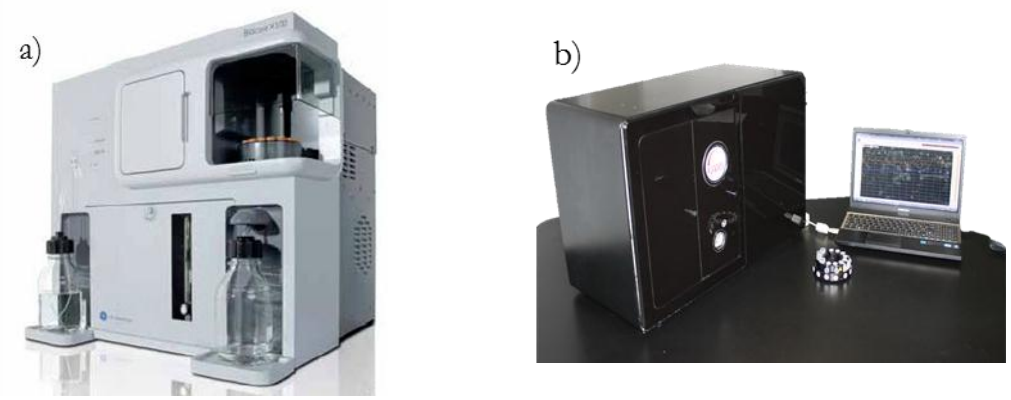

Fig. 1.14: *Commercial equipment based on SPR technology, a) X100 from Biacore and b) Indicator from Sensia.*

Whispering gallery sensors

Optical resonators for sensing technology have been under intensive investigation during the last decade; many works related to this field can be found in some reviews dealing with this topic [ZHU10, HUN10, PAS13]. In a whispering gallery mode (WGM) structure, the light wave is almost perfectly guided in a rounded-shape element by optical total internal reflection. However, the curved boundary between the guiding structure and the external media also provokes the appearance of an evanescent wave at the surface of the structure, which is used to perform the sensing. The existence of analytes around the sensor changes the effective index of the resonant mode and its optical properties as well.

Adversely to what occurred in interferometric biosensors, the interaction with the molecules in WGM sensors is no longer determined by the physical length of the optical path, but rather by the number of the roundtrips of the light inside the cavity. Therefore, the effective interaction of the sensor with the target analytes will be related with the quality factor (Q) of the cavity, and consequently resonators with high Q are desired. High Q factors imply sharper resonances and thus higher interaction times with the molecules on the surface of the structure. As a result, optical resonator sensors exhibit similar or superior performances than interferometer or waveguide based sensors. WGM-based sensing structures are categorized in ring resonators (RR),

microtoroids [ZHU09], microspheres [VOL08] and optofluidic RR (OFRR) [SUT08] among others. Fig. 1.15 schematically depicts these WGM-based sensing structures.

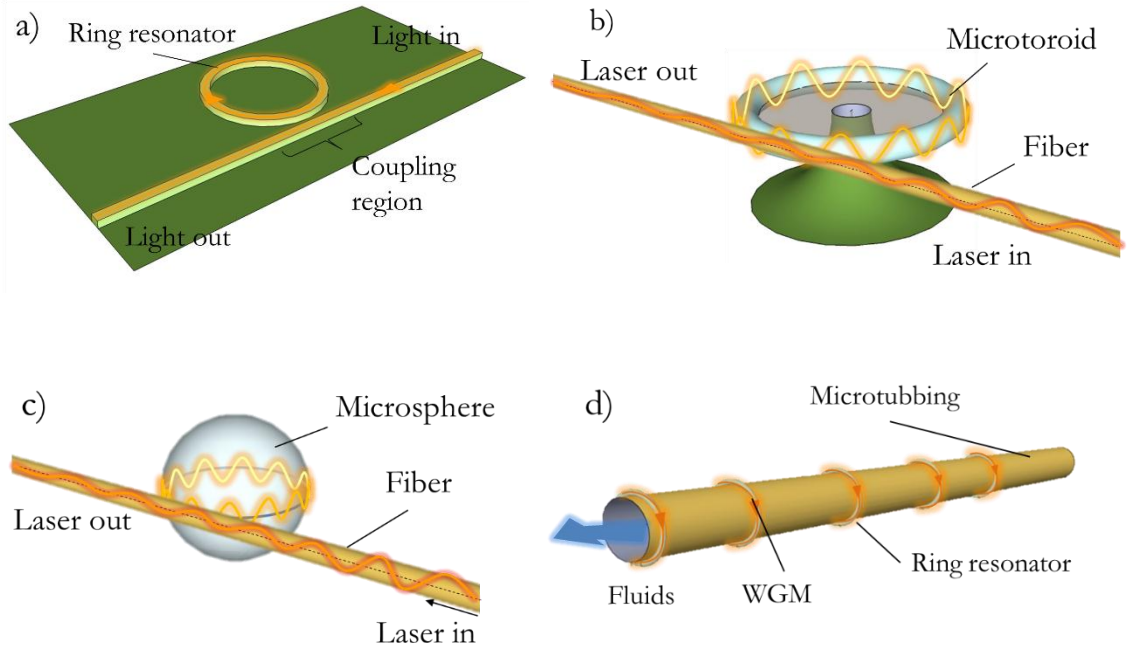

Fig. 1.15: *WGM-based sensing structures: a) planar RR b) microtoroid, c) microsphere and d) OFRR.*

Chapter 4 of this PhD thesis is focused on photonic sensors based in planar optical RR, where their operation principle and performance will be extensively described. Moreover, an overview of the state-of-the-art for this technology will also be introduced. Concerning other WGM-based sensing structures, microspheres can support the confined light in a very small dielectric volume. These structures are characterized for their extremely high Q-factors due to their low surface roughness, what leads to extremely low detection limits. However, not all the bound analytes to the sphere contribute to the shift of the resonance and therefore a large amount of analytes is wasted. A variation of planar RR are microtoroids. These structures are not located on the substrate surface but in an elevated position using a post, what difficult their integration and decrease their robustness due to their fragility. To obtain such structures complex and accurate fabrication processes based on reactive ion etching (RIE) techniques are required. The last type are OFRR which are micrometer sized tubes generally fabricated in silica [WHI09] with the ability to support different optical resonant modes to perform the sensing. The main advantage of these structures is that the target aqueous or gas sample is directly flowed through the tube itself, thus allowing the use of the same structure for the sample delivery and for its analysis.

Photonic crystal sensors

PhC are dielectric structures that present a periodicity in 1, 2 or the 3 dimensions. Due to the multiple reflections caused by the periodicity of the structure, a range of wavelengths cannot propagate through the material. This range of forbidden wavelengths is called photonic bandgap (PBG). By modifying one or several elements from the lattice, photonic defects can be created within the structure and insert one or several optical modes within the PBG. These defects can be mainly linear, leading to the creation of a photonic crystal waveguide (PhC-WG) [SKI07], or punctual, leading to the creation of a PhC cavity [LEE07]. The spectral response of these structures is highly dependent on the refractive index of the environment and therefore any change due to a molecular binding event will induce a shift in the transmitted or reflected spectral response. In addition, the propagation velocity of the modes is slowed down for certain wavelength ranges, yielding almost zero velocity. Such effect, known as slow-light effect, will enhance the interaction of the optical signal with the sample due to the longer travel time through the sensing structure, and the increase of the signal amplitude due to compression of the optical field in the defect region [FIG11, BAB08]. Although PhC technology is in its initial stages of development, several review articles discuss the great potential of this platform compared with other structures [WAS11, PAL12].

In this PhD thesis, chapter 3 will focus on 2D PhC structures for biosensing, whereas chapter 5 is devoted to a novel low-cost sensing approach using 1D photonic structures. More details about PhC structures and their particularities will be given in these chapters, as well as a deeper introduction to the state-of-the-art and the recent progress related to PhC based biosensors.

1.4 Requirements of a biosensor

In order to compare different kinds of biosensors, it is necessary to provide a list of the desired requirements that will determine the performance of the sensing device. Taking this into account, the suitability of a biosensor for a particular application will depend on its performance across a variety of these metrics. For certain application fields, some requirements will be very strict whereas for others, they will be less restrictive or even not important. Although some of these specifications can be defined numerically (either by means of theoretical or experimental calculations) other characteristics are more subjective or simply comparable between available sensing technologies. In the following list, we have selected a number of parameters that are usually considered to evaluate the performance of a biosensor (photonic or not):

- **Bulk sensitivity:** indicates how much the sensor's output changes depending on the homogeneous change of the medium; for example, in an optical sensor, it will depend on the

homogeneous variation of the refractive index. For optical biosensors the sensitivity is directly related with how efficient is the interaction between the light and the matter.

- **Sensitivity:** is given by the relation between the variation of the output signal for a certain chemical/physical variation in an experiment and the amount of the analyte. Besides the sensitivity of the transducer itself, this parameter depends on other factors such as the recognition layer, the affinity of the molecules, the buffer conditions or the fluidic architecture.
- **System noise:** is defined as the variation of the signal in a static measurement. To calculate the resolution, the noise of the system must be characterized in a steady-state condition without any intentional variation of the sensor. The signal noise is typically measured as the standard deviation (σ) of the stabilized signal.
- **Detection limit:** is the lowest concentration or amount of analytes that can be detected. The detection limit in optical sensors can be defined in different units such as in refractive index units (RIU) to characterize the bulk performance of an optical sensor, in surface mass density, in total mass or in analyte concentration.
- **Selectivity:** this parameter is highly dependent on the chemical modification of the transducer and it is the ability to discriminate the target analyte among other substances presented in the analysed sample. A proper functionalization strategy prevents from other particles being attached or adsorbed to the surface while provides a high affinity towards the target analytes, which will bind to the receptors.
- **Dynamic range:** is defined as the range between the largest and the lowest values of the output signal of the sensor that can be directly related with sensing events.
- **Throughput or multiplexing level:** indicates the capability of the sensor to perform several parallel experiments in the same assay for the detection of different analytes or properties of the target sample. Multiplexing approaches are used to obtain higher amounts of information that indirectly reduces the cost per assays and provides a more reliable and complete analysis.
- **Cost:** this parameter must be divided in two different concepts: the cost of the read-out system and the cost of the analysis chip. Typically, the read-out system is quite expensive due to its complexity (e.g., need of sources and detectors); however, it can be reused multiple times. On the other hand, analysis chips are many times designed to be disposable (i.e., for a single use), so it is interesting to minimize their cost.
- **Portability:** this is a subjective parameter that determines the possibility to move the sensing device to different locations to carry out in-situ measurements. This requirement may be crucial for those applications where a rapid response is needed (e.g., chemicals detection, critical information from a patient in an ambulance).
- **Sample volume:** refers to the amount of the sample that is required for the analysis in order to obtain a reliable result from the sensor. In some application fields, such as water analysis,

this parameter is not important, but it may be a significant constrain for others where the target sample is scarce or expensive (e.g., blood analysis for newborns).

- **Energy consumption:** this parameter determines the total energy that is necessary to carry out the assay. This requirement is related to the portability of the device since the higher the consumption the shorter time the device can be used in the desired location. In addition, energy consumption is currently a hot topic that needs to be taken into account.

1.5 Lab-on-a-Chip devices

The concept of lab-on-a-chip LOC was introduced for the first time in the early 80's. LOC devices, which are also known as micro total analysis systems (μTAS), are envisaged to perform regular laboratory functions such as filtering, heating, mixing and detecting the target analytes using a very small device. In the same way that the size of computers has evolved from big rooms with enormous mechanisms to current high-performance handheld devices such as smartphones, it is expected to deliver within the next few years very small and portable LOC devices with comparable or even better performances to those for currently used in lab-based procedures.

Fig. 1.16 schematically depicts a generic LOC device (with photonic-based detection) where several potential processing steps are implemented in different areas of the chip. The two main pillars of LOC devices are microfluidic systems and integrated micro/nano-sensors. Microfluidic systems enable the implementation of revolutionary elements for the manipulation and processing of small volumes of fluids by employing channels, mixers, valves, filters, lids, pumps or heaters. This field is under an exhaustive research and provides new functionalities every year. Integrated micro/nano-sensors (e.g., photonic biosensors) allow the detection of much reduced concentrations of the target analytes present in the sample coming out from the microfluidic sample preparation stage. The combination of these two main technologies (microfluidic systems for sample preparation and integrated micro/nano-sensors) allows performing analyses that, in normal conditions, may not be performed using standard laboratory procedures.

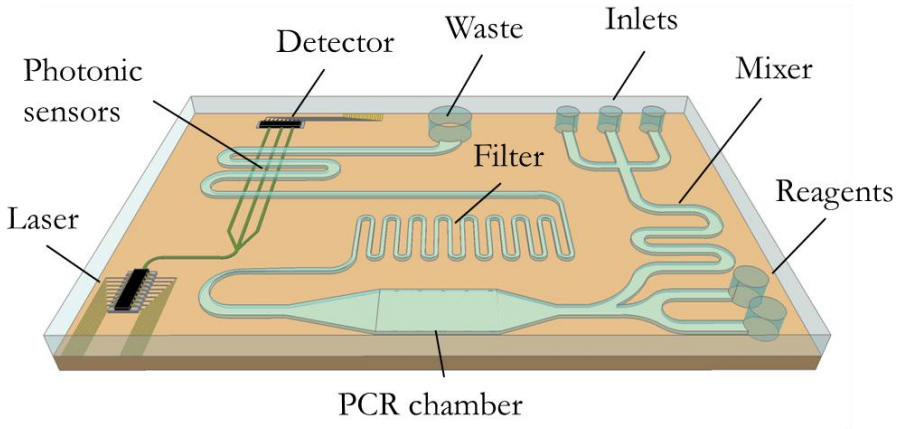

Fig. 1.16: *Schematic illustration of a generic LOC device with photonic-based detection. Any function required for the preparation of the target sample before carrying the detection out is performed in the same chip.*

Pure sensing devices must be differentiated from LOC devices. While sensing devices mainly consider the detection process itself, LOC devices also consider the implementation of any other additional treatment/processing step over the input sample to perform a higher performance analysis in a direct and simpler way. For example, some current sensors such as glucose or pregnancy tests simply consist on a membrane or paper strip with proper immobilized receptors, so that the target sample only needs to be embedded into the strip and the presence of the target markers is indicated by the reaction with the receptors (usually, electrochemical or colorimetric changes are produced). Despite the usefulness of this kind of sensing devices, which can be even used for point-of-care (POC) testing, they cannot be considered as LOC devices due to the lack of other processing steps of the sample apart from the detection itself. In addition, these sensing devices usually provide a very limited number of output parameters (usually, a single parameter is analysed) whereas LOC devices are expected to deliver a wide range of output parameters (i.e., high throughput), which allow to provide a more complex, complete and reliable result from the analysis.

Besides the size reduction itself, the miniaturization of LOC devices provides many advantages compared to current analysis technologies. For example, the volumes of sample and reagents required to carry the analysis out are extremely reduced, just requiring volumes even below the order of μl instead of several ml as for laboratory procedures; this fact will be translated into a significant reduction in the cost per analysis as well as a reduction in the generated waste. Other advantage of LOC devices is the significant reduction in the time required to perform the analysis since the reduced size of the processing structures and the reduced sample/reagents volumes allow that the processing steps required can be implemented in a fast and efficient manner. Finally, since novel high sensitivity micro/nano-sensors are integrated within these LOC devices, they will allow the detection of extremely low concentrations of the target analytes. However, miniaturization may

also give rise some problematic issues. For instance, miniaturization of microfluidic elements is not trivial since this size reduction causes a different and more complex fluid behavior (e.g., mass transport limitation, capillarity effects, etc.) as well as a higher influence of other issues such as the presence of microbubbles within the system. A complete list of advantages and drawbacks of LOC technology is provided at the end of this section.

The growth of LOC technology has been closely related to the development of the micro-fabrication technologies required for the development integrated circuits (IC), which have been successfully applied to the manufacturing of many LOC devices. The use of the same technology for the fabrication of both the microfluidic sample preparation elements and the micro/nano-sensors allows their perfect integration in a direct manner, thus providing a final complete functionality.

In conclusion, LOC devices are envisaged to become the next generation of "analysis laboratories" in a relatively short future. Their unique properties provided from merging different technologies with a multidisciplinary approach open the route to novel high performance equipment which would attract the attention from the most relevant companies. However, these devices are relatively recent and although many achievements have been accomplished during recent years, further developments are still required in all the related fields in order to increase their practical and commercial potential. To summarize the performance of the current LOC devices hereafter we list their main benefits and weaknesses detected throughout the last years.

1.5.1 Advantages of LOC devices:

- **Compactness:** miniaturization of LOC has allowed to include all the steps required to carry out an analysis into a single chip. In addition, the use of some materials and processes such as silicon and CMOS fabrication technology respectively allows benefiting from all the advantages of those technologies.
- **Throughput:** another benefit derived from the reduction of the device size is the possibility of performing multiple simultaneous analyses in a single assay. Furthermore, the integration of multiplexed sensors also allows using reference sensing structures to compensate non desire effects in the signal such as noise or unspecific binding.
- **Faster measurements and lower sample consumption:** microfluidic architecture reduces delivering distances and dead volumes thus improving the performance of the functionalities of the device (e.g., filtering, heating, mixing or sensing). Moreover, the ratio between the sample volume and the sensing surface increases thus leading to a significant reduction of the consumption of sample and reagents.
- **Robustness:** fabrication procedures, especially those from standard and mature CMOS technology, provide high quality and reliable devices. Chips fabricated in commercial

foundries guarantee obtaining minimum physical variations and maximum performances to carry the analyses out.

- **Simpler and automated measurements:** in LOC devices, the process is designed to be performed automatically without the need of any human interaction once the sample has been introduced into the device, thus reducing errors and problems.
- **User friendly:** one of the objectives of LOC devices is to allow that any person is able to carry out tests that currently can only be done by a specialist. LOC devices will provide simple output information that can be comprehensible by a non-expert.
- **Portability:** due to the size reduction of LOC devices, all the complex functions required for the analysis are carried out using a chip-sized system. This size reduction allows carrying out the measurements in-situ for those applications where it is necessary.
- **New opportunities for the IC industry:** LOC devices open the possibility for the micro/nano-technology industry to access to a new market with a high potential of success for the next decades. The mature CMOS industry has the possibility to manufacture new LOC devices using its currently available facilities, thus allowing a direct entrance into this market with a relatively reduced investment.

1.5.2 Drawbacks of LOC devices:

- **Novel technology:** due to technological limitations and lack of maturity, LOC devices developed up to now are relatively simple. Currently, this technology is at its initial stage and, despite several commercial products already exist, it is necessary to enhance the performance in order to obtain more competitive devices with more complex and better functionalities.
- **New physical and chemical effects:** miniaturization of the structures leads to the appearance a new nanoscale effects. These issues involve capillarity forces, surface roughness, diffusion or mass transport limitations. Therefore, it requires studying thoroughly these effects in order to minimize their limitations.
- **Accuracy and precision:** miniaturization of the structures requires smaller features, less roughness and higher accuracies in the micro/nano-fabrication to obtain the required performances. Therefore, new fabrication techniques should be studied and developed in order to allow the implementation of more complex functionalities.

1.6 Application areas of biosensors and LOC devices

One of the main properties of biosensors and LOC devices is their high versatility to be employed in many application areas, including medical diagnosis, environmental monitoring or food control. Herein, we present some of the most common end user applications of biosensors and LOC devices, especially considering the use of optical/photonic technology, which can provide several advantages compared to other existing detection technologies.

1.6.1 Medical diagnosis

Probably, the main area in which biosensors and LOC devices are expected considerably to change the current *modus operandi* for carrying analyses out is medical diagnostics. The main target within this field is the development of the so-called POC devices to be used to provide in-situ, rapid, reliable, minimally-invasive and early information about the patient's health status in order to determine the most appropriate treatment for him/her. Therefore, these novel devices have the potential to change the perspective of the healthcare from curative treatments to preventive diagnostics. Within this context, optical/photonic biosensors have demonstrated to be a suitable platform for developing POC devices due to their high integration level, high sensitivity and reliability.

The use of this type of POC devices has been greatly benefited from current advances achieved in the field of the discovery of novel disease biomarkers. These biomarkers, which can be found in human samples (i.e. blood, serum, plasma, urine, etc.), permit an early and minimally invasive diagnostic of an ever-widening range of diseases. For example, currently there is an enormous concern about cancer-related diseases, for which their diagnosis usually rely on invasive techniques (e.g., biopsy, colonoscopy), which need to be carried out by qualified personnel, require hospitalization of the patient, and most of the times only allow to diagnose the cancer when it is at an advanced stage. Fortunately, several biomarkers related with cancer diseases have been identified (e.g., PSA, HER-2, CEA, miRNA), which allow or will allow an early and minimally-invasive diagnosis of the disease [DNI91, EBE02, ROS98]. The possibility of the detection of such biomarkers using highly-sensitive optical/photonic biosensors for the detection of these disease-related biomarkers will open the door to a more efficient and reliable medical diagnosis.

Another important application of POC devices is their use in developing countries, where population has not an easy access to medical facilities. In these countries, infectious diseases are one of the major causes of death among the population. The use of simple and low-cost POC devices would allow to diagnose these diseases and to immediately provide the proper treatment (which most of the times is very simple and accessible), thus preventing most of these cases and reducing the rate of death. Low-cost and rapid optical sensing devices would allow providing affordable

assays to screen the majority of the population of a region improving the effectiveness of the treatment. In addition, with the multiplex capability of optical biosensors it would be possible to perform multiple detection in a single assay, leading to the detection of several diseases simultaneously and reducing the cost of the analysis.

As a consequence, of these promising advantages of biosensors and LOC devices in the field of advanced medical systems, many research institutions and healthcare companies are focusing their efforts towards the development of novel systems for fast analysis. Some commercial examples of this type of devices are those developed by companies such as Centice which is based on Raman spectroscopy [CEN13] (see Fig. 1.17). This system allows the detection of more than 3600 substances without the necessity of skilled personnel.

Fig. 1.17: *Mobile field lab 3000 from Centice for drug detection in blood.*

1.6.2 Environmental control

The Earth provides the required ecosystem to allow the life for human population, animal and vegetal species. Over the past decades scientist have remarked the importance of protecting our environment; as a result, the environmental monitoring has become one of the prior issues for many governments and organizations. Despite all the efforts spent, the environment is constantly under a great variety of threats mainly caused by human action. Household, industrial and human activity may jeopardize the status of the environment and consequently the life of all the species within the ecosystem including plants, animals and even human population. For instance, the extensive use of herbicides and pesticides in agriculture fields, golf courses and green areas in city parks in order to prevent from plagues has provoked an increasing level of pollutants in the environment that can expose to risk the basic resources (including water resources).

Fig. 1.18: *Environmental pollution caused by factories.*

Within this context, biosensing devices based on optical transduction offer the possibility of performing an on-site analysis of the environment. Their extremely high sensitivity would permit to perform an efficient monitoring of the presence of a wide variety of pollutants and compounds in the water, air or soil in order to control the fulfilment of standard requirements set by governments and environmental regulatory agencies [BAR02].

Besides their use for the environmental monitoring of the ecosystem, optical sensors can also be employed in other situations related with the environmental quality inside buildings [MAU08]. For instance, artworks in museums, galleries or churches can be affected by environmental conditions and chemical factors that can endanger their conservation and substantially reduce their lifespan. In case we want to act in advance to avoid their deterioration, it is necessary to control the parameters inside the rooms where they are exposed. Optical sensors would be capable of taking into account the overall parameters that can affect the artworks and thus anticipate preventive actions to conserve them. Distributed sensors such as optical fibers as well as integrated sensors have demonstrated to be suitable to collect this type of environmental information.

1.6.3 Drug discovery

In pharmaceutical industry is indispensable to perform many assays in order to develop and examine the reliability of new drugs before being released into the market. Therefore, it is fundamental to understand and study molecular interactions that are under research in the development process of new products. For that reason, huge amounts of Euros are invested to obtain platforms that are capable to deliver the information related with the binding kinetics and the affinity between the different studied compounds. The ability to identify, characterize and optimize the molecule recognition processes in assays is crucial in early stages for the research in new products to obtain a high therapeutic efficiency.

Fig. 1.19: *The efficiency of the future drugs is related to the novel methods that currently are applied. Optical sensors permit to study the reactions of new formulas.*

Some of the currently available commercial equipment for drug discovery employs dyes or fluorescence labels to perform assays. However, as previously indicated, these elements can interfere in the assay (e.g., occluding the binding site for another molecule) and prevent from a real-time observation of the molecular interactions. The use of optical label-free biosensors avoids these problems and enables the development of reliable and highly sensitive platforms suitable for its application in this field [COO02]. In addition, their multiplexing capability permits to extract a high throughput of information related to the molecular association among different substances, significantly reducing the number of assays required for the analysis as well as the time required to obtain the results.

1.6.4 CBRN detection

Chemical, biological, radiological and nuclear (CBRN) threats are one of the main concerns in several countries around the world for homeland and security protection. Hostile attacks have been evolving towards much more complex operations using substances that can be highly lethal and have impact over large regions. Preventing these situations, including bioterrorism attacks, and being able to warn the population before they can be exposed to the risk can save numerous lives. Optical sensing technology allows the development of systems for the real-time and highly-sensitive recognition of this type of threatening substances.

The use of optical biosensors is of special interest for the detection of substances that are potentially ignitable. Whereas the use of electronic devices may produce sparks, this danger is completely prevented by using optical sensors, thus minimizing the risk of explosion. Another interest application for photonic sensors is their use for explosives detection, where very small traces of the explosives need to be detected for their identification [ORG10]. Furthermore, LOC

devices based on integrated photonic circuits can perform automated and remote measurement of such substances without the necessity of endangering the life of the specialists [WIL09].

Fig. 1.20: *In the event of a CBRN attack, a fast response is desired in order to maintain the hazard under control.*

1.6.5 Food testing

Food quality and safety control are essential issues in order to obtain healthy products. For that reason, there are strict regulations to control the food industry. On one hand, the need of the food manufacturers to guarantee the safety, quality and traceability of their products until their purchase by the consumers has been growing remarkably during the last years. Consequently, they have been employing several additives to maintain the product in perfect conditions until its consumption. On the other hand, consumers also expect to acquire better products from the market without any substance that can harm their health and without paying an extra price. Nevertheless, some of the elements that are added by the food producers to their products in order to enhance their aspect or taste may cause health problems at high concentrations; hence these concentrations must be under constant supervision. To control the appropriate condition of the food, several parameters can be monitored, including pressure, temperature, water or microbial concentration among others [KRE01]. In this field, optical sensors offer a suitable platform for the implementation of more complete and rigorous analyses that cover a wider range of bio-chemical parameters

For instance, the quality of food and beverages is highly dependent on the oxygen levels during the packaging process. The presence of this element in the package may provide the viability in the growth of many types of pathogenic bacteria that can be harmful for the human health causing multiple diseases. Thereby a real-time monitoring of the oxygen concentration during the packaging process will allow determining the quality level of the final product with remarkable

accuracy. Optical sensing technology has already demonstrated the ability of measuring in-situ the oxygen concentration in the environment while packaging the products [GRS10].

1.7 Silicon photonics

The increasing interest in moving from bulky components to integrated devices has boosted nanophotonic technology, which is the optical alternative to current microelectronic devices. Whereas conductor stripes are used to guide the electrons in electronic devices, semiconductor materials are mainly used to create optical structures comprising photonic circuits. Silicon (and its derivatives) is the most widely employed material for the fabrication of integrated photonic structures due to its compatibility with CMOS (Complementary Metal Oxide Semiconductor) fabrication processes from the microelectronics industry. This fact has led to the creation of the so-called silicon photonics technology platform. Since the emerging of the semiconductor technology in the 50's, silicon has been employed as main material in order to develop small microelectronic functional structures. All the extensively progress in manufacturing tools in the realm of the semiconductor technology during these years has enabled the possibility to fabricate structures with feature sizes in the nanometer scale by using lithographic equipment that are perfectly suitable for photonic structures.

Although most of the work done using the silicon photonics technology has been mainly focused on the development of devices with application in the fields where the electronic bottleneck is a problem (e.g., communications, interconnects or signal processing), this technology is demonstrating to be very convenient for biosensing purposes as well. Photonic biosensing devices have demonstrated to provide many advantages compared to other sensing technologies such as high sensitivity, low detection limit, label-free operation or high integration level. Therefore, after having introduced in this chapter several concepts related with the field of biosensing devices (i.e., elements and requirements of a biosensing device, transduction methods, LOC technology, and application fields), now we will briefly introduce the material and fabrication platform that we have employed in the course of this PhD work.

The most common implementation of silicon photonics is SOI (silicon-on-insulator) technology, which has been used for the development of the sensing structures used in this PhD work. As depicted in the Fig. 1.21, a SOI wafer mainly consists of a thin layer of silicon (of few hundreds of nm) which is on top of a layer of silicon oxide (of several microns); these two layers are created over a thick silicon substrate (around 700 μm) that provides mechanical stability. Due to the high refractive index difference between the top silicon layer, the silicon oxide lower-cladding and the air upper-cladding (~ 3.45 vs. 1.45 vs. 1), light is highly confined in the vertical direction within the top silicon layer, which will be used to create the photonic structures. Lateral

confinement is then achieved by etching two air trenches in the silicon, as shown in the inset of Fig. 1.21, thus defining an optical waveguide where light will be fully confined (i.e., vertically and laterally). Depending on the dimensions of the core of the waveguide, one or several modes will be excited within it; generally, it is sought after the proper dimensions to obtain a single mode waveguide in order to avoid interferences between propagated modes (usually widths in the range of 500 nm are used). Moreover, a larger evanescent field appears for single mode waveguides due to their smaller dimensions, what is suitable for the development of integrated photonic biosensors. On the other hand, a core size reduction has the counter back of an increase in the propagation and radiation losses. This is the reason why multimode and single mode sections are usually combined for the development of integrated photonic circuits (multimode sections for signal distribution and single mode sections for the implementation of optical processing or sensing functions).

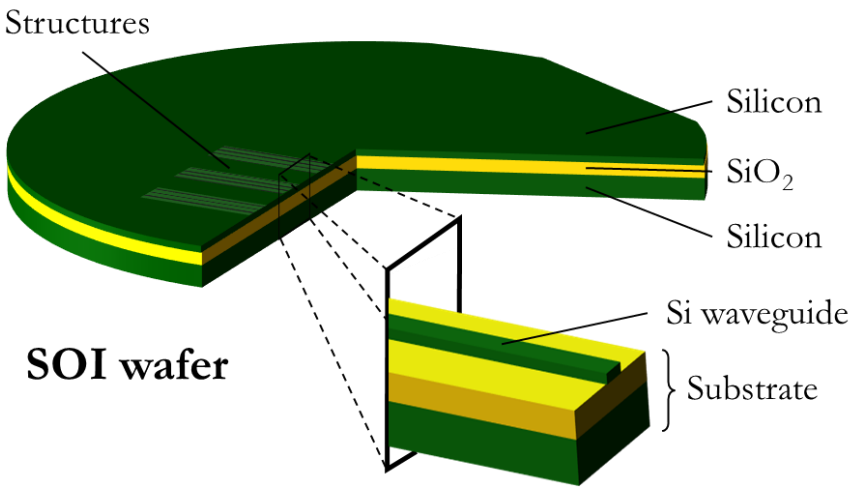

Fig. 1.21: *Layers distribution of a SOI wafer. The inset schematically depicts a SOI waveguide.*

Another consequence of the size reduction of SOI photonic structures is the possibility to integrate many structures and components in a single chip. Therefore, nanophotonic-based devices not only can perform a single functionality, but it exists the possibility of embedding multiple passive and active structures in a chip, thus opening the route to carry out a complete signal processing being able to substitute in the future bulky electrical equipment by optical integrated devices. For the case of photonic sensing devices, this size reduction would allow the integration of a large number of sensing structures in a single chip, thus permitting the possibility to provide multiplex detection for the simultaneous screening of several target analytes in a single analysis. For example, assuming a sensing structure size of the order of 100 μm^2, we might be able to ideally integrate up to 1000 sensors on a chip of just 1 mm^2 size, demonstrating the high integration level due to the high refractive index contrast of the SOI platform. Furthermore, these small dimensions will also be translated into an enhancement of the sensitivity of the sensing structures, since the smaller its footprint is, the less amount of molecules will be required to carry the detection out.

Finally, the integration of a huge amount of sensors in a single chip, combined with the relatively reduced cost and fabrication easiness of mass-manufacturing CMOS technology, also would allow a significant reduction of the cost per chip and per assay. The fabrication of inexpensive sensing chips is highly required in several applications such as in healthcare, where the use of disposable chips is practically mandatory to avoid problems like cross-contamination. In addition, other fields like environmental control will also benefit from the use of disposable chips, such as for example for the realization of massive monitoring campaigns to control the environmental quality of water or air resources.

1.8 Objectives of the thesis

The overall objective of this PhD Thesis was the development of a novel sensing technique based on the use of PBG structures where their interrogation is done without the need of tunable elements, thus reducing drastically the cost, the size and the complexity of the final sensing system. However, until accomplishing this objective, we have also had to work in other tasks such as the development of different types of photonic sensing structures (PhC- and RR-based sensors), their experimental interrogation using typical spectral-based techniques, the implementation and optimization of proper experimental set-ups for the interrogation, or the development of fluidic sample delivery systems. The main specific objectives that have been accomplished in this work can be listed as follows:

1. - Development of the highly sensitive photonic transducers

We have designed and fabricated high-sensitivity photonic structures that are able to measure extremely small refractive index changes on their surface. In this work, we have studied the fundamentals of the photonic structures that we have employed such as PhCs, RRs and corrugated waveguides. These structures exhibit several benefits such as slow-light phenomena in case of PhCs and corrugated waveguides, or the circulating nature of resonant modes in RRs. In both cases, these phenomena provide an increment in the interaction between the light and matter, giving rise an enhancement of the sensitivity. The work that was carried out was focused on the modelling of the structures employing several simulation tools. The analysis of each structure is addressed in a different chapter: PhCs in chapter 3, RRs in chapter 4 and corrugated waveguides in chapter 5.

2. - Establishment of a proper route for surface chemistry modification

The second objective is related to the development and testing of different functionalization routes in order to provide the required specificity to the photonic structures. Such specificity is achieved by attaching proper biological receptors to the surface of the structures by means of a chemical modification protocol. This selectivity is crucial in order to determine the presence of the desired target analytes. Therefore, a trustworthy protocol for the attachment of the

probes is essential and must meet several constrains, such as the compatibility with the surface and being stable along the time. For the purpose of this work, two different approaches have been developed: one based on the use of an isocyanate-ended organosilane and the direct incubation of the receptors, whereas in the second approach, an epoxy-ended organosilane was used and the attachment was boosted with UV light. The work related with the development of the functionalization protocol is addressed in chapter 2.

3. - Implementation of a miniaturised fluidic delivery system

Optimizing the flow of the target sample over the sensing structures is an efficient manner to improve the limit of detection of the device. The flowed particles that are not interacting with the sensing structures are not contributing to the detection, and therefore, are wasted. For that reason, the study of different fluidic delivery systems has been other of the aims proposed for this PhD work. In addition, we have tackled the problem of the appearance of microbubbles by closing hermetically the circuit. We have developed a customized solution for each kind of structure and analysed different materials and shapes, starting with a micromechanically perforated metallic cavity and then employing more advanced microchannels based on a soft polymer package. Finally, we tested a SU8-based microfluidic channel fabricated on top of the structures that, besides delivering the flow to the sensing area, it allows protecting the structures from dust and damages.

4. - Development of an automated read-out platform

One of the main issues related with the use of photonic structures for sensing is the coupling of light to/from them. Therefore, we have implemented proper characterization set-ups for the interrogation of the photonic sensing structures, either using horizontal coupling or vertical coupling based on grating couplers. In addition, we have also worked on increasing the automation of the experimental protocol (e.g., by using an automatic fluidic switch) in order to be able to perform unattended measurements and avoiding the human interaction.

5. - Development of a novel power-based measurement technique

As previously indicated, the main objective of this PhD Thesis is the development of a novel highly sensitive photonic sensing interrogation method based on the use of photonic bandgap structures in which the read-out is carried out without using tunable elements. The principle of the technique is based on the continuous monitoring of the output power of the overlap between the broadband source and the edge of the sensor's response obtaining a real-time measurement. The work related with this objective is explained in chapter 5, both theoretically and experimentally. This technique gives rise a significant reduction of the cost and the size of the photonic equipment required for the interrogation, as well as the possibility to perform a real-time sensing.

6. - Validation of the complete sensing platforms

After the development of all the elements separately in the previous points (photonic transducer, chemical modification, fluidic delivery and read-out), the final objective of this PhD Thesis is the combination of all these parts in order to perform the validation of the whole system. The demonstration of the use of the photonic structures for sensing purposes was proved through several experiments from bulk measurements to monitorization of the hybridization of single-stranded DNA (ssDNA) and antibody detection as well.

1.9 Framework of the thesis

The work carried out along this PhD Thesis has been developed mainly in the Nanophotonics Technology Center (NTC) of the Universitat Politècnica de València, within the frame of the Biophotonics research line. The NTC has state-of-the-art facilities and highly skilled personnel for the development of photonic integrated circuits, what makes the NTC one of the top research centres in its field. In addition, the NTC has also state-of-the-art laboratories for the experimental demonstration of the photonic devices proposed in this PhD Thesis.

The author is currently a junior researcher in the NTC, with more than four years of experience in the field of photonics. This experience is mainly related with the development of photonic biosensors, what also includes other fields such as microfluidics, chemical surface modification and signal processing. During the course of this thesis, the author was granted with a Prometeo grant from the Generalitat de Valencia and a "Beca de especialización" from the Universitat Politècnica de València. In addition, the author had the possibility to join during three months the Photonics Research Group in the University of Gent, thanks to an Erasmus Mundus grant. The detailed work carried out by the author along this thesis is described in the annex A at the end of the document.

In the course of this PhD Thesis, the author has had the opportunity to work in several European projects related to the development of photonic biosensors, what has also allowed him to work together with several top-level European research institutions in a multi-cultural and multidisciplinary environment. Among these projects, we list the most important hereafter:

- FP6-SABIO (Ultrahigh sensitivity slot-waveguide biosensor on a highly integrated chip for simultaneous diagnosis of multiple diseases): This project was granted in the 6th European Framework Programme and had a total duration of 39 months. Its objective was to contribute to the development of intelligent diagnostic equipment for healthcare employing compact polymer and silicon-based CMOS compatible optical slot-waveguide structures. By immobilizing the receptors on the surface, the device offered the interaction

information between biomolecular complexes (antibody-antigen), reaching a surface concentration detection limit of 1 pg/mm^2.

- FP7-INTOPSENS (A highly integrated optical sensor for point of care label free identification of pathogenic bacteria strains and their antibiotic resistance): This project was funded by the 7th European Framework Programme under the ICT call. It had a total duration of 42 months, starting on September of 2009. INTOPSENS was a highly multidisciplinary project that involved several emerging fields including photonics, electronics, fluidics and biochemistry in order to contribute to the development of a high sensitivity biosensor. The main aim of this project was to demonstrate the feasibility of a rapid diagnostic test for sepsis disease at a POC by means of a label-free platform based on SOI photonic sensors with the ability to detect concentrations as low as 0.1 ng/ml. Our role in this project was related to the design, fabrication and characterization of the photonic sensing structures, including PhCs and RRs, and contributing in the integration between photonics, microfluidics and surface modification to develop a valuable sensor.
- FP7-BELERA (Reinforcing carbon nanotubes and photonics research cooperation between the Belarusian State University of Informatics and Radioelectronics and the European Research Area): This project was funded by the 7th European Framework Programme and it aims at increasing the cooperation between European research institutions and Belarus in the fields of carbon nanotubes and photonics. Among the main objectives related with this PhD Thesis, tasks targeting the integration of light sources and detectors with the photonic sensing structures are being carried out. Furthermore, we performed several visits between research centres in order to exchange knowledge and carry out joint experiments in the selected research fields.

1.10 Conclusions

In this chapter, we have introduced the concept of biosensor, which consists of different parts responsible of different tasks related with the detection. Mainly, a biochemical sensing device is divided in the transducer, the recognition layer, the sample delivery system and the read-out equipment. We have reviewed different technologies for the transduction method, from the maturity of the electrochemical sensors invented in the 50's to the new alternatives such as photonic integrated biosensors based on plasmonics or evanescent wave. It is noteworthy to indicate that the majority of the presented technologies have reached the market what clearly confirms the high possibilities to give rise a commercial product in this field. Regarding the

specificity of the sensing devices, it is provided by the recognition layer, which comprises the receptors that are attached to the transducer by proper chemical functionalization processes.

Among the different demands of a biosensing device, probably the two main requirements are the sensitivity and the limit of detection. The importance of other parameters will depend on the final application of the sensor. In addition, some of these requirements are subjective (e.g. compactness, portability) whereas others can be defined numerically (e.g. dynamic range, noise…).

In this chapter, we also presented LOC devices, which are devices capable to perform the analysis processes that are currently carried out in regular laboratories, but simply using a single integrated chip instead. These platforms are envisaged to be the next generation of sample analysis devices. Due to their benefits, LOC devices can be applied to a wide range of applications such as medical diagnosis, environmental control, drug discovery CBRN detection or food testing among others.

Finally, we have also introduced and commented the advantages of the technology platform that we employed in the course of this PhD Thesis, silicon photonics. Silicon is transparent to IR wavelengths, exhibits low losses, and provides a high index contrast with typical cladding materials (e.g., silicon oxide or air) that permits an incredible reduction in the size of the integrated photonic structures. Furthermore, its compatibility with typical CMOS equipment and processes allows adopting those from the standard microelectronics industry, thus enabling a mass fabrication of the devices and subsequently a remarkable reduction in the cost of each unity. Therefore, silicon photonics is possibly one of the best technology platforms to develop novel integrated photonic sensors.

References

[ACE13] www.aceabio.com, 2013

[AKO12] E.K. Akowuah, T. Gorman, and S. Haxha, "A planar waveguide surface plasmon resonance biosensor based on Otto configuration." in 2012 IEEE 4th International Conference on Adaptive Science & Technology (ICAST), proceedings, pp. 126-131, 2012.

[BAB08] T. Baba, "Slow light in photonic crystals." Nature Photonics, vol. 2(8), pp. 465-473, 2008.

[BAR02] C. Barzen, A. Brecht and G. Gauglitz, "Optical multiple-analyte immunosensor for water pollution control." Biosensor & bioelectronics, vol. 17(4), pp. 289-295, 2002.

[BIA13] www.biacore.com, 2013.

[BIO13a] www.biophysics.com, 2013.

[BIO13b] www.bioscale.com, 2013.

[BRU11] R. Bruck, E. Melnik, P. Muellner, R. Hainberger and M. Lämmerhofer, "Integrated polymer-based Mach-Zehnder interferometer label-free streptavidin biosensor compatible with injection molding." Biosensors & Bioelectronics, vol. 26(9), pp. 3832-3837, 2011.

[BUC11] K.R. Buchapudi, X. Huang, X. Yang, H.F. Ji, and T. Thundat, "Microcantilever biosensors for chemicals and bioorganisms." The Analyst, vol. 136(8), pp. 1539-56, 2011.

[CAN13] www.cantion.com, 2013.

[CAR06] L.G. Carrascosa, M. Moreno, M. Alvarez, and L.M. Lechuga. "Nanomechanical biosensors: a new sensing tool." Trac-Trends in Analytical Chemistry, vol. 25(3), pp. 196-206, 2006.

[CEN13] www.centice.com, 2013.

[CHE13] C. Chen, Q. Xie, D. Yang, H. Xiao, Y. Fu, Y. Tan, and S. Yao, "Recent advances in electrochemical glucose biosensors: a review." RSC Advances, vol. 3(14), p. 4473, 2013.

[CHI12] F. Chiavaioli, C. Trono, A. Giannetti, M. Brenci, and F. Baldini, "Characterisation of a label-free biosensor based on long period grating." Journal of biophotonics, Nov. 2012.

[CLA56] L.C. Clark, "Monitor and control of blood and tissue oxygen tensions." Transactions American, Society for Artificial Internal Organs, vol. 2,pp. 41-48, 1956.

[CON13] www.concentris.com, 2013

[COO02] M.A. Cooper, "Optical Biosensors in drug discovery." Nature reviews, vol. 1, pp. 515-528, 2002.

[COO09] M.A. Cooper, "Label-free biosensors: Techniques and applications." Cambridge, U.K., Cambridge University Press, 2009.

[CRE10] A. Crespi, Y. Gu, B. Ngamsom, H.J.W. M. Hoekstra, C. Dongre, M. Pollnau, R. Ramponi, H.H. van den Vlekkert, P. Watts, G. Cerullo, and R. Osellame, "Three-dimensional Mach-Zehnder interferometer in a microfluidic chip for spatially-resolved label-free detection." Lab on a chip, vol. 10(9), pp. 1167–73, 2010.

[CUI01] Y. Cui, Q. Wei, H. Park, and C. M. Lieber, "Nanowire nanosensors for highly sensitive and selective detection of biological and chemical species." Science (New York, N.Y.), vol. 293(5533), pp. 1289–9122, 2001.

[DEN09] A. Densmore, M. Vachon, D.-X. Xu, S. Janz, R. Ma, Y.-H. Li, G. Lopinski, a Delâge, J. Lapointe, C. C. Luebbert, Q. Y. Liu, P. Cheben, and J. H. Schmid, "Silicon photonic wire biosensor array for multiplexed real-time and label-free molecular detection." Optics letters, vol. 34(23), pp. 3598–600, 2009.

[DEN11] A. Densmore, D.-X. Xu, N.A. Sabourin, H. McIntosh, P. Cheben, J.H. Schmid, R. Ma, M. Vachon, A. Delage, W. Sinclair, J. Lapointe, Y. Li, G. Lopinski, B. Lamontagne, and S. Janz, "A fully integrated silicon photonic wire sensor array chip and reader instrument.", 8th IEEE International Conference on Group IV Photonics (GFP), proceedings, 2011.

[DEY12] M.A. Deyab and S.T. Keera, "Cyclic voltammetric studies of carbon steel corrosion in chloride-formation water solution and effect of some inorganic salts." Egyptian Journal of Petroleum, vol. 21(1), pp. 31–36, 2012.

[DNI91] A.M. Dnistrian, M.K. Schwartz, E.J. Greenberg, C.A. Smith, and D.C. Schwartz, "CA 15-3 and carcinoembryonic antigen in the clinical evaluation of breast cancer." Clinica Chimica Acta, vol. 200(2-3),pp. 81-93, 1991.

[EBE02] F.G. Ebeling, P. Stieber, M. Untch, D. Nagel, G.E. Konecny, U.M. Schmitt, A. Fateh-Moghadam, and D. Seidel, "Serum CEA and CA 15-3 as prognostic factors in primary breast cancer." Br. J Cancer. Vol. 22(8), pp. 1217-22, 2002.

[ESI05] D. Esinenco, S.D. Psoma, M. Kusko, A. Schneider, and R. Muller. "SU-8 micro-biosensor based on Mach-Zehnder interferometer." Rev. Adv. Mater. Sci, 10(4), 295-299, 2005.

[FAN12] X. Fan, S. Sang, J. Hu, P. Li, G. Li, and W. Zhang, "Recent Development of Silicon Nanowire FET Biosensor for DNA Detection." International Conference on Computing, Measurement, Control and Sensor Network, proceedings, pp. 201–205, 2012.

[FAR13] www.farfield-group.com, 2013.

[FIG11] A. Figotin and I. Vitebskiy, "Slow wave phenomena in photonic crystals." Laser & Photonics Reviews, vol. 5(2), pp. 201–213, 2011.

[FRI08] J. Fritz, "Cantilever biosensors." The Analyst, vol. 133(7), pp. 855-63, 2008.

[GOS94] D.K. Gosser, "Cyclic Voltammetry, Simulation and Analysis of Reaction Mechanisms." VHC Publishers, Inc., 1994.

[GRI08] D. Grieshaber, R. MacKenzie, J. Vörös, and E. Reimhult, "Electrochemical Biosensors - Sensor Principles and Architectures." Sensors, vol. 8(3), pp. 1400-1458, 2008.

[GRS10] S.M. Grist, L. Chrostowski, and K.C. Cheung, "Optical Oxygen Sensors for Applications in Microfluidic Cell Culture." Sensors, vol. 10(10), pp. 9286-9316, 2010.

[HIG94] S. P. J. Higson and P. M. Vadgama, "Biosensors: a viable monitoring technology." Medical & Biological Engineering & Computing, vol. 32(6), pp. 601-609, 1994.

[HUN10] H.K. Hunt and A.M. Armani, "Label-free biological and chemical sensors." Nanoscale, vol. 2(9), pp. 1544-59, 2010.

[ION11] R. E. Ionescu, K. Jia, T. Thoury, E. Eltzov, and R. Marks, "Acoustic biosensors for medical and environmental purposes." 2011 International Symposium on Applications of Ferroelectrics (ISAF/PFM) and 2011 International Symposium on Piezoresponse Force Microscopy and Nanoscale Phenomena in Polar Materials, proceedings, pp. 1–4, 2011.

[ISM12] A. H. Ismail, C. Schäfer, A. Heiss, M. Walter, W. Jahnen-Dechent, and S. Leonhardt, "An electrochemical impedance spectroscopy (EIS) assay measuring the calcification inhibition capacity in biological fluids." Biosensors & bioelectronics, vol. 26(12), pp. 4702-7, 2011.

[JOH12] B. N. Johnson and R. Mutharasan, "Sample preparation-free, real-time detection of microRNA in human serum using piezoelectric cantilever biosensors at attomole level." Analytical chemistry, vol. 84(23), pp. 10426-36, 2012.

[KOS13] P. M. Kosaka, J. Tamayo, J. J. Ruz, S. Puertas, E. Polo, V. Grazu, J. M. de la Fuente, and M. Calleja, "Tackling reproducibility in microcantilever biosensors: a statistical approach for sensitive and specific end-point detection of immunoreactions." The Analyst, vol. 138(3), pp. 863-72, 2013.

[KRE01] E. Kress-Rogers, and C.J.B. Brimelow, "Instrumentation and Sensors for the Food Industry." Woodhead publishing limited, Cambrige, 2001.

[LAN08] K. Lange, B. E. Rapp, and M. Rapp. "Surface acoustic wave biosensors: a review." Analytical and Bioanalytical Chemistry, vol. 391(5), pp. 1509-1519, 2008.

[LAV04] N. V. Lavrik, M. J. Sepaniak, and P. G. Datskos, "Cantilever transducers as a platform for chemical and biological sensors." Review of Scientific Instruments, vol. 75(7), pp. 2229, 2004.

[LEE03] B. Lee, "Review of the present status of optical fiber sensors." Optical Fiber Technology, vol. 9(2), pp. 57-79, 2003.

[LEE07] M. R. Lee and P. M. Fauchet, "Nanoscale microcavity sensor for single particle detection." Optics letters, vol. 32(22), pp. 3284-3286, 2007.

[LIS08] F. Lisdat and D. Schäfer, "The use of electrochemical impedance spectroscopy for biosensing." Analytical and bioanalytical chemistry, vol. 391(5), pp. 1555–1567, 2008.

[LIU12] N. Liu, Z. Zhao, Y. Chen, and Z. Gao, "Rapid Detection of Staphylococcal Enterotoxin B by Two-Dimensional Molecularly Imprinted Film-Coated Quartz Crystal Microbalance." Analytical Letters, vol. 45(2–3), pp. 283–295, 2012.

[MAN10] A. Manickam, A. Chevalier, M. McDermott, A. D. Ellington, and A. Hassibi, "A CMOS Electrochemical Impedance Spectroscopy (EIS) Biosensor Array." IEEE Transactions on Biomedical Circuits and Systems, vol. 4(6), pp. 379-390, 2010.

[MAT13] D. Matatagui, J. Fontecha, M. J. Fernández, M. J. Oliver, J. Hernando-García, J. L. Sánchez-Rojas, I. Gràcia, C. Cané, J. P. Santos, and M. C. Horrillo, "Comparison of two types of acoustic biosensors to detect immunoreactions: Love-wave sensor working in dynamic mode and QCM working in static mode." Sensors and Actuators B: Chemical, online, 2013.

[MAU08] M. Bacci, C. Cucci, A. Azelio-Mencaglia, and A. Grazia-Mignani, "Innovative Sensors for Environmental Monitoring in Museums.", Sensors, vol. 8, pp. 1984-2005, 2008.

[MOH06] S.P. Mohanty and E. Kougianos, "Biosensors: a tutorial review." IEEE Potentials, vol. 25(2), pp. 35-40, 2006.

[ORG10] R. Orghici, P. Lützow, J. Burgmeier, J. Koch, H. Heidrich, W. Schade, N. Welschoff, and S. Waldvogel, "A Microring Resonator Sensor for Sensitive Detection of 1,3,5-Trinitrotoluene (TNT)." Sensors, vol. 10(7), pp. 6788-6795, 2010.

[PAL12] S. Pal, P. M. Fauchet, and B. L. Miller, "1-D and 2-D photonic crystals as optical methods for amplifying biomolecular recognition." Analytical chemistry, vol. 84, no. 21, pp. 8900–8, 2012.

[PAS13] V.M.N. Passaro, B. Troia, M. La Notte, and F. De Leonardis, "Photonic resonant microcavities for chemical and biochemical sensing." RSC Advances, vol. 3, no. 1, p. 25, 2013.

[PET11] E. Petryayeva and U.J. Krull, "Localized surface plasmon resonance: nanostructures, bioassays and biosensing--a review." Analytica chimica acta, vol. 706(1), pp. 8–24, 2011.

[RIN06] L. Rindorf, J.B. Jensen, M. Dufva, L.H. Pedersen, P.E. Høiby, and O. Bang, "Photonic crystal fiber long-period gratings for biochemical sensing." Optics Express, Vol. 14(18), pp. 8224-8231, 2006.

[ROS98] J.S. Ross, and J.A. Fletcher, "The HER-2/neu Oncogene in Breast Cancer: Prognostic Factor, Predictive Factor, and Target for Therapy." The Oncologist August 1998 vol. 3(4), pp. 237-252, 1998.

[ROY09] S. Roy and Z. Gao, "Nanostructure-based electrical biosensors." Nano Today, vol. 4(4), pp. 318–334, 2009.

[SAW13] www.saw-instruments.com, 2013.

[SCA10] S. Scarano, M. Mascini, A. P. F. Turner, and M. Minunni, "Surface plasmon resonance imaging for affinity-based biosensors." Biosensors & bioelectronics, vol. 25(5), pp. 957–66, 2010.

[SEN13] www.sensia.es, 2013

[SEP06] B. Sepúlveda, J. S. Del Río, M. Moreno, F. J. Blanco, K. Mayora, C. Domínguez, and L. M. Lechuga, "Optical biosensor microsystems based on the integration of highly sensitive Mach – Zehnder interferometer devices." Journal of Optics A: Pure and Applied Optics, vol. 8, pp. 561–566, 2006.

[SEP09] B. Sepúlveda, P. C. Angelomé, L. M. Lechuga, and L. M. Liz-Marzán, "LSPR-based nanobiosensors." Nano Today, vol. 4(3), pp. 244–251, 2009.

[SHO12] A. Shooshtari, S. Marzieh Hoseini, S. Nima Mahmoodi, and H. Kalhori, "Analytical solution for nonlinear free vibrations of viscoelastic microcantilevers covered with a piezoelectric layer." Smart Materials and Structures, vol. 21(7), p. 075015, 2012.

[SIP13] H. Šípová and J. Homola, "Surface plasmon resonance sensing of nucleic acids: a review." Analytica chimica acta, vol. 773, pp. 9–23, 2013.

[SKI07] N. Skivesen, A. Têtu, M. Kristensen, J. Kjems, L. H. Frandsen, and P. I. Borel, "Photonic-crystal waveguide biosensor." Optics Express, vol. 15(6), pp. 3169-76, 2007.

[STE04] G. Steiner, "Surface plasmon resonance imaging." Analytical and bioanalytical chemistry, vol. 379(3), pp. 328–31, 2004.

[TAM13] J. Tamayo, P. M. Kosaka, J. J. Ruz, A. San Paulo, and M. Calleja, "Biosensors based on nanomechanical systems." Chemical Society reviews, vol. 42(3), pp. 1287-311, 2013.

[TAN12] C.W. Tan, K.H. Tan, Y.T. Ong, A. R. Mohamed, S.H.S. Zein, and S.H.Tan, "Energy and environmental applications of carbon nanotubes." Environmental Chemistry Letters, vol. 10, no. 3, pp. 265–273, 2012.

[UDD11] E. Udd and W. B. Spillman, Eds., "Fiber Optic Sensors." Hoboken, NJ, USA: John Wiley & Sons, Inc., 2011.

[VOL08] F. Vollmer and S. Arnold, "Whispering-gallery-mode biosensing: label-free detection down to single molecules." Nature methods, vol. 5(7), pp. 591–6, 2008.

[WAN04] J. Wang, "Carbon-Nanotube Based Electrochemical Biosensors: A Review." Electroanalysis, vol. 17(1), pp. 7–14, 2004.

[WAN11] P. Wang, and Q. Liu, "Biomedical Sensors and Measurement." Springer; 2011 edition, 2011.

[WAN13] X.-D. Wang and O. S. Wolfbeis, "Fiber-optic chemical sensors and biosensors (2008-2012)." Analytical chemistry, vol. 85(2), pp. 487–508, 2013.

[WAS11] A. L. Washburn and R. C. Bailey, "Photonics-on-a-chip: recent advances in integrated waveguides as enabling detection elements for real-world, lab-on-a-chip biosensing applications." The Analyst, vol. 136(2), pp. 227–36, 2011.

[WEI08] T. Wei, Y. Han, Y. Li, H. Tsai, and H. Xiao, "Temperature-insensitive miniaturized fiber inline Fabry-Perot interferometer for highly sensitive refractive index measurement." Opt. Express 16, pp. 5764-5769, 2008.

[WHI09] I. M. White, H. Zhu, J. D. Suter, and X. Fan, "Advanced Photonic Structures for Biological and Chemical Detection." New York, NY: Springer US, pp. 377–393, 2009.

[WIL09] U. Willer, and W. Schade, "Photonic sensor devices for explosive detection." Analytical and Bioanalytical Chemistry, vol. 395(2), pp. 275-282, 2009

[ZAM08] E. Zampetti, S. Pantalei, A. Macagnano, E. Proietti, C. Di Natale, and A. D'Amico. "Use of a multiplexed oscillator in a miniaturized electronic nose based on a multichannel quartz crystal microbalance." Sensors and Actuators B-Chemical, vol. 131(1), pp. 159-166, 2008.

[ZAN04] B. Zhang, Q.G. Mao, X. Zhang, T.L. Jiang, M. Chen, F. Yu, and W.L. Fu. "A novel piezoelectric quartz micro-array immunosensor based on selfassembled monolayer for determination of human chorionic gonadotropin." Biosensors & Bioelectronics, vol. 19(7), pp. 711-720, 2004.

[ZHA10] H. Zhang, W. Pang, M. S. Marma, C.-Y. Lee, S. Kamal-Bahl, E. S. Kim, and C. E. McKenna, "Label-free detection of protein-ligand interactions in real time using micromachined bulk acoustic resonators." Applied Physics Letters, vol. 96(12), p.

123702, 2010.

[ZHA11] Z.-W. Zhang, T.-D. Wen, and Z.-F. Wu, "A Novel Method for Heightening Sensitivity of Prism Coupler-Based SPR Sensor." Chinese Physics Letters, vol. 28(5), p. 054211, 2011.

[ZHU09] J. Zhu, S. K. Ozdemir, Y.-F. Xiao, L. Li, L. He, D.-R. Chen, and L. Yang, "On-chip single nanoparticle detection and sizing by mode splitting in an ultrahigh-Q microresonator." Nature Photonics, vol. 4(1), pp. 46–49, 2009.

[ZHU10] H. Zhu, J. D. Suter, and X. Fan, "Optical Guided-wave Chemical and Biosensors II." vol. 8. Berlin, Heidelberg: Springer Berlin Heidelberg, 2010.

[ZIN11] K.E. Zinoviev, A.B. Gonzalez-Guerrero, C. Dominguez, and L.M. Lechuga, "Integrated Bimodal Waveguide Interferometric Biosensor for Label-Free Analysis." Journal of Lightwave Technology, vol. 29(13), pp. 1926–1930, 2011.

[ZOU08] M. Zourob, S. Elwary, and A. Turner, Eds., "Principles of Bacterial Detection: Biosensors, Recognition Receptors and Microsystems." New York, NY: Springer New York, 2008.

2

Biochemical surface modification

2.1 Introduction

As we introduced in the previous chapter, sensors based on evanescent wave have the ability to measure the variations of the refractive index in the surroundings of the structure and convert it into a measurable signal. Optical sensors employ this kind of mechanism in order to detect the presence of particles or molecules on the structure's surface. However, these devices do not own the attribute to specifically recognize the presence of certain biological molecules and differentiate them from the background molecules, which should not be detected. To provide such characteristic to the photonic sensor, the sensing area needs generally to be coated with an additional functional layer that permits the attachment to the surface of proper receptors specific to the target molecules to be detected as well as to simultaneously repel the binding of the non-desirable particles of the analysed sample [ROG00]. Fig. 2.1 shows the main parts involved in the detection process: sample, receptors, functional layer and transducer. The role of the functional layer in an affinity biosensor is

to promote the binding of an organic molecule (i.e., the receptor) to an inorganic substrate or surface.

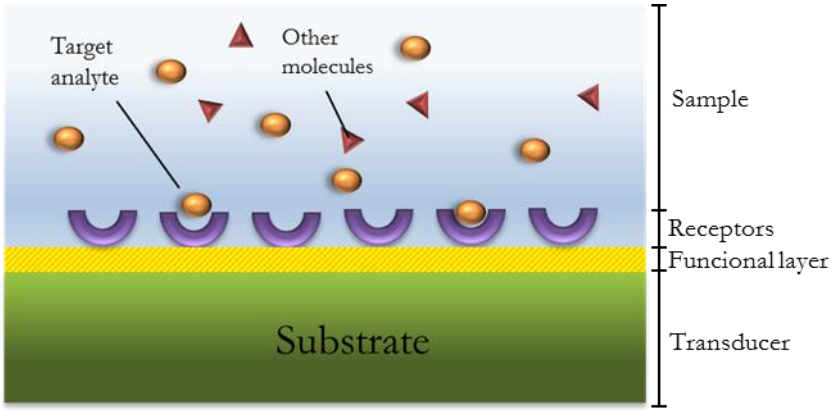

Fig. 2.1: *Schematic representation of the parts involved in the detection process for an affinity-based biosensor.*

Due to the intrinsic physical and biological properties of the target analyte, its direct detection can be very challenging. In those cases, biological research has relied upon attachment of a sort of label to the target analyte what makes easier its indirect detection by measuring the presence of this attached element instead. Labels are designed to be easily recognized, for instance, by their fluorescence, radioactivity or metallic nature; therefore, we can indirectly determine the presence of the target analyte by measuring those parameters. However, the use of labels imply several disadvantages. Labelled assays require a sample pre-treatment for attaching the label to the molecules, thus making more difficult and requiring longer times to obtain the results. Furthermore, these labels can interfere with the original sample masking the real signal from the target analyte. Moreover, in many cases it is not possible to extract the kinetic information of the reaction between the receptor and the target analyte since we only look at the "end point" of the assay. The appearance of quenching effects when using fluorescent labels is another obstacle related with the detection of the labelled molecules (e.g. silicon quenches the fluorescence of Cy5 label).

Due to the arguments above, there has been a general trend in trying to avoid the use of labels for the analyte detection, thus reducing the time, the complexity and the cost of the biosensing assays. In a direct affinity assay between two molecules, for instance, an antigen-antibody binding detection, the output signal directly provides the fundamental information of the kinetics of the interaction between both molecules. Moreover, it allows a rapid quantification of the concentration of the target analyte without the necessity to perform any additional complex sample preparation for labelling the analytes, what may also alter the results.

In a direct sensing procedure, one partner of the couple, the receptor, is attached on the surface and then the detection is carried out by flowing the complementary analyte diluted in a buffer. Target molecules will bind to the immobilized probes via affinity interaction, thus varying

the refractive index on the surface. This refractive index change can be modelled as a thin layer of thickness *h* as follows:

$$\Delta n_d = \left(\frac{dn}{dc}\right)\frac{\Delta\Gamma}{h}, \tag{2.1}$$

where *(dn/dc)* is the variation of refractive index due to the concentration of the analyte and ∠*IΓ* is the surface concentration of the bound molecules [FEI78].

In this kind of affinity reaction between two compounds, the most widely model used to describe the binding between the receptor and the target analyte can be expressed as a simple bimolecular formation:

$$A + B \underset{k_d}{\overset{k_a}{\rightleftharpoons}} AB \tag{2.2}$$

where k_a and k_d are respectively the association and dissociation rate constants of the couple. From the output signal of the biosensor we can extract three characteristics of the interaction: the concentration of the target analyte, the affinity between molecules and the kinetics of the interaction.

The ideal behavior of a biorecognition assay is shown in the sensorgram of Fig. 2.2. First, the buffer shows a stable signal known as baseline. When the target analyte is injected the response of the sensor rises due to the recognition between the receptor and the analyte; this step is called association or binding. Assuming a first order interaction between molecules determined by the Eq. 2.2, the differential rate equations could be derived from the binding model in order to analyse how the experimental data agree with the model. The complex formation is given by:

$$\frac{dR(t)}{dt} = k_a C R_{max} - (k_a C + k_d)R(t) \tag{2.3}$$

where the *R(t)* is the response of the sensor as a function of time, *C* is the concentration of the target analyte, and R_{max} is the maximum variation of the sensor's response when the surface is completely saturated at a certain surface density. Once the flow of the target analyte finishes and the buffer starts to flow again over the sensor, we will observe the dissociation phase of the attached analytes from the surface. In this phase the sensor's response is only affected by the factor k_d showing a response given by

$$\frac{dR(\mathrm{t})}{dt} = -k_d R(t). \tag{2.4}$$

Finally, in some cases we can also perform a regeneration step in order to remove all the analytes bound to the receptors. This procedure will allow recovering the initial baseline and reuse the sensor for further experiments.

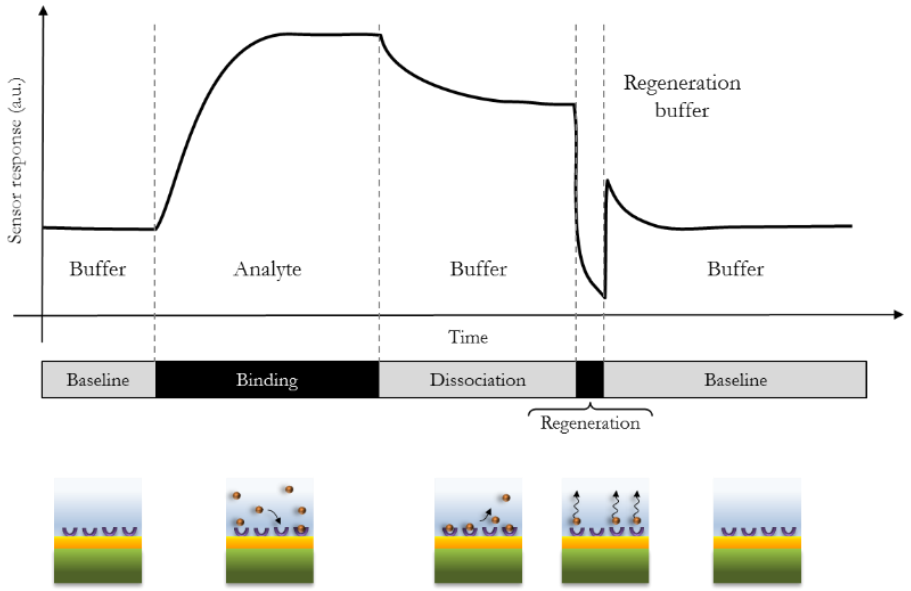

Fig. 2.2: *Schematic representation of a sensorgram for an affinity-based biosensor. The interaction between the receptors and the target analytes is also schematically shown below. The functional layer provides the proper attachment of the receptors for the recognition of the target analyte.*

When the functional layer with the ability to immobilize the receptor agents is combined with the nanostructured material, the intrinsic properties of the sensor should be invariable. In other words, the immobilized layer must provide the specificity required to the detection without influencing the operation of the transduction element or interfere in the mass transport of the molecules in the target sample. In addition, other important issue to take into account when designing the functional layer is its thickness. Since planar photonic structure sensors are based on the use of the evanescent field, which has an exponential decay from the surface, the sensitivity will strongly depend on the distance of the analyte to the surface. Therefore, thin biological layers are highly desired in order to enhance the interaction between the wave and the target molecules.

To obtain a proper functional layer in order to attach the receptors for the sensor structure, the sensor's surface (in our case, of silicon) needs to be chemically modified. This layer provides active groups that react with the specific moieties of the receptors to be immobilized on top of the surface. To manage a proper functionalization, there are several parameters related to the immobilization process of the receptors to the surface of the sensor that may influence in the final performance as listed hereafter:

- **The chemical and physical properties of the surface,** what may affect both specific and non-specific binding of the molecules.
- **The orientation** of the receptor molecules attached on the surface, which can be optimized for a specific position.
- **The distance** between the bound target analyte and the surface of the transducer.

- **The surface coverage** with the receptors, which will influence the sensitivity and detection limit.

For these reasons, it is crucial to determine the optimal surface modification steps for the development of affinity sensors. There is a wide range of materials that may be employed to develop high sensitivity biochemical sensors as well as many strategies to coat the surfaces with a receptor layer in order to provide biological functionalities [JON08]. However, since each surface has its own properties, it is impossible to define a universal method to anchor the probes. For that reason, the surface treatment and the chemical compounds to be employed need to be thoroughly studied before releasing a final functionalization protocol. A suitable strategy should provide a proper linkage of the probes to the surface with a high affinity to the target analytes for a specific substrate.

Several immobilization techniques have been developed in the past years following mainly three mechanisms: physical, covalent and bioaffinity attachment [RUS07].

- **Physical immobilization:** is a straightforward method to adhere ligands to the surface of the transducer [ABO11]. Several molecules can be adsorbed on the surfaces via intermolecular forces such as ionic bonds or polar interactions as shown in Fig. 2.3a. The result of this process is a heterogeneous layer randomly oriented due to the fact that each molecule may form many contacts with different orientations trying to minimize the repulsive forces produced by previous molecules attached on the surface. Clearly, the adsorption mechanism is not optimal due to the random orientation of the receptor. Moreover, the layer may be easily removed using buffers or detergents due to the weak attachment of the molecules. This fact has led to use this procedure only to perform some assays as proof of principle due to its simplicity but not for a robust selective detection method.
- **Covalent immobilization:** some molecules can be covalently attached to a modified substrate through accessible functional groups as depicted in Fig. 2.3b. This process produces an irreversible strong bond, allowing a homogeneous coating of the surface and providing well-defined oriented sites. Furthermore, when this approach is optimally implemented, the molecules are attached to the surfaces in a well-ordered manner leading to a high reproducibility and stability. There are several chemistry procedures for the covalent immobilization according to the functional group that are used, being those based on amine, thiol, carboxyl and epoxy groups the most popular. Additionally, we would like to mention the use of novel immobilization techniques that employs UV light in order to foster the covalent bound reaction. These types of techniques are known as photoactivated or light assisted chemistry, and have several benefits such as spatial selectivity using photomasks and reduced incubation times in relation to current methods. We have employed one of these photoactivated immobilization techniques to perform the

functionalization of some of the structures used in this PhD work, as it will be described in section 2.2.2.

- **Bioaffinity immobilization:** sometimes there is no possibility to couple the receptor molecules on the surface neither using physical immobilization nor covalent attachment. In those situations, a couple of molecules with a remarkable affinity will be used to promote the binding of the receptor. One molecule from the affinity couple will be immobilized on the surface via adsorption or covalent linkage and then the specific capture probe, which is marked with the couple of the molecule attached on the surface, will be immobilized using that intermediate layer as shown in Fig. 2.3c. Due to their high affinity constant, streptavidin-biotin system is one of the most used couples for this purpose; e.g., streptavidin is attached on the surface while the biotin is used to mark the capture probe molecule. Besides the advantage of having an optimal orientation of the binding sites, this strategy also allows to detach the molecules and reuse the system several times.

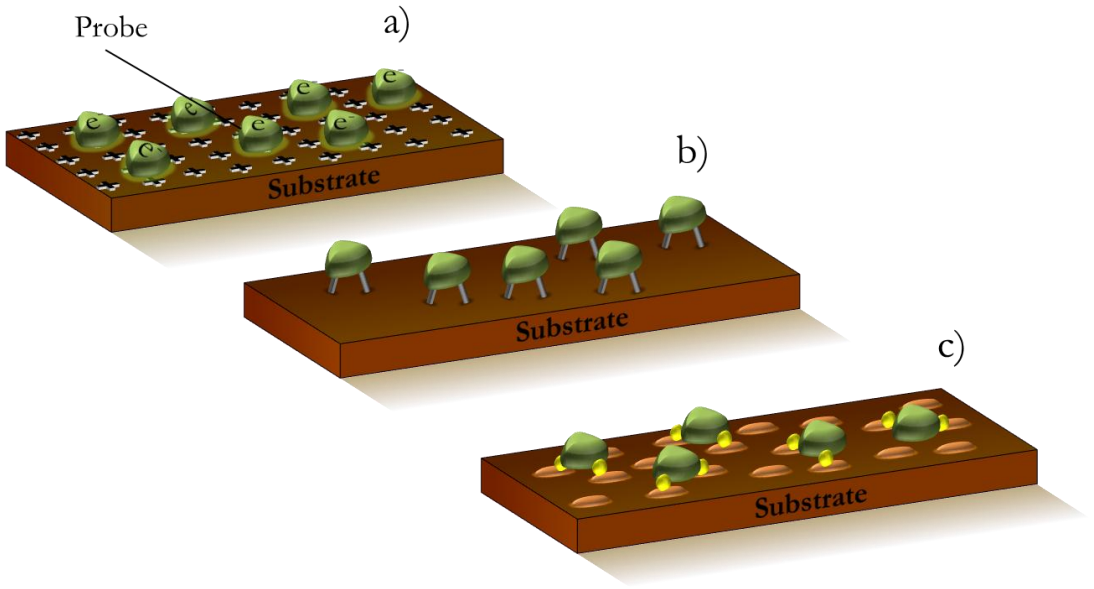

Fig. 2.3: *Receptor immobilization techniques, a) physical adsorption, b) covalent binding and c) bioaffinity with a couple of molecules.*

Despite the use of these types of immobilization procedures, a perfect coverage of the surface with the probe molecules is difficult to be achieved. This fact leads to one of the main non-desirable effects in biosensors that reduce their performance: the non-specific absorption. Generally, the analysed sample does not only contain the target analyte that we want to detect, but also many other molecular components. The non-specific absorption is produced when these other particles, which are not the target analyte of the ligand, bind to the surface and subsequently interfere in the signal of the transducer leading to false positives and deteriorating the reliability of

the system. In order to prevent from non-specific absorption, the biological layer must be blocked with other molecules in order to avoid the interaction of such particles with the sensor's surface.

All the chemical functionalization procedures within the frame of this PhD work were carried out in close collaboration with researchers from the "Centro de Reconocimiento Molecular y Desarrollo Tecnológico" in Universitat Politècnica de València, namely Dr. María José Bañuls, Dr. Jorge Escorihuela, Dr. Sergio Peransí and Prof. Ángel Maquieira. Their expertise in the field of bioconjugation chemistry is widely recognized through valuable publications throughout the last years.

2.2 Receptor immobilization using silanes

Once we generally presented in the previous section the different methods available for attaching the probes to sensing surfaces, in this part, we will explain the specific methods used in this PhD work for the bio-functionalization of the photonic sensors.

The generation of an amorphous thin layer of silicon oxide due to natural oxidation will determine the functionalization protocol. Silicon structures are characterized by the presence of hydroxyl (–OH) groups on its surface due to the formation of that silicon oxide layer. This chemical group can react with silane groups to create hydrogen bonds and anchor the organosilanes molecules to the surface.

We have used a covalent attachment strategy based on silane compounds due to their excellent properties and robustness. Silane coupling strategies are reliable and well-known processes that are relatively easy to apply on surfaces [LUC12, GRE08]. As a result, the surface obtains biological functionalities to promote the attachment of the ligand by covalent bonding. Therefore, we needed to establish an optimal strategy to immobilize the probes to our silicon-based photonic sensing structures in order to form a homogeneous layer for the detection of the target analytes.

A silane compound, which is shown in Fig. 2.4, is a monomeric silicon-based molecule that is able to form stable covalent bond with the groups of the sensor's surface and at the same time to promote a particular functional group for immobilizing the probes. Those silanes that contain at least one bonded carbon are called organosilanes and some of its derivatives are highly reactive towards inorganic compounds. Silanes are used to create a new functional group on the surface of the sensor in order to immobilize other molecules. The most useful organosilanes are those that contain a functional organic component in addition to one or more silane reactive groups, which can conjugate with other organic compounds. The organosilanes presented here include those with amino, thiol, carboxyl, isocyanate and epoxy termination functional groups for subsequent modification steps.

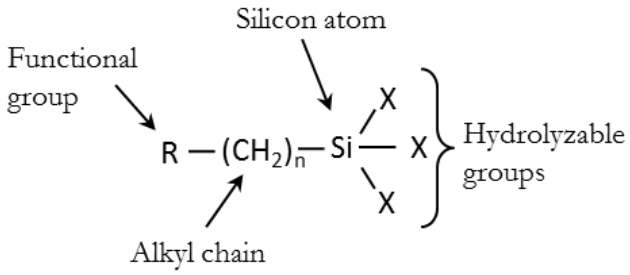

Fig. 2.4: *General structure of a functional silane coupling agent. The hydrolysable groups covalently attach to the inorganic substrate whereas the functional group permits the conjugation with organic compounds.*

Different strategies of silane deposition have been studied in order to provide an optimal coverage, including those based on aqueous dilution, on organic solvents or in vapour phase deposition [HUN10]. The thickness of such layer is highly dependent on the concentration of silane and the amount of water present during the deposition. Those depositions that imply the use of water to facilitate the hydrolysis of the akoxyl groups for coupling should be avoided due to the formation of aggregates. However, by using organic solvents such as toluene or ethanol or even vapour phase organosilanes we can form a homogeneous thin monolayer directly coupled to the substrate via siloxane bonds. In any case, it is recommended to perform an optimization of all these immobilization chemical procedures using other well-established technologies (e.g., microarray technology) prior to using it for the surface modification of the integrated photonics biosensors.

Summarizing, organosilanes are bi-functional compounds that create a covalent bonding with inorganic surfaces and promote the selective immobilization of an organic layer of molecules such as proteins, DNA or antibodies among others. Among the different organosilanes commercially available [HAE10], there are a few that are preferred for the functionalization of integrated biosensors based on silicon surfaces. The main reasons are related with the proximity of the ligand to the surface, the steps required to attach the probe, or the stability of the reaction having into account the pH or the solvent.

Generally, silane compounds can be classified according to their functional termination. In a first group, we can find amine-ended organosilanes that reacts with aldehyde, carboxylic acid and epoxy groups. 3-aminopropyl-triethoxysilane (APTES) and 3-aminopropyl-trimethoxysilane (APTMS) are the most widely used silanes during the last years [WAS10, GUO10, GOD09, IQB10, SCU11, CHA13]. Albeit their termination group is identical, the deposition conditions vary. Whereas the coating using APTMS is carried out with a pure organic solvent, in the case of the APTES water must be present in the dilution in order to create the organic layer. In addition, due to the reactivity between the amine and the silicon oxide layer, there is the possibility of not being well oriented towards the surface in both compounds. However, the major drawback of these kind of organosilanes roots in the necessity of employing crosslinkers to attach the capture probes

leading to additional functionalization steps and a higher distance to the surface of the sensing structure. Crosslinkers such as N-Hydroxysuccinimide ester-ended biotin (NHS-bt), 1 ethyl-3-(3-dimethylaminopropyl) carbodiimide (EDC-NHS) [HUN10], gluteraldehyde [CHA12] or Succinimidyl 6-hydrazinonicotinamide acetone hydrazone (S-HyNiC) [WAS10] have been developed with successful results for the linkage of the amine-ended analyte with the bioreceptor.

(3-mercaptopropyl)trimethoxysilane (MPTS) is other kind of organosilane that is also employed for the functionalization of silicon surfaces. Its thiol termination permits the linkage of ligands through amine groups using a similar crosslinker to APTES forming disulfide bonds. This bond offers the benefit of reusability due to its reversibility and thus the surface can be regenerated leading to multiple reutilizations [SEP06]. Another benefit of MPTS is the possibility to implement "click" chemistry reactions between thiol and alkene groups, what has been recently demonstrated exhibiting good performance to reproduce affinity assays [ESC12a].

Other group of silanes is that with carboxylic (-COOH) termination, which is reactive towards molecules such as ester groups, amides or nitriles. In a recent publication, carboxyethylsilanetriol sodium salt silane (CTES) and a complementary crosslinker (EDC/NHS) were employed to selectively attach proteins on a Si_3N_4 surface [DUV12]. After the silanization of the chip, the following steps were performed simultaneously whilst monitoring the optical signal of the biosensor in order to control the deposition of the receptor on the structure. However, these organosilanes must also employ crosslinkers and, albeit they may be attached in one-step modification, they are very dependent on the experimental conditions. In addition, the reaction must be precisely controlled in order to prevent the ester from hydrolysis or protein aggregates on the surface.

Throughout the course of this PhD Thesis we used two different organosilanes for the development of the chemical surface modification methods for our photonic biosensors. The first one was based on Isocyanatopropyltriethoxysilane (ICPTS), whose major advantage is the ability to anchor directly to amino groups, thus avoiding the use of crosslinkers. This fact permits to attach the capture probes closer to the surface and therefore obtaining higher sensitivities due to the higher interaction between the evanescent wave and the target analytes. However, we observed several instability issues for ICPTS-based functionalization during the implementation of the affinity assays. Therefore, we also worked in a second functionalization approach based on 3-(glycidyloxypropyl)trimethoxysilane (GOPTS), which provides similar features to ICPTS regarding the surface linkage but with a best stability during the receptor immobilization step. This GOPTS-based immobilization technique was UV-light assisted what provides several benefits such as a reduction of the incubation times and a spatial selective attachment by using photomasking [ESC12b].

In the next sections, we will introduce the processes followed to optimize the functionalization protocols for each approach (i.e., ICTPS- and GOPTS-based chemistries) using

microarray format in planar structures. After this optimization process, these chemical protocols were transferred and adapted to the photonic sensing structures in order to carry out the assays in our custom optical set-up, as it will be described in chapters 3, 4 and 5.

2.2.1 ICPTS-based functionalization

As it was described in section 1.9, one of the projects in the frame of which part of this PhD work was developed, was the FP7-INTOPSENS project. In this project, the main objective was the detection of pathogenic bacteria causing sepsis by means of their specific DNA identification. For that reason, most the work related with the development of the functionalization process was focused on the implementation of DNA detection experiments. However, other couples of molecules such as bovine serum albumin (BSA)/antiBSA have also been used for the optimization of the functionalization procedure.

ICPTS silanization was the first chemical procedure that we employed in order to complete the functionalization of the photonic structures. ICPTS, whose structure is shown in Fig. 2.5, is a silane that contains an isocyanate group at one extreme of a short propyl spacer. The fact that the end of the ICPTS reacts with many nucleophiles, including amines and thiols, is attracting a great interest from bioconjugate researchers, especially from those who want to attach molecules that contain amino groups, N-terminal groups or other aminated compounds such as oligonucleotides. As previously indicated, the foremost advantage of ICPTS compared to other techniques is that it does not require the use of crosslinkers or spacers, thus leading to two great benefits: 1) the possibility to carry out the functionalization process in only one-step, thus reducing the preparation time, and 2) the reduction in the distance between the sensing structure and the bound target analytes, thus enhancing the sensitivity of the assay. Although in microarray technology this distance is not so relevant, it is crucial for the case of planar photonic biosensing structures. For these reasons, the employment of ICPTS-based chemistry is foreseen as a very promising approach for the development integrated photonic sensing devices.

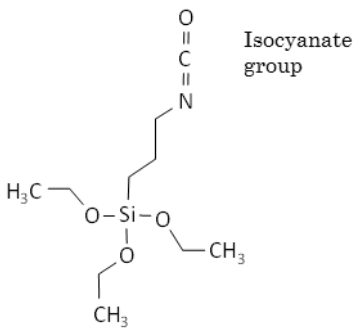

Fig. 2.5: *ICPTS molecule which can be used to couple hydroxyl molecules*
The isocyanate-ended group promote the binding of aminated molecules.

The triethoxysilane groups from the ICPTS will react with –OH groups from the native oxide layer on the surface of the inorganic substrate. This effect permits to use similar procedures both for chips based on silicon and on silicon oxide since the interface will be identical. The isocyanate group, which will be properly oriented upwards, will conjugate with amine molecules creating isourea linkages. However, one drawback of this chemistry approach is that the isocyanate group hydrolyzes rapidly in the presence of a moist environment losing its functionality. Hence, the experimental conditions have to be under a strict control to obtain the desired reproducibility, preventing from humidity once the chip has been functionalized. A schematic representation of the overall immobilization process is depicted in Fig. 2.6.

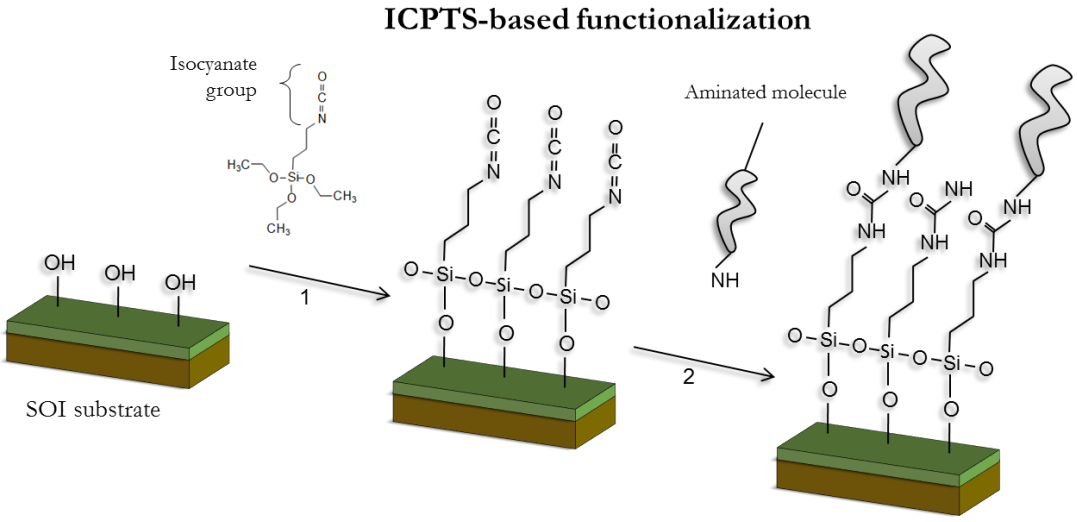

Fig. 2.6: *Sketch of the one-step modification of the silicon-based surface by using ICPTS-based chemistry to attach the receptors. 1) The silane agent is coupled to the –OH terminations of the substrate surface. 2) After incubation, the aminated molecules are attached to the isocyanate moieties forming isourea bonds.*

The procedure to be described in the following paragraphs was determined to work properly in microarray format. We began studying the attachment of BSA molecules to the surface in order to optimize the procedure and afterwards, the attachment of aminated DNA probes to the surface was studied. However, when this protocol was transferred to photonic structures, some parameters needed to be changed according to the results obtained during the optical assays. For the development of the functionalization process in microarray, Cy5 fluorescent dyes were used to label the molecules. By measuring the fluorescence intensity in the substrates, we can know the degree of attachment of the labelled molecule, thus determining the efficiency of the developed procedures. However, silicon material has the problem of quenching the intensity of the fluorescent label for the range of distances used in the experiments (of a few nanometers) thus not permitting to optimize the process directly into silicon surfaces. For this reason, we also used planar silicon oxide substrates for the optimization in microarray format, what is not really an issue since, as previously

indicated, the native silicon oxide layer is the one used for the functionalization of the photonic sensing structures.

2.2.1.1 ICPTS deposition

To optimize the bio-functionalization process using ICPTS, we used silicon-based material substrates (silicon and silicon oxide) that were diced from a wafer. Then the samples were cleaned in piranha solution (H_2SO_4/H_2O_2, 3:1, v/v) during 1 hour at 50ºC. Afterwards, the chips were rinsed with copious amounts of deionized water (DIW) and air-dried. Besides removing the organic residues from the surface, the reaction with the piranha solution generates reactive -OH groups on the silicon's native oxide surface, what is decisive to properly anchor the silane to the inorganic substrate. Once the chip was completely cleaned, we proceed with the silanization. The chips were immersed in a solution of 2% of ICPTS in pure toluene as organic solvent under argon atmosphere during 2 hours in order to coat the chips with a silane monolayer. The surfaces were then washed with 2-propanol to remove the excess of matter from the surface. Organic solvents were employed due to the previously commented problem with the deactivation of the isocyanate groups in the presence of a water environment. Finally, the chips were baked in the oven at 150ºC during 10 minutes to remove the humidity from the surface. In order to keep the chips activated, they were stored under an inert atmosphere in a dry chamber to maintain the isocyanate moieties active. In the event of losing its biological functionality to attach the receptors due to the reaction of the isocyanate group with the humidity, the chip must be baked again to remove the humidity. At this point, the chips are coated with the functional layer that will enable to immobilize the receptors to the isocyanate moieties of the organosilane attached on the surface.

2.2.1.2 Surface characterization of the ICPTS deposition

In order to be sure that the ICPTS deposition was performed successfully, the sample was characterized by water contact angle (WCA) technique and with X-ray Photoelectron Spectroscopy (XPS). The use of these characterization techniques allows us to determine how the efficient the attachment is.

WCA is a straightforward method that provides the degree of surface hydrophobicity. This technique consists in spotting one small drop of water (~ 10 µl) on top of the coated material and measuring the angle formed between the drop and the surface. Fig. 2.7a shows an image of the WCA measurement for a substrate right after its treatment with piranha solution, where we can see that the surface is very hydrophilic with an angle close to 0. Fig. 2.7b shows the WCA measurement for the same substrate after silane deposition, clearly seeing the increase in the hydrophobicity of the substrate because of the silane deposition. WCA measurements were taken five times in both substrates, Si and SiO_2, obtaining the main results shown in Table 2.1.

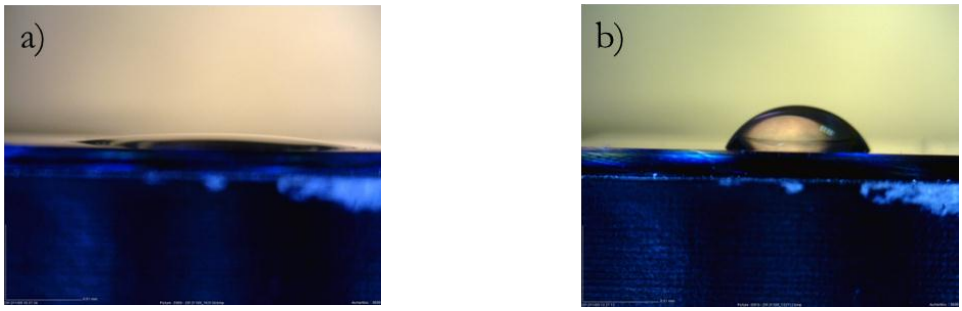

Fig. 2.7: *Images of WCA measurements for a) a substrate treated with piranha exhibiting a contact angle close to 0º, and b) the same substrate after the silanization process.*

Layer	Si	SiO2
Bare substrate	27±2	36±2
Substrate + ICPTS	71±3	72±3

Table 2.1: *WCA measurements for a bare substrate of silicon and silicon oxide without any treatment, and after the silanization process. The homogeneous deposition of the ICPTS produces an increment in the hydrophobicity of the surface reaching the same value.*

In bare substrates of silicon and silicon oxide the measured contact angle was 27º and 36º respectively. This difference of contact angle between bare substrates of both materials is due to the intrinsic physical properties of each of them. After the piranha treatment, –OH groups are generated on the surface, what provokes a complete hydrophilization of the surface and the measurement of a contact angle of nearly 0º as it was shown Fig. 2.7a. After the silanization step with 2% ICPTS in toluene, the surface is homogeneously modified thus increasing the hydrophobicity resulting in WCA values of 71º for the silicon substrate and 72º for the SiO_2 substrate. These similar values confirm that the silane was successfully anchored to the surface of both materials providing a monolayer of ICPTS on both substrates.

In order to obtain the chemical composition of the surfaces, we employed XPS characterization. The basic operation of this technique is based on the registered energy of the emitted electrons from the material when an X-ray impacts on the surface. The chemical composition of a bare silicon surface is shown in Table 2.2 and it was determined to be 54.6% of silicon, 35.8% of oxygen, 10.2% of carbon and no nitrogen. Once the ICPTS deposition was finished resulting a layer of organosilane on the surface, we observed a variation in the composition values. An increment in the carbon compound from 10.2% to 20.6% and the appearance of nitrogen (6.7%) evidence the formation of the layer of ICPTS. In addition, a reduction of the composition of silicon and oxygen was also observed. Therefore, the results obtained by WCA

measurements and by XPS analysis demonstrated that the planar silicon substrates were successfully coated with ICPTS organosilane.

Layer	%Si	%O	%C	%N
Si Bare substrate	54.6	35.8	10.2	---
SiO_2 + ICPTS	40.6	31.0	20.6	6.7

Table 2.2: *Chemical composition of the silicon substrate before and after the silanization. The composition of the substrates varies due to the ICPTS deposition. The values were obtained using XPS measurements.*

2.2.1.3 BSA attachment

ICPTS-based surface modification allows creating a covalent linkage of aminated receptors without the necessity of introducing a crosslinker. Furthermore, after the silanization step the isocyanate moieties are oriented properly to attach the ligands. In order to demonstrate the feasibility of this approach for the development of integrated photonic biosensors, we employed the BSA/antiBSA couple as a biological model in order to validate the protocol.

A simple experiment spotting several concentrations of BSA labelled with Cy5 in a silicon-based substrate functionalized with ICPTS was carried out in order to obtain the BSA concentration required for a good surface coverage. As a result, an array of BSA spots in the planar substrate was obtained. Note that in this step, we are using only silicon oxide substrates because of the commented problem with the fluorescence quenching that occurs in silicon substrates. However, since results obtained with WCA and XPS indicated that the silicon surface was also properly coated with ICPTS, we can assume a similar coating in both materials and thus the validity of the developed protocol for both materials.

To promote the binding between the isocyanate groups and the BSA, the slides were incubated in a dark and humidified chamber during 18 hours. After the incubation, the chip was rinsed and dried under a stream of air. Then, the fluorescence was measured in order to characterize the attachment of the proteins to the surface, as shown in Fig. 2.8a. From Fig. 2.8b we can determine the optimal concentration of BSA to functionalize the surface, which corresponds to 4 μg/ml.

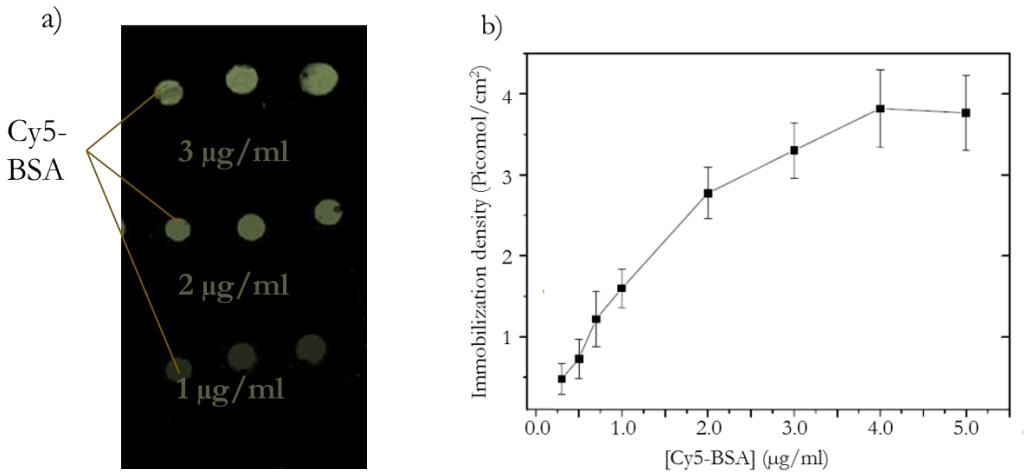

Fig. 2.8: *a) Fluorescence spots for different concentrations of Cy5-labelled BSA immobilized on an ICPTS-modified silicon oxide substrate. b) Immobilization density curve of BSA.*

The deposition of BSA protein on the surface will not be completely homogeneous, so it will not occupy all the binding sites provided by the ICPTS. Therefore, the remaining isocyanate moieties might be able to react with any other molecule that is not the specific target analyte that we want to detect, thus leading to non-specific sensing. For that reason, an additional blocking step must be used to prevent this issue. To this aim, we used two blocking agents during the tests, OVA at 1% in PBS and ethanolamine 0.1 M, in order to block the remaining active sites of the ICPTS. By spotting a drop of the blocking agent and incubating it during 30 minutes, the isocyanate moieties were deactivated, thus preventing from other molecules to non-specifically bind on the surface and leaving available the active sites of the probes for the ligand-analyte interaction.

2.2.1.4 Immunoassay

The final objective of the assay is to detect an analyte through the recognition with the receptor attached on the surface, for instance, by means of an immunoassay. An immunoassay is a biochemical procedure that determines the presence or the concentration of a specific molecule in a sample by means of recognition. Since the antibodies are generated to the three-dimensional structure of an antigen, they are remarkably specific to bind only on a certain structure. In the case of employing a labelled format, as we are doing here to test the feasibility of each step in planar substrate, the concentration of the target analyte will be directly related with the amount of signal measured due to the fluorescent label.

Now, in order to carry out the immunoassay using microarray technology, BSA without the Cy5 fluorescent label was immobilized on the chip's surface using the optimal conditions determined in the previous step. Then, the remaining active sites of the silane were blocked as previously described. Subsequently, Cy5-labelled antiBSA was dispensed over the bio-

functionalized surface and incubated during 15 minutes. The chip was rinsed with PBS-T and water to remove the non-bound antibodies. Finally, the sample was dried and the fluorescence of the Cy5 spots was measured in order to characterize the binding efficiency of the antiBSA with the BSA probes previously attached to the surface obtaining successful results.

2.2.1.5 DNA immobilization

Besides the immobilization of the BSA receptors, we also evaluated the immobilization of ssDNA probes to be used for the specific detection of DNA, what was the final aim of the FP7-INTOPSENS project. Probes with the sequence ((T)15-GATTACAGCCGGTGTACGACCCT) modified with an amino group at the 5' end and labelled with Cy5 at the 3' end were linked to the surface of the ICPTS modified planar substrates. Starting with a silicon-based substrate, we functionalized the surface with ICPTS as previously demonstrated. Then, we immobilized the oligonucleotide using different incubation times at room temperature in a humid chamber. In order to avoid the evaporation of the drop on the surface during the incubation procedure, a 5% of glycerol was added to the PBS 1x buffer where the ssDNA probes were contained. In this study, we determined that a maximum fluorescence intensity of the Cy5 label, and thus an optimal immobilization of the ssDNA probes on the surface, was measured after an incubation time of 8 hours.

2.2.1.6 Conclusions for the ICPTS-based functionalization

According to the obtained results, we confirmed the suitability of the developed protocol for the attachment of capture probes (both based on proteins and on DNA strands) on silicon-based planar substrates using ICPTS-based chemistry. Therefore, the surface modification of the photonic structures was carried out according to previously described steps. However, we had to introduce several slight variations in the functionalization process for the photonic structures after observing a variation on the performance. These modifications will be commented in the sections related to the chemical modification in each chapter.

2.2.2 GOPTS-based functionalization

The second approach that we employed for the covalent immobilization of the probes on the sensor surface was based on GOPTS organosilane, whose structure is shown in Fig. 2.9, combined with a novel approach where the probe attachment is assisted using incident UV light [ESC12b]. As previously commented, ICPTS is a silane characterized by its high reactivity toward nucleophiles, so it easily loses its activity in aqueous media. This fact makes that the optimization of the functionalization protocol becomes difficult and all the steps must carefully controlled. During

the development of this PhD work we observed several stability issues when ICPTS was used to functionalize the sensing structures; therefore, we searched for an alternative organosilane-based immobilization approach with a more stable behaviour. The choice of GOPTS silane to functionalize the silicon surface was determined by two main reasons. First, GOPTS is a solid alternative because its reactive group, to be used for the immobilization of the receptors, consists on an epoxy group. The versatility of this group permits its conjugation with a wide variety of biomolecules with different terminations including thiol-, amine- or hydroxyl- ligands. Considering this issue, we decided to use thiol-ended DNA strands as probes to be attached to the epoxy termination of the GOPTS. The second advantage of this chemical approach is that the efficiency of the binding reaction is significantly enhanced by UV light exposure. Therefore, by exposing certain areas of the chip with UV light (e.g., by using a photomask) we will be able to selectively boost the binding of the receptors only in the desired regions of the chip, whereas the linkage will be practically negligible in the non-exposed regions. In addition, epoxy groups at the end of the GOPTS are compatible with aqueous media, what is very important to keep their bioactivity. Similarly described in the previous functionalization procedure, before applying the chemical modification to the integrated optical structures, it was firstly optimized in planar substrates using microarray format to obtain a proper bioconjugation between the molecules and the surface.

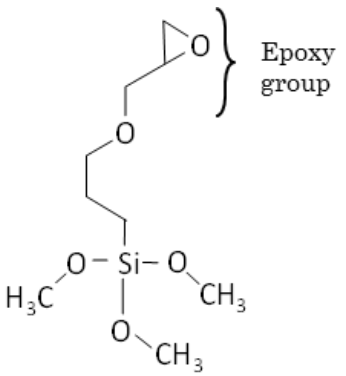

Fig. 2.9: *GOPTS with an epoxy termination, which can be used to couple amine-,thiol-, or hydroxyl-containing ligands.*

2.2.2.1 GOPTS deposition

As previously confirmed for the ICPTS-based chemistry by measuring the WCA, the results of the silanization procedure using silicon and silicon oxide substrates were similar. For that reason, in this second approach we only employed silicon oxide wafers in order to develop the functionalization procedures and avoiding the fluorescence quenching problems occurring for silicon substrates. We started from bare silicon oxide chips that were cleaned with piranha treatment to remove any organic contamination that may be pernicious in the following steps. The chips were then rinsed under water stream and dried. Immediately, they were immersed in a solution of 2% GOPTS in toluene to achieve the surface activation. After 2 hours of incubation at

room temperature under argon atmosphere, the chips were cleaned using dichloromethane (CH_2Cl_2) or 2-propanol to remove the unbound material and obtain a monolayer of GOPTS. The rinsing step of the GOPTS layer is key to obtain a uniform homogeneous layer. A deficient wash may cause the formation of agglomerates, which would be ruinous for the sensitivity of the biosensor, especially in photonic structures where a homogeneous layer is fundamental to obtain a successful detection. Finally, to get rid of moisture, the silicon oxide slides were baked at 150º during 1 hour.

2.2.2.2 Surface characterization of GOPTS deposition

The physical and chemical properties were measured after the coating the surface with the layer of GOPTS. WCA was employed to confirm the deposition of the organosilane on the surface of the slides. The contact angle between the recently cleaned chip using piranha solution and the silanized chip was 63.7º, as it is shown in Fig. 2.10, what indicates the adhesion of the functional layer to the surface.

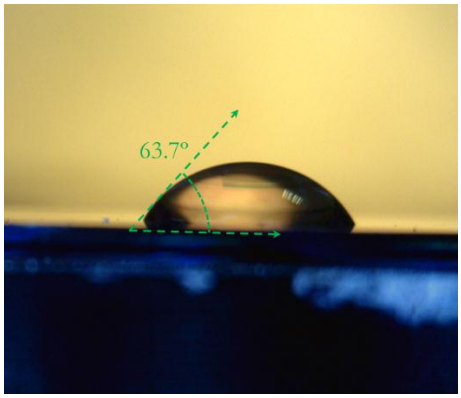

Fig. 2.10: *Measurement of the WCA of the silanized surface by means of GOPTS immersion.*

In addition, a XPS study was performed in order to characterize the change in the composition of the surface after the silanization step. XPS results exhibited a composition of the bare silicon oxide surfaces of 28.9% silicon, 54.6% oxygen and 16.5% carbon; as expected, no nitrogen molecules were detected. Note that previous XPS results shown for the ICTPS-based functionalization (Table 2.2) were obtained for bare silicon chips while here we are using silicon oxide chips, thus leading to a different composition of the initial substrate (e.g., the percentage of oxygen is significantly higher for the silicon oxide substrate). However, as we also commented previously, obtained results using silicon oxide samples can be translated to silicon chips, since in the latter case what we are using to perform the functionalization is the native oxide layer formed on top of the silicon. According to data of Table 2.3, the reduction of the percentage of silicon and oxygen from 28.9% and 54.6% to 23.8% and 45.5% respectively, and the increment of the carbon concentration to 31.1% confirm the deposition of the GOPTS layer on the surface of the chip.

Layer	%Si	%O	%C	%N
SiO_2 Bare substrate	28.9	54.6	16.5	---
SiO_2 + GOPTS	23.8	45.5	31.1	---

Table 2.3: *Chemical composition of the silicon oxide substrate before and after the silanization. The composition of the substrates varies due to the GOPTS deposition. The values were obtained using XPS measurements.*

2.2.2.3 DNA immobilization

In this case, we are going to attach oligonucleotide probes on the surface by means of a thioeter linkage in order to carry out hybridization experiments. GOPTS has already been employed in microarrays to covalently immobilize oligonucleotides to different types of substrates [MAH09]. However, incubation times required anchoring them to the substrate are very long since the efficiency of the reaction between thiol and epoxy groups is very low. Several groups have been pursuing new methods to accelerate this reaction. Within this context, we proposed the use of UV light to accelerate the covalent attachment reaction between the thiol-modified probes and the GOPTS-modified silicon-based surfaces. The major advantage of this method is the requirement of short incubation times as well as the need of neither a coupling reagent nor chemical manipulations for the immobilization of the DNA strands. In comparison with other non-assisted approaches such as ICPTS, whose preparation time of a single chip is more than 20 hours, the light induced modification only takes about 4 hours (or even less according to the power of the illumination). The procedure to obtain an effective immobilization of the thiol-modified DNA probes listed in Table 2.4 in microarray format is similar as that presented in the previous section for the ICPTS-based chemistry.

Name	Oligonucleotide Sequence	5' end	3'end
Probe A	(T)15-CCCGATTGACCAGCTAGCATT	SH	Cy5
Probe B	(T)15-CCCGATTGACCAGCTAGCATT	SH	none
Target	AATGCTAGCTGGTCAATCGGG	Cy5	none

Table 2.4: *List of probes and targets oligonucleotide sequences employed for the development of the GOPTS-based immobilization of DNA probes and hybridization detection.*

Starting from the silanization of the substrates with GOPTS, the surface was terminated with an epoxy group with the proper orientation of the active sites. Then, an array of thiolated DNA probes marked with Cy5 (Probe A) were spotted on the silanized slides and subsequently illuminated during 10 minutes using a 365 nm UV light from a photolithography equipment to induce the immobilization between the thiolated DNA and the epoxy group on the surface. Due to the high power of the UV equipment illumination, the drops were evaporated over the optical

structured materials, thus leading to a non-homogeneous coating. Therefore, we had to use a smaller UV lamp with a lower power than the photolithography equipment, leading to longer incubation times of around 2 h. Despite the increase in the required incubation/exposure time, this lapse is even shorter than other regular protocols to attach DNA probes on sensing structures. Finally, the chip was rinsed with PBS-T and dried under air stream. The schematic representation of the attachment of the oligonucleotides probes to the surface using GOPTS chemistry is shown in Fig. 2.11.

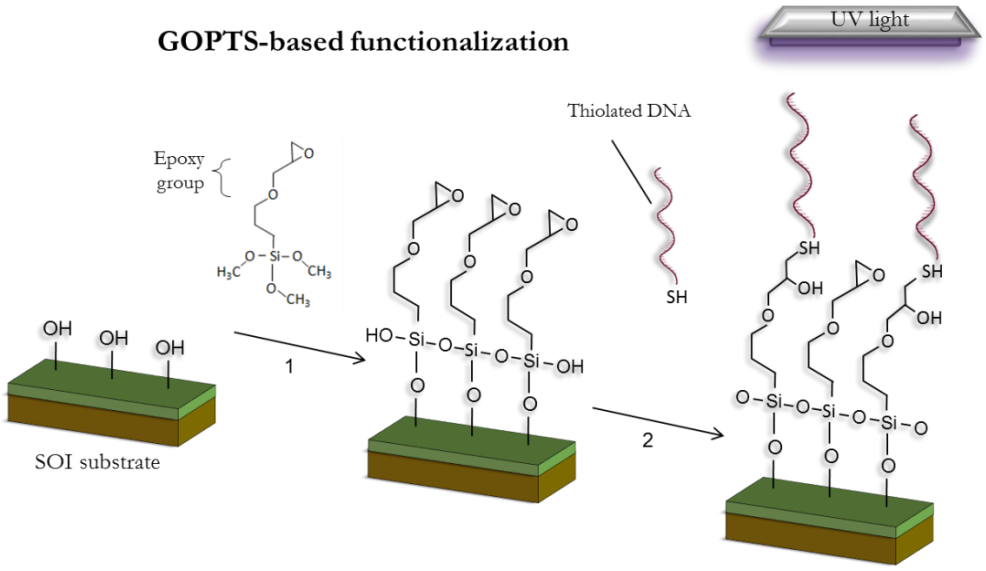

Fig. 2.11: *Sketch of the one-step modification of the silicon-based surface by using GOPTS-based chemistry to attach the receptors (in this case, the attachment of thiolated DNA probes is depicted). 1) The silane agent is coupled to the –OH terminations of the substrate surface. 2) Incubation at room temperature of the probes under UV light exposure.*

The fluorescence measurements confirmed the proper attachment between the epoxy-ended GOPTS silane and the thiolated DNA probes by using the light assisted functionalization approach. Fig. 2.12 shows the registered fluorescence of the spots for different concentrations of the DNA probe. From these results, we observed that it reaches the maximum intensity for DNA probes concentrations larger than 2 μM; therefore, this is the DNA probes concentration that will be used for the functionalization of the sensing devices from this moment on.

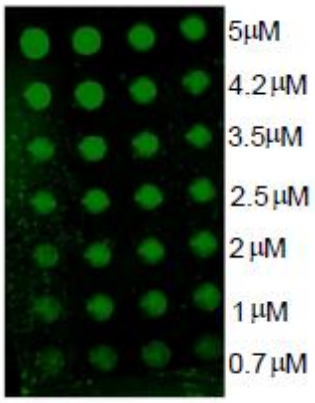

Fig. 2.12: *Fluorescence spots for different concentrations of thiolated DNA probes labelled with Cy5 immobilized on a GOPTS-modified silicon oxide surface. The fluorescence intensity increases for higher concentrations of the immobilized oligonucleotides.*

2.2.2.4 Hybridization

With the aim of determining the suitability of this protocol, we carried out hybridization experiments employing the ssDNA strands complementary to those probes immobilized in the planar chip surface. To this aim, the samples were silanized as mentioned above, but then the thiolated DNA probe without the Cy5 label (Probe B in Table 2.4) was incubated under UV light exposure at a concentration of 2.5 µM. Subsequently, several washing steps using PBS and water were done in order to remove the excess of oligonucleotides. In order to prevent from non-specific detection, a 2-mercaptoethanol solution at 0.1 M in carbonate buffer (CB) 1x was employed as blocking agent. This blocking step also requires of UV light exposure in order to enhance the reaction between the thiol groups of the mercaptoethanol with the remaining epoxy active sites of the GOPTS. This reaction allows modifying these remaining active sites into a hydroxyl group, thus preventing from the reactivity of the sites to other molecules different to the target molecule. Next, the sample was rinsed with water, dried and the complementary Cy5-labelled oligonucleotide sequence (Target in Table 2.4) dissolved in saline-sodium citrate (SSC) 1x buffer was incubated during 1 hour at 37º. Finally, the chip was rinsed with water and the fluorescence of the spots was visualized, confirming the hybridization of the complementary strand with the capture probes previously immobilized on the chip using the proposed UV light assisted GOPTS-based functionalization process.

2.3 Conclusions

In this chapter, we have discussed several concepts related to the chemical surface modification of a biosensor. In order to provide the selectivity towards certain target of molecules,

the sensor needs to be coated with a proper layer known as recognition layer. This layer permits a selective attachment of the bioreceptors on the sensing area. One of the major challenges in the field of biosensors development is the lack of a unique optimal protocol to immobilize the receptors to the surfaces; for that reason, many efforts have been carried out to develop immobilization strategies suitable to obtain an optimal coverage of the sensor surface with the desired receptors. For a high performance functionalization, we have determined that it is necessary to take into account the chemical and physical properties of the surface, the orientation of the receptor, the distance between the surface and the analyte, and the surface coverage with the receptors.

We classified the linkage of the receptors to the surface in three methods: adsorption-based immobilization, covalent attachment and bioaffinity-based immobilization where a molecule system with a high affinity constant is used. Although adsorption is a straightforward method for anchoring the receptors to the surface, the orientation is generally random and the coverage is non-homogeneus. The covalent link permits to anchor the receptor through functional groups resulting in an irreversible binding producing a high surface coverage. The last method offers a gentle oriented immobilization of the receptors. The suitability of each method will depend on the final application.

We studied that silanes are suitable compounds that permit the attachment of the probes to the silicon-based materials. A silane molecule is able to form a stable covalent bond with the sensor surface and provides a particular functional group for immobilizing the receptors. Therefore, silane-based chemical methods provide attractive opportunities for the functionalization of silicon-based surfaces for biological modification. In this work, we developed two complete functionalization strategies to immobilize the receptors on silicon-based surfaces. Chemical immobilization methods for silicon material were firstly optimized in planar substrates to allow the immobilization of the molecules in highly controlled conditions, previously to being applied to the structured photonic sensors. Ideally, the selected functionalization approaches allows to perform the in one-step thus leading to a simpler process, shorter times and leaving the receptor as close to the sensing surface as possible.

The first route to immobilize the molecules to the surface was based on ICPTS, an organosilane ended with an isocyanate group that is reactive towards amine-based molecules. This method was verified to be efficient, simple and rapid. The functionalization was corroborated by means of WCA measurements observing the increment of the hydrophobicity, and XPS measurements resulting in a change in the chemical composition proving that this strategy was appropriate for receptor attachment. This functionalization has demonstrated the capability of the attachment of BSA proteins and the subsequently detection of antiBSA. However, the modification conditions must be controlled thoroughly because the isocyanate groups hydrolyze in presence of humidity losing its functionality.

The second strategy was based in a novel method employing GOPTS and enhancing the reaction between the epoxy-ended surface with the thiolated receptors by means of UV light, reducing significantly the preparation time. Similarly to the ICPTS-based method, the GOPTS functionalization was also verified with WCA and XPS measurements. Besides being a one-step modification method, the main advantage of this new protocol was the reduction of the incubation time due to the light-boosted reaction. This strategy was also employed for DNA detection in microarray platform. The GOPTS silane exhibited to be a more robust functionalization strategy because its epoxy termination is not hydrolyzed by the presence of moisture.

Therefore, the developed methodologies allowed the chemical anchoring of biomolecules onto the sensor surface. In addition, they exhibit the requirements of compatibility with biological functionalities, specificity, simplicity and versatility that are crucial to provide a competitive functionalization process.

References

[ABO11] M. H.Abouzar, A. Poghossian, A.M. Pedraza, D. Gandhi, and S. Ingebrandt, "An array of field-effect nanoplate SOI capacitors for (bio-) chemical sensing." Biosensors & Bioelectronics, vol. 26(6), pp. 3023-3028, 2011.

[CHA12] S. Chakravarty, Y. Zou, W.cheng Lai, and R.T. Chen, "Slow light engineering for high Q high sensitivity photonic crystal microcavity biosensors in silicon." Biosensors & Bioelectronics, vol. 38(1), pp. 170-176, 2012.

[CHA13] S. Chakravarty, W. Lai, Y. Zou, H.A. Drabkin, R.M. Gemmill, G.R. Simon, S.H. Chin, and R.T. Chen, "Multiplexed specificlabel-free detection of NCI-H358 lung cancer cell line lysates with silico based photonic cristal microcavitybiosensors." Biosensors & Bioelectronics, vol. 43, pp. 50-55, 2013.

[DUV12] D. Duval, A.B. Gonzalez-Gerrero, S. Dante, J. Osmond, R. Monge, L.J. Fernandez, K.E. Zinoviev, C. Dominguez, and L.M. Lechuga, "Nanophotonic lab-on-a-chip platform including novel bimodal interferometers ,microfluidics and grating couplers." Lab on a chip, vol. 12, pp. 1987-1994, 2012.

[ESC12a] J. Escorihuela, M. J. Bañuls, R. Puchades, and Á. Maquieira, "DNA microarrays on silicon surfaces through thiol-ene chemistry." Chemical Communications (Cambridge, England), vol. 48(15), pp. 2116-2118, 2012.

[ESC12b] J. Escorihuela, M.J. Bañuls, R. Puchades, and A.Maquieira, "Development of Oligonucleotide Microarrays onto Si-Based Surfaces via Thioether Linkage Mediated by UV Irradiation." Bioconjugate Chemistry, 23(10), 2121-2128, 2012.

[FEI78] J.A. de Feijter, F.A. Veer, Biopolymers, 17, pp. 1759, 1978

[GOD09] S. Mandal, M. Goddard, and D. Erickson, "A multiplexed optofluidic biomolecular sensor for low mass detection." Lab on a chip, vol. 9, pp. 2924-2932, 2009.

[GRE08] G.T. Hermanson, "Bioconjugate Techniques." 2nd Ed Academic Press: London, UK, proceedings, pp 562-581, 2008.

[GUO10] Y. Guo, J.Y. Ye, C. Divin, B. Huang, T.P. Thomas, P. Thommey, J.R. Baker, T.B. Norris, "Real-time biomolecular binding detection using a sensitive photonic crystal biosensor.," Analytical Chemistry, vol. 82(12), pp. 5211-8, 2010.

[HAE10] C. Haensch, U. S. Schubert, and S. Hoeppener, "Chemical modification of self-assembled silane based monolayers by surface reactions," Chemical Society reviews, vol. 39, pp. 2323-2334, 2010.

[HUN10] H.K. Hunt, C. Soteropulos and A.M. Armani, "Bioconjugation strategies for microtoroidal optical resonators." Sensors, 10 pp. 9317-9335, 2010.

[IQB10] M. Iqbal, M.A. Gleeson, B. Spaugh, F. Tybor, W.G. Gunn, M. Hochberg, "Label-Free biosensor arrays basedon silicon scanning instrumentation," IEEE Journal of Selected Topics in Quantum Electronic", vol. 16(3), pp. 654-661, 2010.

[JON08] P. Jonkheijm, D. Weinrich, H. Schröder, C.G. Niemeyer, and H. Waldmann, "Chemical strategies for generating protein Biochips." Angewandte Chemie International. Edition. 47, pp. 9618-9647, 2008.

[LUC12] M.S. Luchansky and R.C. Bailey, "High-Q optical sensors for chemical and biological analysis." Analytical chemistry, vol. 84(2), pp. 793-821, 2012.

[MAH09] S. Mahajan, D. Sethi, S. Seth, A. Kumar, P. Kumar, and K. C. Gupta, "Construction of oligonucleotide mkicroarrays (Biochips) via thioether linkage for the detection of Bacterial Meningitis", Bioconjugate Chemistry, vol. 20(9), 1703-1710, 2009.

[ROG00] K.R. Rogers. "Principles of affinity-based biosensors", Molecular Biotechnology, Vol. 14(2), pp. 109-129, 2000.

[RUS07] F. Rusmini, Z.Z. hong, and, and J. Feijen, "Protein immobilization strategies for protein biochips" Biomacro-molecules, Vol. 8(6), pp. 1775-1789, 2007.

[SCU11] M.G. Scullion, A.D. Falco, and T.F. Krauss, "Slotted photonic crystal cavities with integrated microfluidicsfor biosensing applications," Biosensors and Bioelectronics, vol. 27(1), pp. 101-105, 2011.

[SEP06] B. Sepúlveda, J. Sánchez del Río, M. Moreno, F.J. Blanco, K. Mayora, L.M.Lechuga,"Optical biosensor microsystems based on the integration of highly sensitive Mach–Zehnder interferometer devices." J. Opt. A: PureAppl. Opt. 8, pp. 561-566, 2006.

[WAS10] A.L. Washburn, M.S. Luchansky, A.L. Bowman, and R.C. Bailey, "Quantitative, Label-free detection of five protein biomarkers using multiplexed arrays of silicon photonic microring resonators." Letters to Analytical Chemistry, vol. 82(1), pp. 69-72, 2010.

3

Biosensing using photonic crystals

3.1 Introduction

Since first articles published by Yablonovich and John in 1987 [YAB87, JOH87] showing the potential of the so-called photonic crystals PhC, such structures have attracted a great interest due to their ability to tailor the material for electromagnetic interactions. The work done since then has led to the development of many photonic devices based on PhCs that can confine, control and route the light in a photonic chip. Besides these applications, PhCs are also recognized as a good solution for the development of chemical and biological sensing structures. Such structures owe the capability of extraordinarily enhancing the light-matter interaction by means of the slow-light effect, which implies an enhancement in the interaction in terms of time and intensity. This fact, combined with the high dependence on their spectral response with the surrounding medium, makes PhCs very sensitive devices for the detection of molecular interactions.

In section 3.2, we will introduce the fundamentals of 1D and 2D PhC structures, since they have been the main configurations used in this PhD work for the development of photonic biosensing structures. 1D periodic structures will be used in chapter 5 for the development of low-cost and real-time biosensors whereas 2D PhC will be used in this chapter. We will also describe the slow-light effect generated in PhC waveguides (PhC-WG). In section 3.3, we will overview the current state-of-the-art of PhC technology in the field of biosensing applications. Section 3.4 will be focused on the design of the PhC-WG to be used in our sensing experiments and in a theoretical propagation study showing the possibility of using Fabry-Perot fringes at the edge of the guided band (i.e., slow-light region) for sensing purposes. The fabrication of the PhC sensing structures will also be described in this section. The experimental set-up employed for the sensing measurements is described in section 3.5, including the optical interrogation system as well as the fluidic delivery system. Finally, section 3.6 will show the experimental results obtained using PhC-WG sensing structures within the frame of this PhD Thesis, which are focused on refractive index, antibody and DNA sensing.

3.2 Fundamentals of photonic crystals

We define PhCs as structures in which the dielectric constant has a periodic variation in one, two or in all three orthogonal dimensions [BOG05]. They are named after their periodicity; therefore, we can find one-dimensional (1D), two dimensional (2D), and three dimensional (3D) PhCs. Depending on the configuration of the structure (i.e., dielectric constant, distribution), that periodicity can give rise the formation of a range of frequencies in which optical modes cannot propagate through the device. This portion of the spectrum is called stop-band or more usually, PBG. This phenomenon is present in the nature, for instance in the butterflies wings as shown in Fig. 3.1, making that the colours perceived are not due to the presence of pigments but to the reflection of determined wavelengths in the visible spectral range.

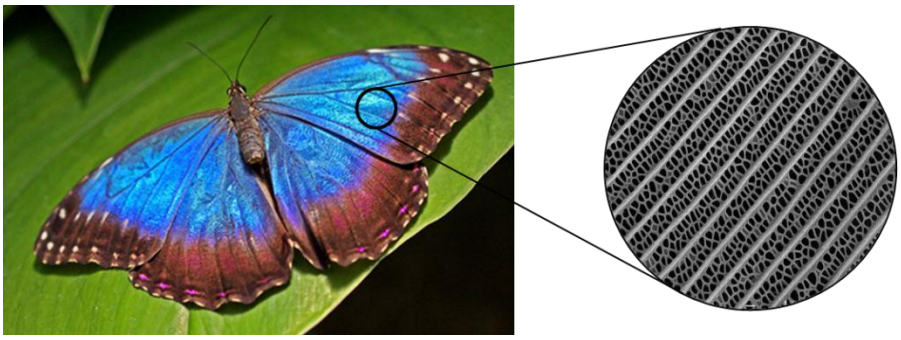

Fig. 3.1: *The periodic structure forming the butterfly wing reflects a certain range of wavelengths in the visible range, which do not coincide with its pigment.*

1D PhCs are those structures that present a periodicity in only one dimension. The simplest 1D PhCs are based on multilayer structures, as schematically depicted in Fig. 3.2a. This type of structures, where the refractive index is periodic in one direction and homogeneous in the other two, are well known and widely reported in literature [CAL11, ZHA10, YAN13, BAR09]. It is also possible to obtain these 1D PhC structures, for instance, by periodically modulating the refractive index of a planar waveguide by inserting transversal elements along the direction of the propagation [GNA06, NUN10, JUG12]. This type of 1D PhC will be presented in chapter 5 and it will be used for the experimental demonstration of a novel power-based read-out technique for the development of low-cost and real-time photonic biosensors.

On the other hand, 2D PhCs are those structures in which the periodicity varies in two directions while there is no periodic variation in the third direction, as shown in Fig. 3.2b. These structures can be obtained, for instance, by means of drilling holes with a determined periodicity in a high refractive indexmaterial [SKI07, BUS08, GOP12, LEE07, SCU11] or by placing cylinders of high index material in a low index core material (e.g.: pillars of silicon in air) [XU10, HUA12]. Since this type of structure is the objective of the work to be described in this chapter, it will be thoroughly analysed in following sections.

Finally, 3-D PhCs are structures in which the refractive indexvaries in all three dimensions of the space [LIA12] as shown in Fig. 3.2c. These periodical structures can be obtained by different methods such as self-assembled colloidal crystals of high refractive indexspheres in air [MIY12], woodpile structures [VAS12] or by nanosphere lithography [VLA12]. Although 3D structures are potentially applicable to biosensiong purposes they are not objective of these PhD thesis.

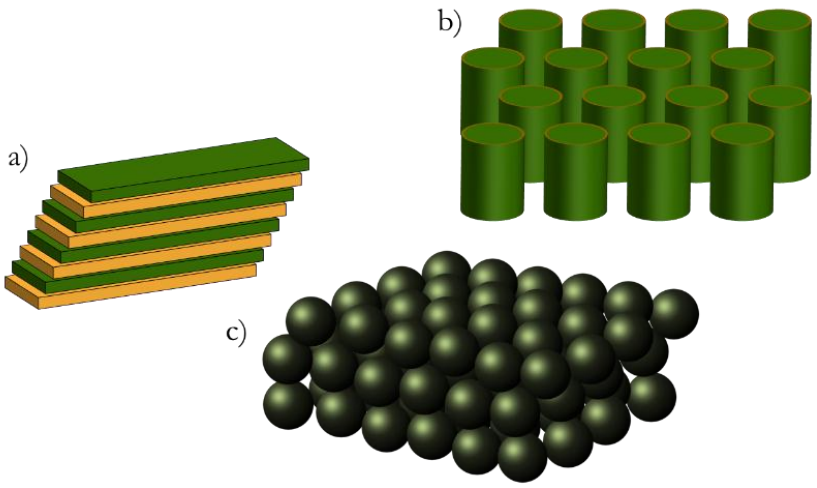

Fig. 3.2: *Schematic representation of different configurations of PhCs with different periodicities: a) 1D, b) 2D and c) 3D.*

3.2.1 Propagation in homogeneous media

Before analysing the propagation of light inside PhCs, first we will study how light propagates in a homogeneous medium. Let us assume monochromatic electromagnetic waves of frequency *f* propagating in a linear, isotropic and homogeneous (LIH) dielectric medium. As well known, light propagation in such material can be explained using Maxwell's equations in differential notation for electric and magnetic fields[1]:

$$\nabla \mathrm{x}\mathbf{E} = -\frac{\partial \mathbf{B}}{\partial t} \tag{3.1}$$

$$\nabla \mathrm{x}\mathbf{H} = \frac{\partial \mathbf{D}}{\partial t} + \mathbf{J} \tag{3.2}$$

$$\nabla \cdot \mathbf{D} = \rho \tag{3.3}$$

$$\nabla \cdot \mathbf{B} = 0 \tag{3.4}$$

where $\boldsymbol{E}$ and $\boldsymbol{H}$ are the electrical and magnetic fields, $\boldsymbol{D}$, and $\boldsymbol{B}$ are the displacement and magnetic induction fields and ρ and $\boldsymbol{J}$ are the free charge and current densities respectively. Then, by considering a relative magnetic permeability μ_r and a relative dielectric constant ϵ_r for the medium, the constitutive relations for the electrical and the magnetic fields are given by:

$$\mathbf{D} = \epsilon_r \epsilon_0 \mathbf{E} = \varepsilon \mathbf{E} \tag{3.5}$$

$$\mathbf{B} = \mu_r \mu_0 \mathbf{H} = \mu \mathbf{H} \tag{3.6}$$

In free space, or in a LIH medium, the permeability and the permittivity are scalar functions of the frequency. However, we can assume that there is no dispersion for these terms within the spectral range that we are considering, leading to ε_r and μ_r to be constant. If we introduce the constitutive relations into the Maxwell's equations and we set the currents to zero (we consider that there are no sources), we obtain the equations as follows:

$$\nabla^2 \mathbf{E}(\mathbf{r}, \mathrm{t}) - \epsilon\mu \frac{\partial^2 \mathbf{E}(\mathbf{r}, \mathrm{t})}{\partial \mathrm{t}^2} = 0 \tag{3.7}$$

$$\nabla^2 \mathbf{B}(\mathbf{r}, \mathrm{t}) - \epsilon\mu \frac{\partial^2 \mathbf{B}(\mathbf{r}, \mathrm{t})}{\partial \mathrm{t}^2} = 0 \tag{3.8}$$

The solution of these equations are known as plane waves, which travel at the speed v determined by the dielectric constant ε and the magnetic permittivity μ of each material:

[1] Vectorial magnitudes are designated in bold, those magnitudes without bold indicates the module of the magnitude.

$$v = \frac{1}{\sqrt{\epsilon\mu}} = \frac{c}{\sqrt{\epsilon_r \mu_r}} = \frac{c}{n'} \tag{3.9}$$

where c is the speed of light in vacuum and n' is the refractive index of the medium. Consider Eq. 3.9, we can rewrite Eqs. 3.7 and 3.8 as:

$$\left(\frac{c}{n}\right)^2 \nabla^2 \mathbf{E}(\mathbf{r}, \mathrm{t}) - \frac{\partial^2 \mathbf{E}(\mathbf{r}, \mathrm{t})}{\partial \mathrm{t}^2} = 0 \tag{3.10}$$

$$\left(\frac{c}{n}\right)^2 \nabla^2 \mathbf{B}(\mathbf{r}, \mathrm{t}) - \frac{\partial^2 \mathbf{B}(\mathbf{r}, \mathrm{t})}{\partial \mathrm{t}^2} = 0 \tag{3.11}$$

The solution for the previous Maxwell's equations for the electric field as a function of time t and position $\boldsymbol{r}$ is a superposition of different waves given by the general equation of a plane wave according to:

$$\boldsymbol{E}(\boldsymbol{r}, t) = \mathrm{Re}[\boldsymbol{E}_0 e^{j\boldsymbol{k}\cdot\boldsymbol{r}} e^{-j\omega t}] \tag{3.12}$$

where the amplitude and the phase of the plane wave is given by $\boldsymbol{E_0}$, which is a complex magnitude, ω is the angular frequency (given by $\omega=2\pi f$) and $\boldsymbol{k}$ is the wave vector which indicates the propagation direction of the electromagnetic wave. The relation between the angular frequency and the wave vector for a homogeneous material is linearly dependent:

$$\frac{\omega}{|\boldsymbol{k}|} = \frac{\omega}{k} = \frac{c}{n} \tag{3.13}$$

This relation between k and ω is called dispersion relation and it is dependent on the medium through which the plane wave is travelling and, therefore, of its refractive index. For a LIH medium, the dispersion relation is lineal, as it is shown in Fig. 3.3 for three different media (air, silicon oxide and silicon). The slope of the dispersion curve becomes lower as the refractive index of the material increases, thus decreasing the wave velocity in the medium.

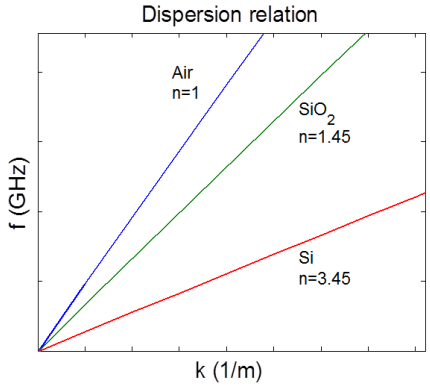

Fig. 3.3: *Dispersion relation for a LIH medium with different refractive indices. The slope is lower as the refractive index increases.*

If we assume a modulated wave with a certain bandwidth, the modulation and the phase fronts of the carrier wave do not necessary travel at the same speed. In this case, the phase velocity will be determined by $v_p=\omega/k$ whereas the group velocity v_g of the information transmitted along the wave is given by the derivative of the relation given in Eq. 3.13. A singular case is obtained in a LIH material, in which an electromagnetic wave composed of a single wavelength (i.e., a monochromatic plane wave) propagates through the material at a speed c/n or ω/k, which corresponds to the slope of the dispersion relation:

$$v_g = \frac{\partial \omega}{\partial k} = 2\pi \frac{\partial f}{\partial k} \tag{3.14}$$

Clearly, in LIH media where the dispersion relation is linear, the group and the phase velocities are equal. However, this effect will change when the material is no longer homogeneous as occurs in PhC structures.

3.2.2 1D periodic structure

When the medium where the wave propagates is periodic instead of homogeneous, the situation changes completely. In this section, we tackle the study of the propagation of a wave in the simplest configuration of PhC: the 1D PhC. As previously mentioned, a 1D PhC is periodic along one direction, which coincides with the direction of the electromagnetic propagation, whilst it is homogeneous in the other two directions. This configuration is schematically represented in Fig. 3.4, where the structure is comprised of alternated layers of materials with different dielectric constants.

1D PhCs consist of a basic cell (depicted with a box in Fig. 3.4) that is periodically replicated in the space each certain distance a, known as lattice constant or period. Therefore, the refractive index distribution will also be periodic according to $n(r) = (\mathbf{r} + aR)$, where R represents any integral multiple of the lattice vector and $\boldsymbol{a}$ the primitive lattice vector along the propagation of the light. In the case of Fig. 3.4, where the medium is periodic along the z axis and homogeneous in x and y, the refractive index will only vary in the z direction and it will be given by $n(z)$.

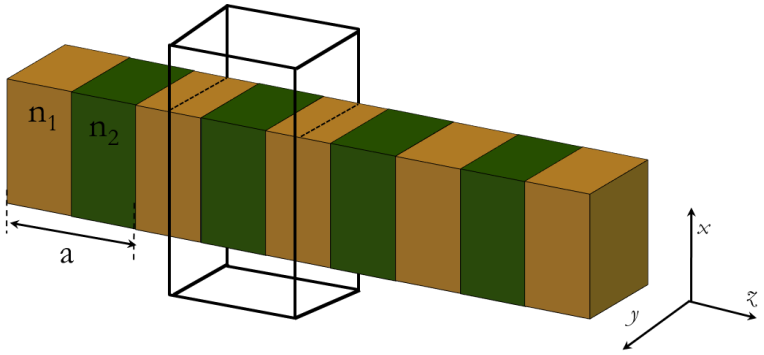

Fig. 3.4: *1D PhC formed by alternate layers of materials with different refractive indices (n_1 and n_2) and with a constant lattice of a. The structure extends infinitely along the three axis.*

Such periodicity of the medium also leads to a periodic dependence on the electromagnetic field in the structure. According to the Floquet-Bloch theorem, the solution of the wave equation in this periodic medium will be given by a plane wave that is modulated by the periodic function of the refractive index. This solution is commonly known as Bloch's mode and is given by:

$$\boldsymbol{E}(z,t) = Re\left[\boldsymbol{u_k}(z) \cdot \boldsymbol{E_0} e^{jk_z(\omega)\cdot z} e^{-j\omega t}\right] \tag{3.15}$$

where $\boldsymbol{u_k(z)}$ is a periodic function with the same period as the dielectric distribution. Therefore, its optical modes are waves that maintain their form in the periodicity direction and that are only modified by a phase factor given by:

$$\boldsymbol{u_k}(z) = \boldsymbol{p_k}(z) e^{-jk_z z} \tag{3.16}$$

where k_z is the propagation constant and $\boldsymbol{p_k(z)}$ is a periodic function of period a. In an ideal medium the function that modulates the plane wave only alters the plane wave by a phase factor.

As a result, due to the periodicity of the structure, k_z is no longer linearly dependent on ω and an infinite number of solutions with different frequencies will exist for each wave vector, since the modes are coupled between them by the periodic lattice. These solutions, known as dispersion relation or band diagram, will be sorted in modes and the frequency of each of them will vary continuously as a function of k.

Another consequence of the periodicity of the structure is that two modes with Bloch wavenumbers $k_z = k_z' = k_z + m \cdot 2\pi/a$ are equivalent since they correspond to the same phase factor. Therefore, for a complete solution of all modes, we only need to consider values of k in a wave vector interval of $k=2\pi/a$ in the direction of the primitive lattice vector. These solutions can be plotted in the range of $-\pi/a < k_z \leq \pi/a$. This region of non-redundant values of k_z is called the Brillouin zone. Fig. 3.5 shows several examples of band diagram $\omega(k_z)$, for different configurations

of multilayer 1D PhCs where we can see that only solutions within the Brillouin zone need to be obtained.

Several conclusions can be extracted from band diagrams of Fig. 3.5:

- The diagram on the left is obtained for a bulk material, which has been defined considering alternate layers of the same material (i.e., with the same refractive index). Therefore, this case corresponds to the case of a homogenous material that was introduced in section 3.2.1 and the band diagram shows a normalized frequency that depends linearly on the wave vector.
- The diagram on the center represents the case when the refractive indices of the alternating layers are very similar (n_1=3.6 and n_2=3.46). In this situation, a small PBG where no guided modes are allowed appears.
- In the diagram of the right, the difference between the refractive indices of the alternate materials increases (n_1=3.6 and n_2=1), leading to the appearance of a wider PBG. For that reason, it is desirable to use a high refractive index contrast between materials in case we want to achieve large PBG. In our case, we will work with SOI technology, which provides a very high index contrast (n_{Si}=3.45 and n_{SiO2}= 1.45), making the technology suitable for the fabrication of PhC structures with large PBGs.

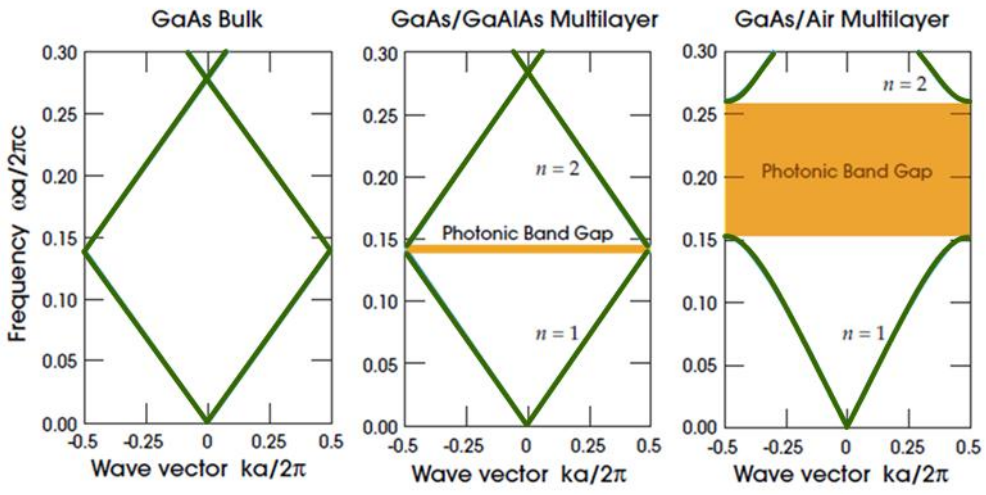

Fig. 3.5: *Normalized band diagrams for different configurations of 1D PhC. (Left) Homogeneous material with n=3.6. (Center) Multilayer of n_1=3.6 and n_2=3.46. (Right) Multilayer of n_1=3.6 and n_2=1. Figure adapted from [JOA08].*

Finally, another intriguing issue that is observed in Fig. 3.5 is that the structure behaves similarly to a homogeneous medium for lower frequencies independently on the configuration of materials. This is because the period of the structure is much smaller than the wavelength of the

propagating light, so that the wave perceives it as a homogeneous-like medium. However, as frequency increases, the dispersion relation does not behave linearly and tends to flatten, mainly at the edges of the Brillouin zone. Here we can note one of the main properties of the PhCs. As above mentioned, the group velocity is determined by the slope of the $\omega(k)$; therefore, when the wave vector k_z is close to the edge of the Brillouin zone ($k_z = \pi/2$), a reduction of the slope will also mean a reduction of the group velocity, which may reach a value equal to 0 yielding to the creation of a *quasi-stopped* wave in the PhC at a certain wavelength. This effect is known as slow-light effect and it is a key phenomenon for the development of PhC-based biosensors, since group velocity reduction is translated into an enhanced interaction between the optical mode and the target matter, as it will be described in more detail in section 3.2.6.

3.2.3 2D periodic structure

The concepts introduced in the previous section for the case of optical wave propagation in a 1D PhC can be generalized for periodicity in multiple dimensions. In 1D structures, the periodic lattice can be expressed just using a single vector of the length of the period of the structure and oriented towards the periodicity. However, in case the structure is periodic in more dimensions, we can add additional base vectors to represent those periodicities in the structure employing a lineal combination. These vectors will be the unity vectors of the lattice of the periodic structure. Therefore, in 2D and 3D PhC structures, $\boldsymbol{n(r)}$ is a periodic function given by the lattice vectors $\boldsymbol{a_1}$, $\boldsymbol{a_2}$ and $\boldsymbol{a_3}$. Likewise, the function $\boldsymbol{u_k(r)}$ that represents the Bloch modes within the structure, will also be periodic with the same periodicity of the structure itself.

In a 2D PhC we will have dielectric elements with a periodic distribution in two dimensions (we will consider a periodicity in the x and z axis) and uniform and infinite in the third dimension (in this case, in the y axis) embedded in a homogeneous host medium. Since the periodicity is given in a plane, the light will be controlled in those two dimensions, whereas in the third dimension the electromagnetic wave will not be confined.

An example of a 2D PhC consisting on a periodic distribution of low index columns in a high index material is schematically depicted in Fig. 3.6. Analogously to the case of 1D periodicity, Bloch's theorem states that modes with wave vector k and wave vector $\boldsymbol{k+G}$ are identical if $\boldsymbol{G}$ is a linear combination of the unity vectors $\mathbf{a_1}$ and $\mathbf{a_2}$. This means that we can constrain the analysed modes to a certain domain known as first Brillouin zone. Fig. 3.6 represents the first Brillouin zone for a hexagonal periodic distribution, which will also be hexagonal. When the band diagram of a 2D PhC is obtained, modes along the edges of the so-called reduced Brillouin zone (yellow shaded triangle in the figure for the case of a hexagonal periodic distribution) are only calculated. Modes distribution within this path allows to determine the frequency ranges where the modes exist, and thus to determine the presence of PBG.

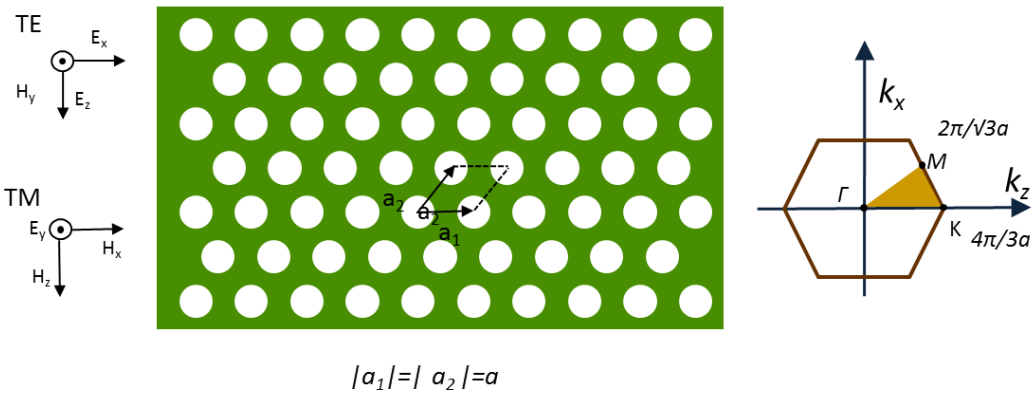

$|a_1|=|a_2|=a$

Fig. 3.6: *2D periodic structure with a hexagonal distribution given by the lattice vectors a_1 and a_2. The structure consists of low index columns of radius r in a high index material.*

This structure is invariant along the third axis, so we can consider that the wave only travels in the plane in order to simplify the analysis. This feature enables to split the problem into two different polarizations, thus simplifying the problem:

- TE modes (Transversal electric field): The electric field is in the plane of the periodicity whereas the magnetic field only has a component in the vertical dimension.
- TM modes (Transversal magnetic field): Unlike TE modes, the magnetic field is included in the plane of the periodicity and the component of the electric field is in the vertical dimension.

The fact that the problem can be solved by dividing it into two polarizations makes that the behaviour of the PhC is different for each of them. Fig. 3.7 shows the band diagram for wave vectors along the edges of the reduced Brillouin zone for the periodic structure shown in Fig. 3.6 when the columns are made of air (n = 1), their radius is $r=0.3\cdot a$, and the core material is silicon (n=3.45), and considering the polarization splitting. In the plots, we can observe that the band diagrams are completely different for each polarization, leading also to the creation of different PBGs for TE and TM. We can also observe that an overlap between both PBG exists; this frequency region where light is not permitted to travel along the plane of the structure in any polarization is called complete PBG.

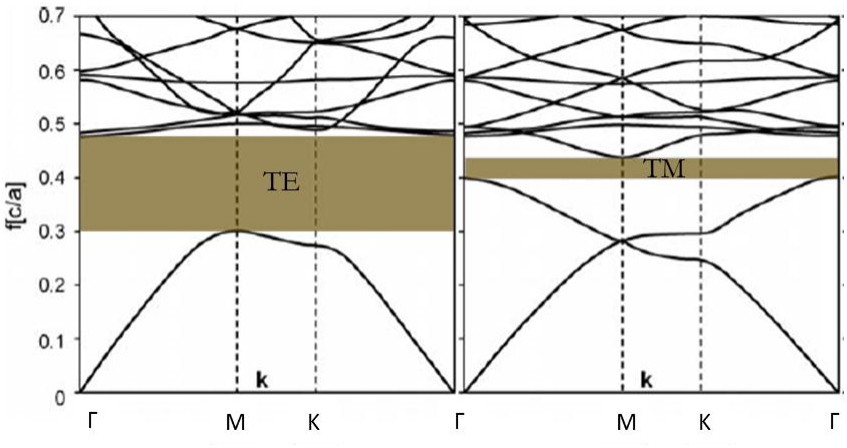

Fig. 3.7: *Illustration of the band diagram for the periodic distribution shown in Fig. 3.6 when the columns are made of air (n = 1), their radius is r = 0.3·a, and the core material is silicon (n = 3.45). The band distribution is different for each polarization. A periodic distribution of low index elements into a high index background favours the appearance of PBGs for the polarization.*

Obviously, the band diagram will also depend on the dielectric distribution of the PhC. Fig. 3.8 shows the band diagram for two opposite configurations of 2D PhC: 1) a periodic distribution of low index columns (e.g., air holes) in a high index medium, and 2) a periodic distribution of high index columns in a low index medium (e.g., air). From the band diagrams depicted in Fig. 3.8, we can see that a periodic distribution of isolated elements of low index in a high index medium (e.g., air holes in dielectric) favours the appearance of PBGs for TE modes. On the other hand, isolated elements of high index in a low index medium (e.g., pillars in air) favours the appearance of TM PBGs.

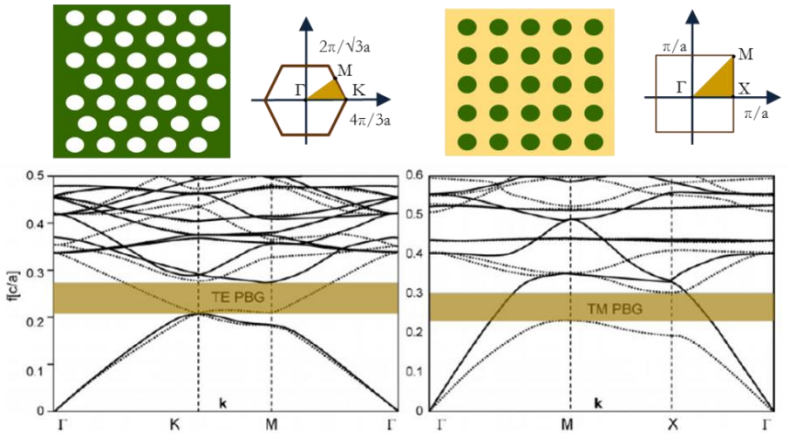

Fig. 3.8: *Band diagram for two different configurations of 2D PhC structure. In both graphs, TE modes are represented with solid line and TM modes with dotted line. The structure of the left, made of low index elements in a high index medium, exhibits a bandgap for TE polarization, whereas the structure of the right, made of high index columns in a low index medium, exhibits a bandgap for TM polarization.*

Therefore, if we want to have a complete PBG covering both polarizations, we will need to carefully design the structure in order to overlap both PBGs (for TE and TM). This fact may be a strong limitation in the design of a PhC due to the complexity to obtain such overlap between PBGs. However, in practice it is not necessary to obtain PhC structures exhibiting a complete PBG for both polarizations, since it is possible to employ single polarized light and to work only for that polarization that exhibits a strong PBG. For example, in our work we will use a holes-on-dielectric periodic distribution for the development of the PhC-based biosensing structures, where a PBG for the TE polarization will be exhibited; therefore, we will only couple TE-polarized light for the interrogation of the sensing structure.

3.2.4 Vertical confinement

In the previous section, we have presented how the electromagnetic modes are distributed within the periodic structure when we assume that they only propagate along the plane of the periodicity (*x*-*z* in our case) while being infinitely invariant in the vertical direction (*y*). Nevertheless, in real case, there is not a perfect propagation in the *x*-*z* plane and the light may be diffracted and radiated in the vertical direction. For that reason, as well as because of the impossibility to achieve a structure that is infinite in one of its dimensions, it is necessary to provide light confinement in the vertical direction of the PhC.

In order to confine the light in the plane of the PhC, the height of the periodic structure will be limited to a certain thickness *h*, and it will be surrounded by layers of materials with lower refractive indices. In this manner, if the refractive index contrast between the cladding materials and the PhC structures is adequate, the mechanism of total internal reflection (TIR) will provide the necessary confinement in the vertical direction. By combining the PBG mechanism to confine the light in the plane of periodicity, and the index guiding mechanism to confine the light in the vertical direction, we can obtain planar photonic structures that will be feasible to fabricate using current planar fabrication processes.

However, not all the previously calculated modes for an ideal infinite 2D PhC will be confined inside the planar photonic structure with the same in-plane periodic distribution. The new upper and lower cladding layers support radiative modes, which may travel along the cladding instead of being confined in the PhC. The range of modes that will be confined inside the structure is determined by the light cone of the cladding material, which is given by the band diagram of the homogeneous medium:

$$\omega = \frac{c|k|}{n_s} \tag{3.17}$$

where c is the speed of light in vacuum, $|k|$ is the modulus of the wave vector in the plane of the periodicity and n_s is the refractive index of the material comprising the substrate. When the planar PhC is surrounded by two different dielectric materials, i.e., the lower cladding material is different to the upper cladding, we will have to consider the light cone for both materials, being the material of higher refractive index the one that will limit the total confinement in the vertical direction. This will be our case for sensing application, where we will have a dielectric lower cladding (usually made of SiO_2) and a liquid or gas upper cladding corresponding to the target substance. Fig. 3.9 shows the band structure of a 2D PhC overlapped with the light cone of the two claddings surrounding it (i.e., air and SiO_2). As previously indicated, the cladding of the material with higher refractive index (SiO_2 in this case) will determine the modes of the PhC structure that will be confined on the plane and guided without losses. On the other hand, those modes above the light cone will not be perfectly confined within the planar PhC, thus leading to a radiative propagation with higher losses.

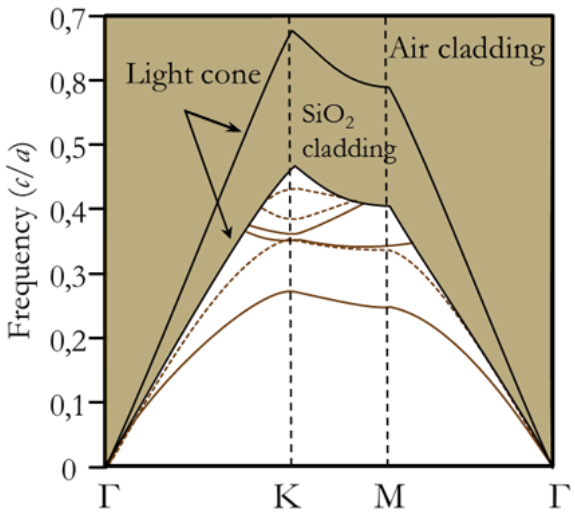

Fig. 3.9: *Band diagram of a planar 2D PhC with claddings of air and SiO_2. The shaded area represents the light cones of the claddings. The material with the higher index will limit the confinement of the modes.*

3.2.5 Photonic crystal waveguide

Modifying locally the PhC structure it is possible to break its periodicity and therefore localize the light in such region forming waveguides or cavities. While in 1D PhCs the insertion of defects is reduced only to the creation of cavities by breaking the periodicity on a single point, in 2D PhCs we also have the possibility to create PhC waveguides (PhC-WGs) by introducing a linear defect on the original periodic configuration. In that case, the structure is no longer translational symmetric in two dimensions. Since no modes are allowed within the PBG region of the bulk PhC surrounding these defects, light will be perfectly confined on them: in the plane by the PBG and vertically by means of TIR.

The manner to define a waveguide in a 2D PhC is by either by changing the dimensions or the refractive inex of the constitutive elements of the PhC [JOH00]. For our sensing objectives, we will considered a PhC-waveguide consisting on a slab of high refractive index with periodic holes in which a complete row of holes is removed. Such waveguide is also called W1 PhC-WG. The appearance of one or more optical modes within the PBG can be designed with a very flat dispersion curve that leads to a slow propagation velocity. Besides the pure guiding function, the phenomenon of slow-light can be used for other purposes such sensing, signal modulation or data storage.

Fig. 3.10 shows the TE-like band diagram for a W1 PhC-WG, which consists of a PhC formed by a hexagonal periodic distribution of holes in a high index medium where an entire row of low index columns is removed from the lattice. The shaded grey area represents the light cone, where the modes will radiate to the substrate, while the brown shaded area represents the supported modes in the PhC region, where light is not confined in the periodicity plane because modes may propagate through the raw PhC structure surrounding the linear defect. We can see that this W1 PhC-WG exhibits two guided modes that are under the light cone and within the PBG of the PhC. The lower band represents the fundamental mode within the bandgap. Besides these PBG-guided modes, those under the PhC modes region are index-guided modes. These low frequency modes (i.e., long wavelength) do not see the periodic dielectric distribution of the PhC structure but simply an effective refractive index for it, thus leading to a pure index-guided confinement on the structure. Since these modes are not confined due to the PBG effect, they will suffer from higher radiation losses when any variation in the shape of the waveguide is produced (e.g., when a sharp bend is created). Therefore, we will not consider these type of modes for sensing applications.

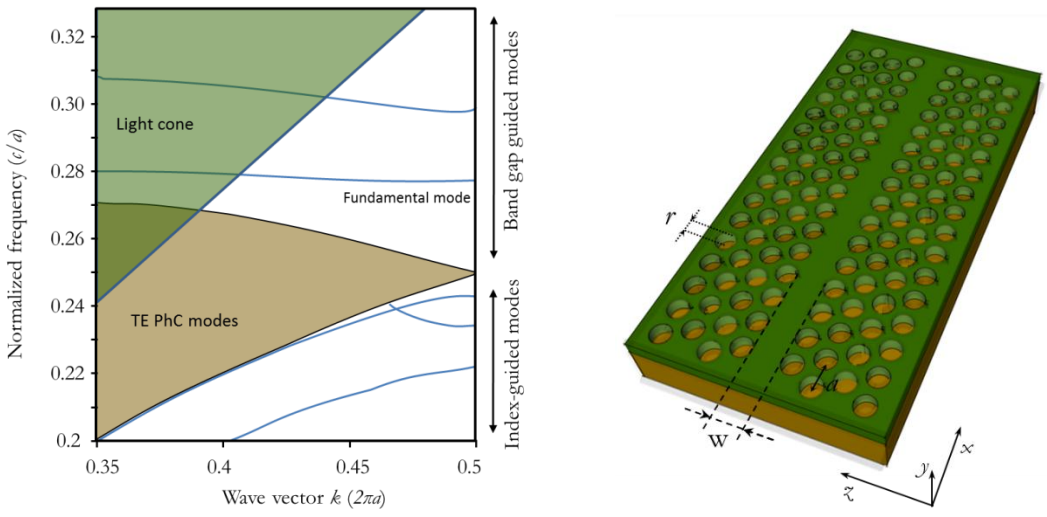

Fig. 3.10: *Band diagram of a W1 PhC-WG corresponding to a hexagonal PhC slab structure of air holes. The lower cladding is made of SiO_2 and the upper cladding is made of air. The structure exhibits two PBG-guided modes within the bandgap of the structure.*

However, as previously indicated, the W1 waveguide is not the only manner to obtain waveguides in PhCs. For example, it is possible to tune the separation between holes or even removing more than one row of holes in order to attract or repel more modes to the PBG. For instance, in a W3 waveguide, three rows of holes are removed. This variation will attract more guided modes to the PBG becoming multimodal with a large number of modes. The drawback of this waveguide is the interaction of the fundamental mode with other high order modes that will produce distortion and thus deteriorating the sensing signal. There are more complex PhC-WGs structures that will be reviewed in the state-of-the-art.

3.2.6 Slow-light effect

During the past years, many groups have been working in developing new methods to significantly reduce the propagation velocity of light. Structures featuring low propagation velocity can be used for the implementation of many new practical applications including, among others, the enhancement of nonlinear effects, the creation of ultra-compact delay lines, data storage for signal processing, or the development of highly sensitive sensing devices [KRA08, POV05, LI12]. Namely, in sensing applications, PhCs that exhibit slow-light phenomenon can provide higher sensitivities and lower detection limits due to the enhancement of the interaction between the electromagnetic field and the target analytes/substances. In this section, we will introduce the mechanism of the slow-light effect and how the light-matter interaction is enhanced.

There are several ways to slow down the propagation velocity of the light, which is given by its group velocity v_g. As previously described, the wave velocity is directly related to the refractive index of the medium where the light is travelling for the case of a homogeneous medium. Therefore, by using high refractive index materials, it is possible to reduce the group velocity by a factor given by the optical properties of the material. However, the refractive index of the materials available for optical guiding is not very large at optical frequencies, thus significantly limiting the group velocity reduction that can be obtained in this way. For this reason, it is desirable to obtain new approaches where light can propagate at much lower speeds. One technique for the reduction of the propagation velocity of light is the electromagnetically induced transparency (EIT) [TUC05, KHU05]. This technique consists on changing the absorption coefficient of the material leading to a change of the refractive index. A rapid change in the refractive index causes an extremely low velocity of the light. However, the main drawback of this method is the requirement of very low temperatures for its operation. Another option to achieve a reduction in the propagation velocity of light is the use of structured materials, as it is the case for structures like Bragg waveguides, RRs or PhCs. These structures have the property of exhibiting an extreme reduction of the group velocity

for those frequencies located near the edges of the confined/guided bands, without the need of harsh conditions.

Fig. 3.11a shows an example of band diagram and a schematic illustration of the mode propagation for a generic W1 PhC-WG, which is the type of photonic structure that will be used in our case for biosensing purposes. As it is observed in the band diagram of Fig. 3.11a, the symmetry occurring at the edge of the Brillouin zone provokes a bending of the guided mode. This reduction in the slope of the dispersion relation of the mode is translated into a reduction in the group velocity, which reaches a limit value of zero exactly at the edge of the Brillouin zone. As it can be seen in the schematic illustration in Fig. 3.11b, propagated light is scattered backward and forward due to the periodicity of the PhC. For a wave vector exactly in the edge of the Brillouin zone (k = 0.5), the wave reflections match in phase and amplitude and create a *standing-like* wave with theoretically zero velocity. As we move away from the edge of the Brillouin zone, the interference waves become out of phase and the group velocity of the resulting mode will gradually increase until it reaches a regular propagation velocity. Therefore, the slow-light effect will only occur for a certain frequency range, what will limit the effective bandwidth for our applications. Furthermore, it will usually be highly dispersive, since group velocity will vary as a function of frequency. However, the generation of slow-light is not limited to the Brillouin edge region, but a proper design of the PhC-WG can exhibit the slow-light effect at a different wave vector.

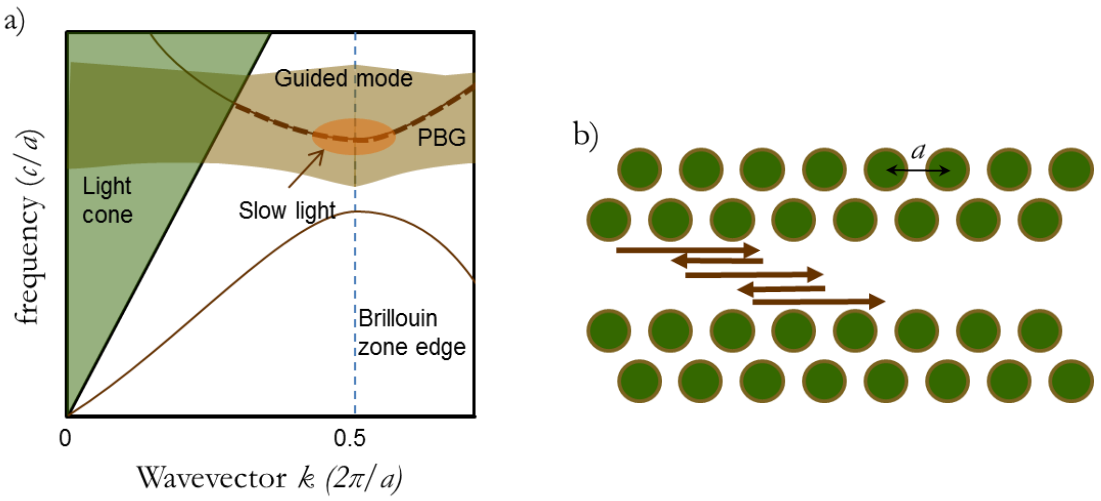

Fig. 3.11: *(Top) Band diagram of a W1 PhC-WG. Black dashed line represents the band-guide mode of the waveguide. The shaded orange area indicated the region where the slow-light appears, which is located around the edge of the Brillouin zone. Brown solid line represents an index-guided mode. (Bottom) Schematic depiction of the mode propagation in a PhC-WG in the slow-light regime. The interference between the different scattered waves provokes the reduction in the group velocity of the mode. Adapted from [KRA08].*

The appearance of the slow-light phenomenon has two main direct consequences that are potentially interesting for biosensing purposes: the increment of the propagation time along the waveguide and the compression of the optical wave. These two effects are conceptually represented in Fig. 3.12. According to the first consequence, a reduction in the propagation velocity of the mode is translated into an increase in the time that light interacts with the target substance/analyte located near the surface of the sensing structure. The second consequence refers to the increment of the optical field that occurs due to the compression of the propagating waves when the mode is slowed down. By combining both effects, the longer interaction time and the increment of the wave intensity, we can expect a significant increase of the sensor sensitivity because of the enhanced interaction of the optical field with the target substances/analytes.

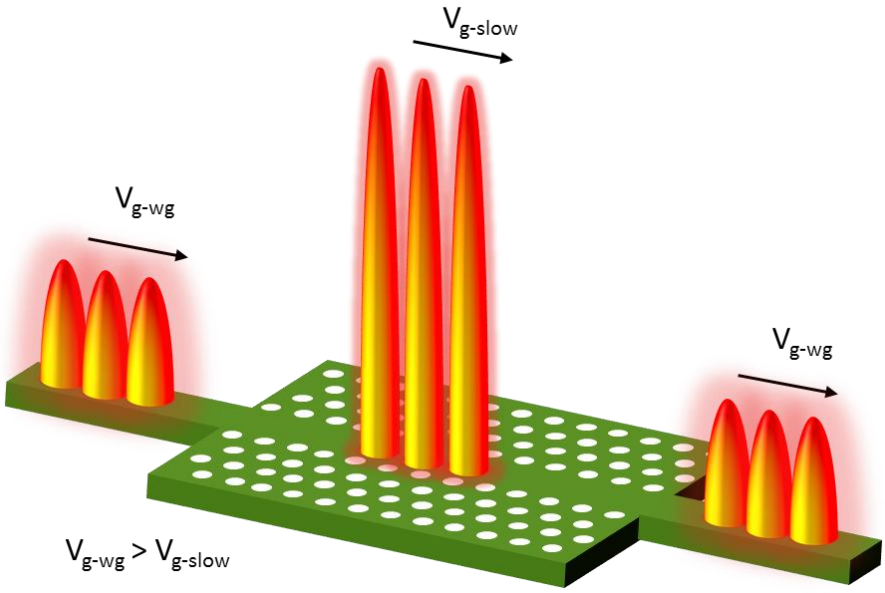

Fig. 3.12: *Conceptual illustration of the slow-light effect in a PhC-WG. The velocity of the wave is reduced and the amplitude is increased when the light is coupled in the structure so the light-matter interaction is enhanced on the PhC area.*

3.3 State-of-the-art of PhC-based biosensors

In the recent years, the application of PhC structures for optical sensing purposes is a research field that attracts a significant interest from the scientific community. PhC-based sensors allows performing a label-free detection based on the interaction of the evanescent field in the structure to detect changes in the refractive index induced by the target analytes. As described in the previous section, the high sensitivity of PhC-based sensing structures arises from the high confinement of the optical field in the defect regions designed for sensing purposes, as well as from the enhancement in the light-matter interaction provoked by the slow-light effect. In this section,

we will review some of the most interesting state-of-the-art results in the field of photonic biosensors based on 2D PhC, with application in several fields such as protein and antibodies sensing, or gas detection among others.

PhC structures for sensing can be fabricated using diverse configurations of materials, which might also depend on the aim of the target application. Besides the periodic structure distribution, the spectral response of the PhC will strongly depend on the refractive index contrast between its materials. Among the configurations of materials currently employed for the development of PhC structures showing PBGs wide enough for sensing applications, we can find aluminium gallium arsenide (AlGaAs, $n_{AlGaAs}=3.37$) on gallium arsenide (GaAs, $n_{AlGa}=2.89$), indium gallium arsenide phosphate (InGaAsP, $n_{InGaAsP}=3.4$) on gallium arsenide, silicon nitride (Si_3N_4, $n_{Si3N4}=1.98$) on silicon oxide (SiO_2, $n_{SiO}=1.45$) and silicon (Si, $n_{Si}=3.45$) on silicon oxide. Undoubtedly, the last materials combination (silicon on silicon oxide, i.e., silicon-on-insulator) is the one most widely employed by researchers and developers, and more frequently reported in the literature. The fabrication of PhC structures based on all these materials combination is carried out by means of lithographic techniques (e.g., electron beam lithography, UV lithographyn nanoimprinting lithography) in combination with the etching of the material. The use of polymers for the development of PhC structures has also attracted some interest during the past years; however, their low refractive index values difficult obtaining good quality PBGs and optical performances of the sensing structure.

Looking at specific results reported in the literature based in the use of PhC structures for the implementation of biosensing applications, one of the firsts was reported by Skivesen et al. In [SKI07] they use a W1 PhC-WG of air holes in SOI for the detection of adsorbed BSA with concentrations down to values around 10 μg/ml. Using a similar PhC-WG, Buswell et al. carried out a proper chemical functionalization to covalently attach biotin as a probe in order to specifically detect a thin streptavidin layer of thickness 2.5 nm (see Fig. 3.13a) [BUS08]. Although these works did not show extremely low detection limits or an outstanding performance, they showed the potential of the development of PhC-based biosensing devices.

A different approach to the development PhC-WG-based sensing structures is the use of slotted PhC-WGs, which were firstly proposed by the group of T. F. Krauss. This type of structure, where a narrow trench is created in the middle of a PhC-WG as shown in Fig. 3.13b and Fig. 3.13c, tries to combine the previously commented benefits of PhC-based sensing structures with the extremely high confinement and intensity of the optical field in slot waveguides [ALM04]. This structure exhibited a sensitivity of 800 nm/RIU for bulk refractive index sensing [FAL09] and concentrations of avidin as low as 15 nM were detected by using a PDMS-based microfluidic delivery system [SCU11]. Moreover, the small size of this structure (~2.2 μm^2) allowed to achieve a minimum detectable mass of 100 ag. Also using PhC-based slotted structures (although different to

the structures used in the previous works), [WAN10] reports the creation of a slot waveguide between only two rows of holes created in InGaAsP and with embedded InAs quantum dots, as shown in Fig. 3.13d. This structure exhibited a resonance around 1550 nm by exciting the quantum dots using a CW laser at 633 nm. An experimental sensitivity of ~700 nm/RIU was obtained using sugar dilutions for the experiments. By simply increasing the radius of the central holes of the structure (see Fig. 3.13d), the slot waveguide becomes narrower and a cavity is created, what allows an enhancement of the sensitivity up to 900 nm/RIU.

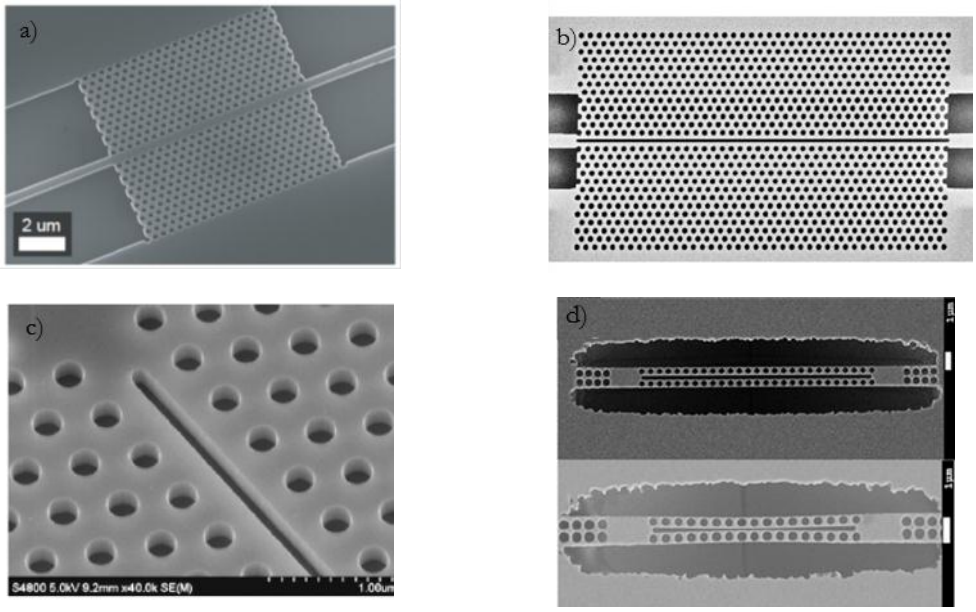

Fig. 3.13: *Scanning electron microscope (SEM) images from different PhC configurations. a) PhC-WG from [BUS08], b) and c) slotted PhC-WG from [FAL09] and [SCU11]. d) Two similar PhC nanobeam from [WAN10].*

Sünner et al. proposed the creation of a cavity by varying the radii of the holes delimiting a W1 PhC-WG type [SUN08]. This variation creates two mirrors that will confine the light inside the cavity. According to the measurements, the structure exhibited a remarkable quality factor (Q) of 40000. Experimental results proved the use of this sensing structure for the detection of different gases with different refractive indices.

Despite in the previous work a PhC cavity based on modifying a W1 PhC-WG, the most typical configuration of a 2D PhC cavity sensor is based on the introduction of a punctual defect into the periodic structure. This defect can be simply designed by either increasing, decreasing or removing one element of the raw periodic structure. Due to the strong light confinement in the cavity, a sharp peak or dip will appear in the transmitted spectrum, whose position will be extremely sensitive to changes of the refractive index within the cavity region.

Two similar works, [LEE07a] and [ZLA09], presented a SOI PhC cavity created by reducing the size of the central hole in the periodic structure, as shown in Fig. 3.14a and Fig. 3.14b, respectively. In the former work, TE light was coupled to the cavity using a single mode waveguide in order to detect deposited BSA protein with an estimation of the minimal detectable mass of 2.5 fg (assuming a perfect monolayer in the sensing area of 50 μm^2). The latter work employed a similar cavity, but in this case, the assay is carried out by flowing the target analytes using a PDMS-based microfluidic delivery system that allows a dynamic observation of the association kinetics of the molecules. Reported results shown a sensitivity of 170 nm/RIU, and by functionalizing the sensor with biotinylated-BSA molecules, it was possible to extract the association and dissociation rates of the antigen-antibody system by employing biotin-antibiotin complex.

In another work by the same authors [LEE07b], they demonstrated a further improvement of the sensitivity reaching a mass detection limit as low as 1 fg. In this case, the structure was designed by widening a hole in the center of the PhC as it is illustrated in Fig. 3.14c, reaching a Q factor of 2000. In order to validate the extremely high sensitivity of the sensing cavity, they carried out the detection of a single latex sphere of 50 nm of diameter, as shown in Fig. 3.14c. By precisely placing the sphere inside the cavity, they obtained a resonance shift of 4.2 nm. Despite this result, the main challenge of this type of sensors is how to precisely deliver the target molecules into the defect in order to carry out a proper detection.

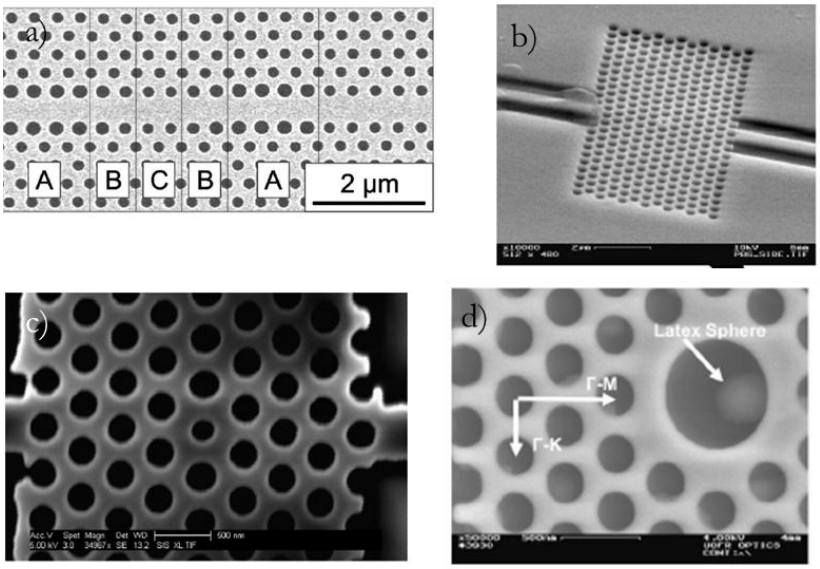

Fig. 3.14: *SEM images of four PhC cavities. The cavity in a) is created by varying the the radii of the holes delimiting the waveguide. In b) and c) the cavity is designed by reducing the radius of a single hole[LEE07a, ZLA09]. c) The cavity is created by increasing the radius of a hole where a latex microsphere is placed inside the cavity [LEE07b].*

A different research was presented by Dorfner et al., who performed a complete study employing two different cavities [DOR08]: a H1 cavity, where a single hole was removed from the lattice, and a L3 cavity, where three consecutively holes were removed. Reported results showed that, although the L3 cavity presented a higher Q factor than the H1 (~2700 vs. <1000), the best sensitivity for bulk refractive index sensing was obtained for the smaller cavity. This effect can be attributed to the larger area of the L3 cavity, what leads to a lower confinement than for the H1 cavity. In a later publication, the same group compared the performance of several cavities in order to perform biosensing measurements with proteins [DOR09]: the above presented H1 and L3 cavities, see Fig. 3.15a, and an additional width modulated cavity (WMC) that was created by shifting several holes perpendicularly to the waveguide orientation. The best results were achieved using the WMC with a Q factor of 6000, obtaining a total mass detection limit of 4 fg assuming a sensitive area of 8.2 μm^2.

So far, surface modification procedures and biosensing experiments reported in most works are fairly simple. However, a big leap regarding the experimental procedures was recently headed by Chakravarty et al., where they reported a more complex biomolecular detection using cell lysates [CHA13]. In that work, an array of 4 multiplexed cavities of type L13 (see Fig. 3.15a) with a high Q (~26000) was employed to detect a protein associated with lung cancer, showing a sensitivity as low as 2 cells/µl for a sensing surface area of 11 μm^2. The specifity of the sensing device was also demonstrated by showing no non-specific binding with control antibodies, thus showing its potential as biosensing platform.

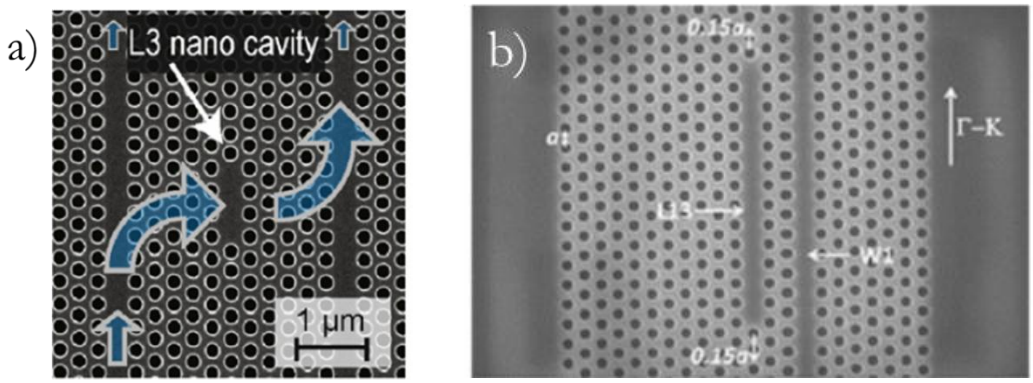

Fig. 3.15: *SEM images of a) PhC structure with a L3 coupled caviy in the middle of two PhC-WGs, and b) a L13 cavity coupled to a W1 PhC-WG used for the detection of biomarkers associated with lung cancer [CHA13].*

Other recent work presented a micromanipulation technique to release an InGaAsP H0 PhC cavity from a wafer and transfer it to the facet of a single mode fiber for direct measurement [WAN12]. The PhC-based sensing structure is directly attached to the optical fiber used for the interrogation, and a strong resonance can be measured in reflection mode. The performance of this

photonic sensing configuration was demonstrated by carrying out several refractive index detection experiments by inserting the fiber in different liquids. The robustness and the portability of this configuration make it very promising for its use in a wide range of applications fields. However, it has not been tested for biosensing yet.

Bulk PhCs without any defect can also be used for sensing purposes. In [HUA09], the authors introduced a novel sensing approach where nano-photonics and nano-fluidics were combined on a single platform. The working principle is depicted in Fig. 3.16. In this approach, the sensing structure consisted on a PhC membrane of air holes in silicon nitride, across of which the target liquid sample was directly flowed through the PhC thus increasing the sensitivity. Both simulated and experimental measurements showed a sensitivity of 510 nm/RIU when the stream delivery is performed through the nanohole openings of the PhC sensing structure instead of using the laminar flows.

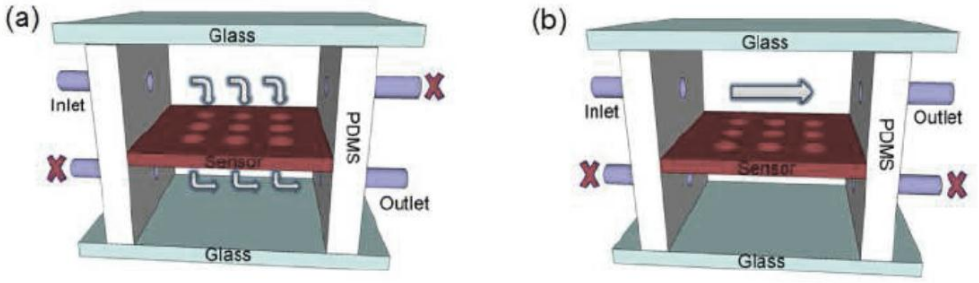

Fig. 3.16: *Illustration of the actively controlled flow scheme presented by [HUA09]. a) The solution flows through the hole array b) conventional flowing scheme.*

Another less usual approach for the development of PhC structures whose feasibility has been demonstrated at different publications are those made using ring-shaped elements, as that shown in Fig. 3.17a. This structure basically consists on a holes-based PhC where each hole is filled with a pillar made of the same material as that where the holes are made. The insertion of the columns within the holes permits a higher flexibility for tailoring the modes of the structure in order to obtain larger bandgaps and small dispersion. Säynätjoki et al. presented a theoretical and experimental study of these structures and demonstrated a proper tunability of the PBG by engineering the rings [SAY08]. In addition, they compared by simulation the performance of the ring-shaped photonic structures against normal holes-based PhCs, obtaining an enhancement factor of 2x. In the same context, a ring-shaped PhC-WG in SOI was used by Pu et al. to experimentally demonstrate the potential of this type of structure for biosensing purposes, obtaining a refractive index sensitivity of 110 nm/RIU [PU10] by measuring the transmission spectrum of the device using different refractive index solutions.

Finally, it is worth noting that not all the configurations of PhCs used for biosensing purposes are based on a holes-on-dielectric configuration (as for all the results previously described). Xu et al. proposed and experimentally demonstrated a PhC sensor based on nanopillars of silicon surrounded by air in a silicon oxide substrate [XU10], which is shown in Fig. 3.17c. The major benefit of this configuration, which exhibits a PBG for TM polarization, is the high overlap between the PhC modes and the target sample, which can be directly flowed between the pillars, thus leading to a significant enhancement of the sensitivity. The authors created a cavity within the PhC by changing the lattice constant in the central region, obtaining a Q factor of 27000. Using this cavity for refractive index sensing, they obtained a sensitivity of 350 nm/RIU. The main drawbacks of this approach are the higher propagation losses, the difficulty to effectively couple the light to the pillars-based structure, and the fragility of the pillars, which makes challenging the integration of a microfluidic system to deliver the samples.

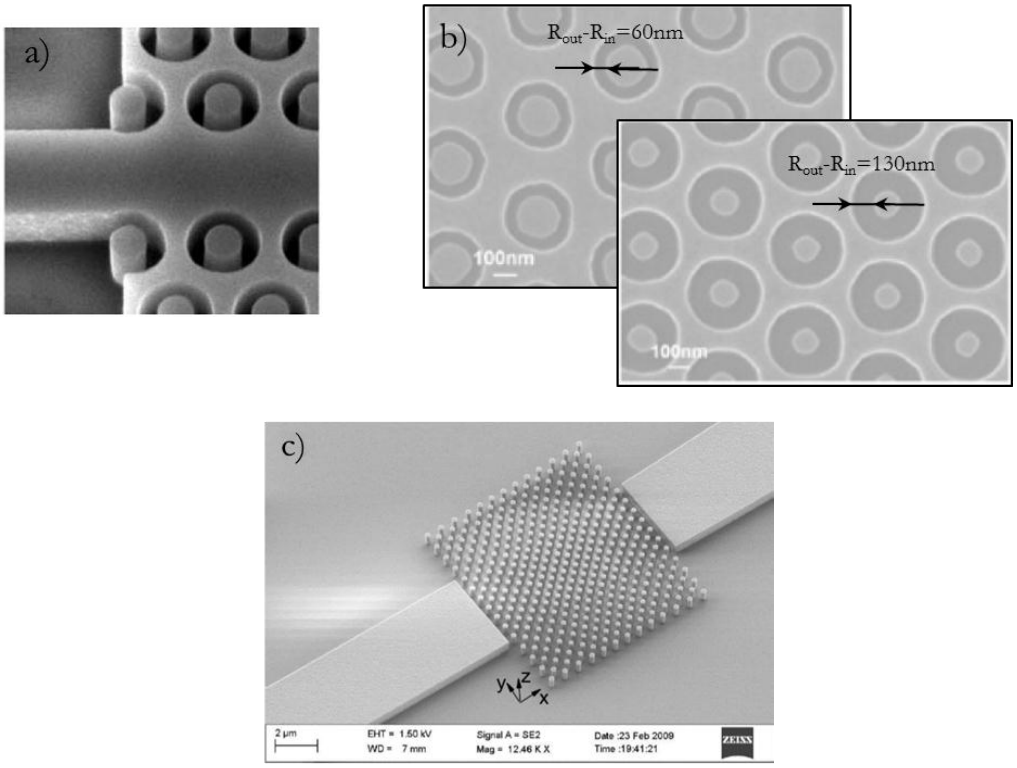

Fig. 3.17: *SEM images of a) a ring-shaped PhC-WG [PU10], and b)a cavity created within PhC structure made of silicon pillars in air over a silicon oxide substrate [XU10].*

Summarizing, in this section we have reviewed the state-of-the-art and the current trends in the field of PhC structures for label-free biochemical sensing.

Some of the advantages shown for the presented PhC-based sensing structure are related to the high confinement of the optical field within the defects included in the PhC structures (either linear or punctual), what is translated into high sensitivities and much reduced dimensions. We have

seen how this combination of an extremely small footprint with a high light-matter interaction provides incredibly low total mass detection limit values. Furthermore, the reduced dimensions of these PhC-based sensing structures makes them suitable for the development of multiplexed sensing chips, providing a high throughput of information with the possibility of carrying several assays simultaneously. Table 3.1 shows a summary of the works presented. Despite several works presented should be considered just as proof-of-concept results due to the simplicity of the experimental measurements or simply because they only report simulation results, the majority of the proposals that have been discussed have demonstrated the extraordinary potential of PhC-based sensing structures for the future development of novel LOC devices. However, there is still further considerable work to be done in order to deploy high-performance commercial devices based on these structures.

Reference	Sensitivity nm/RIU	Detection limit	PhC structure	Q factor	Target analyte	Material	Sensing Area (μm^2)
[LEE07a]	-	2.5 fg	Cavity	-	BSA	SOI	50
[LEE07b]	-	1 fg	Cavity	2000	Latex microsphere	SOI	40
[SKI07]	63	10 ug/ml	PhC-WG	-	BSA	SOI	>100
[BUS08]	88	-	PhC-WG	-	streptavidin	SOI	~70
[SUN08]	80	-	PhC-WG	40000	Helium, nitrogen, argon, Sf6	GaAs/AlGaAs	-
[DOR09]	103	4 fg	Cavity	3000	BSA	SOI	8.2
[FAL09]	800	-	Slotted PhC-WG	4000	-	SOI	2.2
[HUA09]	510	-	PhC	-	-	Si_3N_4	-
[ZLA09]	150	4.5 fg	Cavity	690	Antibiotin	SOI	50
[WAN10]	700	-	Membrane slot	3000	-	InGaAsP with InAs QD	2.25
[PU10]	110	-	Ring PhC	-	-	SOI	-
[SCU11]	-	1 ug/ml	Slotted PhC-WG	3000	Avidin	SOI	2.2
[YAN11]	115	-	Multiplexed cavities	3000	-	SOI	-
[HOS12]	332	-	PhC-WG	950	-	simulation	176
[WAN12]	70	-	Cavity in a fiber facet	-	-	InGaAsP	28
[CHA13]	-	2 cells/ml	Cavity	13000	Cell biomarkers	SOI	11

Table 3.1: *Overview of the main characteristics of the PhC-based biosensing structures. (Classified by year of publication.)*

3.4 Development of PhC-based sensing structures

The work to be described in the following sections was mainly enclosed in the frame of the European project FP7-ICT-INTOPSENS, which aimed at developing a silicon-based photonic sensor system in order to be used as POC for the diagnosis of sepsis. Briefly, sepsis is a systemic inflammatory response to infection, often associated with organ dysfunction that can lead to severe consequences. In order to detect the presence and identify pathogenic bacteria, a complete analysis platform was proposed. This multidisciplinary project was divided into several work packages related to each part of the system including the bioassay development, the photonic sensing structure, electronics, fluidic integration, biochemistry and packaging. We contributed mainly in the work package related to the development of the photonic structures for biological sensing. In summary, such task consisted on developing the photonic transducers for the sensing platform, targeting a high sensitivity, stability and multiplexing capability. Two types of photonic structures were proposed within the project: PhC-based sensors and sensors based on RRs. In this chapter, we will present the work related with the PhC sensors, whereas the work related with RR-based sensors will be described in chapter 4. The development of the PhC-based structures was carried out in collaboration with the department of engineering and photonics from Aahrus University. Dr. Martin Kristensen and Dr. Asger C. Krüger provided a good guidance and recommendations for the modelling of such structures during the course of this PhD work.

3.4.1 Photonic crystal configurationand design

Designing a PhC-based biosensor is not a straightforward task. In principle, we will need to look for a configuration with a maximum interaction between the light and the target molecules, leading to a maximum spectral sensitivity. According to this, several parameters have to be selected in order to obtain the desired response. For that purpose, computer simulations must be carried out to obtain such dimensions. However, prior the modelization of the structure, some configuration issues need to be taken into account such as materials, structure type, or thicknesses. In overall, the main factors that need to be considered to design a PhC-based sensing structure are:

- **Materials:** as previously commented, a wide range of materials can be employed for the fabrication of PhCs, such as GaAs, AlGaAs, SOI, Si_3N_4 or polymers. The higher the index contrast between materials is, the larger the PBG region for controlling the light will be. Therefore, there are several reasons to argue that SOI platform is probably the most convenient material platform for sensor fabrication such as its high refractive index contrast, the existence of many approaches to chemically modify the surface to attach the receptors (as introduced in chapter 2), and the possibility to use CMOS-compatible processes for the fabrication.

- **Structure:** as it has been described throughout the previous sections, 2D PhCs are basically based on two approaches: an array of holes created in a high index medium, or an array of isolated high index pillars in a low index medium (usually air). This is an important consideration after choosing the material, since it will determine the working polarization and the properties of the PBG. Whereas using an approach of high index pillars provides a higher interaction between the field and the target analytes due to the lower confinement of the wave, this will also be translated into a weaker guiding with higher losses what will penalize the performance of the sensor. Furthermore, the fabrication process of a pillar-based configuration can be more complex due to the reduced size and the high aspect ratio of the features. On the other hand, a holes-on-dielectric configuration permits a much easier guiding of the light and a more reliable, faster and convenient fabrication of the structures.
- **Thickness:** the thickness of the core layer where the PhC structure is going to be created must also be taken into account. The thinner the core layer is, the higher amount of evanescent field will interact with the target molecules, thus leading to a higher sensitivity. However, this higher amount of evanescent field will also provoke a significant increase of radiation losses and will difficult the guiding of the wave. Additionally, it is desirable to use slab thicknesses such that only the fundamental mode is allowed in the vertical direction. Normally, for the case of silicon-based PhC structures, the thickness of the silicon layer in commercial SOI wafers ranges from 200 nm to 300 nm.
- **Wavelength range:** usually, the working wavelength range of available equipment (e.g., laser source) will mainly determine the range of operation. For the case of near infrared biosensors, this decision is usually limited to either 1310 nm or 1550 nm because of the extensive use of telecommunication equipment for the characterization of the biosensing structures. Although water absorption is lower at the second window (i.e., around 1310 nm), this effect is not a critical issue for biosensors that are working in the third window (i.e., around 1550 nm).
- **Defects:** as described in section 3.3 in the review of the state-of-the-art in the field of PhC-based biosensors, there exists different kind of defects that we can introduce in order to localize the light to perform the sensing (e.g.: cavities, PhC-WG, slotted-PhC). In our case, we have decided to develop W1 PhC-WG by removing only one row of elements in a holes-on-silicon PhC.
- **Interface:** the impedance mismatching between the PhC structure and the access optical waveguides can produce multiple reflections at the interfaces that deteriorate the signal. Therefore, the coupling between the access waveguides and the PhC structure must be designed in a precise manner in order to have an efficient signal coupling and to reduce these non-desirable reflections. For an efficient mode excitation at the slow-light regime, a coupling taper can be introduced for enhancing the coupling and reduce the reflections.

Considering these issues , we decided to use 2D W1 PhC-WG on SOI material technology for the development of the PhC-based sensing structures to be used on this part of the PhD work. We decided to work in SOI technology due to the high refractive index contrast that provides, as previously commented. The thicknesses of the silicon core layer and the silicon oxide lower cladding were 250 nm and 3 μm respectively[2], which ensure a proper confinement of the light in the vertical direction when a liquid upper cladding (n≈1.33) is used for the sensing experiments. Concerning the type of PhC structure, we decided to create a holes-on-dielectric structure with hexagonal periodic distribution due to several factors which include the easiness of fabricating this type of structures (compared to a pillars-on-air configuration), the easiness of coupling light from access single mode waveguides, and the possibility to obtain wide PBGs for the TE polarization. Then a W1 waveguide was defined within the PhC structure by removing an entire row of holes in the Γ–K direction, as schematically depicted in Fig. 3.18. Regarding the working wavelength, we selected the range around 1550 nm due to the availability of proper equipment for the characterization of the photonic structures (mainly used for the development of photonic devices for communications applications), thus avoiding from buying new equipment. Regarding other parameters such as the holes radius, the lattice constant, or the interface between the PhC-WG and the access waveguides, they were determined by computer simulations.

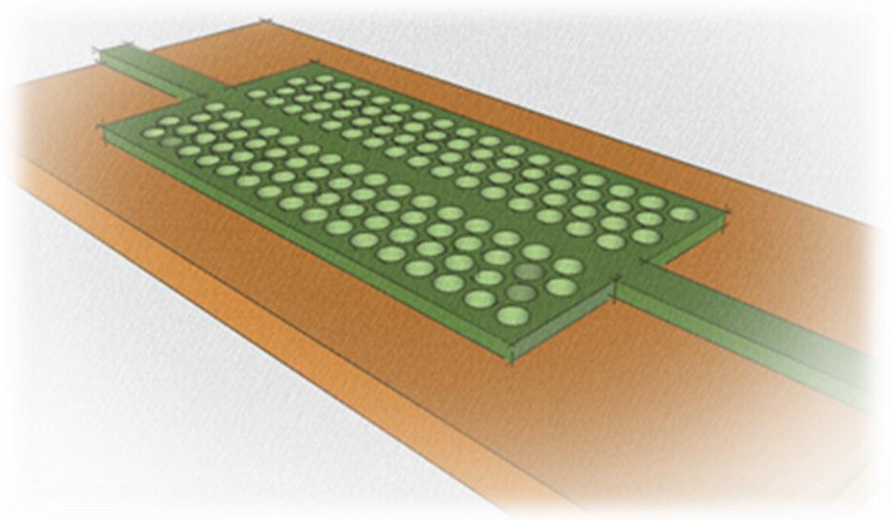

Fig. 3.18: *Schematic depiction of the selected PhC-WG configuration to be used for the development of our biosensing structures.*

In order to decide the dimensions to be used for the creation of the PhC structure, it is necessary to use modelling software that can solve the propagation of the light across it. Nowadays, there are some powerful commercial and freeware tools to solve that problem. Among the different

[2] It is also noteworthy that these were the type of SOI wafers available at the moment of doing this work.

available alternatives, we can find several methods that allows us to solve the Maxwell's equations and to calculate the electromagnetic fields in these structures, such as the finite-difference time-domain (FDTD), the plane wave expansion (PWE) or the eigenmode expansion (EME) methods. In our case, we have extensively used these three methods (FDTD, PWE and EME) to simulate the structure in the design phase in order to determine the optimal parameters of the PhC as well as to characterize the behaviour of the structure during the sensing.

FDTD method employs a discretization of the Maxwell's equations on a spatial user-defined grid in order to obtain the solution of the electromagnetic field in the structure. The schematic defining the dielectric structure is divided using a grid where the electromagnetic field is iteratively calculated in a certain time step. The benefit of this method is that it is possible to solve the electromagnetic field for structures with arbitrary shapes, making it suitable for novel structures that includes any kind of defect. In addition, it is possible to obtain the value of the electromagnetic field in each position of the structure. However, due to the elevated number of calculations and the huge amount of required memory to carry them out, this method needs powerful equipment to run the simulations.

On the other hand, the PWE method is used to determine the band diagram of a periodic structure. Therefore, it is ideal for the study and the design of PhC structures. It uses an infinite periodic arrangement of the user-defined unit cell in order to find the solutions of the Maxwell's equations as a sum of different monochromatic wavelengths by a Floquet-mode analysis. Therefore, the PWE tool solves the Maxwell's equations in the spectral domain obtaining the solution of the eigenmode problem. The solutions will allow us to determine the band structure of the PhC and to determine the presence of PBGs or of guided/confined modes for PhC structures with defects. With this method, the number of calculations is significantly reduced producing an accurate solution.

The combination of both methods will allow us to determine a proper solution for the geometrical parameters of the PhC. With the PWE method, we can simply calculate the band diagram of the PhC structure depending on its parameters in order to obtain a bandgap and guided modes located in the desired wavelength position and with the properties required (e.g., bandwidth). On the other hand, the FDTD method will allow us to see the temporal behaviour of the light when it propagates along the structure, thus allowing to determine minor changes to be applied to the determined configuration. Moreover, we can compare the output spectrum obtained using both calculation methods in order to confirm the expected behaviour of the structure.

We started the design process by carrying PWE simulations out in order to determine the approximated dimensions of the PhC-WG. We used the unity cell shown in the Fig. 3.19 for the simulation of an infinite PhC which exhibits a wide PBG for TE polarization and with a guided

mode with its edge located around 1550 nm, which will be used for sensing. Specifically, we looked for a TE-polarized guided mode with even in-plane symmetry in order to excite it more easily and efficiently by means of the access single mode waveguides (which have these symmetries). According to this conditions, we calculated a PhC-WG with a lattice constant of 390 nm and with a hole radius of 110 nm, which showed the band diagram depicted in Fig. 3.19. The y-axis of the plot is de-normalized and transformed into wavelength units for clarity reasons. The two thick black lines represent the light cone of an air upper cladding (left line) and of the silicon oxide lower cladding (right line). Modes located on the left side of the air light cone will radiate both to the upper and the lower cladding, while modes located between both light cones will only radiate to the silicon oxide lower cladding. Consequently, all these modes will have higher losses and will not be confined within the structure after a certain travel distance; therefore, they will not be considered guided modes valid for sensing purposes.

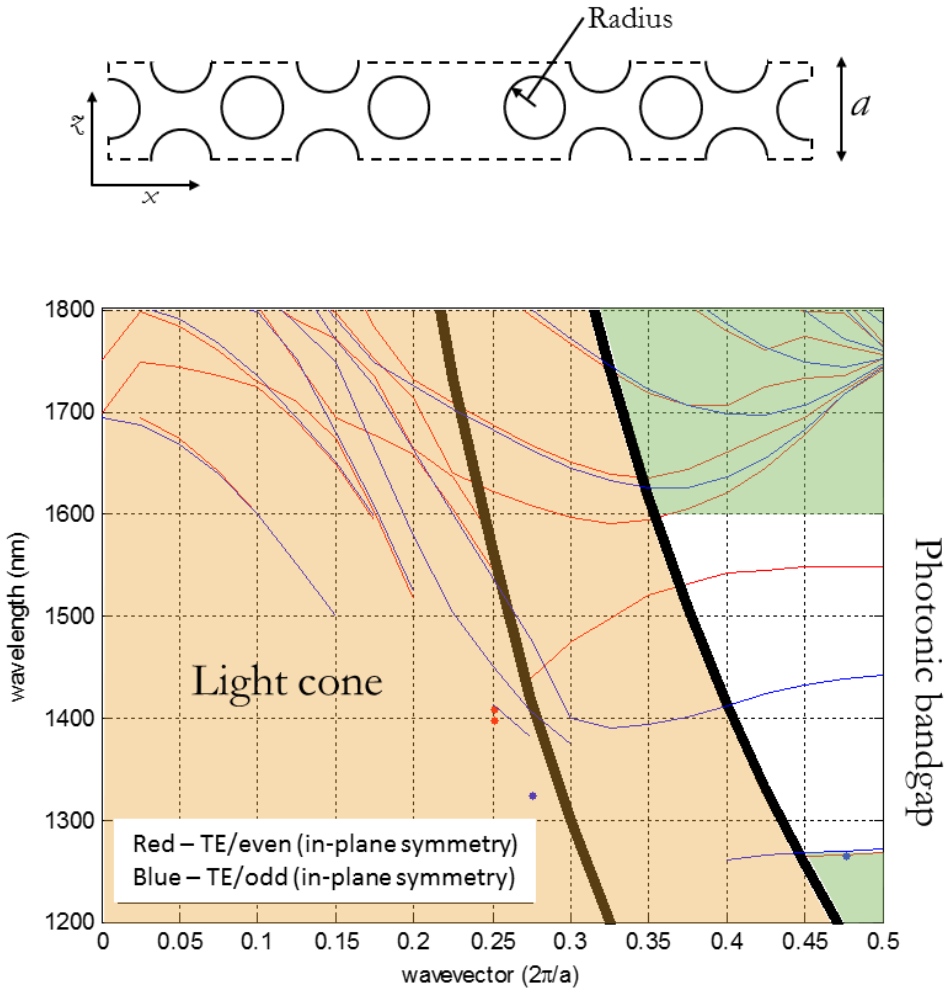

Fig. 3.19: *On top the cell unit for the band calculations of a infinite PhC. Bottom, band diagram for the TE polarization for the W1 PhC-WG based on holes in silicon with a hexagonal distribution. The radius of the holes is 110 nm, the lattice constant 390 nm and the thickness 250 nm. The guided band edge is located around 1550 nm.*

Once the parameters of the PhC-WG were obtained, new simulations were carried out using FDTD in order to confirm the results obtained with the PWE method. The simulations were carried out using Rsoft's FullWAVE software, a commercial modelling tool that includes a FDTD solver for photonic structures. The simulations were carried out using a 3D modelling with the initial parameters extracted from PWE simulations. As depicted in Fig. 3.20, a Gaussian pulse was launched from an input waveguide of width 500 nm and a power monitor was placed at the end of the output waveguide to collect the light from the structure. As it can be appreciated, the coupled signal does not excite any mode in the PhC-WG when its wavelength is within the PBG region (see Fig. 3.20a), but it does when the input wavelength matches a guided mode (see Fig. 3.20b).

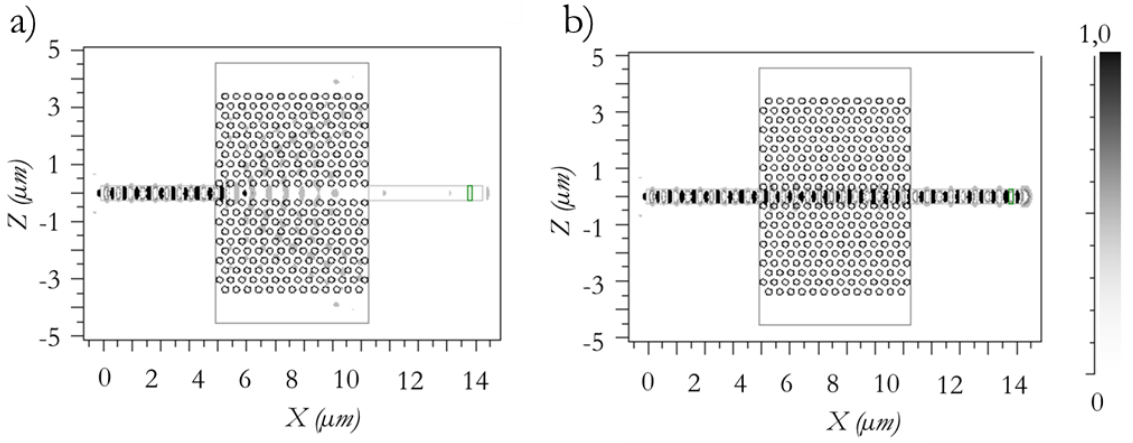

Fig. 3.20: *FDTD simulation of the PhC-WG when it is excited with an input wavelength a) within the PBG (λ=1580 nm) and b) matching a guided mode (λ=1540 nm).*

By Fast Fourier Transform analysis, the FDTD software can calculate the spectral response of the structure. Fig. 3.21 shows the variation in the transmission spectrum of the PhC-WG when some of its structural parameters are varied. For example, Fig. 3.21a shows how a reduction in the thickness provokes a shift of the guided band and of the PBG towards lower wavelengths (i.e., shifted towards higher frequencies) due to the reduction in the effective refractive index of the structure. Fig. 3.21b shows the influence of a variation of the hole radius for a fixed value of the lattice constant. Following the same reasoning as for the case of the thickness, a decrement of the hole radius is translated into a shift of the spectral response towards higher wavelengths (i.e., to lower frequencies) due to the increment in the effective refractive index of the structure At this point, it is noteworthy to point out the appearance of several ripple peaks located at the edge of the guided mode. The origin of these peaks as well as our proposal of using them for sensing purposes will be described in the next section.

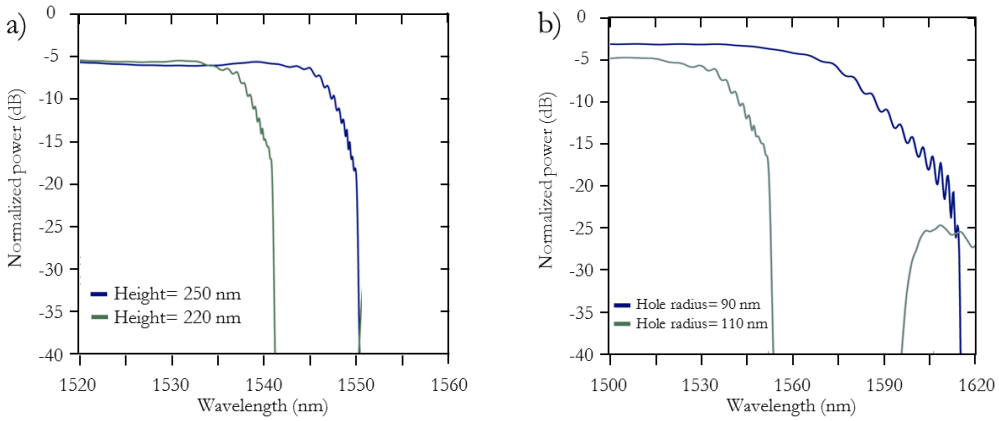

Fig. 3.21: *Transmission spectra obtained by means of FDTD simulations for the PhC-WG when varying a) the height of the silicon slab and b) the holes radius.*

3.4.2 Fabry-Perot fringes for sensing applications

As previously observed in Fig. 3.21, the transmitted spectrum of the PhC-WG exhibits several fringes in the edge of the guided band. This effect is due to the mismatch produced in the interface of the waveguide accesses and the PhC structure, what causes infinite optical reflection pulses travelling along the PhC backward and forward making that the finite structure has the same behavior as a Fabry-Perot (FP) cavity [GAR06]. As we get closer to the edge of the guided band, we can observe two consequences. The first one is the increment of the ripple amplitude due to the worst coupling efficiency between the structures, and the second one is the variation of the frequency of the Fabry-Perot ripple. Since the group velocity is lower as we get close to the band edge, the effective optical length of the cavity will increase, leading to a proportional increase in the ripple frequency.

Fig. 3.22 schematically depicts a W1 PhC-WG of length L with the corresponding access waveguides. In an ideal behaviour, both access waveguides are semi-infinite in the direction out of the PhC structure; hence, we are not going to consider reflections towards the PhC-WG. As previously indicated, the coupling between the access and the PhC-WG will not be perfect due to the mismatching between modes. Therefore, a transmitted and a reflected signal will be generated at each interface. These contributions can be modelled using transmission and reflection coefficients in each interface.

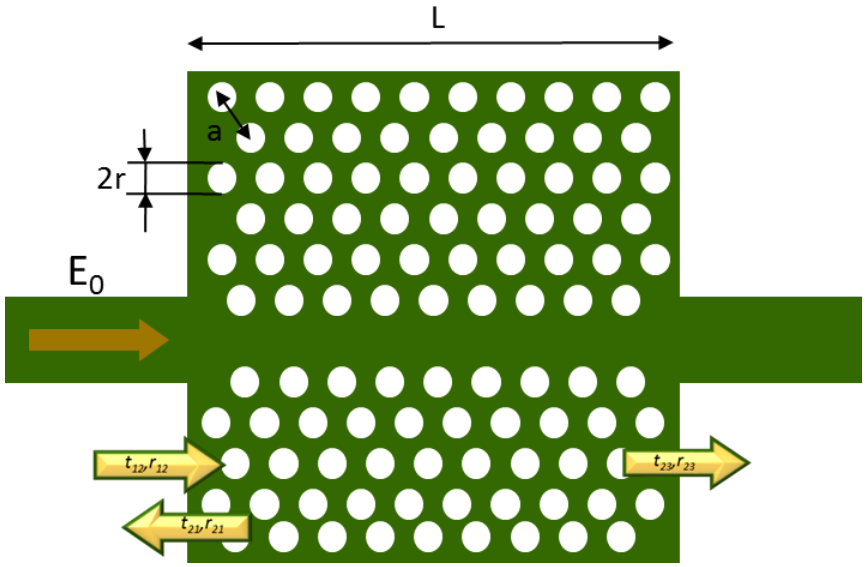

Fig. 3.22: *Schematic representation of the transmission and reflection coefficients in a W1 PhC-WG based on holes in silicon with two access waveguides.*

Fig. 3.23 schematically depicts the different contributions generated at the output of the PhC-WG due to the reflections generated at the interfaces. Each output contribution will be given by the equation:

$$E_n = E_0 t_{12} t_{23} (r_{23} r_{21})^{n-1} e^{j(2n-1)\beta L} \tag{3.18}$$

where E_0 is the amplitude of the input signal, t_{nm} and r_{nm} are the transmission and reflection coefficients of the interface between the medium m and n, β is the propagation constant of the guided mode in the PhC and L is the length of the PhC-WG. Taking into account all the contributions generated at the output of the cavity, the total response of the finite-length PhC-WG will be given by:

$$E_t = \sum_{n=1}^{\infty} E_n = E_0 \frac{t_{12} t_{23} e^{(j\beta L)}}{1 - r_{23} r_{21} e^{(j2\beta L)}} \tag{3.19}$$

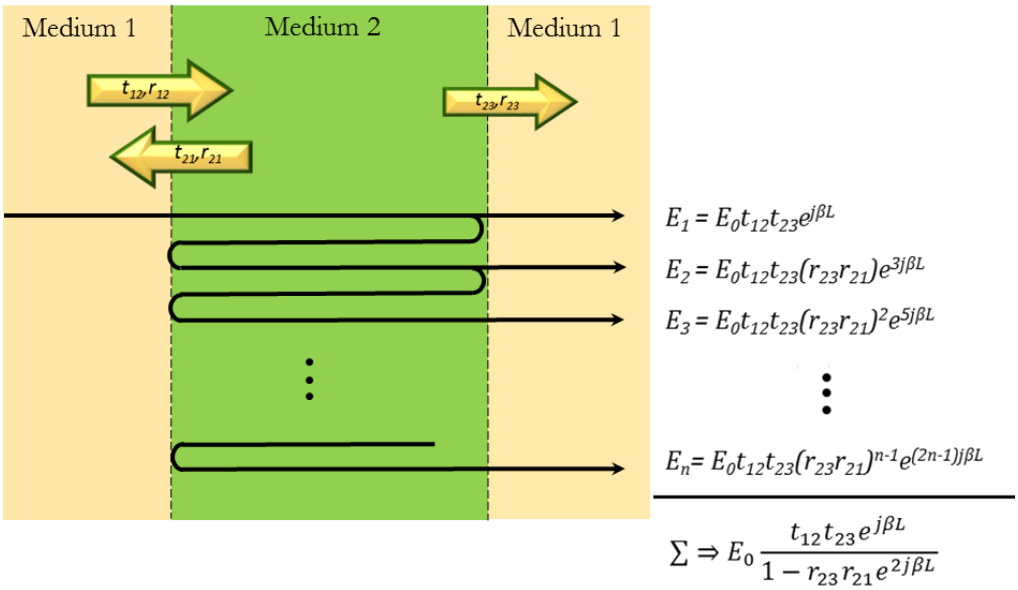

Fig. 3.23: *Schematic representation of the analytic model employed to obtain the response of a finite-length PhC-WG. Medium 1 represents the input access waveguide, medium 2 represents the PhC structure, and medium 3 represents the output access waveguide.*

In order to determine the signal at the output of our finite-length PhC-WG, we calculated the propagation constant and the transmission and reflection coefficients (the three parameters are dependent on the frequency of the signal). These parameters were calculated using the freely available CAMFR (Cavity Modelling FRamework) software [CAM13], which has been developed by researchers of the Gent University. This software is based on the eigenmode expansion (EME) method to solve the bands of the PhC. Then, using the semi-analytical method proposed in [SAN05], we obtained the transmission and reflection coefficients at the interfaces as well as the propagation constant of the PhC-guided mode from the band diagram. Note that only the reflection coefficient for the incidence from the PhC-WG to the access waveguide (r_{21},r_{23}) is needed for the calculations and that the transmission coefficient is the same for the incidence from the PhC-WG to the access waveguide and vice versa due to reciprocity properties ($t_{mn} = t_{nn}$).

In Fig. 3.24, the three parameters calculated using CAMFR as a function of the wavelength are plotted. These parameters correspond to the hexagonal distribution of air holes in silicon with a radius of 110 nm and a period of 390 nm. It is worth noting that, since the CAMFR software does not allow 3D calculations, we have made a generic 2D modelling (i.e., infinite height of the structure) using an effective refractive index of 2.8 for the silicon slab and 1.33 for the cladding surrounding the structure; these are not the exact refractive index values for our real 3D structure but they are close enough to allow us to realistically predict the appearance of FP fringes in the transmission spectrum As expected, the transmission coefficient tends to 0 as we get closer to the edge of the guided band, while the behaviour of the reflection coefficient is the opposite, increasing

as we get closer to the band edge. This will be translated into a decrease of the power coupled to the PhC-WG and an increase in the amplitude of the Fabry-Perot fringes of the cavity. Regarding the propagation constant of the guided mode of the PhC-WG, it is observed that thevalue is rising in relation to the wavelength as we approach to 1550 nm, what indicates that the group velocity is decreasing. The wavelength region around 1550 nm is where the slow-light effect takes place, resulting the compression of the optical field.

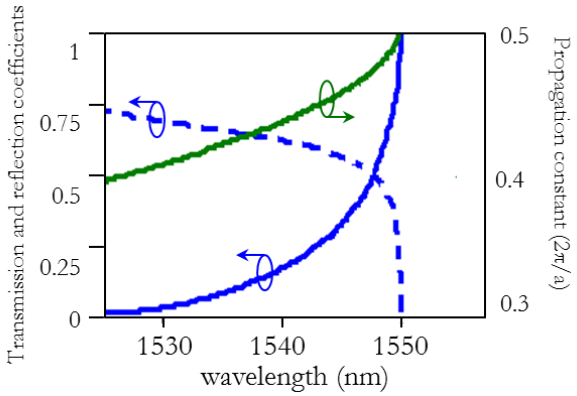

Fig. 3.24: *Theoretical coefficients for transmission (dashed blue line), reflection (blue solid line) and propagation constant (green solid line) of the PhC-WG calculated using CAMFR.*

By combining the calculated parameters with the expression from Eq. (3.19) that described the total response of the finite-length PhC-WG, we have obtain the output spectrum depicted with solid blue line in Fig. 3.25 for a 20 μm-long PhC-WG, where the FP fringes can be clearly seen. We can also see how FP resonances fringes become stronger and narrower as we approach the edge of the guided band because of the increase of the reflection coefficient and the decrease of the group velocity.

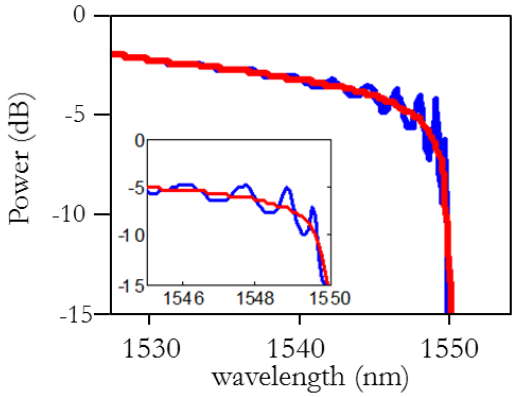

Fig. 3.25: *Transmission spectrum of a 20 μm-long PhC-WG when the created FP cavity is considered (blue solid line) and when no cavity is considered (red solid line). In the inset, a close up view of the FP fringes is depicted, showing how they become stronger and narrower near the band edge.*

For the case of sensing purposes, the optical wave propagated through the PhC-WG will interact with the target molecules localized on the surface of the structure through the evanescent wave. Due to the high dispersion of this propagated mode, the slow-light regime becomes stronger as we get closer to the band edge. Therefore, the use of the Fabry-Perot resonances for sensing will ensure that we are working in the slow-light spectral region, as well as allowing a more accurate determination of the spectral features to be tracked during the sensing process.

The structure was then simulated using 3D FDTD calculations in order to corroborate the appearance of the FP fringes in the edge of the guided mode of the PhC-WG and to analyse their potential use for biosensing purposes. The performance of the planar PhC-WG as a biosensor was evaluated using two different upper claddings (n_1=1.3173 and n_2=1.32; as it will be described in section 3.6.1, these are the refractive indices for DIW and an ethanol-DIW dilution at 4%) in order to obtain the variation of the spectrum of the structure. Fig. 3.26 shows the simulation results for each of these two upper claddings. It is worth noting that, during the 3D FDTD simulations, it was necessary to make a compromise between the spatial and spectral resolution, and the duration of the simulation. This limitation in the total time used for the simulations provoked a smoothing of Fabry-Perot resonances, as observed in Fig. 3.26.

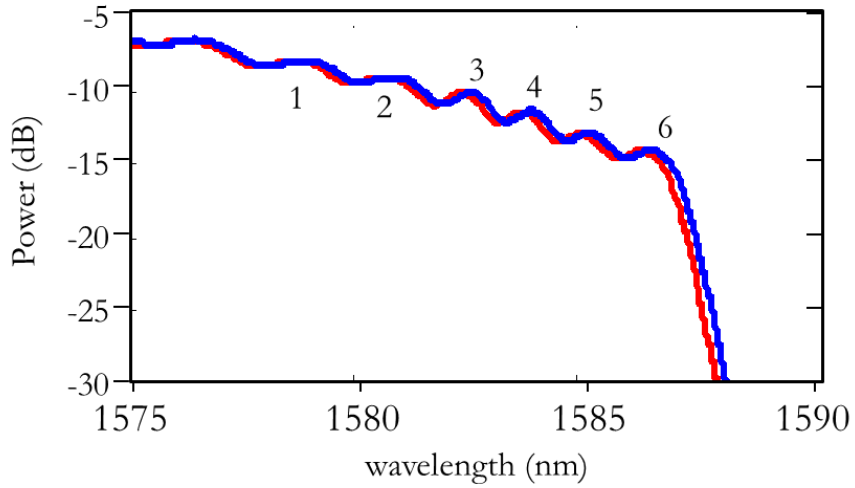

Fig. 3.26: *3D FDTD simulations of the transmission spectrum for a 20µm-long PhC-WG using two different upper claddings (n_1=1.3173 (red line) and n_2=1.32 (blue line)). The Fabry-Perot fringes are labelled from 1 to 6.*

By measuring the shift of each Fabry-Perot fringe, we obtained the sensitivity for each of them. Calculated values are shown in Table 3.2. As predicted, the progressive reduction of the group velocity as we get closer to the band edge provoke an enhancement of the light-matter interaction, leading to an increase in the sensitivity. We can observe a sensitivity increment of 40% between the resonance closest to the band edge (#6, 78.70 nm/RIU) compared to the first one

(#1, 57.15 nm/RIU), thus demonstrating how the sensitivity can be improved by tracking those fringes closer to the band edge.

Fringe #	1	2	3	4	5	6
Wavelength shift (nm)	0.1543	0.1865	0.192	0.2002	0.2039	0.2125
Sensitivity (nm/RIU)	57.15	69.07	71.11	74.15	75.52	78.70

Table 3.2: *Wavelength shift and sensitivity for each FP fringe near the guided band edge calculated by means of 3D FDTD simulations.*

3.4.3 Fabrication of the photonic crystals

In the previous section, we obtained the parameters of the PhC-WG structure to be used for sensing purposes. We also theoretically studied its operation and performance by means of simulation. The next step is the fabrication of the structures in SOI platform. All the processes required for the fabrication of the PhC structures were entirely carried out in-house in the facilities of the Nanophotonics Technology Center of the Universitat Politècnica de València, which has state-of-the-art fabrication facilities for the production integrated photonic devices. The fabrication procedure of the PhC structures, which is schematically depicted in Fig. 3.27, is summarized as follows:

1. Starting from a SOI wafer with the layer thicknesses required, the first step consists on the deposition of a thin resist layer on top of it. There are two types of resist: positive and negative. When the areas of a positive resist are exposed, these regions will be removed in the developing process. However, by using a negative resist, the areas to be removed must not be exposed. For the fabrication of holes-based PhC structures, positive resists are preferred due to the higher accuracy in the definition of the holes and the shorter times required to carry out the exposure (in the case of e-beam lithography). In our case, a layer of 100 nm of PMMA (positive resist) was deposited on top of the SOI wafer using a spin coater (EGV 101). The resits layer was baked after the deposition process.

2. The layout of the photonic structures was written in the positive resist using the e-beam lithography (EBL) toll Raith 150. EBL uses high-energy electrons to define the structure, allowing very high resolutions of up to 2 nm. This fabrication technique is very flexible, since it does not need to use lithographic masks. Therefore, it is very useful for research and for prototyping purposes, where novel designs need to be processed for rapid testing. The main drawback of this method is that the structures need to be written serially, what makes it a slow process. Therefore, depending on the area covered by the layout, the time

required will significantly vary (it may last even more than 1 day depending on the size of the structure).

3. After the resist exposure using EBL, the chip was developed in order to remove the resist from the exposed regions to create the mask on top of the silicon layer of the wafer.

4. The structures created on the PMMA resist are subsequently transferred to the silicon layer using a dry etching technique with a STS AOE-multiplex equipment. Reactive-Ion Etching Inductive Coupled Plasma (RIE-ICP) is employed to transfer the pattern from the mask to the silicon layer. This is a decisive step where it is necessary to obtain a high selectivity of the material in order to reduce the roughness of the structures, what may produce undesirable losses and a bad performance of the structure.

5. Finally, the resist layer used to transfer the design to the silicon material is removed by chemical treatment or plasma. Then the samples are rinsed using different solvents to remove any residue from the surface and the fabrication process is finished.

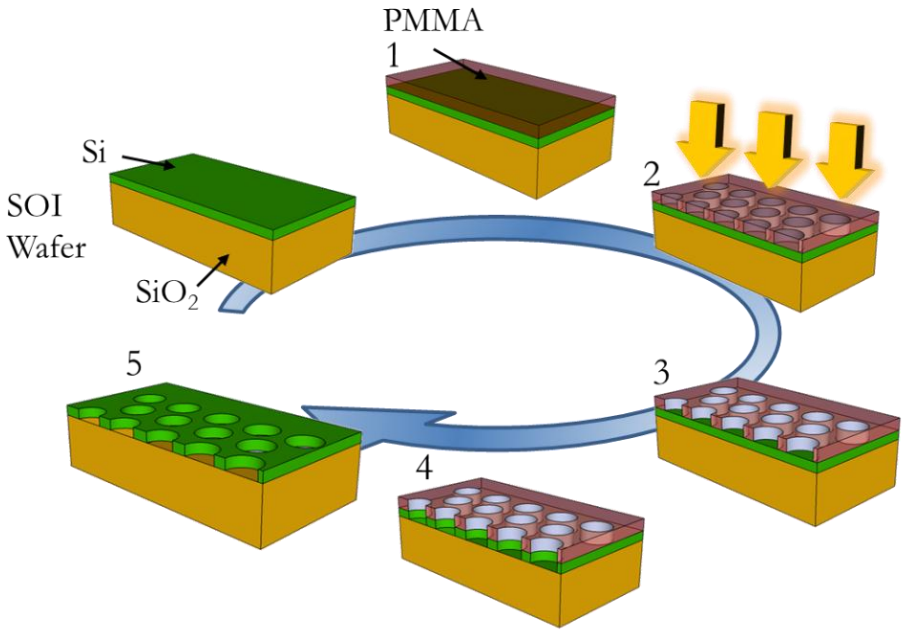

Fig. 3.27: *Fabrication process of the photonic structures on a SOI wafer using electron beam process. 1) Resist deposition, 2) e-beam lithography, 3) resist development, 4) pattern transfer by dry etching, and 5) resist removal.*

Several fabrication runs were carried out to determine the optimal procedures for the different fabrication steps, analysing some parameters such as the thickness of the resist, the exposure dose, the etching time, or the appearance of proximity effects between the holes. Fig. 3.28 shows two SEM images of PhC-WG fabricated at different runs at the beginning of the optimization stage. There we can see the imperfections of the holes (e.g., non-perfect circular shape, different shape between the holes comprising the PhC), which were mainly due to proximity effects. Fig. 3.29 shows a study of the relation between the fabricated holes radii compared to the theoretical dimension, where we can see a slight deviation between the real and the theoretical values.

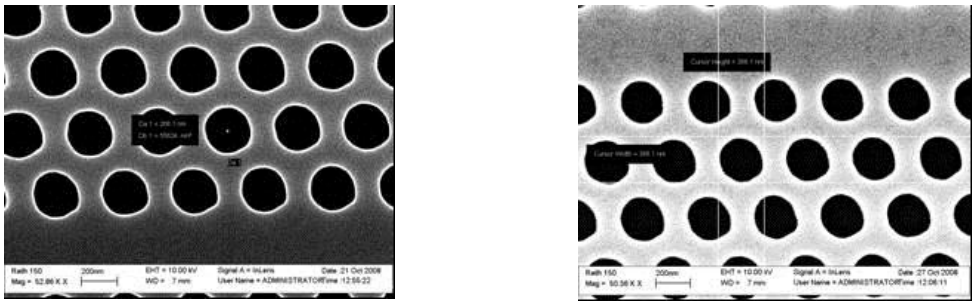

Fig. 3.28: *SEM images of different PhC structures obtained at some of the firsts fabrication runs. The theoretical period and diameter were 390 nm and 220 nm respectively.*

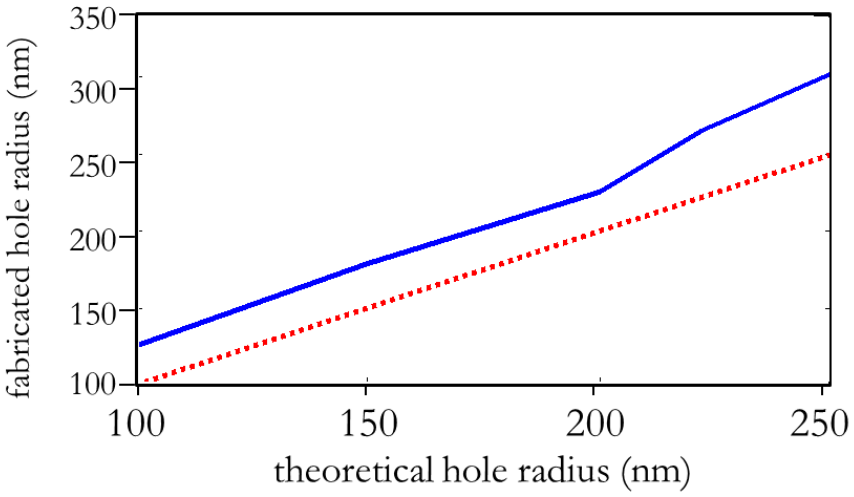

Fig. 3.29: *Study of the relation between the theoretical holes radii and the real values. Blue solid line represents the measured radius of the hole, while the ideal relation is depicted with red dotted line.*

All these defects and deviations of the fabrication process were gradually corrected during the optimization process. As a result, we were able to obtain a perfectly defined PhC-WG structure,

as shown in Fig. 3.30, where light is coupled in/out by 450 nm-wide single mode access waveguides.

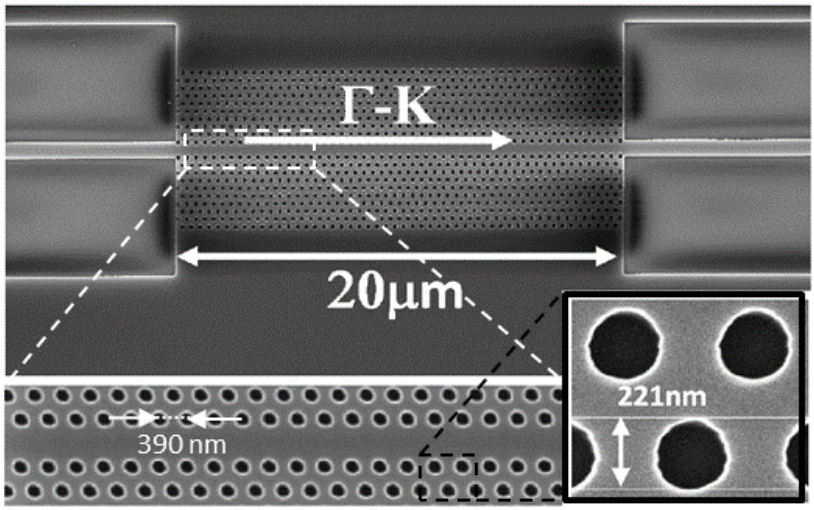

Fig. 3.30: *SEM image of a PhC-WG fabricated at the NTC facilities. The structure has a period of 390 nm and a hole diameter of 221 nm.*

3.5 Experimental set-up

In chapter 1, we introduced the principal parts of a generic affinity biosensor, which consisted on the transducer, the recognition layer, the fluidic delivery system and the optical read-out. At the beginning of this chapter, we explained the working principle of the PhC-based transducer and, in chapter 2, the recognition layer was described. In this section, we will describe the parts comprising the experimental set-up, which consist on the optical read-out and the fluidic delivery systems. First, we will introduce how we performed the optical interrogation of the chips and then we will show the metallic fluidic system employed to deliver the samples on the sensing area.

3.5.1 Optical interrogation

To optically characterise the PhC sensing devices, we used the characterization laboratories at NTC, where all the required equipment was available. Briefly, the photonic structures were optically interrogated by acquiring their spectrum using a tunable laser source and a power meter, while the target liquids were flowed over the chip by means of an in-house fabricated flowcell.

For their interrogation, the photonic chips were mounted on a 2-axis holder and fixed by using vacuum. In order to obtain the spectral response of the photonic structure, a tunable laser source was used. Depending on the availability in our laboratories, we used both a Santec TSL 210F

(with a resolution of 10 pm and a range from 1260 nm to 1630 nm) and a Photonetics 3642CR-00 (with a resolution of 1 pm and a wavelength range from 1500 nm to 1600 nm) as light source. A polarization controller was then used to set the desired polarization of the light before coupling it to the photonic integrated device. Note that our PhC structures were designed to work in TE polarization, so this will be the polarization to be set by means of the controller.

Coupling the light from the external fiber to the optical structures is a crucial step. Due to the mismatching between the sizes of the standard single mode optical fiber (9 μm) and the photonic access waveguide (450 nm x 220 nm), extremely high losses are produced when trying to perform a direct coupling between them [ALM03]. Therefore, it will be practically impossible to couple light between the fiber and the photonic structures in a direct manner. To solve this issue, a lensed fiber was employed to focus the optical field at the edge of 3μm-wide photonic waveguide, as schematically represented in Fig. 3.31. This wider multimode photonic waveguide was then linearly tapered until achieving the 450nm-wide single mode waveguide used for accessing the PhC-WG.

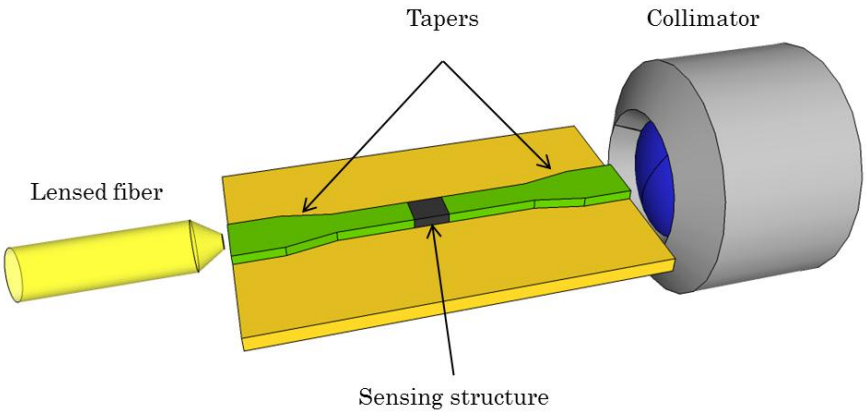

Fig. 3.31: *Schematic illustration of the horizontal coupling measurement. Light from the lensed fiber is focused on the facet of the photonic waveguide to address the light to the sensing structure. The light is collected at the output by an optical collimator.*

Although the alignment tolerance of the horizontal coupling scheme is very low, it is very suitable for measuring prototypes in the laboratory because of the possibility to couple both TE and TM polarization and to the fact that there is no bandwidth limitation. To align the lensed fiber with the edge of the photonic waveguide on the chip, a 3-axis translation stage from Thorlabs (Nanomax TS Max 312/M) was used. The translation stage was connected to a piezoelectric controller, which allowed obtaining an accuracy of 20 nm that results acceptable for the characterization of photonic structures using a horizontal coupling scheme. A picture of the

experimental set-up based on horizontal coupling is shown in Fig. 3.32a. Additionally, an optical microscope was employed to observe the chip from the top during the alignment process.

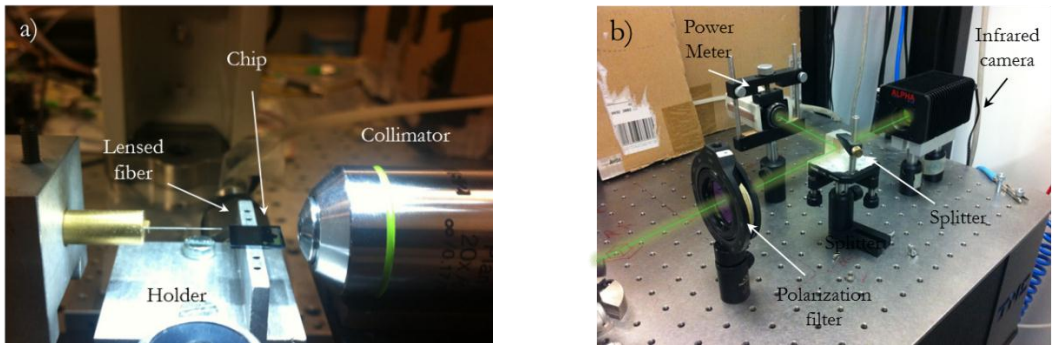

Fig. 3.32: *a) Close up view of the set-up based on horizontal coupling used for the interrogation of the photonic sensing structures. b) Output section of the characterization set-up, where the light is passes through a polarizer, it is divided by a splitter and then sent to an infrared camera and to a power meter.*

The output light from the chip was then collected by using a 20x Olympus collimator (numerical aperture of 0.4), and filtered using a free-space polarizer configured for TE polarization. As it is shown in Fig. 3.32b, after passing through the free-space polarizer, the optical beam was splitted in two paths: one path was sent to an IR camera (Indigo Alpha with an InGaAs sensor) in order to observe the output signal of the chip during the alignment process, and the other path was sent to a power meter (Ando AQ2140) in order to measure the output optical intensity.

A LabVIEW-based program was developed for the synchronization of the wavelength sweep carried out using the input tunable laser source and the measurements done by the output power meter, in order to obtain the transmission spectrum of the photonic sensing structure. The program also allowed a continuous spectral acquisition in order to study the evolution during the sensing process. Additionally, the program was adapted in order to adjust the sweep resolution depending on the presence of a spectral feature of interest. Spectral scans are very time consuming, requiring longer times when higher spectral resolutions are used (as required obtaining good sensitivities). Therefore, a compromise between scan velocity and resolution will exist. Therefore, in order to reduce the scan time, our program performed a fine sweep only for those regions of interest (e.g.: the band edge in a PhC, resonances in RRs), whereas a coarse sweep was performed in the regions where there was no presence of useful information. With this variation, we were able to reduce the scan time by a factor of ~2x (e.g., a scan of a 30 nm wavelength range with a resolution of 1 pm decreased from 3 minutes to less than 1:30 minutes); however, despite this enhancement, scan times still being quite long. Finally, the measured spectra were saved to a file and subsequently analysed using a Matlab-based program that allows to determine and track position of one or several spectral features along the time.

3.5.2 Fluidic delivery system based on a metallic cavity

On the other hand, for carrying out the biosensing measurements it is necessary to deliver the liquid samples to the sensor surface. The basic requirements for a fluidic delivery architecture are to be able to deliver the sample to a small area without any leakage or bubbles, preventing possible contamination and with a continuous constant flow. Taking into account these issues, we designed a customized flowcell to be placed on top of the photonic chip to deliver the target sample without interfering with the optical interrogation of the chip. The developed flowcell, which is shown in Fig. 3.33a, consisted on a drilled aluminium cavity of dimensions 5.5 mm x 2 mm x 3 mm with two access ports on the top part of it. We selected a metallic flowcell due to its durability and robustness. In order to achieve a good sealing of the flowcell with the photonic chip, a rubber o-ring was employed (see Fig. 3.33a). Once the metallic flowcell is placed on top of the photonic chip, it will be fixed to the chip holder employing two screws in order to seal perfectly the microfluidic circuit, as shown in Fig. 3.33b. Finally, two metallic needles were used to connect the fluidic cavity with silicone tubes in order to pump the target liquids.

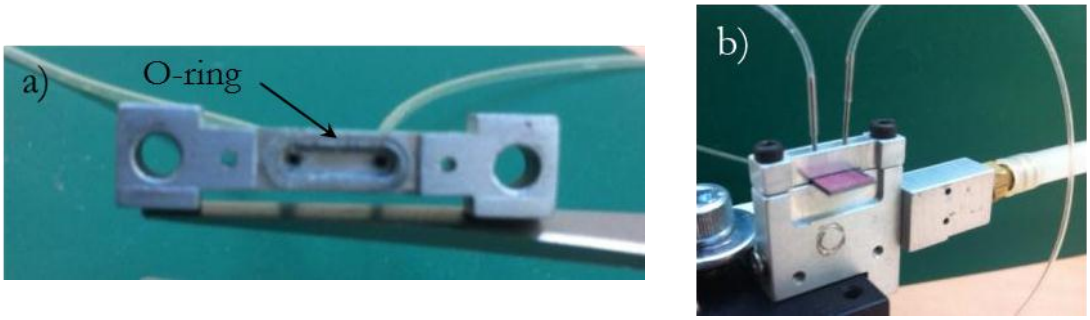

Fig. 3.33: *a) Bottom view of the metallic flowcell used to carry out the experiments. Input and output accesses are located on the top of the cavity. A rubber o-ring is placed along the elliptic contour of the cavity in order to achieve a good sealing with the photonic chip. b) Image of the chip holder, where the metallic flowcell is properly placed on top of the photonic chip.*

The liquids used in the experiments were inserted into the cavity and flowed over the chip employing a syringe pump (TSE 540060) working in withdraw mode. Initially, we began working with the pump in injection mode; however, we observed a slight leakage of the flowcell that was due to the increment of the pressure inside the cavity. In addition, working in injection mode difficults the change of the liquid to be flowed, since it is needed to halt the flow and change the syringe, thus increasing the possibility of the appearance of bubbles. On the other hand, working with the pump in withdraw mode improves the sealing of the cavity of the flowcell, thus preventing from leakage, and significantly eases the change of the liquid to be flowed, what can be simply done by manually changing the source vial without stopping the flow. Finally, the flow rate used to deliver the samples was not fixed, and it ranged from 10 μl/min to 50 μl/min depending on the experiment to be carried out (e.g., bulk RI, protein, or DNA sensing).

3.6 Experimental sensing results using PhC-WG

In previous sections, we described the design of the PhC-WGs, their fabrication employing e-beam and the measurement set-up including the optical and the fluidic parts. Herein, we will present the successful experimental results obtained using the PhC-WG as sensing structure. Several samples with the same nominal parameters were employed in order to extract the characteristics of the sensing structures.

In sensing measurements, a refractive index variation on the surface of the PhC due to the binding of the target analytes leads to a change in the PBG position. Therefore, by tracking the position of the PBG or the guided band edge we can determine the presence of the target analyte. Nevertheless, measuring the exact position of this edge is quite challenging. In order to overtake this drawback, we employed a novel sensing approach in order to measure the shift of the guided band due to refractive index change by using the Fabry-Perot fringes described in section 3.4.2. This technique permits to enhance the sensitivity of the photonic device, since it ensures us that we are working in the slow-light regime and their sharper peaks allows us to determine their position with higher accuracy (compared to directly using the position of the band or the PBG edge).

During the course of this work, we have continuously been optimizing the set-up and the chemical attachment with the consequent improvement of the characteristics of the platform, thus being able to properly observe the interactions between molecules. In order to achieve that purpose, we used the following approach. First, we extracted the intrinsic sensing parameters of the photonic structure such as sensitivity and detection limit by carrying bulk refractive index measurements. Next step was to perform antibody detection experiments by applying a proper chemical functionalization. Finally, the detection of the DNA hybridization was performed with this platform obtaining a good reproducibility and values in the state-of-the-art of PhC sensing structures.

3.6.1 Bulk refractive index sensing

Bulk refractive index sensing is a simple method to evaluate the sensing performance of the PhC-WG sensor in order to compare it with other photonic-based sensing devices. As previously described in section 3.4.2, we used the FP fringes appearing at the edge of the guided band in order perform the sensing. Fig. 3.34 shows the transmission spectrum of the PhC-WG sensing structure surrounded by DIW, where FP fringes at the edge of the guided band can be clearly seen.

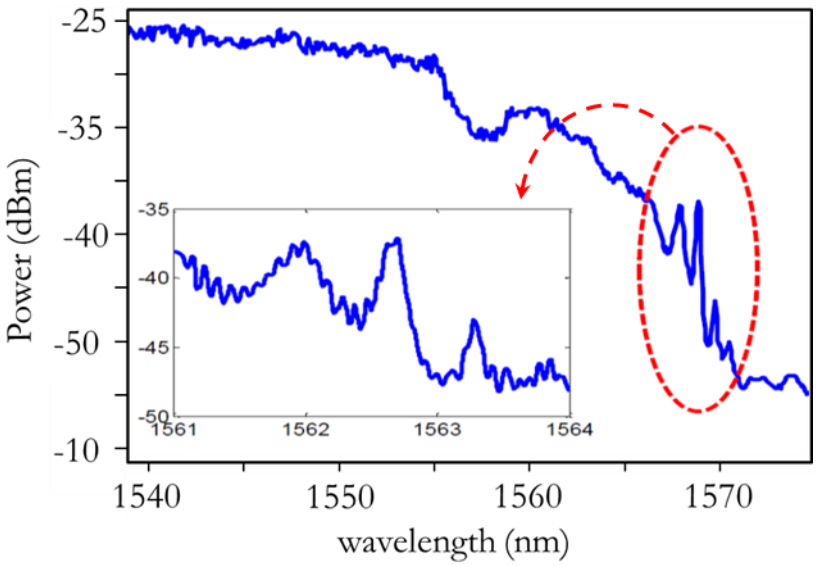

Fig. 3.34: *Transmission spectrum of the PhC-WG around the guided band edge region with deionized water as upper cladding. In the inset figure, a close up view of the fringes in the band edge is shown.*

For these refractive index sensing experiments, several concentrations of a dilution of ethanol in DIW (in mass %) were flowed at a rate of 15 µl/min over the PhC-WG sensing structure. The refractive indices of the dilutions used were as follows: pure DIW ($n_{0\%}$=1.3173), ethanol 2% in DIW ($n_{2\%}$=1.3186), and ethanol 4% in DIW ($n_{4\%}$=1.32); these refractive index values were calculated for a λ = 1550 nm and T = 25ºC [LID08]. During the sensing experiment, the transmission spectrum of the PhC-WG was continuously recorded while the source vial (with the target dilution) was changed.

Fig. 3.35 shows the time evolution of the spectral position of the band edge as the target liquid were changed. When DIW was flowing over the sensor, the resonance position was located around 1563.27 nm. When a 2% dilution of ethanol in DIW was introduced, the resonance moved to 1563.45, a net shift around 0.18 nm. Finally, with the highest concentration of ethanol in DIW (4%), we observed a position of the peak corresponding to 1563.7 nm. These shifts reached a sensitivity of the PhC structure of 118 pm/% as a function of the ethanol concentration. For low concentrations of ethanol in DIW, the refractive index variation is practically linear and it is given by $\Delta n \approx 6.75 \times 10^{-4}$ RIU/%. Therefore, the sensitivity of the sensor defined by $S = \Delta\lambda/\Delta n$ was calculated to be 174.8 nm/RIU. By comparing this result with the result obtained in the 3D FDTD simulations shown in section 3.4.1, we can observe a difference in a factor 2.2x. The reason of this variation may be attributed to the discretization of the simulation, which may lead to a non-accurate modelling of the optical field that senses the variation of the refractive index of the upper cladding. Finally, in order to calculate the detection limit of the structure we obtained the noise of the experiment, which is calculated from the standard deviation of the signal baseline and was as low as

σ=0.6 pm. Considering this noise value and the sensitivity of the structure, the estimation of the limit of detection is calculated as DL= σ /S achieving finally a value as low as $3.5x10^{-6}$ RIU.

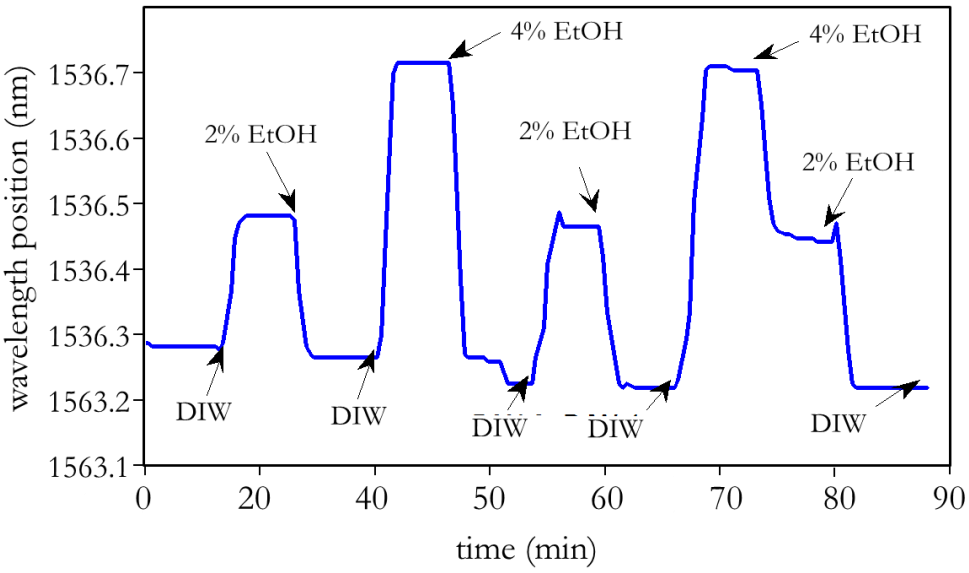

Fig. 3.35: *Temporal evolution of the Fabry-Perot position when different concentrations of ethanol in DIW were flowed over the PhC.*

Therefore, we have seen that our PhC-WG sensing structure based on holes in silicon exhibits a high sensitivity and a low detection limit, what make it suitable for biosensing applications. Furthermore, we have experimentally demonstrated the possibility of using FP fringes appearing on the edge of the guided band for sensing purposes, thus guaranteeing that the structure is working in the slow-light regime, thus providing an enhancement of the light-matter interaction.

3.6.2 Antibody sensing

In this section, we will provide results of antibody detection employing PhC-WG structures. Now, by a proper chemical treatment of the surface, we can provide the specificity required to the sensing structure in order to make it sensitive only to certain target molecules. For the antibody sensing experiments to be described within this section, a new PhC-WG structure with the same nominal parameters as that used in the refractive index sensing experiments has been used. The surface of this PhC-WG sensing structure was functionalized with BSA antigen probes as receptors for the target antiBSA antibodies to be flowed over it. The BSA-antiBSA system was chosen due to its high affinity, what eases the implementation of the biosensing experiments on the photonic platform. By continuously tracking the peaks of the FP fringes at the edge of the transmitted band, we will be able to study the binding of the antiBSA molecules to the BSA receptors attached to the surface.

Briefly, the functionalization steps, which were defined from the optimization process in planar surfaces described in chapter 2, are listed hereafter. Firstly, the chip was cleaned with piranha solution. To achieve the surface functionalization we employed ICPTS, which was deposited on the structure by chemical vapour deposition (CVD) during 2 hours in a controlled atmosphere. Then a drop of BSA 10 µg/ml in PBS 0.1x was incubated for 2 hours. In order to avoid unspecific adsorption during the experiment, the remaining active sites of the ICPTS were blocked using ovalbumin protein (OVA) 1% in PBS 0.1x. In addition, to avoid molecule absorption in the microfluidic system, silicon tubes and the metal flowcell were also blocked with OVA before carrying the measurements out.

Fig. 3.36 shows the transmitted spectrum at the output of the PhC-WG when PBS 0.1x was continuously flowed over the sensor. In the close up view, one can see the Fabry-Perot fringes appearing at the edge of the guided band of the PhC-WG. In this experiment, 4 of these FP fringes (those initially located at 1542.1 nm, 1543.5 nm, 1544.2 nm, 1544.7 nm) were tracked during the biosensing experiment in order to compare the sensing performance between the different spectral features located in the slow-light region.

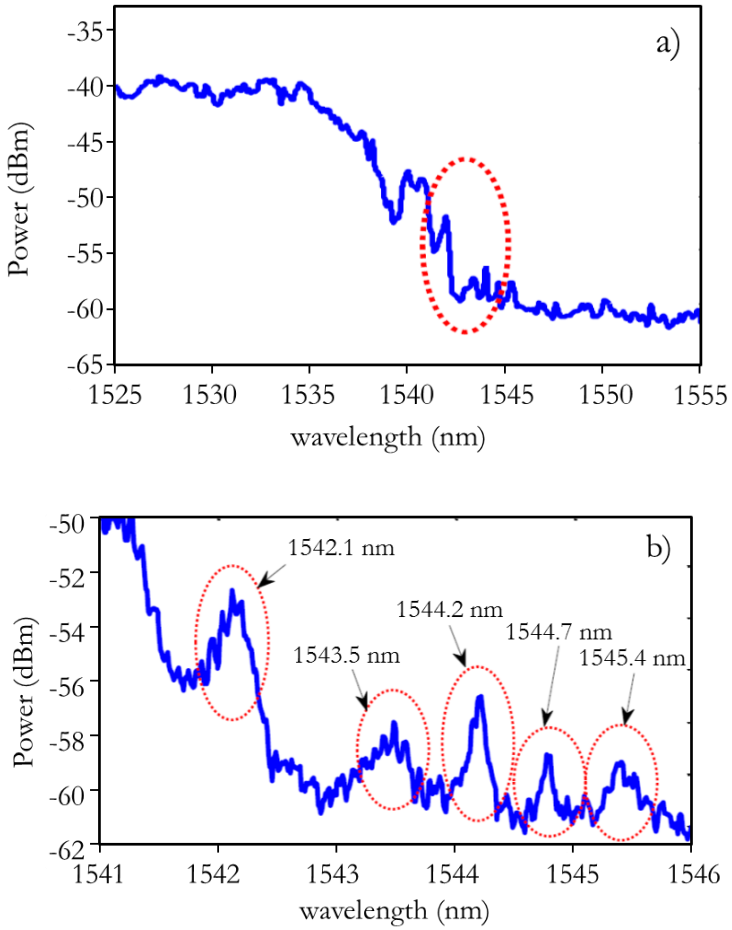

Fig. 3.36: *a) Initial spectrum of the PhC-WG in the region of the PBG when PBS 0.1x is flowed over the chip. b) Close up view of the Fabry-Perot fringes in the band edge region.*

Fig. 3.37 represents the time evolution of the relative shift of the four FP peaks previously indicated during the antibody sensing experiments. Initially, PBS 0.1x was flowed during sufficient time in order to stabilize the signal and obtain a proper baseline. The flow rate used during the experiments was set to 15 µl/min in order to ensure that the molecules had time enough to interact with the receptors attached to the surface. Then, the flow was switched to an antiBSA concentration of 10 µg/ml in PBS 0.1x. We can see that a rapid shift of the position of the peaks is observed as soon as the antiBSA molecules reach the photonic sensing structure. This shift is due to the variation of the refractive index produced when the antiBSA molecules bind to the BSA probes attached to the surface of the sensing structure. The antiBSA concentration was flowed sufficient time to provide a monolayer on the surface as we can see in the figure, where the signal reaches a plateau around minute 50. Once the signal was saturated because all the BSA binding sites were occupied by the target antiBSA antibodies, PBS 0.1x was flowed again in order to remove all the molecules that were not specifically bound to the BSA receptors. At this point, the shift corresponds to the net shift of the antiBSA molecules bounded to the surface.

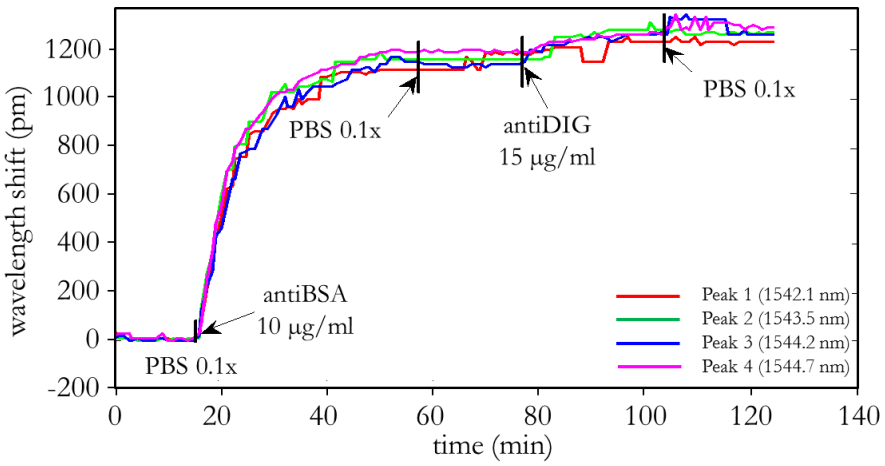

Fig. 3.37: *Wavelength shift vs. time for the different solutions flowed in the experiment. Each line correspond to the relative shift of each tracked peak respect its initial wavelength position. The time instants when the flowed solution is switched are depicted in the figure.*

Besides the detection of the antiBSA molecules in the surface, we studied the selectivity of the chemical modification. A high selectivity is provided by the low interaction between the sensor surface and interfering molecules. To verify that selectivity, a test by flowing a concentration of 15 µg/ml antiDIG antibody was carried out. No significant change in the position of the band edge was observed during the introduction of the antiDIG. These results indicate that the surface functionalized with BSA owed specificity and was able to discriminate between antiBSA and antiDIG molecules.

Concerning the behaviour of the different FP peaks used for the detection, we can clearly observe in Fig. 3.37 that all of them have the same trend and that only slight differences occur during the binding process until the signal reaches the plateau position. Table 3.3 summarizes the performance of each analysed peak. In the table, we can see that the total shift of the peak for the BSA monolayer slightly increases as it is closer to the band edge, as previously calculated using the 3D FDTD simulations. Again, this effect is explained by the reduction of the group velocity of the guided mode, which leads to a higher sensitivity because of the increment of the optical intensity (due to the compression of the wave) and the velocity reduction that increases the interaction between the light and the molecules on the surface. The increment in the total shift is around 10% from peak #1 to peak #4 (with a slight difference in the peak #3). This result coincide with that from the 3D FDTD simulations, where an enhancement around the same amount was obtained when the four peaks closer to the band edge were considered. Note that, as shown in the simulations, a higher separation between peaks will provide a higher improvement of the performance of the sensor.

Peak	$\lambda_{initial}$ (nm)	$\Delta\lambda_{antiBSA}$ (nm)	$S_{antiBSA}$ (nm/ng/mm²)	σ_{PBS} (pm)	$DL_{antiBSA}$ (pg/mm²)	$DL_{antiBSA}$ (fg)	$\Delta\lambda_{antiDIG}$ (nm)
#1	1542.128	1.123	0.661	0.5	2.3	0.23	0.114
#2	1543.471	1.17	0.688	1.5	2.2	0.22	0.108
#3	1544.235	1.142	0.672	3.1	4.6	0.46	0.128
#4	1544.7	1.2	□.706	1.5	2.1	0.21	0.1

Table 3.3: *Parameters characterizing the performance of the FP peaks used for the sensing experiments.*

When the signal of the sensor reached the saturation, all the BSA binding sites were totally occupied and a close-packed antiBSA monolayer was formed on top of the sensor. The surface density of a close-packed antiBSA monolayer considering a 100% binding efficiency is $\varrho_{antiBSA}$=1.7 ng/mm² [BAR08]. From this value, we calculated the sensitivity for the antiBSA detection, which is given by $S_{antiBSA}= \Delta\lambda_{antiBSA}/\varrho_{antiBSA}$ and it is shown in the 4th column of Table 3.3. From this sensitivity value and the noise of the system σ_{PBS}, we can estimate the upper limit for the surface mass detection limit of the device when a binding efficiency of 100% is considered (in a real situation, we will not have a close-pack monolayer and binding efficiency of 100%), which is shown in the 6th column of Table 3.3. We can see that a value as low as 2.1 pg/mm² has been obtained for the surface mass detection limit. Additionally, the total mass detection limit can also be calculated from the surface mass detection limit and considering the total surface of the PhC sensing structure. For this calculation, we have not considered the whole area of the PhC structure, but only the active region of the PhC-WG, which mainly extends up to the third row of holes from the

linear defect as we observed in the simulations. Considering this fact, we assume a surface around 100 μm^2 that leads to a mass detection limit of ~0.2 fg for the peak #4.

3.6.3 DNA sensing

The importance of the DNA detection is remarkable and can be used in many fields including genetic screening, disease diagnosis or food identification. Label-free sensing technologies enable to monitor the hybridization between complementary DNA strands, providing real-time kinetic information with quantitative results. In our case, we have also employed our PhC-WG biosensor for the detection of DNA hybridization by properly biofunctionalizing it and adapting the experimental procedure.

The strategy to anchor the ssDNA capture probes to the surface of the photonic sensing structure for these specific experiments was based on a bioaffinity immobilization (see chapter 2), where the couple biotin-streptavidin was used for the chemical attachment. Since biotin has a high affinity towards the streptavidin (and vice versa), we can chemically conjugate biotin molecules with the ssDNA probes and bind them to the streptavidin that is immobilized to the surface using a covalent attachment.

The protocol to attach the ssDNA probes to the surface of the sensing structure started with a cleaning step of the chip by immersing it in piranha solution during 1 hour to remove any organic particle. After washing it, the chip was activated with pure ICPTS organosilane, which was deposited by CVD in a closed jar during 30 minutes. Then a concentration of 100 ng/ml of streptavidin in PBS 0.1x was spotted on the sensor and incubated overnight at room temperature in order to obtain a uniform layer. Next, the chip was rinsed with DIW. One of the advantages of this functionalization process is that it permits to chemically modify with streptavidin several chips simultaneously and store them in the fridge at 4ºC for several days until their utilization. In order to continue the protocol, a drop of 10 µM of biotinylated ssDNA probe was spotted on top of the streptavidin-functionalized surface and was incubated during 30 minutes to allow the binding between the molecules. Subsequently, the surface was rinsed with DIW to remove the non-attached strands and dried under air stream. Finally, to prevent from other molecules to bind in the surface, a solution of OVA at 1% in PBS was spotted to block the remaining moieties of the streptavidin. Subsequently the chip was rinsed and air-dried, becoming ready for its use.

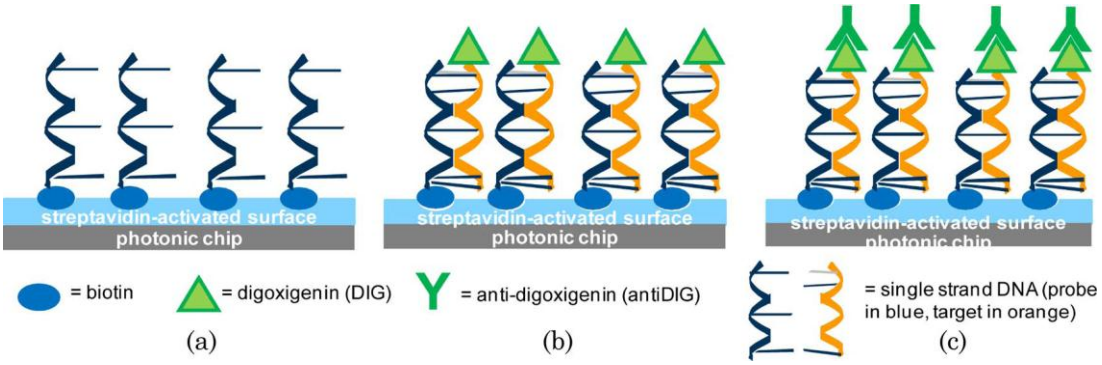

Fig. 3.38: *Schematic representation of the protocol used during the hybridization experiments. a) Surface of the chip after the functionalization with the ssDNA capture probes. b) Hybridization of the complementary ssDNA marked with DIG. c) Control step where antiDIG molecules bind to the labelled ssDNA confirming the hybridization.*

Fig. 3.38 and Fig. 3.39 show the experimental protocol used for the specific detection of ssDNA and the temporal evolution of the position of the PhC-WG sensor response during the experiment (a FP fringe was tracked during the experiment), respectively. The experiment began with a continuous flow of PBS 0.1x buffer solution at a flow rate of 20 µl/min in order to obtain a stable baseline. Then, to evaluate the hybridization process, a 500 nM concentration of ssDNA complementary to the probe attached on the surface was flowed. This complementary ssDNA was marked at one end with a DIG molecule in order to perform a control assay at the end of the experiment, as it is shown in Fig. 3.39. After the introduction of the complementary ssDNA, we observed an initial transient period, (probably, some air microbubbles appeared or slight turbulences were produced in the sensing region) before the band edge position exhibits a permanent wavelength shift of $\Delta\lambda$=47.1 pm due to the hybridization with the capture probe, as shown in Fig. 3.39a. The sensitivity of the sensor was calculated as $S = \Delta\lambda/\Delta C$, where ΔC represented the variation of the DNA concentration, obtaining a value of S = 94.2 pm/µM. Using the standard deviation of the signal after the hybridization event, we obtain a noise level of the sensing platform of σ=1.865 pm. Defining the detection limit as $DL = \sigma/S$, we estimated a value of 19.8 nM as the lowest concentration that the sensor platform can measure in a hybridization experiment.

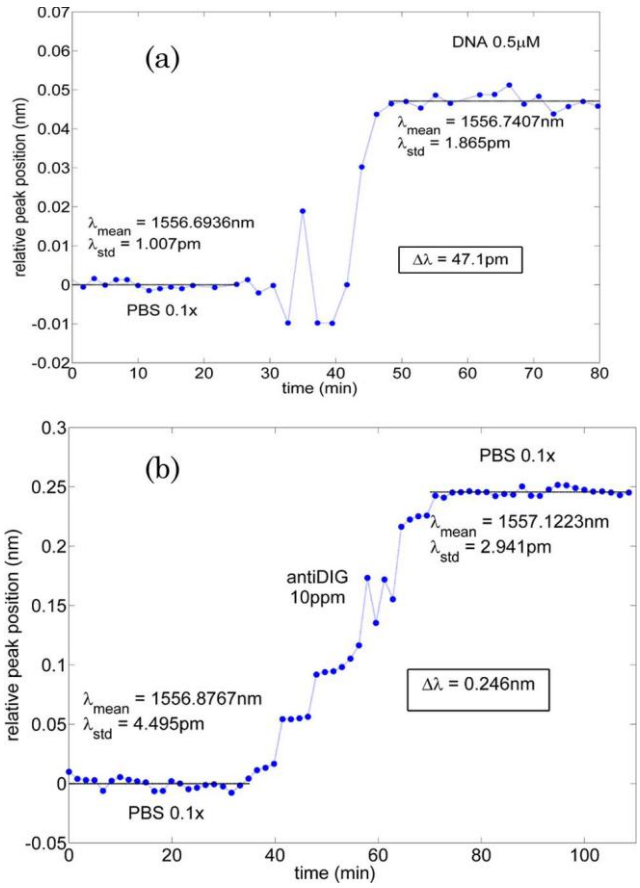

Fig. 3.39: *Wavelength shift vs. time for (a) ssDNA 0.5 µM sensing and for (b) antiDIG 10 ppm sensing. Relative wavelength shift from the initial baseline (mean position) is represented.*

Since the molecular weight of the complementary ssDNA is very low, the hybridization with the capture probes provoked a relatively small shift of the band edge (less than 50 pm). In order to confirm the hybridization, the complementary ssDNA flowed in the experiment was labelled with digoxigenin (DIG), which has a strong affinity with antiDIG antibody. This couple was used as a control after the DNA hybridization because antiDIG will produce a larger refractive index change due to its higher molecular weight. After the hybridization experiment, a concentration of antiDIG 10 ppm was flowed. As expected, the molecules bound to the DIG labels of the complementary ssDNA causing a larger shift of the peak position as shown in Fig. 3.39b (~250 pm), what confirmed the hybridization of the DNA strands to the biotinylated probes of ssDNA.

Finally, we can note several issues related to this experiment. The first one is the confirmation that FP fringes can also be used to perform the hybridization detection of the complementary strand of DNA; as shown in previous experiments, these fringes have demonstrated an enhancement of the sensitivity due to the use of the slow-light effect. An extremely low detection limit below 20 nM has been obtained for the label-free detection of

ssDNA, a value that is in the range of current state-of-the-art results using other planar photonic sensing structures. Finally, we would like to point out the remarkable stability of the sensing platform; despite performing this experiment at room temperature and without the use of any thermal control, a quite high stability of the signal is achieved. Therefore, we certainly expect to enhance even more the performance of the sensing platform by using temperature control mechanisms and enhancing the sensitivity of the structure.

3.7 Conclusions

The work described in this chapter has been focused on the development of a sensing structure based on PhCs, from its design to its fabrication and experimental characterization. One of the main benefits of this type of sensing structures is the appearance of the slow-light effect, which provides an enhancement of the light-mater interaction, and thus an improvement of the performance of the sensing structures. This enhancement is determined by two reasons: on one hand, the reduction of the propagation velocity through the structure that implies longer interaction times, and on the other hand, the optical field compression that provokes an increment of the optical intensity inside the PhC.

The slow-light effect takes place close in the region near to the PBG where is not straightforward to determine the position of the edge of the guided mode. However, we modelled the appearance of FP fringes close to the edge for a finite PhC that allow determining more accurately and easier the position of the spectrum, thus reducing the detection limit. In addition, FP fringes provide the optimal wavelength range to obtain the highest interaction of the light with the matter increasing the sensitivity of the structure.

In our experiments, we used a tunable laser based interrogation setup and a metallic flow cavity in order to deliver the fluids on top of the sensing structures. Initially, simple refractive index sensing experiments were carried out using dilutions of EtOH in DIW in order to obtain the intrinsic parameters of the sensor, such as the sensitivity and the detection limit, which were determined to be 174.8 nm/RIU and $3 \cdot 10^{-6}$ RIU respectively. Then, we applied the functionalization protocols described in chapter 2 in order to observe the interaction between BSA-antiBSA, achieving a detection limit as low as 0.2 fg. Finally, we also successfully demonstrated the detection of the DNA hybridization on the surface of the structure. Employing bioaffinity immobilization by means of streptavidin and biotinylated DNA probes, we attached the ssDNA probes to the surface and then flowed the complementary DNA strand to observe a shift of the edge of the guided mode due to the hybridization. The smallest concentration of DNA that is

possible to be detected was estimated below 20 nM, which shows the outstanding potential of the PhC-WG for its use in sensing applications.

References

[ALM03] V.R. Almeida, R R. Panepucci, and M. Lipson, "Nanotaper for compact mode conversion." Optics Letters, vol. 28(15), pp. 1302, 2003.

[ALM04] V. R. Almeida, Q. Xu, C. a Barrios, and M. Lipson, "Guiding and confining light in void nanostructure." Optics letters, vol. 29(11), pp. 1209–11, 2004.

[BAR08] Barrios, C. A., Bañuls, M. J., González-Pedro, V., Gylfason, K. B., Sánchez, B., Griol, A., Maquieira, A., Sohlström, H., Holgado, M., and Casquel, R. (2008). "Label-free optical biosensing with slot-waveguides." Optics Letters, Vol. 33(7), pp. 708, 2008.

[BAR09] G. Barillaro, S. Merlo, and L. M. Strambini, "Optical characterization of alcohol-infiltrated one-dimensional silicon photonic crystals."Optics letters, vol. 34(12), pp. 1912-4 2009.

[BOG05] W. Bogaerts, R. Baets, P. Dumon, V. Wiaux, S. Beckx, D. Taillaert, B. Luyssaert. ; J. Van Campenhout, P. Bienstman, and D. Van Thourhout, "Nanophotonic waveguides in silicon-on-insulator fabricated with CMOS technology."Journal of Lightwave Technology, vol. 23(1), pp. 401-412, 2005.

[BUS08] S.C. Buswell,V.A. Wright, J.M. Buriak, V. VanandS. Evoy."Specific detection of proteins using photonic crystals waveguides." Optics Express, Vol. 16(20), pp. 15949-15957, , 2008.

[CAL11] M.E. Calvo , S. Colodrero , N. Hidalgo , G. Lozano , C. López-López , O. Sánchez-Sobrado and H. Míguez."Porous one dimensional photonic crystals: novel multifunctional materials for environmental and energy applications."Energy Environ. Sci.,Vol.4, pp. 4800-4812, 2011.

[CAM13] http://camfr.sourceforge.net/index.html, 2013.

[CHA13] S. Chakravarty, W. Lai, Y. Zou, H. A. Drabkin, R. M. Gemmill, G. R. Simon, S. H. Chin, and R. T. Chen, "Multiplexed specific label-free detection of NCI-H358 lung cancer cell line lysates with silicon based photonic crystal microcavity biosensors," Biosensors & Bioelectronics, vol. 43, pp. 50–55, 2013.

[DOR09] D. Dorfner, T. Zabel, T. Hürlimann, N. Hauke, L. Frandsen, U. Rant, G. Abstreiter, and J. Finley, "Photonic crystal nanostructures for optical biosensing applications.," Biosensors & bioelectronics, vol. 24(12), pp. 3688–92, 2009.

[FAL09] A. Di Falco, L. O. Faolain, and T. F. Krauss, "Slotted Photonic Crystal waveguides and cavities for slow light and sensing applications." Optics Express, pp. 228–230, 2008.

[GAR06] J. García, P. Sanchis, and J. Martí. "Detailed analysis of the influence of structure length on pulse propagation through finite-size photonic crystal waveguides". Optics Express, vol. 14(15), pp. 6879-6893, 2006.

[GNA06] M. Gnan, G. Bellanca, H.M.H. Chong, P. Bassi and R.M. de la Rue, "Modelling of photonic wire Bragg gratings." Optical and Quantum Electronics, vol. 38, pp.

133-148, 2006.

[GOP12] G. Palai and S.K. Tripathy, "A novel method for measurement of concentration using two dimensional photonic crystal structures." Optics Communications, Volume 285(10-11) ,pp. 2765-2768, 2012.

[HOS12] F. Hosseinibalam, S. Hassanzadeh, and C. Karnutsch, "Design of an optofluidic biosensor using the slow-light effect in photonic crystal structures," Applied optics, vol. 51(5), pp. 568–576, 2012.

[HUA09] M. Huang, A. A. Yanik, T.-Y. Chang, and H. Altug, "Sub-wavelength nanofluidics in photonic crystal sensors.," Optics express, vol. 17(26), pp. 24224–33, 2009.

[HUA12] Y. Huang, G. Pandraud, and P. Sarro, "Reflectance-based two-dimensional TiO2 photonic crystal liquid sensors." Optics LettersVol. 37, pp. 3162-3164, 2012.

[JOA08] J. D. Joannopoulos, S. G. Johnson, J. N. Winn, and R. D. Meade, "Photonic Crystal: Molding the Flow of Light." Princeton University Press, 2008.

[JOH00] S. G. Johnson, and P. R. Villeneuve, we have to telepranspote, and J.D. Joannopoulos, "Linear waveguides in photonic-crystal slabs."Physical review B, vol. 62(12), 2000.

[JOH87] S. John, "Strong localization of photons in certain disordered dielectric superlattices.", Physical Review Letters, 58(23): pp. 2486–2489, 1987.

[JUG12] A. S. Jugessur, M. Yagnyukova, J. Dou and J. S. Aitchison,"Bragg-grating Air-slot Optical Waveguide For Label-Free Sensing."Proc. SPIE 8231, Nanoscale Imaging, Sensing, and Actuation for Biomedical Applications VIII, 82310N, 2012.

[KHU05] J.B Khurgin, "Optical buffers based on slow light in electromagnetically induced transparent media and coupled resonator structures: Comparative analysis."J. Opt. Soc. Am. B Vol. 22, pp. 1062–1074, 2005.

[KRA08] T.F. Krauss, "Why do we need slow light?." Nature Photon. Vol. 2, pp. 448–449 (2008).

[LEE07a] M. R. Lee and P. M. Fauchet, "Two-dimensional silicon photonic crystal based biosensing platform for protein detection." Optics express, vol. 15(8), pp. 4530–5, 2007.

[LEE07b] Lee, M. R., & Fauchet, P. M. "Nanoscale microcavity sensor for single particle detection."Optics Letters, Vol. 32(22), pp. 3284-3286, 2007.

[LI12] J. Li, L. O'Faolain, S.A. Schulz, T.F. Krauss, "Low loss propagation in slow light photonic crystal waveguides at group indices up to 60." Photonics and Nanostructures - Fundamentals and Applications, V (4), pp. 589-593, 2012.

[LID08] D. R. Lide, Handbook of Chemistry and Physics (CRC Press, 2008).

[MIY12] G.M. Miyake, V. A. Piunova, R.A. Weitekamp, and R.H. Grubbs."Precisely Tunable photonic crystals From Rapidly Self-Assembling Brush Block Copolymer Blends." Angew. Chem. Int. Ed. vol. 51, pp. 11246 –11248, 2012.

[NUN10] P. S. Nunes, N. A. Mortensen, J. P. Kutter, and K. B. Mogensen, "Refractive index sensor based on a 1D photonic crystal in a microfluidic channel." Sensors, vol. 108(3), pp. 2348-58, 2010.

[POV05] M.L. Povinelli, Steven G. Johnson, and J. D. Joannopoulos, "Slow-light, band-edge waveguides for tunable time delays." Optics Express, vol. 13(18), pp-7145-7159, 2005.

[PU10] M. Pu, L. Liu, L. H. Frandsen, H. Ou, K. Yvind, and J. M. Hvam, "Silicon-on-Insulator Ring-Shaped Photonic Crystal Waveguides for Refractive Index Sensing." Photonics and Nanostructures, vol. 2, pp. 3–5, 2010.

[SAN05] P. Sanchis, J. Martí, P. Bienstman, and R. Baets, "Semi-analytic approach for analyzing coupling issues in photonic crystal structures." Appl. Phys. Lett., vol. 87, pp. 203107, 2005.

[SCU11] M.G. Scullion, A.D. Falco, and T.F. Krauss, "Slotted photonic crystal cavities with integrated microfluidics for biosensing applications" Biosensors & Bioelectronics, vol. 27(1), pp. 101-105, 2011.

[SKI07] N. Skivesen, A. Têtu, M. Kristensen, J. Kjems, L.H. Frandsen,and P.I. Borel, "Photonic-crystal waveguide biosensor". Optics Express, Vol. 15(6), pp. 3169-3176, 2007.

[SUN08] T. Sünner, T. Stichel, S.-H. Kwon, T. W. Schlereth, S. Höfling, M. Kamp, and a. Forchel, "Photonic crystal cavity based gas sensor." Applied Physics Letters, vol. 92(26), p. 261112, 2008.

[TUC05] R.S. Tucker, P.C. Ku, and C.J. Chang-Hasnain,"Slow-light optical buffers – capabilities and fundamental limitations."J. LightwaveTechnol., vol.23, pp.4046–4066, 2005.

[VAS12] N. Vasilantonakis, K. Terzaki, I. Sakellari, V. Purlys, D. Gray, C.M. Soukoulis, M. Vamvakaki, M. Kafesaki, and M. Farsari, "Three-Dimensional Metallic photonic crystals with Optical Bandgaps",Adv. Mater., vol. 24, pp. 1101–1105, 2012.

[VLA12] A. Vlad, A. Frölich, T. Zebrowski, C. A. Dutu, K. Busch, S. Melinte, M. Wegener, and I. Huynen, "Direct Transcription of Two-Dimensional Colloidal Crystal Arrays into Three-Dimensional Photonic Crystals."Advanced Functional Materials, vol. 23(9), pp. 1164–1171, 2013.

[WAN10] B. Wang, M. a. Dündar, R. Nötzel, F. Karouta, S. He, and R. W. van der Heijden, "Photonic crystal slot nanobeam slow light waveguides for refractive index sensing." Applied Physics Letters, vol. 97(15), p. 151105, 2010.

[WAN12] B. Wang, B.T. Siahaan, M. Dündar, R. Nötzel, M.J. van der Hoek, S. He, and W.R. van der Heijden dimvr "Photonic crystal cavity on optical fiber facet for refractive index sensing."Optics letters, vol. 37(5), pp. 833-5, 2012.

[XU10] Xu, T., Zhu, N., Xu, M. Y.-C., Wosinski, L., Aitchison, J. S., and Ruda, H. E. "Pillar-array based optical sensor." Optics Express, vol. 18(6), pp. 5420-5425, 2010.

[YAB87] E. Yablonovitch, "Inhibited Spontaneous Emission in Solid-State Physics and Electronics." Physical Review Letters, vol. bol 58(20): pp. 2059–2062, 1987.

[YAN11] D. Yang, H. Tian, and Y. Ji, "Nanoscale photonic crystal sensor arrays on monolithic substrates using side-coupled resonant cavity arrays." Optics express, vol. 19(21), pp. 11709–11717, 2011.

[YAN13] P. Yan, G. T. Fei, G. L. Shang, B. Wu, and L. De Zhang, "Fabrication of one-dimensional alumina photonic crystals with a narrow band gap and their application to high-sensitivity sensors." Journal of Materials Chemistry C, vol. 1(8), p. 1659, 2013.

[ZHA10] Z. Wang, J. Zhang, J. Xie, C. Li, Y. Li, S. Liang, Z. Tian, T. Wang, H. Zhang, H. Li, W. Xu and B. Yang, "Bioinspired Water Vapor Responsive Organic/Inorganic Hybrid One-Dimensional photonic crystals with Tunable Full-Color Stop Band.", Adv. Funct. Mater. 2010.

[ZLA09] [S. Zlatanovic, L. W. Mirkarimi, M. M. Sigalas, M. A. Bynum, E. Chow, K. M. Robotti, G. W. Burr, S. Esener, and A. Grot, "Photonic crystal microcavity sensor for ultracompact monitoring of reaction kinetics and protein concentration." Sensors & Actuators: B. Chemical, vol. 141, pp. 13–19, 2009.

4

Biosensing using ring resonators

4.1 Introduction

The second structure used in this PhD thesis for the development of photonic biosensing structures is the RR. An optical RR, as illustrated in Fig. 4.1, can be regarded as a ring shaped structure that is close-coupled to a straight waveguide. The RR will thus behave as a cavity that supports WGM and that present different resonances in the spectrum. The position of such resonances depends directly on the refractive index of the surroundings; therefore, the detection employing RRs will be based on tracking the change in the position of the resonances induced by the local refractive index variations in the structure due to the analyte binding.

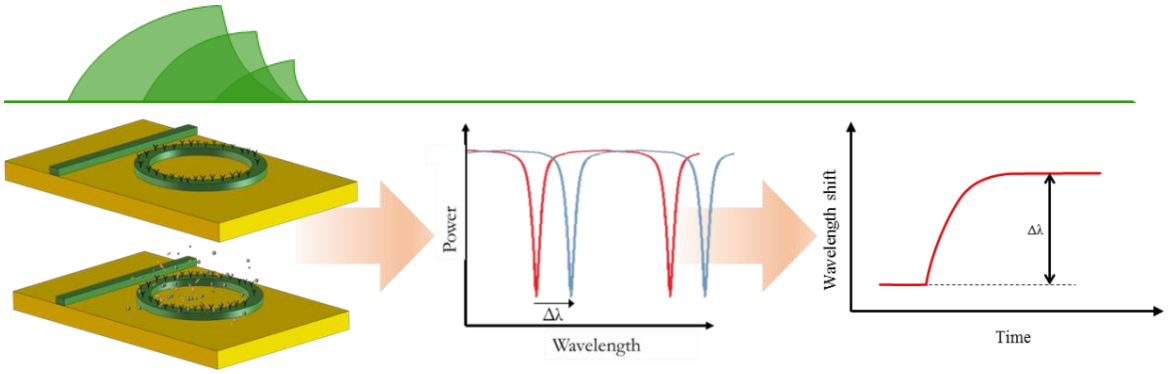

Fig. 4.1: *Schematic illustration of the working principle of an optical RR-based biosensor. When the target analytes reach the RR surface, the resonances will shift to higher wavelengths.*

In this chapter, we will firstly present in section 4.2 the working principle of the RR as well as its main parameters and how the transduction is carried out for the biosensing assays. Afterwards, in section 4.3 we will give an overview of some of the more relevant works published during the last years related to biosensing experiments using planar photonic RR; especially, we will point at the capability of these structures to provide multiplexed detection of several analytes in a single assay. Section 4.4 will deal with the design and the fabrication of the RR-based sensing structures used in this PhD work. In section 4.5, we will describe the experimental set-up employed for measuring the RR-based sensing structures. This experimental set-up was slightly different to that employed for the interrogation of PhC-based sensors (described in section 3.5) and several improvements were added such as the possibility of carry out fully-automated measurement or a new microfluidic delivery system based on elastomer material. In the last section of this chapter, the 4.6, we will present the experimental sensing results obtained making use of these RR-based photonic sensors. In these experiments, we have demonstrated the capability of these sensing structures to detect refractive index variations, DNA hybridization and proteins recognition. Two biofunctionalization approaches, which were introduced in chapter 2, were optimized for these sensing experiments: a first one based on ICPTS modification of the surface and a second one based on GOPTS modification and light assisted immobilization of DNA probes. We obtained very remarkable results in the experiments performed, mainly for the GOPTS-based approach, where a limit of detection below 5 nM was experimentally demonstrated for DNA hybridization experiments. In that section, we will also discuss about several problematic aspects that we faced during the implementation of the sensing experiments as well as the strategies we followed in order to solve or minimize these problems.

4.2 Fundamentals of ring resonators

The generic configuration of a RR, which is depicted in Fig. 4.2, consists on a closed-loop waveguide that is coupled to one or two access waveguides (coupling to two waveguides is depicted in this case). Light from the input waveguide is coupled to the ring through the coupling region (see Fig. 4.2) and it will excite the supported modes inside it. Such modes are generated in the cavity due to constructive and destructive interferences in the structure leading to resonant modes [RAB07]. When the phase of the round-trip signal along the loop is equal to a multiple of 2π, the wave interference is constructive and thus the resonant mode is excited. The wavelength position of the resonant modes inside the cavity can be obtained by using the following equation:

$$\lambda_{res} = \frac{L \cdot n_{eff}}{m} \tag{4.1}$$

where L is the length of the RR ($L=2\pi R$ for a perfectly circular RR), n_{eff} is the effective refractive index of the structure and m is an integer. Once the basic equation of a RR has been presented, we will focus on the description of the theory describing the operation of a RR.

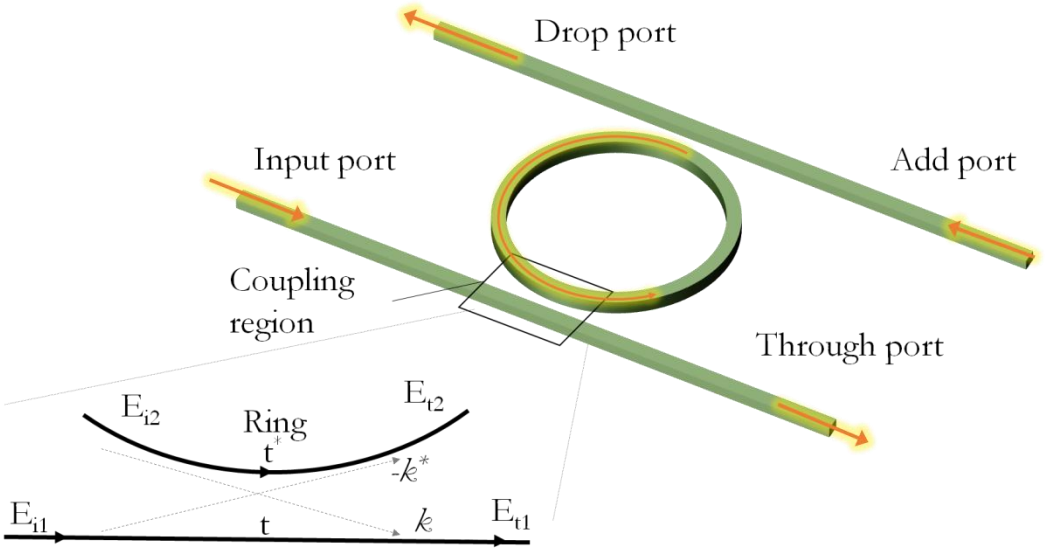

Fig. 4.2: *Schematic view of a RR closely coupled to two access waveguides. A close-up view of the coupling region is also depicted, where the main parameters employed to model the coupling are indicated.*

For the case of a RR with only one coupling waveguide (all-pass RR resonator), we can relate the incoming electrical field coupled to the ring through the input port and the transmitted electrical field employing the following matrix:

$$\begin{pmatrix} E_{t1} \\ E_{t2} \end{pmatrix} = \begin{pmatrix} t & \kappa \\ -\kappa^* & t^* \end{pmatrix} \begin{pmatrix} E_{i1} \\ E_{i2} \end{pmatrix} \tag{4.2}$$

where the electrical field amplitude is normalized corresponding with the power of a single mode of the wave, the parameters κ and t are related to the intrinsic properties of the RR coupling region, and * implies the conjugate of the values. Due to the reciprocity of the structure, the matrix in Eq. 4.2 is symmetric, leading to a relationship between the coupling coefficients:

$$|\kappa^2| + |t^2| = 1 \tag{4.3}$$

For these calculations, we assume that E_{i1} is equal to 1 for simplification. Therefore, the roundtrip of the wave along the ring is defined as follows:

$$E_{i2} = \alpha \cdot e^{j\beta L} \cdot E_{t2} \tag{4.4}$$

where α are the intrinsic waveguide losses (which can be divided in propagation losses and bend losses and zero loss corresponds to $\alpha = 1$), L is the physical length of the ring, and β is the propagation constant in the waveguide comprising the RR that corresponds to:

$$\beta = k \cdot n_{eff} = \frac{2\pi \cdot n_{eff}}{\lambda} \tag{4.5}$$

The phase velocity of the wave in the ring corresponds to c ($c=c_0/n_{eff}$) and the angular frequency is $\omega=k\cdot c_0$. The wavenumber in the vacuum is related to λ according $k=2\pi/\lambda$. Therefore, these equations lead to the phase variation in the circular-shape ring structure given by:

$$\theta = \beta \cdot L = \frac{2\pi \cdot n_{eff}}{\lambda} \cdot 2\pi r \tag{4.6}$$

In order to calculate the transmitted electric field as well as the input and the output fields in the RR, we combine Eqs. 4.2-4.6 resulting in:

$$E_{t1} = \frac{-\alpha + t \cdot e^{-j\theta}}{-\alpha t^* + e^{-j\theta}} \tag{4.7}$$

$$E_{i2} = \frac{-\alpha\kappa^*}{-\alpha t^* + e^{-j\theta}} \tag{4.8}$$

$$E_{t2} = \frac{-\kappa^*}{1 - \alpha t^* e^{j\theta}} \tag{4.9}$$

Finally, we can calculate the transmitted power at the output waveguide as the square of the electrical field amplitude from Eq. 4.7 and plotted in Fig. 4.3, which corresponds to output at the through port:

$$P_{t1} = |E_{t1}|^2 = \frac{\alpha^2 + |t|^2 - 2\alpha|t|\cos(\theta+\varphi_t)}{1 + \alpha^2|t|^2 - 2\alpha|t|\cos(\theta+\varphi_t)} \tag{4.10}$$

where t is a complex value symbolizing the coupling losses and φ_t the phase of the coupler. The response for the through port given by Eq. 4.10 is depicted in Fig. 4.3. When the phase variation is an integer times of 2π, we obtain a minimum in the spectral response. This condition is known as a resonance and it is accomplished for wavelengths given by Eq. 4.1 ($\lambda_{res} = n_{eff} \cdot L/m$). Therefore, when the condition of resonance $(\theta+\varphi_t) = 2\pi m$ is accomplished, we can obtain the particular solution of the transmitted power at the output waveguide as follows:

$$P_{t1} = |E_{t1}|^2 = \frac{(\alpha - |t|)^2}{(1 - \alpha|t|)^2} \tag{4.11}$$

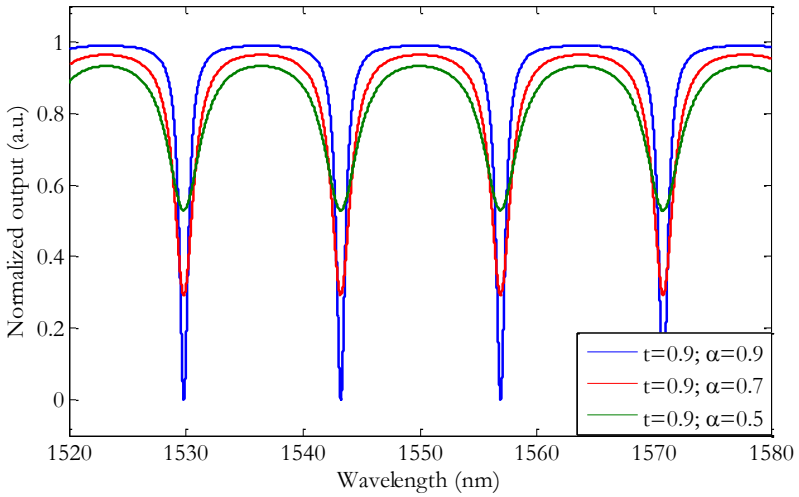

Fig. 4.3: *Typical output spectra for the through port of a RR in all-pass configuration for different loss values.*

A special case occurs when the losses α are equal to the coupling parameter t, what leads to a complete cancellation of the transmitted power due to the destructive interference. This condition is known as critical coupling and exhibits sharper resonances, as it is shown with blue line in Fig. 4.3, where the dips reach the minimum signal. However, sometimes it is very difficult to exactly predict the propagation losses of the RR waveguide (which can be due to several factors such as

roughness, bending, non-linearities, etc.), and therefore, accomplishing this critical coupling condition.

In the case of assuming two access waveguides coupled to the ring (an add-drop RR configuration) instead of only one, as it was shown in the schematic of Fig. 4.2, the transmitted electric field in the through port will be given by:

$$E_{t1} = t_1 + \frac{-k_1 k_1^* t_2^* \alpha_{1/2}^2 e^{j\theta(|t_1|^2+|k|^2)}}{1 - t_1^* t_2^* \alpha_{1/2}^2 e^{j\theta}} = \frac{t_1 - t_2^* \alpha e^{j\theta}}{1 - t_1^* t_2^* \alpha e^{j\theta}} \tag{4.12}$$

It is noteworthy to mention that, in this case, $\alpha_{1/2}$ and $\theta_{1/2}$ are modelled for being the half roundtrip loss and phase of the RR length. In order to calculate the electrical field in the output drop port, it is necessary to consider that the light passes through the second coupler in order to be dropped in the second bus waveguide, leading to the expression:

$$E_{t2} = \frac{-k_1^* k_2 \alpha_{1/2} e^{j\theta_{1/2}}}{1 - t_1^* t_2^* \alpha e^{j\theta}} \tag{4.13}$$

Fig. 4.4 shows a common spectra at the output of the through and the drop ports for a RR coupled to two access waveguides.

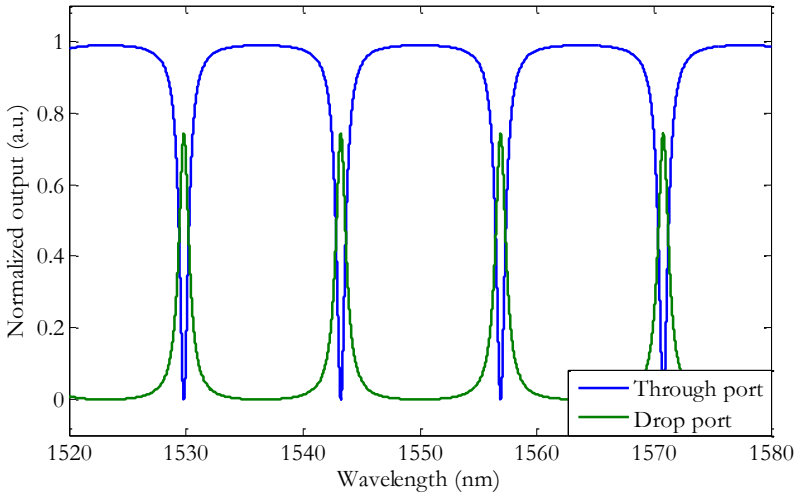

Fig. 4.4: *Typical output spectra of a RR in add-drop configuration. It is characterized for exhibiting periodic dips in the through port (blue line) and peaks in the drop port (green line) resulting from the RR resonances.*

From Eq. 4.12 we can extract that now, for the configuration with two access waveguides, the critical coupling condition will be accomplished when $t_1 = t_2^* \cdot \alpha$. For a typical case where

propagation losses are low, this condition will be reduced to having two coupling regions (for each access waveguide) which are almost equal, thus simplifying the achievement of the critical coupling condition compared to the case of a single access waveguide.

Regarding the spectral response of the RRs, it will be characterized by several parameters such as periodicity, quality or finesse. One of the most important RR parameters is the distance between two consecutive resonances, what is called free spectral range (FSR). We may obtain an approximation of the FSR by using the propagation constant of the mode and ignoring the wavelength dependence due to the dispersion of the material, thus obtaining:

$$\frac{\partial \beta}{\partial \lambda} = -\frac{\beta}{\lambda} + k\frac{\partial n_{eff}}{\partial \lambda} \approx -\frac{\beta}{\lambda} \tag{4.14}$$

$$FSR = \Delta\lambda = -\frac{2\pi}{L}\left(\frac{\partial \beta}{\partial \lambda}\right)^{-1} \approx \frac{\lambda^2}{n_{eff} \cdot L} \tag{4.15}$$

However, in the cases where the wavelength dependence on the transmitted signal cannot be neglected, we need to use the group index defined as $n_g = n_{eff} - \lambda\frac{\partial n_{eff}}{\partial \lambda}$, which includes the waveguide dispersion. For that, we calculate:

$$\frac{\partial \beta}{\partial \lambda} = -\frac{k}{\lambda}n_g \tag{4.16}$$

$$FSR = \Delta\lambda = \frac{\lambda^2}{n_g \cdot L} \tag{4.17}$$

Another parameter related to the spectral response of the RR deals with the resonance peak width. The full width at half maximum (FWHM) is the width of the resonance dip when the power decreases 3 dB, which is obtained theoretically as follows from Eq. 4.10:

$$FWHM = \frac{\kappa^2\lambda^2}{\pi L n_{eff}} \tag{4.18}$$

Consequently, the finesse of the resonance can be defined directly from the previous parameters as the ratio between the FSR and the width of the resonance (assuming $\kappa << 1$):

$$F = \frac{FSR}{FWHM} \approx \frac{\pi}{\kappa^2} \tag{4.19}$$

Finally, an important parameter to compare the performance between RRs is the quality factor (Q). Q factor can be seen as the stored energy divided by the losses in each cycle. It is also considered as the number of roundtrips that the light travel until it leaves the cavity through the drop waveguide or dissipated by the internal losses of the ring. The Q factor is defined as:

$$Q = \frac{n_{eff} L}{\lambda} F \tag{4.20}$$

It is straightforward to think that in order to maximize the Q factor, the intrinsic losses and the bending losses should be reduced as well as the coupling factors between the bus waveguides and the cavity. Generally, the all-pass configuration shows higher Q-factors than add-drop configurations when they are operating close to the critical coupling regime.

For the case of using a RR for biosensing purposes, Q-factor will determine the level of interaction of the field with the target analytes, since it will determine the number of times that the light "sees" the analytes. This effect leads to a larger effective light-analyte interaction length, which can be calculated by:

$$L_{eff} = \Gamma \frac{Q\lambda}{2\pi n_{eff}} \tag{4.21}$$

where Γ is the factor related to the amount of interaction between the light and matter in the cavity and the other parameters were defined previously. A good RR usually exhibits high Q-factors (e.g., from 10^4 to 10^8); therefore, a RR with a physical length of tens of microns might exhibit an effective interaction length of tens of centimetres. Additionally, a high Q-factor also means having very sharp resonances, whose position can be more accurately determined when carrying a sensing experiment out.. Therefore, for biosensing purposes it will be highly desirable to obtain a response with an elevated Q-factor in order to provide a high resolution and larger interactions between the molecules and the light.

4.3 State-of-the-art of RR-based biosensors

The versatility of RR-based biosensors has been extensively reported in numerous works and reviews in which such structures have been employed for sensing in gas or liquid environment [FAN08, PAS13, LUC12]. These structures are characterized by their high Q factor and the possibility of using different cavity geometries. In this section, we will review some of the most interesting state-of-the-art results in the field of photonic biosensors based on optical RRs, mainly

focusing on biological detection experiments. We have structured this section by classifying the RR-based biosensors according to their geometries, materials and multiplexing approach.

4.3.1 Waveguide cross section

Photonic sensors based on RRs must be designed to obtain the highest sensitivity. As previously described within this PhD work, one of the possibilities to increase the sensitivity is by maximizing the overlap between the light and matter. For such purpose, several waveguide cross sections have been employed by different research groups. The three most employed approaches in order to design RRs devices are wire, rib and slot waveguides, which are schematically shown in Fig. 4.5, together with their field distribution.

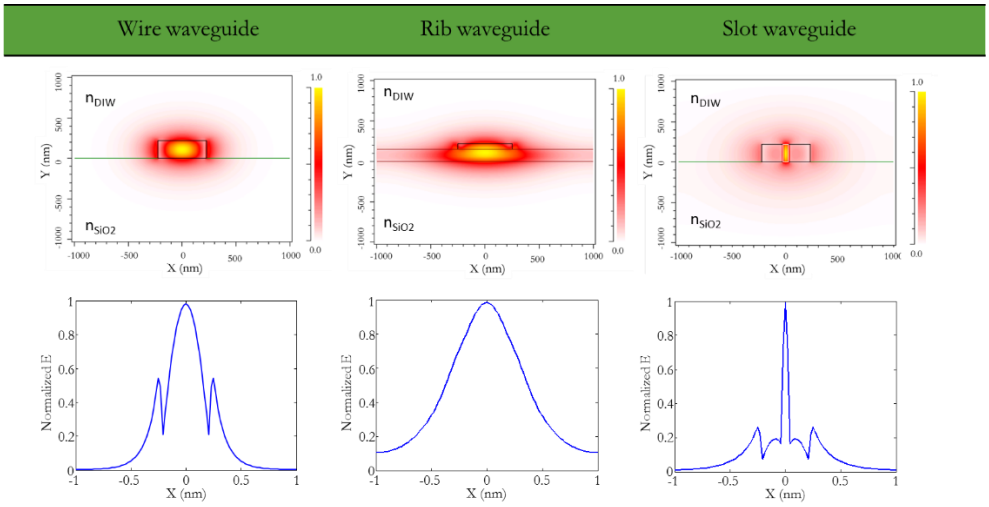

Fig. 4.5: *Electric field distribution of the cross section of the different waveguide architectures and relative magnitude of the electric field along the x direction across the center of the waveguide. These calculations have been carried out using silicon as core material, SiO_2 as lower cladding and DIW as upper cladding.*

Currently, photonic wire waveguides are mostly employed to implement photonic RRs because of their simplicity and good performance in most materials. Its cross section is characterized by a rectangular shape and it is created in a high refractive index material (at least, with a higher refractive index that the cladding in order to confine the optical field). For the case when a high contrast configuration is used (as for the case of SOI technology), light will be highly confined inside the waveguide core, what permits to tailor structures with small bending radius and fabricate ultra-compact designs with reduced small footprints (usually in the order of 100 μm^2).

Rib waveguides are the second type of cross section considered. This structure is similar to the wire waveguide, but instead of having the guiding structure directly located on top of a low

index lower cladding, it is placed over a layer of high index pedestal. This structure is achieved by partially etching the waveguide. This waveguide configuration makes that the electromagnetic field is mainly located within the high index material, thus yielding low losses. However, that allocation of the field in the high index material is not beneficial for biological detection purposes, since it leads to a lower light-matter interaction for the rib waveguide compared with wire waveguides.

The last type of cross section architecture considered is the slot waveguide proposed by Cornell University [ALM04]. This structure is completely different from the other two previous approaches. Whereas the common wire and rib waveguides confine the light in a high refractive index region by means of TIR, the slot waveguide confines exceptionally the electromagnetic field in a very narrow low index region located within two high index regions. A great advantage of this structure is that the slot section of the waveguide can be filled up with the sample containing the target analytes, what leads to a remarkable high interaction between the light and the molecules. However, due to the small size of the slot region (usually below 100 nm), it requires a high accuracy in the fabrication process. In addition, the high field intensity within the slot region will also make the structure very sensitive to surface roughness, what is translated into higher propagation losses that may limit the performance of the device.

As a conclusion for the three types of waveguides considered, and according to the numerous works published focused on the development of RR-based sensors, we can state that:

- Even though structures based on rib waveguides present lower propagation losses than wire and slot configurations, their sensitivity may significantly be overtaken by these two configurations.
- Despite slot-based configurations exhibit an incredible performance due to the high interaction of the light with the target sample located within the slot region, its propagation losses are higher than for wire and rib configurations, and its fabrication might be challenging.
- The fabrication simplicity and the good performance in terms of sensitivity and propagation losses of common wire-based RRs, make them the preferred option for the development of photonic RR-based sensing structures for biochemical detection.

One of the first demonstrations of biosensing using SOI wire-based RRs was presented by De Vos et al. from Gent University [VOS07]. Fig. 4.6a shows a SEM picture of this structure. They obtained an acceptable sensitivity of 70 nm/RIU with a detection limit of 10^{-5} RIU by performing salt concentrations experiments. Besides the bulk sensitivity of the structure, they also perform biosensing experiments, being able to detect a concentration as low as 10 ng/ml of avidin using biotin receptors. This sensitivity is comparable with that obtained for other structures such as PhC or MZI, but the extremely small footprint of the RR (~100 μm^2) allowed them to calculate an

outstanding theoretical mass detection limit of 1 fg, thus confirming the huge potential of RRs for the development of high sensitivity sensing structures.

Concerning the use of rib-based RRs for sensing, less works can be found in the literature. One example of this type of sensing device was presented by Passaro et al., which reported an exhaustive theoretical study of an ultracompact rib-based RR sensor [PAS07]. Once again, SOI technology was proposed for the development of the structure, leading to a significant reduction of the footprint of the structure (~40 μm^2). By simulating a coating of the sensing structure using PMMA doped with bromocresol purple, the studied RR was able to detect ammonia with an approximated detection limit of $8 \cdot 10^{-5}$ RIU.

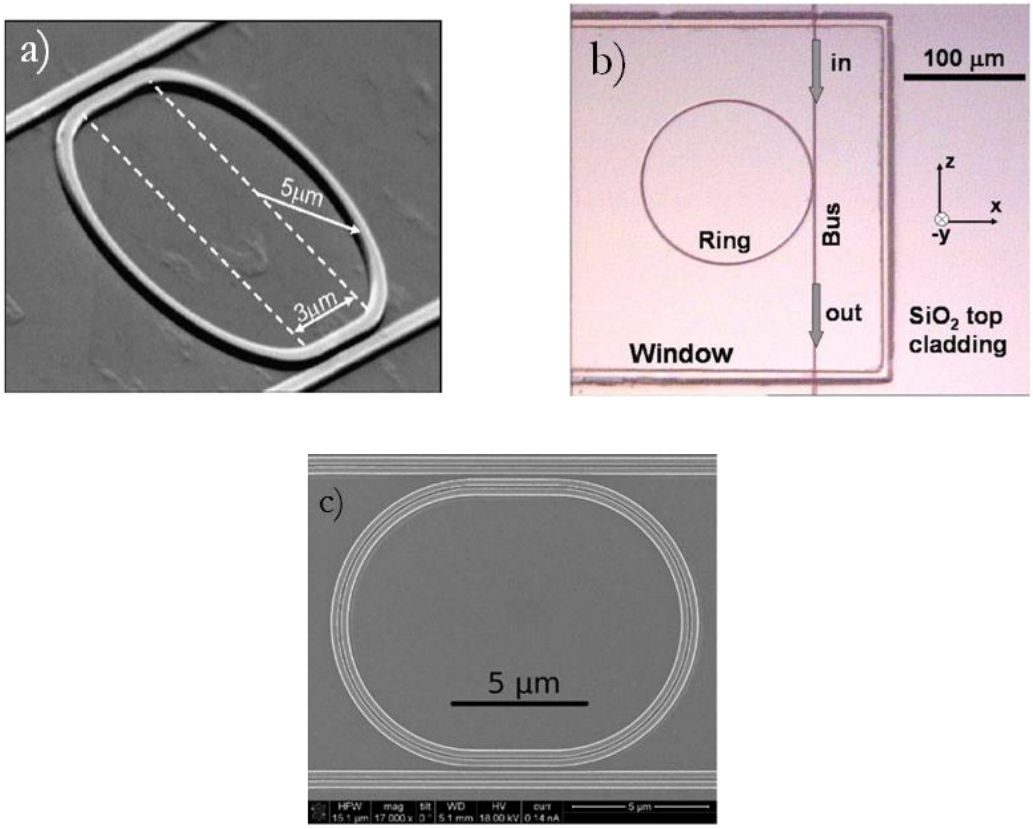

Fig. 4.6: *a) SEM picture of a wire-based RR on SOI [VOS07]. b) Microscope image of a slot-based RR in Si_3N_4 [BAR07]. c) SEM picture of a slotted SIO RR [CLA09]*

On the other hand, several works have shown the extraordinary benefits of slot waveguides for chemical and biochemical sensing. Barrios et al. demonstrated the sensing potential of a Si_3N_4 asymmetrical slot waveguide, displayed in Fig. 4.6b, obtaining a sensitivity of 212 nm/RIU [BAR07]. However, the detection limit for those experiments was a bit high ($2 \cdot 10^{-4}$ RIU) due to the limitations of their optical characterization set-up. Additionally, Claes et al. presented experimental results of slot-based RRs on SOI technology [CLA09]. This structure was based in the previous

RR-based sensor presented by De Vos et al., but where a central air slot was created by FIB (Focused Ion Beam) etching as observed in Fig. 4.6c. By means of this change in the waveguide structure, they were able to increase the sensitivity of the SOI RR-based sensor (from 70 nm/RIU to 298 nm/RIU), but the detection limit got worse (from 10^{-5} RIU to $4.2 \cdot 10^{-5}$ RIU) due to the increase in the losses of the structure. Finally, an example of biosensing experiments employing slot waveguides was presented also by Barrios et Al. [BAR08]. There, they showed a sensitivity of 1.8 nm/(ng/mm^2) and a detection limit as low as 28 pg for antiBSA detection, whereas for BSA the sensitivity was 3.2 nm/(ng/mm^2) and the mass detection limit 16 pg.

4.3.2 Materials

As we have been indicating throughout this document, the most employed material for the development of integrated photonic biosensing structures is silicon (more concretely, SOI technology). This is not only due to the good performances that it exhibit, but also because of its CMOS compatibility (see section 1.7, where the benefits of silicon photonics were explained). This is also true for the development of RR-based photonic biosensors. But, besides silicon, we can also find other material platforms such as silicon nitride or polymers on top of low index material, that are also usually used for the development of RR-based biosensors.

Despite polymer-based platform does not owe all the benefits of other high-contrast platforms (as SOI technology), in the last years this material has been the center of attention of an intensive investigation obtaining relevant results. Among the wide variety of polymers that we can find, PMMA, SU8, polystyrene, or polycarbonate are probably those more commonly used for the fabrication of photonic structures. Probably the main advantage of polymer-based platform is easiness of fabrication. For example, nanoimprinting lithography (NIL) can be used for the fabrication, where structures are directly created by stamping using a mold with the reverse pattern. Another advantage of polymer materials for the creation of photonic structures is their biocompatibility, what is an extra for the development of sensing structures to be used with biological samples. However, the low refractive index contrast between the polymer waveguide core and the cladding lead to several drawbacks such as higher losses, larger sizes of the structures and larger bending radii.

Looking at specific results where polymer-based structures are developed, Halldorson et al. employed Cytop material, a novel fluorinated polymer with a refractive index close to that of the water (n = 1.34), in order to be used as lower cladding for the fabrication of PMMA-based RRs, as depicted in Fig. 4.7a [HAL10]. In that work, a detailed theoretical and experimental study of the properties of optical waveguides, rings and directional couplers was presented. The structures were fabricated by means of e-beam lithography and wet etching, reporting integrated optical RRs based

on PMMA over Cytop with small diameters ranging from 20 μm to 60 μm with satisfactory Q-factors in the order of ~10^4, which are suitable for biosensing applications.

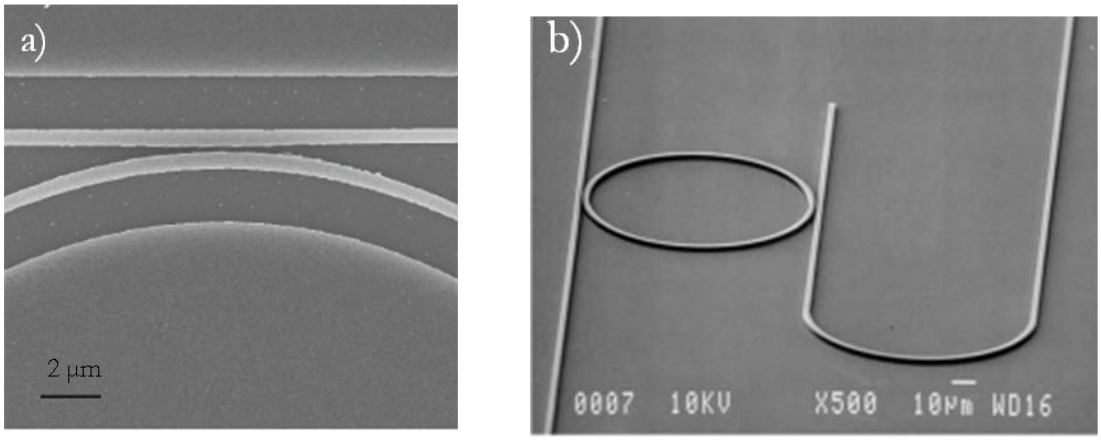

Fig. 4.7: *a) SEM picture of the coupling region of a PMMA-based RR on top of a Cytop lower cladding [HAL10]. b) SEM picture of a polystyrene-based RR fabricated by NIL [CHA06].*

Another example of polymer-based development was reported by Chao et al. [CHA06]. They employed NIL technology to fabricate polystyrene-based RRs for sensing purposes, as shown in Fig. 4.7b. In order to confine the fundamental mode in the polymer structure, the photonic wire dimensions were 1.8 μm in height and 2.3 μm in width. Fabricated RRs with a radius of 30 μm exhibited a Q-factor of $2 \cdot 10^4$ in air and of $5 \cdot 10^3$ when a liquid solution was flowed over them for sensing applications. They estimated a detection limit of the polymer structure as low as 10^{-7} RIU by means of refractive index sensing experiments using different concentrations of glucose in DIW. Furthermore, they also tested the operation of the sensor for the specific detection of biomolecules using biotin-streptavidin with a surface mass detection limit of 250 pg/mm^2. Although these sensors exhibited a competitive performance, the dimensions of the structures are substantially higher than for other high index contrast technologies such as SOI, thus significantly limiting the integration density.

Another interesting approach, where the authors merged a polymer platform with slot waveguides reported in [SUN09]. In this work, Sun et al. presented a new integrated optical sensor based on multislot waveguides fabricated in SU8 polymer, as shown in Fig. 4.8. The structure mainly consists on replicating a slot structure that is created by means of several SU8 waveguides of 2 μm in height and 500 nm in width, and separated 200 nm. The structure sensitivity is increased according to the number of slots comprising the structure, due to the higher amount of light travelling along the low index region and thus increasing the interaction with the target sample.

Nevertheless, due to the scattering losses and the fabrication limitations, the final fabricated structure was designed with only three slots. The sensing experiments were carried out using a RR of radius 200 μm created using this multislot waveguide, and exposing it to different salt concentrations. The optical sensor exhibited a bulk sensitivity of 244 nm/RIU.

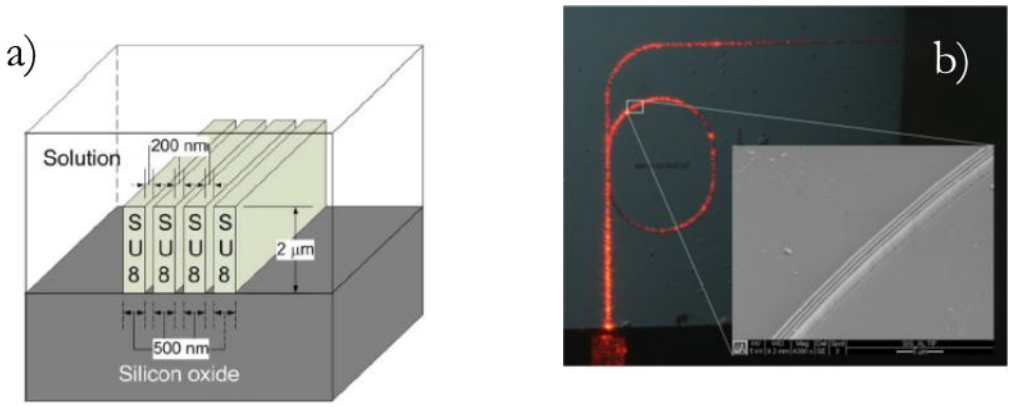

Fig. 4.8: *a) Cross section of the SU8-based multislot structure. b) Excitation of the multislot-based RR with a 636-nm laser through fiber coupling [SUN09].*

Finally, the last material approach considered here for the development of RRs for biosensing purposes is based in the use of porous materials for the creation of the structures. Contrary to the rest of sensing configurations that we have presented, where biosensing is based on the detection of molecular interactions taking place in the outer surface of the structure, the use of porous materials allows that the target molecules can enter into the structure itself. This will increase the interaction of the analytes with the optical field, and so the sensitivity of the device. By using nanoporous polymer material, Mancuso et al. proposed and measured a photonic integrated RR-based biosensor, which is shown in Fig. 4.9 [MAN12]. The structure was fabricated in porous PMMA using NIL technology. They fabricated a set of RRs with a minimum radius of 35 μm. An experimental comparison between porous and non-porous RRs was performed, obtaining a sensitivity enhancement of 40% for porous structures due to higher interaction of the mode with the analytes when the latter can penetrate inside the structure.

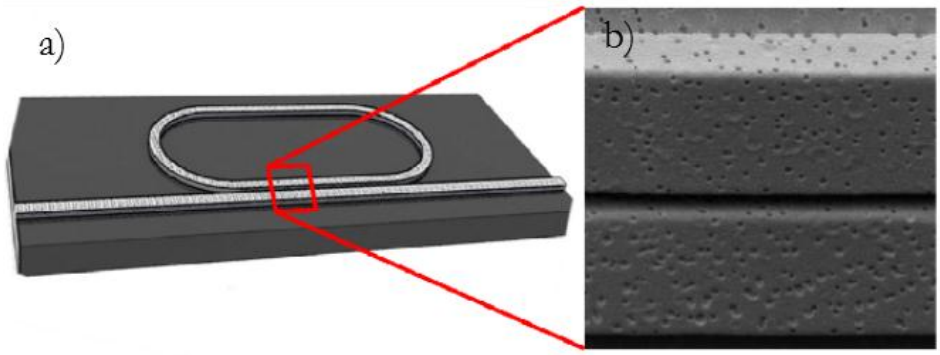

Fig. 4.9: *a) Schematic illustration of the RR fabricated in porous material. b) Close up view of the coupling region of the RR, where the porosity of the waveguide can be clearly seen.*

4.3.3 Multiplexing approaches

In the previous sections, we discussed two aspects related with the configuration of RRs: the waveguide cross section and the materials employed for their fabrication. In this section, we will focus our review on an extremely important issue for the development of biosensing devices with practical application: the multiplexing approach used for the simultaneous interrogation of several RR-based sensing structures. Multiplexing of sensing structures opens the route towards performing multiparametric analyses simultaneously, thus significantly increasing the throughput of information [BAR12]. Several considerations need to be addressed in order to develop a multiplexed RR-based platform, including a spatially specific chemical modification, the optical coupling mechanism from the source and to the detector, and a proper sample delivery to each sensing structure.

Regarding the individual or group coating with different biological receptors of the RRs, several techniques based on either flowing the receptors or spotting directly on the surfaces exist. The former method has the advantage of being possible to monitor the functionalization in real-time, thus having a higher control of the process. However, this procedure provides a lower throughput (i.e., we only do the functionalization of a chip each time) and requires flowing the reagent during a certain time, thus leading to a higher reagent consumption. On the other hand, automated spotting tools are suitable for the functionalization of a large number of different sensors with a high throughput and allow a reduction of the reagent consumption since only the required volume of reagent needs to be spotted on the sensing areas.

A second consideration when a multiplexed photonic sensing system needs to be implemented is related to the coupling of light to the structures. In order to carry the interrogation of the sensing structure out, light needs to be coupled to all the structures in order to analyse each

target sample. It is required to couple light to the chip with enough efficiency, since the higher the power inside the rings is, the more evanescent field will interact with the target molecules and the sensing performance of the device will be enhanced. To tackle this issue, two main coupling approaches are found in the literature: vertical and horizontal methods. Grating couplers for vertical coupling permit a higher tolerance in the alignment process and they provide sufficient bandwidth for sensing application, whereas horizontal coupling is polarization independent and there is no necessity to design couplers in order to excite the light within the waveguide. Some considerations such as cost, complexity, coupling efficiency or optical bandwidth must be evaluated in order to select between them.

One example of multiplexed RR-based sensing device where vertical coupling is used was reported by Ramachandran et al. [RAM08]. They developed an array of 5 RRs using a glass-based material called Hydex™, with a diameter of each ring of 100 μm, as shown in Fig. 4.10a. Light was horizontally coupled to the access waveguide of each RR by means of a fiber array, which was glued to the optical chip. In order to perform the experiments, the chip was directly immersed in the liquid sample to be analysed. This platform was successfully characterized for the label-free, specific and rapid (in 10 minutes) detection of bacteria (E. Coli detected with a concentration of 10^5 CFU/ml), proteins and DNA.

Other approach of multiplexed structure, where in this case a vertical light coupling by means of grating couplers was used, was reported by De Vos et al. [VOS09]. In that work, a collimator was used to expand the light beam in order to be able to excite several access structures at the same time (in this case, three grating couplers were excited). Each bus waveguide coupled the light to four RRs with slightly different dimensions, obtaining an array of 12 RRs with a maximum coupling efficiency of 31%. The output signal from every output coupling structure was collected simultaneously with an infrared camera tilted 10º from the vertical, as schematically shown in Fig. 4.10b. Target sample was delivered by means of a PDMS microfluidic structure. The resonant wavelength of each RR was mathematically tracked, obtaining a limit of detection of 3 ng/ml for antiHSA. A total mass detection limit of 74 ag was calculated employing this platform. The main advantage of this set-up is that it permits a relatively high alignment tolerance, what eases the realization of the experimental measurements. Another example of multiplexed interrogation, where several RR structures are excited using a single access waveguide was presented by Xu et al. and it is shown in Fig. 4.10c [XU10]. They called this strategy "WDM approach". In that work, they addressed the input light to five RRs through a single bus waveguide. These RRs were optimized for TM polarization and they demonstrated the simultaneous monitoring of molecular bindings with a resolution as low as 0.3 pg/mm^2. Furthermore, several concentrations of protein were detected over a dynamic range of 4 orders of magnitude.

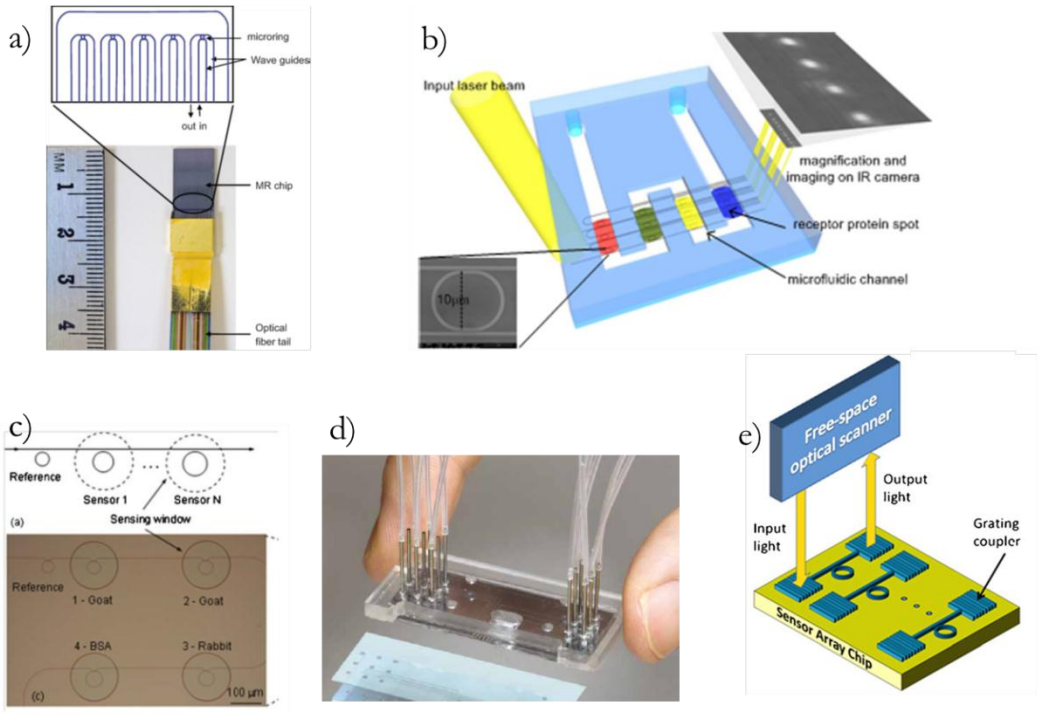

Fig. 4.10: *a) Picture of the sensing device consisting on five RRs in silicon and Hydex materials that are horizontally coupled using a fiber array [RAM08]. b) Concept of a multiplexed RR platform where the different outputs are simultaneously measured using an IR camera [VOS09]. c) Microscope image of multiplexed RR sensors in a WDM scheme [XU10]. d) Packaged sensing device consisting on six RR-based sensors integrated with a microfluidic sample delivery system [CAR10]. e) Optical scanning platform in which the RRs are sequentially interrogated by focusing the light on the access grating couplers [IQB10].*

A higher degree of integration was demonstrated in the work by Carlborg et al., which is shown in Fig. 4.10d [CAR10]. In that work, they fabricated an array of silicon nitride slotted RR-based sensors with a PDMS-based microfluidic sample delivery system, and they finally packaged them into a compact cartridge to be inserted in a read-out equipment. Light is coupled to the Si_3N_4 structures by means of fully etched vertical grating couplers and the output of the RR sensors was detected using a 1D array of photo-detectors. This packaged multiplexed sensing device showed a high sensitivity due to the use of slot waveguide and reference rings, reaching a detection limit of $5 \cdot 10^{-6}$ RIU. Regarding biosensing experiments, they estimated a minimum surface mass detection limit of 0.9 pg/mm^2 using antibody detection experiments.

However, the most remarkable results in the field of RR-based biosensors are those reported by the group headed by Dr. Bailey in the University of Illinois. In [IQB10], they presented a sensor array of 32 rings that were vertically coupled using a free-space optical scanner depicted in Fig. 4.10e. During the measurement, the spot of the source dwells on each input grating for the time required to carry out a spectral sweep; then the signal is filtered, detected and a lorentzian

fitting is automatically applied in order to obtain the position of the resonances and their spectral shift. The fact of using a sequential scan for each sensor avoids splitting the signal to multiple RRs, thus obtaining more power at the output. However, for a full spectral characterization of all the multiplexed sensing elements will require longer times. With this platform and using 24 RRs of the 32 RRs as sensing structures, the detection limit of the system was determined to be $7.6 \cdot 10^{-7}$ RIU. In addition, they performed bioassays with streptavidin obtaining a detection limit of 60 fM.

This sensing platform has been extensively used for multiple detection experiments for a wide range of molecules. For instance, Luchansky and Bailey performed an assay where a human cytokine interleukin (IL-2) was detected for concentrations smaller than 100 pg/ml, what corresponds to 6.5 pM [LUC11]. In addition, they demonstrated the versatility of the sandwich assay methodology using antibodies for the detection of another cytokine interleukin (IL-8). In other work, a protein detection was carried out in three different steps. First the rings were modified with the antibodies in order to determine the binding of the cardiac marker C-reactive protein (CRP), then a biotinilated antibody was recognized due to the binding to the attached CRP on the surface, and finally streptavidin-functionalized beads were bound to the surface and detected.

Washburn et al. employed the same ring-based platform in order to quantify different protein biomarkers clinically related to cancer diseases [WAS09]. In that work, they determined the protein concentration by measuring the initial slope of the resonance's shift, thus significantly reducing the time required to carry the detection out. These label-free detection assays were performed in complex buffer, providing a detection limit of 2 ng/ml. In addition, in another work, the functionalization procedure was validated for five different proteins using the same platform, what indicates the versatility of the RRs for biosensing applications [WAS10].

The detection of the hybridization of microRNA and tmRNA using the RR array was also studied in several works [QAV10, SCH12]. The complementary capture probes were covalently attached to the surface of the sensing structures. Obtained results of specific hybridization detection showed a detection limit of 1.95 nM for simple microRNA, whereas a detection limit as low as 53 fmol was obtained for the specific detection of a streptococcus pneumonia tmRNA.

All these last works (those from Bailey's group) have been performed using a novel prototype of sensing equipment based on integrated photonic RRs that is commercialized by Genalyte Inc.. This device, called Maverick Detection System, is shown in Fig. 4.11. The commercial equipment is based on photonic RRs where each ring is individually functionalized with isotype specific capture antibodies. One of the main advantages of this system is that the assays are fully compatible with current sample preparation techniques. In only one year, they have been able

to release 4 different measurement platforms, exhibiting the great potential of the RR photonic technology for biological detection.

Fig. 4.11: *Maverick Detection System based on RR technology from Genalyte Inc. Schematic depiction of an antibody attachment on top of the RRs provided by the company.*

To finalize this section, we have included the next table where the main parameters of the different state-of-the-art results in the field of optical RR-based biosensors are listed. In some cases, certain parameters were not indicated in the reference, so a blank space was left intentionally in the table.

Reference/year	Structure	Size/diameter	Fluidics	Material	Functionalization process	Buffer	Target nalyte	Limit of Detection	Sensitivity	DL (RIU)	Q factor
[CHA06]	Single ring	60 μm	-	Polyestyrene	Spotting	DIW	Streptavidin	250 pg/mm2	-	10^{-7}	20000
[BAR07]	Single slotted ring	140 μm	-	Si_3N_4	-	DIW	Ethanol	-	212 nm/RIU	$2{\cdot}10^{-4}$	-
[PAS07]	Single ring	3 μm	Imersion	SOI	-	Gas nitrogen	Ammonia	-	132 nm/RIU	$8{\cdot}10^{-5}$	-
[VOS07]	Single racetrack ring	10 μm x14 μm	PDMS	SOI	Hand	PBS	Avidin	0.7 fg	70 nm/RIU	10^{-5}	-
[BAR08]	Single slotted ring	140 μm	-	Si_3N_4	Hand	DIW	BSA-antiBSA	28 and 16 pg/mm^2	-	-	-
[KIM08]	Vertical coupled ring	800 μm	-	LFR-S708U polymer	-	-	Glucose	-	200 nm/RIU	$5{\cdot}10^{-6}$	-
[XU08]	Spiral	110 μm x 100 μm	PDMS	SOI	Spotting	PBS	Streptavidin	3pg/mm^2	-	-	-
[RAM08]	5 rings	100 μm	-	Glass	-	PBS	Bacteria cell/DNA	10^5 CFU --- 100 ng/ml		-	-
[CLA09]	Racetrack single slot	13 μm x 10 μm	PDMS	SOI	-	DIW	Salt	-	298 nm/RIU	$4.2{\cdot}10^{-5}$	330
[VOS09]	12 Racetrack rings	10 μm x 14 μm	PDMS	SOI	Spotting	PBS	Human IgG and antiBSA	3.4 pg/mm2	-	-	1.00E+04
[WAS09]	32 rings	30 μm	Mylar	SOI	Mylar	PBS/Serum	Cancer biomarker	2 ng/ml ---25ng/ml	-	-	-
[SUN09]	Multislot	400 μm	-	SU8 polymer	Hand	PBS	Biotin-BSA	-	8333nm/RIU	-	15000
[CLA10]	2 rings inVernier configuration	folded 200 μm x 70 μm	PDMS	SOI	-	DIW	Salt	-	2169 nm/RIU	$8.3{\cdot}10^{-6}$	-
[HALL10]	Single ring	60 μm	-	PMMA	-	-	-	-	-	-	-
[IQB10]	24 rings	30 μm	Mylar	SOI	Mylar	PBS	Streptavidin	-	163 nm/RIU	$7.6{\cdot}10^{-7}$	-
[LUC10]	32 rings	30 μm	Mylar	SOI	Mylar	PBS	Human citokine	100 pg/ml	-	-	-
[QAV10]	32 rings	30 μm	Mylar	SOI	Mylar	PBS	Four microRNA	150 fmol	-	-	-
[WAS10]	32 rings	30 μm	Mylar	SOI	PDMS	PBS	Five proteins biomarkers, PSA,IL-8,CEA,AFP,TNF	2 ng/ml	-	-	-
[LEE10]	Microdisk	30 μm	Spoted	Si_3N_4	Immersion	PBS	Streptavidin	30 ng/ml	-	-	7000
[XU10]	5 rings	20 μm	SU8	SOI	Mylar	PBS	Two IgG proteins	0,3 pg/mm^2	-	-	-
[CAR11]	7 slot rings	140 μm	PDMS	Si_3N_4	PDMS	PBS	antiBSA	0.9 pg/mm^2	-	-	-
[QAV11]	32 rings	30 μm	Mylar	SOI	Mylar	PBS	DNA	195 fmol	-	-	-
[LUC11]	32 rings	30 μm	Mylar	SOI	Mylar	Serum	C-reactive protein	200 fM	-	-	-
[MAN11]	Porous ring	60 μm	PDMS	Porous PMMA	-	-	-	-	94.05 nm/RIU	-	3000
[YEB12]	Single racetrack ring	10 μm	Chamber	SOI	Atomic layer deposition	Gas nitrogen	Ammonia	5 ppm	-	-	-
[SCH12]	32 ring	30 μm	Mylar	SOI	Mylar	Hybrid buffer	Bacterial tmRNA	53 fmol	-	-	-

Table 4.1: *List of main results reported for RR-based sensors (classified by year of publication).*

4.4 Development of the RR-based sensing structures

As explained in section 3.4 for the case of PhC-based sensors, part of this PhD work was enclosed in the frame of the European project FP7-ICT-INTOPSENS. The work package related to the development of the photonic structures for biological sensing, in which we participated, also dealt with RR-based photonic sensors. This work was carried out in collaboration with the Photonics Research Group of Gent University, led by Dr. Peter Bienstman, which contributed with the design and fabrication of the structures. Then, the experimental development of the biosensing experiments was mainly carried out by the Universitat Politècnica de València. Therefore, despite we did not have prominent role in the design process, we closely collaborated with the other partners in order to provide proper feedback to enhance the designs.

In this section, we will mainly discuss about the design of the structural parameters of the RRs, the chip layout, and the fabrication process.

4.4.1 Ring resonator configuration and layout

One of the main aspects for a proper operation of a RR is a good design of the coupling section between the RR and the access waveguides. For example, parameters such as the critical coupling condition or the Q-factor of the resonances are highly dependent on the coupling. Fig. 4.12 schematically illustrates the two main configurations of RR depending on its coupling region: a circular ring and a racetrack ring. In a circular shape RR, the parameters for coupling design are limited to the gap between the RR and the waveguide, and the radius of the RR. However, for an efficient coupling between the access waveguide and the RR we will usually need to have narrow gaps, thus making more precisely and difficult the fabrication process. On the other hand, a better control over the coupling region can be obtained by using racetrack-shaped RRs, where a straight coupling section is introduced, as shown in Fig. 4.12b. For this configuration, the coupling efficiency is not only determined by the gap distance but also by the coupling length. Furthermore, the gap condition is more relaxed enabling to design wider gaps in racetrack RRs compared to circular RRs, thus easing the fabrication. As a drawback, there are some additional losses due to the mode mismatch produced in the interface between the radial waveguide and the straight waveguide, where the mode changes adiabatically from one section to the other. Furthermore, the fact of adding a straight waveguide to the RR increases the total length of the RR, thus leading to a reduction of the FSR (note that FSR is inversely proportional to the ring length).

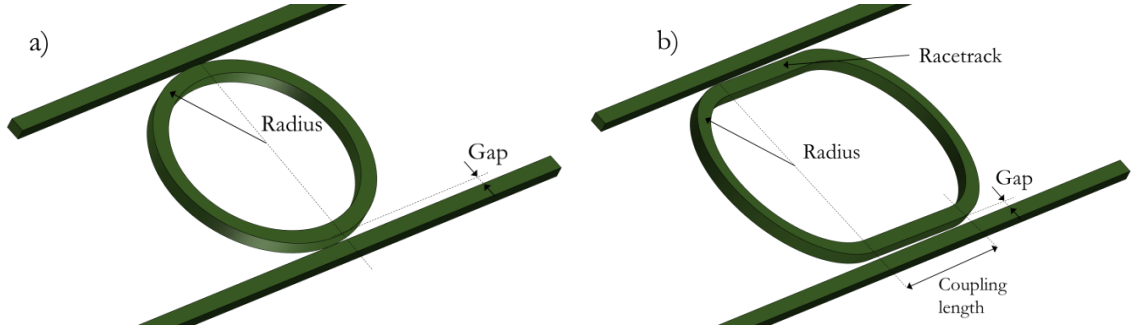

Fig. 4.12: *Illustration of a) a circular-shaped RR and b) a racetrack-shaped RR. In both cases, add-drop configuration with the main design parameters are depicted.*

The coupling region also need to be designed in order to maximize the power exchange between the waveguide to the RR at the resonant wavelength to enhance the light-matter interaction. To this aim, a FDTD software can be employed to simulate the propagation of the light through the structure. In order to obtain the proper coupling length, several simulations with different length values were performed obtaining the optimal value for the gap of 160 nm and for the coupling length of 2 μm. In Fig. 4.13, we can observe the simulations of a RR with a gap of 160 nm in which different wavelengths were excited (resonant and non-resonant mode). At the resonant mode, the coupled light is practically fully transmitted to the drop port.

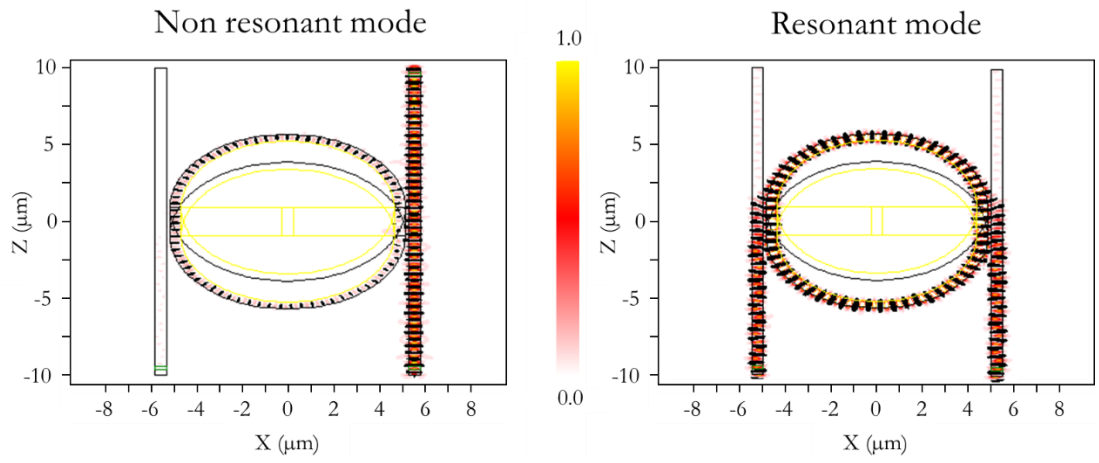

Fig. 4.13: *Simulation of the optical RR for different wavelengths where we can appreciate the excitation of the WGM in the RR at the resonant wavelength.*

Once we have obtained the physical parameters of the RRs for the implementation of the photonic sensing structures, we have to organize spatially the sensors on the chip. The layout of the chip must meet several requirements and, therefore, some constrains have to be taken into account

when defining it. The first condition was being able to measure simultaneously several sensing structures in order to carry out multi-analyte detection; hence, a proper signal distribution scheme must be used in order to route the light to the structures with low losses. In addition, the distribution of the photonic sensing structures must be compatible with the integration of the microfluidic delivery system, which will be explained in section 4.5.2. Finally, it was also considered to place the structures with sufficient separation between them in order to ease their spotting with the required reagents during the chemical functionalization process.

According to these constraints, the layout of the photonic sensing chip consisted of 20 RRs distributed as schematically shown in Fig. 4.14. The structure consisted of five independent input waveguides, which address the light to four RRs simultaneously, thus using a "WDM approach". The idea of using more than one input waveguide to address the light to the RRs, instead of for example using a single input waveguide and splitting into five waveguides using a MMI or splitter, was carried out for two main reasons. The first one was to add redundancy in the input stage, in such manner of any of the waveguide or rings are not working we still have four more input structures working. The second argument because the final objective of the work within the FP7-INTOPSENS project was to do the read-out of the chip by exciting the five access grating couplers simultaneously using an optical collimator to measure the output signal from all the sensing structures by means of an IR camera, thus being able to interrogate the 20 RRs in parallel.

Regarding the FSR between the resonances of the RR, we need to design a FSR wide enough to avoid the overlap between the resonances of the different RRs coupled to the same waveguide. For that purpose, the dimension of the radius must be as small as possible. The high index contrast that SOI platform exhibits provides a high confinement of the mode in the structures, thus allowing small bend radius. Although, it is possible to fabricate RRs with radius even smaller than 3 μm, the losses increase significantly for these sizes. For that reason, the radius of the bend section of the RRs was selected to be 5 μm, since this is the smaller radius with acceptable bending losses at 1550 nm.

Finally, the parameters of the designed SOI RRs, considering the constrains mentioned above, are listed in Table 4.2.

Parameter	Value
Height	220 nm
Width	500 nm
Radius	5 μm
Racetrack	2 μm
GAP	160 nm

Table 4.2: *Final fabrication parameters of the RRs.*

Concerning the sensing structures, each RR coupled to the same waveguide was fabricated with a slightly different total length in order to provide a different position of the resonances, thus avoiding the overlap among the responses of different sensors. This difference in the total length between RRs was achieved by slightly increasing the radius of the circular section of the racetrack RR (radii of 5 μm, 5.01 μm, 5.02 μm, 5.03 μm were used for each RR). According to expressions given in section 4.2, a theoretical FSR of ~15.7 nm and a separation between the resonances of the RRs of ~2.75 nm was calculated (considering a $n_g \approx 4.3$ [DUL06]). These values of FSR and separation between resonances are sufficient to obtain a clear spectrum, differentiate the response of each RR in the through port, and avoid the overlap between them when sensing shifts are produced (initially, we do not expect to observe shifts higher than 2.5 nm).

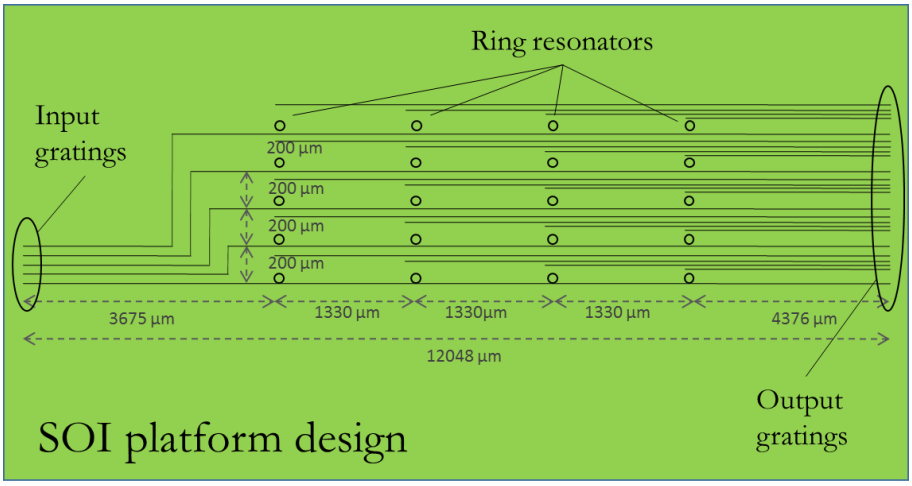

Fig. 4.14: *Schematic illustration of the layout of the photonic chip comprising the RR sensing structures with the access waveguides.*

4.4.2 Fabrication of the ring resonators

The designed photonic sensing chips were fabricated by IMEC (Interuniversity Microelectronic Center) in the frame of the FP7-INTOPSENS project. IMEC possesses a state-of-the-art CMOS compatible production line with the capacity to fabricate nanophotonic structures in SOI technology [IME13]. It is worth noting at this stage that IMEC services can also be accessed through the EC-funded shared-costs nanophotonic fabrication platform ePIXfab [EPI13].

The main difference between the fabrication process described in chapter 3 for the creation of the PhC-based sensing devices using UPV's facilities and the fabrication process used by IMEC is the lithographic technique used for the exposure of the designs. While we used e-beam lithography for the exposure, which is suitable for fast prototyping and offers very high resolutions, IMEC uses UV lithography to transfer the designs to the photoresist [BOG05]. The working

principle for both techniques is schematically depicted in Fig. 4.15. In UV lithography, a predefined mask with the designed structures is placed on top of chip (which is coated with a photoresist) and an illumination system is used to project with UV light the designs of the mask on top of the photoresist, as illustrated in Fig. 4.15b. The main advantage of this method relies on the capacity for exposing the whole design at once, thus obtaining a numerous amount of structures simultaneously. Therefore, a considerable reduction of the cost and the time per fabrication run is achieved, thus being suitable for mass production. As a drawback, UV lithography cannot reach the resolution obtained using e-beam exposure.

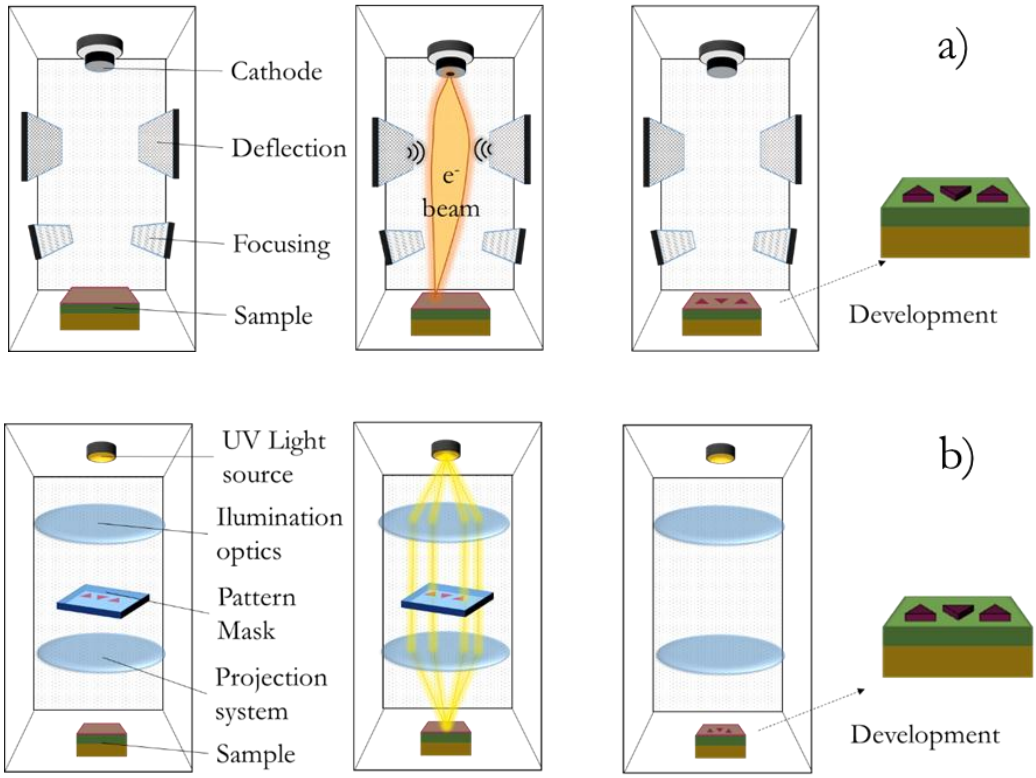

Fig. 4.15: *Schematic explanation of a) the e-beam lithography exposure process and b) the UV lithography exposure system, which allows directly transferring the whole design to the resist at once.*

Several UV light wavelengths can be used in UV lithography in order to transfer the pattern to the photoresist. A standard wavelength employed during many years was 365 nm. However, the minimum feature size that can be obtained using this wavelength is around 600 nm, being optimal for some microelectronic or microphotonic devices, but not for our purposes where minimum features in the range of 100 nm are demanded. Deep UV lithography employs UV light with wavelengths of 248 nm and 193 nm for the exposure, what allows obtaining resolutions below 100 nm and thus smaller structures. Deep UV lithography process is extremely complex and requires the most advance photolithography equipment. However, this method is interesting due to

its compatibility with CMOS processes, what allows the possibility of reusing the standard equipment of the regular processes from microelectronics manufacturing. Fabrication process used by IMEC is based on 193 nm Deep UV lithography.

Briefly, IMEC's fabrication process of our chips begin with a commercial 8" SOI wafer that is coated with a 200 nm layer of photoresist using a spin coater. Then, an antireflective coating is spread on the surface to prevent from undesirable reflections at the interface between the air and the photoresist in order to avoid illumination defects. Afterwards, a completely automated machine illuminates the photoresist with the pattern previously designed with the structures and it is replicated across the wafer by varying the exposure conditions. After the lithographic process, the wafer is introduced to a post-exposure bake, where the photoresist is also developed. In order to transfer the structures to the silicon material, a dry etching process is carried out using the resist as a mask. This step is optimized in order to reduce the roughness of the structures, thus minimizing the losses. The fabrication process is then finished with the resist removal and cleaning the surface using DIW and nitrogen drying.

4.5 Experimental set-up

A different set-up to that previously used for the characterization of the PhC-based sensors was used to measure RR-based sensors. While both have an identical objective, i.e., measuring continuously the spectrum of the photonic structures during the sensing process, there are three main differences between them. First, the light coupling to the chip was carried out vertically by means of grating couplers. Second, instead of sweeping the spectrum using a tunable source at the input and a power meter at the output, now we employed a broadband light source at the input and an optical Spectrum Analyser (OSA) at the output. And third, we employed a custom polydimethylsiloxane (PDMS) microfluidic flowcell to deliver the liquids to all the sensors within the chip instead of the metallic flowcell.

In this section, we will first describe the new optical interrogation set-up, including the vertical coupling using grating structures and the new custom software for the automation of the experimental assays. Then, we will describe in more detail the new microfluidic sample delivery system, including the channel fabrication using PDMS.

4.5.1 Optical interrogation

As previously introduced, in this new experimental set-up we have used a vertical coupling scheme for the interrogation of the photonic sensing structures. Fig. 4.16 schematically illustrates

the light coupling to/from a photonic waveguide by means of grating couplers. Grating coupling methods are extensively used for coupling light to integrated photonic devices [TAI04, LAE07]. The structure consists of a periodic modulation of the refractive index along the waveguide direction and they are typically fabricated by creating several trenches perpendicularly to the direction of propagation. The Bragg condition of the grating is accomplished when the light beam illuminates it with a certain angle of incidence and thus an intensity transference occurs from the fiber mode to the guided mode of the optical waveguide (or vice versa).

Among the advantages of vertical coupling compared to horizontal coupling, the main ones are at that it offers a higher alignment tolerance (making it suitable for fast and stable measurements), the coupling efficiency is relatively higher (usually above 30%), and it does not require employing lensed fibers (which are significantly more expensive than standard fibers). On the other hand, grating couplers exhibit a limited bandwidth (tens of nm), whereas horizontal coupling permits to couple a larger bandwidth (hundreds of nm). However, this limitation does not really affect to our experiments since we usually use a typical scanning span smaller than 30 nm. Other issue of grating couplers is their high polarization selectivity; due to the elevated birefringence of high index contrast 1D grating structures, the effective index of the periodic modulation is significantly different for each polarization, leading to a different Bragg condition for TE and TM. In our designs, we considered TE polarization for the RR and therefore the gratings were optimized for it. The gratings we employed in the input/output waveguides were designed to exhibit a maximum coupling efficiency around 1550 nm when the incident angle is 10º respect to the vertical axis of the chip. Physically, the gratings had a depth of 70 nm, a period of 630 nm, a duty cycle of 50 %, and they were created onto 10 μm-wide access waveguides.

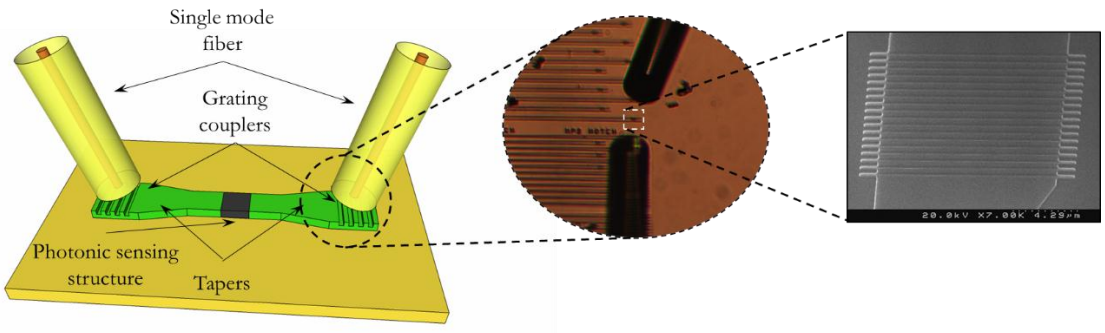

Fig. 4.16: *Schematic illustration of the coupling to the photonic chip using grating couplers.*

For the characterization, the chip was placed on a holder positioned in a 2-axis translation stage from Newport, and the access fibers were aligned with the access grating couplers of the chip using a 3-axis translation stage from Thorlabs. The high tolerance of grating couplers permits to align the fibers in an easy manner (only 1 dB loss increase for ±2 μm alignment variation) and to maintain a good alignment for hours. In order to visualize the position of the fibers during the alignment process, we employed a 3 megapixel camera (Moticam) connected to a microscope. All these elements were placed in an isolated optical bench in order to reduce the vibrations that can interfere in the measurement, as shown in Fig. 4.17.

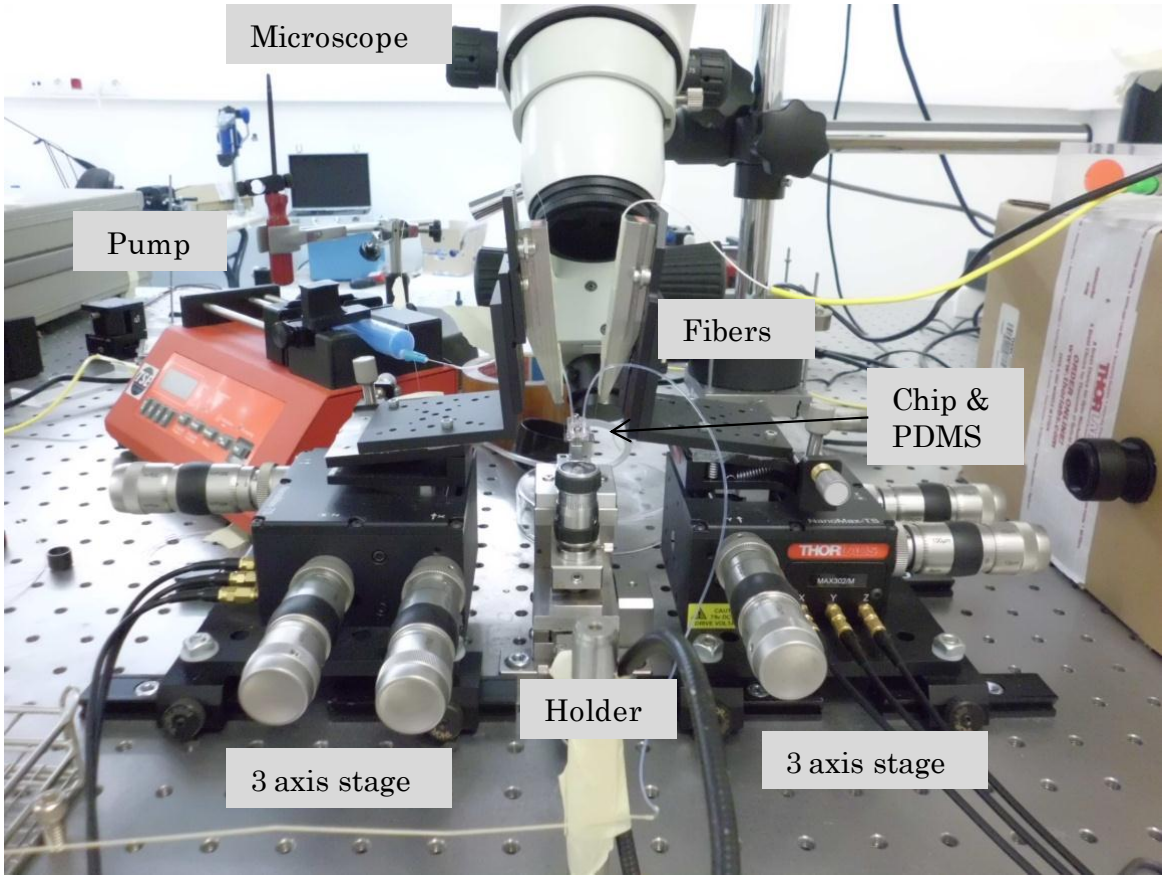

***Fig. 4.17**: Picture of the optical experimental set-up with the light coupling through grating couplers.*

Once the chip is placed on the optical setup and fibers have been aligned with it, light from a superluminescent diode (SLD, Covega SLD1005S) is coupled to the chip. A SLD is a broadband source with an optical bandwidth of 50 nm centered in 1550 nm. Since grating couplers used for coupling were designed for TE polarization, input light was TE-polarized using a polarization controller in order to assure the maximum power coupling. Light coming out from the photonic chip is divided using a fiber 10-90 directional coupler. The 10% arm was connected to a power meter (Newport 1931-C with 918D-IR-OD1 detector) in order to monitor the output power during

the alignment process, and the 90% arm was connected to an OSA to acquire the spectrum of the photonic sensing structures.

The measured spectra from the OSA were collected by means of a GPIB acquisition data instrumentation and a LabVIEW customized program was developed in order to continuously scan the spectrum of the biosensing structures. The screenshot of Fig. 4.18 correspond to the user interface of the dedicated LabVIEW program employed to measure the RRs spectrum, in which we can set the wavelength range and the resolution of the OSA in order to perform the continuous measurements. In fact, the LabVIEW program simply receives the sweeping information from the OSA and saves it to a file in the computer, which will be analysed in Matlab in order to make a Lorentzian fitting of the resonances and to determine the evolution of the sensor's response.

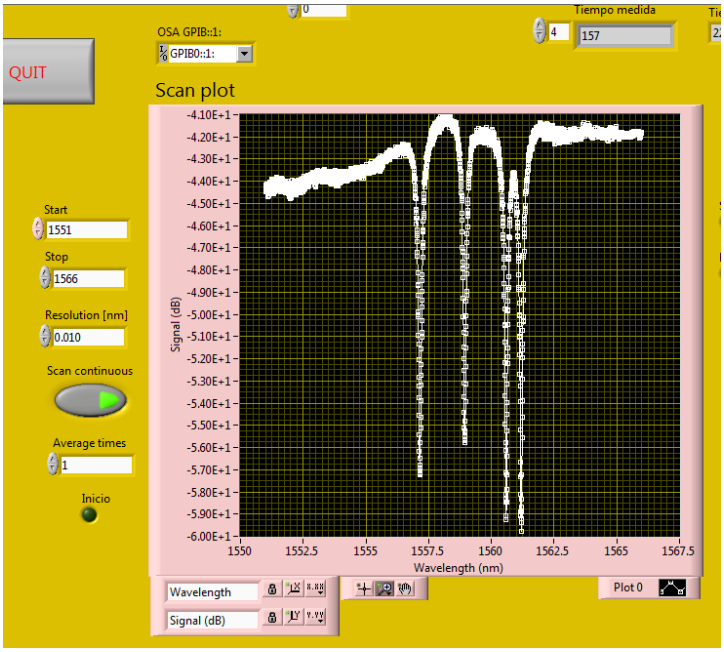

Fig. 4.18: *Screenshot of the user interface of the LabVIEW program used to characterize the integrated photonic sensors. Several measurement parameters can be modified from the computer.*

4.5.2 Microfluidic delivery system based on PDMS

In the PhC-based sensors approach, we employed a relatively large metallic flowcell that flooded a huge area over the chip. However, this large cavity size implies higher sample consumption and the appearance of several non-desired effects such as curls, non-homogeneous flow or mixing, which need to be avoided in order to obtain a cleaner measure. Therefore, it is desirable to reduce the size of the fluid delivery system.

The alternative to the metallic cavity was to implement the fluidic architecture using a common material employed for the fabrication of microfluidic systems, the polydimethylsiloxane (PDMS) [AND00, CHE09]. PDMS is an elastomer that has the ability to adopt the shape of the container after curing, what allows to easily fabricate the microfluidic structures by soft lithography with excellent result and obtaining small features. Additionally, this material exhibits other interesting properties such as its biocompatibility, low cost and production easiness. In addition, it is transparent at visible wavelengths, what makes possible to observe the evolution of the flow along the microchannel and detect any defect such as leakage or obstructions.

The fabrication of the PDMS microchannels consists of two parts: the development of the master mould and the transference of the designs to PDMS. The master mould is fabricated in a silicon wafer by patterning the microchannels in SU8 polymer by standard UV lithography process. In our case, we used a 50 μm-thick layer of SU8, what will lead to 50 μm-height microfluidic structures in the PDMS. For the transference of the designs to PDMS, first a mixture combining PDMS elastomer and curing agent in a ratio of 10:1 in weight is blended. This mixture, which is highly viscous, is degassed using a vacuum chamber in order to remove the bubbles within the PDMS, since they may produce leakage or the entrance of air into the final microfluidic channel. Then, the master mould is covered with the PDMS mixture, degassed again in a vacuum chamber, and cured in an oven at 100º C during 1 hour. One of the advantages of this soft lithography process is its simplicity and the possibility to fabricate many microfluidic elements at the same time as it is shown in Fig. 4.19, besides the possibility to reuse the master mould several times for fabricating more microchannels. Once the elastomer is solid, it is diced using a scalper and the port accesses are made using a hole punch in order to insert the Teflon tubing used to pump the liquids into the microfluidic channel.

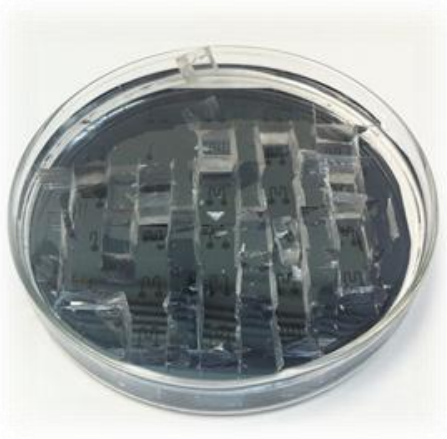

Fig. 4.19: *Fabrication of the microchannels in PDMS material using the soft lithography technique. Many structures can be created in a single process.*

Since our objective was simply to the deliver the liquid samples to the photonic sensing structures in a proper way without developing any complex fluidic preparation, the microfluidic architecture was designed to be as simple as possible. According to this, two flowcell approaches were finally developed and tested: a cavity with two access ports and a zigzag channel, which are shown in Fig. 4.20. The mould of the cavity flowcell was designed and fabricated by KTH, while the mould for the zigzag flowcell was carried out by Gent University, in both cases in the frame of the FP7-INTOPSENS project.

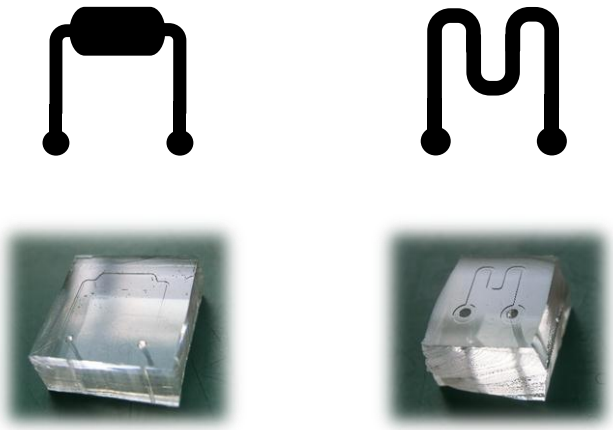

Fig. 4.20: *(Top) Layouts of the microfluidic structures used in the experiments and (bottom) real implementation of these designs in PDMS with a channels height of 50 µm. (Left) Microfluidic cavity developed in collaboration with KTH and (right) zigzag microchannel developed in collaboration with Gent University.*

In order to place the flowcell on top of the chip to deliver the fluids to the sensing structures, we employed two strategies according to the microfluidic design. For the case of the microfluidic cavity, since it provides a high placement tolerance because of the extensive area that it covers, we placed the PDMS piece manually on top of the chip. On the other hand, for the case of the zigzag design, since the channel is 400 µm-wide, we required of a proper equipment to align the channel with the sensing structures. In this case, a flip chip machine (Finetech) with an alignment tolerance of few microns was employed to accurately place the PDMS piece on top of the chip with the microchannels aligned with the array of sensors. The combination of the chip with the microfluidics was then placed on the holder of the optical set-up as illustrated in Fig. 4.21, where it will be interrogated. The assembled chip was clamped using a PMMA piece with two screws in order to obtain a perfect sealing of the channel. Finally, the tubes were inserted in the input and output ports of the PDMS microfluidic system and connected to the syringe pump and to the fluids to be dispensed.

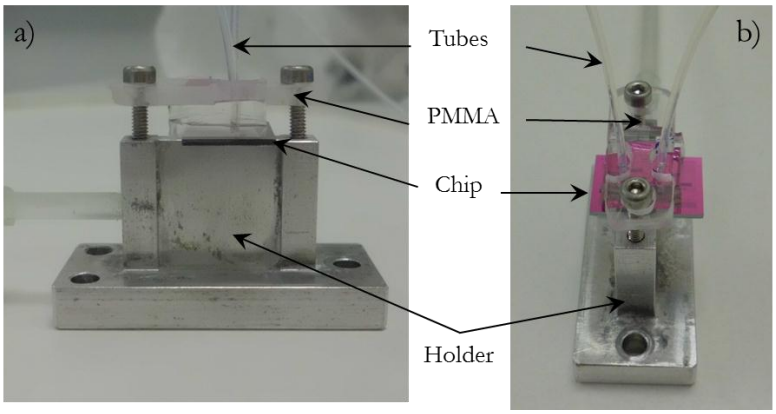

Fig. 4.21: *Photography of the holder with the microfluidic channels. a) Lateral view. b) Top view.*

A study comparing the operation of both microfluidic designs was carried out in order to select the one with the better performance. By using a camera, we monitored the distribution and the behaviour of the liquid flow inside the microfluidic structures. Two examples are shown in Fig. 4.22. We can observe that the cavity-based architecture exhibited a non-homogeneous delivery, what led to the creation of bubbles and empty areas, as shown in Fig. 4.22a, thus making that some of the sensing structures were not in contact with the aqueous sample. This behaviour was observed for different flow rates and different types of fluid. This non-uniform volume distribution may be caused due to the deformation of the PDMS due to the pressure variation inside the cavity. On the other hand, the zigzag-based architecture exhibited a constant flow with no leakage and homogeneous delivery. Therefore, we finally decided to continue the experiments with microfluidic devices based on the zigzag channel.

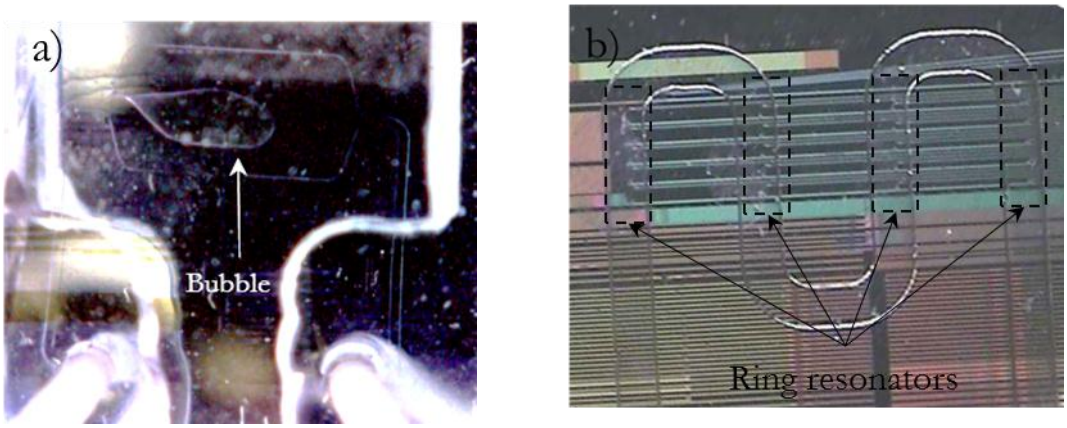

Fig. 4.22: *Flow tests using both microfluidic layouts. a) The cavity structure exhibited a non-uniform liquid flow, while b) the zigzag microchannel offered a stable and uniform liquid flow covering all the sensing structures.*

For the biosensing experiments, the syringe pump was set to a constant flow rate during the whole experiment. As previously indicated in chapter 3, for the experimental set-up used for the PhC-based sensing structures, we worked with the syringe pump in withdraw mode in order to ease the change of the liquid to be flowed and to have a higher stability in the flow. But, now, instead of manually changing the liquids to be flowed over the sensing structures, we employed a multiposition automated switch with an electrical actuator that permits to change from 10 vessels to a common port as shown in Fig. 4.23. The automated switch was controlled via our LabVIEW program by means of a serial communication port connected to the computer. Therefore, our experiments are fully automatized, thus avoiding any human interference in the experimental procedure: once the protocol indicating the order and the time lapse for the flow of each reagent is programmed in the software, the main program synchronizes the automatic valve, the data acquisition from the OSA and the visualization of the spectral response. Fig. 4.24 schematically depicts the whole set-up (optical and fluidic) with the elements comprising it.

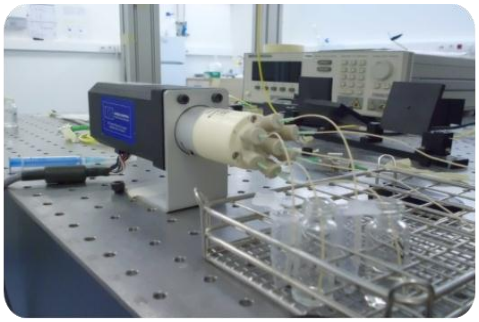

Fig. 4.23: *Automatic switch port employed for change among different liquids during the measurement.*

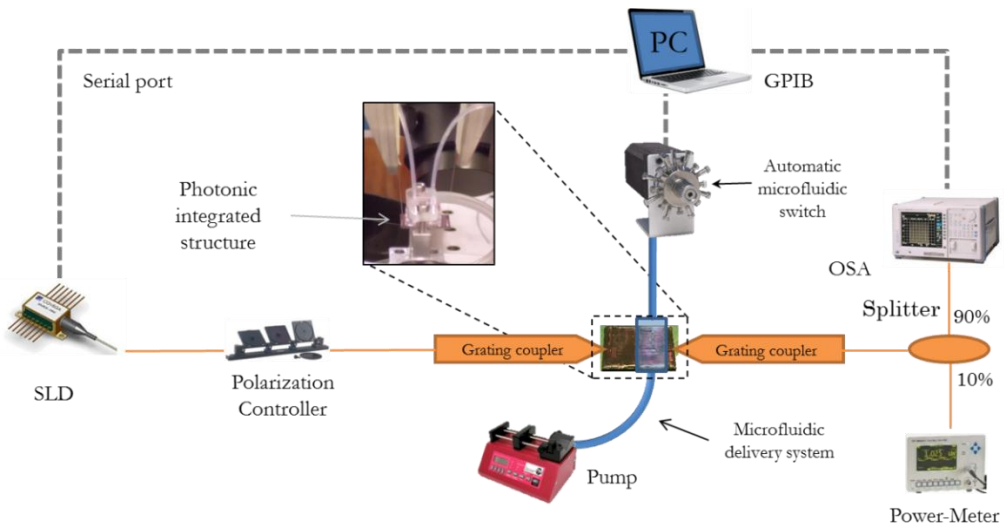

Fig. 4.24: *Schematic representation of the experimental set-up, including the optical and fluidic sections. Blue color represents the microfluidic system, orange the optical path, and dashed grey line the control of the computer.*

4.6 Experimental sensing results using RR

The development of a complete sensing platform requires of numerous experiments and examinations in order to obtain acceptable and reliable results. This has been the case of this PhD work, where a large amount of experiments were carried out in order to optimize the experimental methods and protocols to be applied for the proper performance of our RR-based biosensors. In this section, we will present a compendium of the most relevant experiments and results that became decisive for the final development of the photonic biosensing structures.

Although the sensors based on photonic structures can be applied to a wide range of different applications, as we did for the case of PhC-based sensing structures, we have focused our work on the adaptation of the sensing platform for its use towards antibody sensing (using the BSA-antiBSA pair) and ssDNA sensing. However, since this work was carried out mainly in the frame of the FP7-INTOPSENS project where bacteria identification through the identification of their gene expression was targeted, most of the experiments and efforts were focused on achieving ssDNA hybridization detection using our RR-based sensing structures.

Before experimenting with biological samples, the bulk refractive index sensitivity and detection limit of the photonic sensing platform was measured. Once the ability of the platform to detect refractive index changes was characterized, we used the well-known high affinity molecular couple BSA-antiBSA to study the functionalization procedure for photonic structures using ICPTS, which was optimized in planar structures as described in chapter 2. After the optimization of the molecular attachment using the isocyanate termination of ICPTS, DNA probes were immobilized on the surface to monitor the DNA hybridization using the RR-based sensing platform.

Then, the second selected functionalization strategy based on the use of GOPTS was applied to anchor the receptors to the surface. The versatility of this strategy allowed us to spot the receptors with spatial selectivity determined by its exposure with UV light. In this case, we have only worked in the development of ssDNA sensing experiments using GOPTS-based chemistry.

However, as said at the beginning of this section, in an exhaustive experimental research work not all the results are good neither promising, and many problems arise. For this reason, here we will also show several results from some non-successful experiments in order to explain the main issues observed during the work, and how we proceeded in order to avoid or reduce their influence in the result.

4.6.1 Bulk refractive index sensing

Basic refractive index measurements were carried out in order to obtain the intrinsic sensitivity of the RRs to bulk refractive index variations. Although refractive index sensitivity is not a direct measurement of the biomolecular interaction sensitivity, it allows us to compare with other sensors independently of the technology. Furthermore, during biosensing experiments it is usual to flow different substances, buffers, etc., which may exhibit different refractive indices; by characterizing the bulk refractive index sensitivity, it is possible to compensate the response and remove the bulk effect.

A bare chip without any biomolecular layer was employed for these refractive index sensing experiments. The liquid target was flowed directly in contact with the sensing structures to perform a homogeneous sensing. In order to characterize the RR sensing structures, we flowed over them several dilutions of DIW and sodium chloride (NaCl) with concentrations ranging from 2.5% to 10%. The refractive index of the salt concentration in DIW at 1550 nm follows this equation: $n=1.3173 + 0.17151 \cdot C$, where C represents the salt concentration in % in mass [SU07].

The experiment was carried out at room temperature with a constant flow rate of 20 µl/min. In order to deliver the aqueous solutions to the sensing structures we employed the PDMS structure with the zigzag microchannels. The PDMS-based microfluidic flowcell was previously cleaned with IPA in order to remove any organic residue, then rinsed with copious amounts of DIW and thoroughly air dried.

Fig. 4.25 shows the simultaneous time evolution of two RRs (coupled to the same access waveguide) during the injection of the different DIW-NaCl solutions with different refractive index. Since the position of the resonance depends on the refractive index of the environment, the higher the refractive index of the upper cladding is, the larger the spectral resonance shifts of the RR. Each concentration was flowed over the sensing structures during 10 minutes and DIW was flowed between two different concentrations of salt in order to recover the baseline and to prevent from mixing between concentrations. Since RRs are not identical, they exhibit slightly different responses.

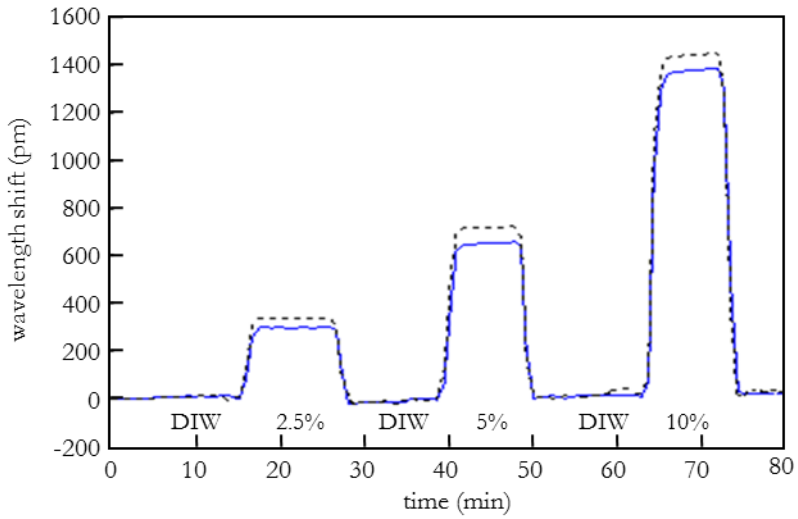

Fig. 4.25: *Successive injections of different DIW-NaCl dilutions with different refractive indices. The shift of the resonances is practically instantaneous.*

By extracting the resonance shift when the concentration was detected and plotting it as function of the refractive index of the medium, we obtain the sensitivity curve shown in Fig. 4.26. The result is a linear dependence on the resonance shift with the refractive index of the solution. The slope value of the regression line represents the bulk sensitivity being 82.78 nm/RIU. The measurement of each concentration is represented with the error bar. Such variations are small enough to point out the remarkable stability of the sensing platform for bulk sensing.

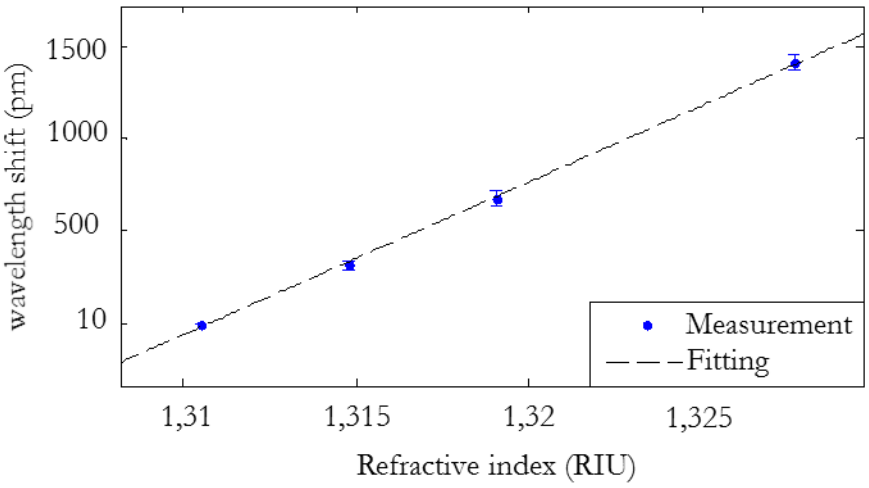

Fig. 4.26: *Sensitivity curve of the RR for refractive index values from 1.31 to 1.33. The slope of the fitting line (dashed line) represents the RR intrinsic sensitivity.*

The detection limit of the structure was also studied. In order to obtain such parameter, it was necessary to calculate the signal noise. The system noise was extracted by obtaining the standard variation of the signal for a continuous and stable flow of DIW. The minimum detectable wavelength shift was estimated to be as low as 1.2 pm, therefore the estimated detection limit of the sensor was $1.44 \cdot 10^{-5}$ RIU which is in the order of reported results for other RR-based sensing structures.

4.6.2 ICPTS-based functionalization experiments

In this section, we will present the results of the experiments performed employing the ICPTS functionalization of the surface. These experiments consisted on antibody sensing experiments and DNA hybridization detection. In addition, we will describe several problems faced during the experiments with this type of functionalization.

4.6.2.1 Antibody sensing

In order to verify the suitability of the platform to perform biosensing experiments we firstly employed the ICPTS-based chemistry, which was previously developed in planar substrates obtaining favourable results as presented in chapters 2 and 3, prior its adaptation to the RR-based photonic sensing structures. BSA molecules were attached to the chip by means of an ICPTS layer and then we flowed its high affinity couple antiBSA in order to monitor the recognition between these two molecules and to verify the appropriateness of this platform for biosensing purposes.

The functionalization procedure started immersing the chip in piranha solution during 30 minutes in order to clean the chip and to remove any organic residue on the surface. Then the chip with the integrated silicon RRs was activated by depositing an ICPTS layer on the surface using CVD technique during 2 hours. Afterwards, RR sensors were spotted with BSA protein at 25 μg/ml and incubated during 70 minutes. Finally the surface was blocked with ethanolamine 0.1 M during 30 minutes.

Then, antiBSA sensing experiments were carried out by consecutively flowing several dilutions of antiBSA, ranging from 10 to 1000 ng/ml in PBS 1x. The position of the resonances of the RRs was recorded during 10 minutes and the temporal evolution of their relative shift plotted, as shown in Fig. 4.27. As we can see in the graph, the slope and the shift of the signal vary depending of the concentration of antiBSA flowed over the chip. However, we can observe that the sensor does not respond in this experiment to an antiBSA concentration of 10 ng/ml (a negative drift is even observed), what indicates that the detection limit of this device is above 10 ng/ml. Additionally, it is noteworthy to mention the fast response of the sensing structure, which is able to differentiate diverse antiBSA concentrations in less than 10 minutes.

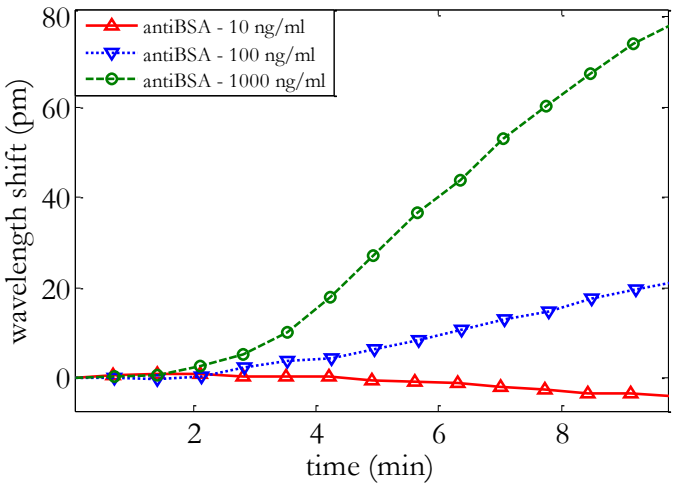

Fig. 4.27: *Time evolution of the RRs response for BSA-antiBSA interaction by varying the concentration of the antiBSA flowed.*

To study the specificity of the recognition layer, we functionalized another chip following the same protocol described previously, but in this case, we flowed several concentrations of antiBSA and antiDIG. The affinity of antiDIG molecules towards BSA receptors attached to the surface is practically negligible, thus no shift should be observed when the antiDIG is flowed over the chip. Fig. 4.28 shows the response of the chip for two concentrations of antiBSA and one concentration of antiDIG. We can observe that the two concentrations of antiBSA produce a significant shift due to the binding to the BSA-coated surface of the chip (net shifts of 60 pm and 120 pm are observed for concentrations of antiBSA of 1 ng/ml and 10 ng/ml, respectively). While, an almost negligible shift is observed for a concentration of 10 ng/ml of antiDIG (a shift of only ~4 pm is observed, what is more than 25 times lower than for the same concentration of antiBSA). The noise level was calculated to be as low as ~1.2 pm during the signal stabilization.

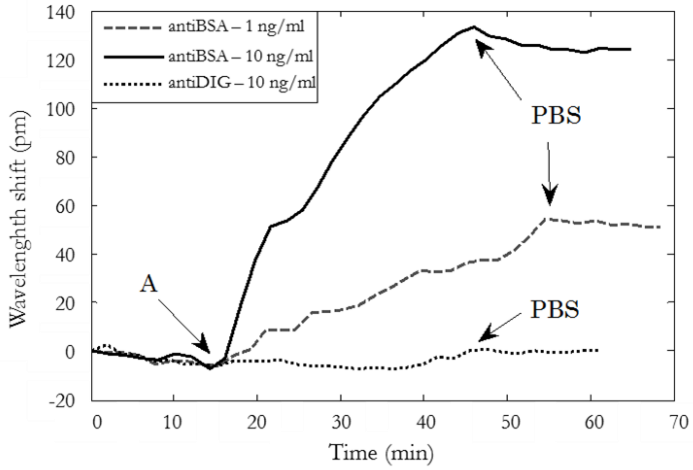

Fig. 4.28: *Time evolution of the RRs response for BSA-antiBSA and BSA-antiDIG interaction. The point A represents the instant when the target analyte reaches the sensor surface.*

It is important to note the difference of sensitivity between the first reported experiment with BSA and the second one. This is explained by the continuous enhancement that we were achieving during the course of our work (i.e., the second experiment was carried out when the optimization process of the experimental procedures was at a more advanced stage).

4.6.2.2 DNA sensing

The use of DNA as selective recognition element in a biosensor is an intriguing and exciting area in analytical chemistry due to the large number of potential applications, in which can be implemented. As it has been previously mentioned, the main goal of the FP7-INTOPSENS project, in which part of the work carried out in this PhD thesis was framed, is bacteria identification by detecting several specific DNA strains. Therefore, we have worked in adapting the RR-based sensing platform for the specific label-free detection of DNA strands. To this aim, we firstly employed ICPTS-based functionalization, which allows directly attaching aminated ssDNA probes to its isocyanate groups. However, instead of directly attaching these aminated ssDNA probes to the ICPTS in the chip, in these experiments we anchored the DNA probes on its hybridized form (i.e., dsDNA), and then they were dehybridized leaving only the ssDNA probe with better conditions for the hybridization. Unlike the functionalization of the surface that we employed for PhC in which the surface was covered with streptavidin, in this approach we anchor directly the aminated probes to the recognition layer by using the isocyanate moieties of the surface. In this way, we obtained two advantages: the DNA strands were closer to the surface due to the direct attachment, thus enhancing the sensitivity of the sensing device and the functionalization process was carried out only in one step, thus reducing the preparation time.

The anchoring of the DNA strands was carried out using a similar protocol to that described in chapter 2. Concisely, the chip was cleaned with piranha solution during 30 minutes at 50ºC and immediately the structures were silanized by means of chemical vapour deposition (CVD) during 2 hours to ensure a homogeneous coverage with the ICPTS. Then, a rinse was performed to remove the unbound material using 2-propanol. After that, the chip was cured inside the oven at 150ºC during 10 minutes in order to remove the humidity. Then, the chip was kept in a dry environment before attaching the probes to the RRs. The probes were firstly hybridized "off-line" with the complementary strands and afterwards, these dilutions were used to functionalize the RRs. In these experiments, the four RR sensors were functionalized with 1 μM dsDNA. Afterwards, the chips were incubated during 70 minutes at room temperature in a humid chamber to prevent the drop from evaporation. Later, the chip was cleaned with PBS-T (PBS Tween) and air dried. In order to block the residual active ICPTS moieties to avoid the non-specific sensing, a drop of 0.1 M of ethanolamine was drop on the rings and incubated. Finally, the dsDNA strands were dehybridized rinsing with ethanol and drying. From that moment on, the chip was ready to be measured.

Before assembling the chip with the microfluidic system, the tubes and the PDMS microchannels were blocked in order to prevent from adsorption of the DNA in the fluidic system, what would reduce significantly the performance of the sensing device. To this aim, a concentration of 25 μg/ml of BSA was flowed during 1 hour along the tubes and the PDMS microchannels to assure a proper blockage of the microfluidic elements. Then, the system was rinsed with DIW in order to remove the molecules that were not bounded to the surface of the microfluidic elements, leaving them ready to be used.

The experiment started flowing SSC (saline sodium citrate) over the chip until a stable baseline was obtained. Then, the first concentration of complementary ssDNA injected in the system was 100 nM in SSC. Fig. 4.29 shows how the RRs resonances shift to higher wavelengths when the complementary DNA reaches the sensors and hybridizes with the capture probes,. The fact that each ring response undergoes a slightly different shift is mainly due to the different surface coverage of the DNA probes. However, it is remarkable that this difference was very slight and the initial slope for all the RRs was rather similar, what indicates that the rate of hybridization was comparable in all the RRs. The complementary ssDNA was flowed over the RRs during 30 minutes, and then SSC was flowed again. A permanent shift of the response from 110 pm to 130 pm was observed, what confirmed the hybridization of the complementary strand to the sensor surface.

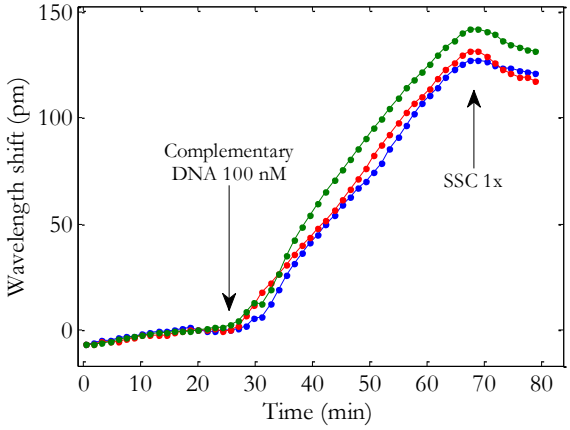

Fig. 4.29: *Response of the four RR sensors to the complementary ssDNA with a concentration of 100 nM.*

After the hybridization of the first concentration, the sensors were regenerated by dehybridizing the DNA probes with an injection of 80% ethanol in DIW during 5 minutes. The covalent attachment between the aminated probe and the ICPTS was strong enough to keep the probes attached to the surface. This dehybridization strategy allowed us to perform several DNA detections using the same chip. SSC was flowed again to obtain a baseline signal, and subsequently a complementary ssDNA concentration of 200 nM was pumped in the system. Fig. 4.30 shows the response of the sensors to this second concentration of ssDNA. Since the concentration of DNA is higher, the hybridization rate is faster and as a result, the slope of the response is also higher. Moreover, we can observe the saturation of the sensors response after ~10 minutes of complementary ssDNA flow, indicating that all the probes on the surface were hybridized and the rate of dehybridization was too low. After 20 minutes of the injection, SSC was flowed again and a backshift in the response was observed which might be caused by ssDNA strands that were not properly hybridized with the probes but were trapped among them. In addition, remark again the high similarity between the responses of the four RR sensors in this experiment.

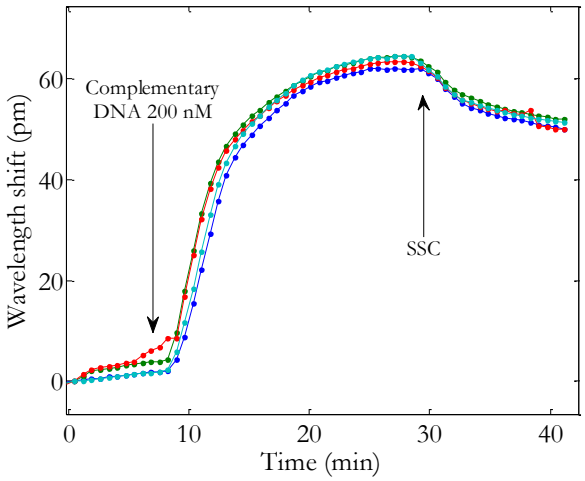

Fig. 4.30: *Response of the four RR sensors to the complementary ssDNA with a concentration of 200 nM*

Finally, in order to validate the sensor specificity we flowed one concentration of non-complementary ssDNA over the functionalized rings. As shown in Fig. 4.31, no significant shift due to the non-complementary strand was observed. In addition, Fig. 4.32 compares the initial slope of the three samples. The bars represent the average of the value of the initial slope of the RR with the variation between rings. We observe that the initial slope depends on the concentration of the complementary DNA and moreover, the non-complementary DNA did not cause any shift to the RR resonances confirming the high specificity of the sensor for the label-free detection of DNA hybridization.

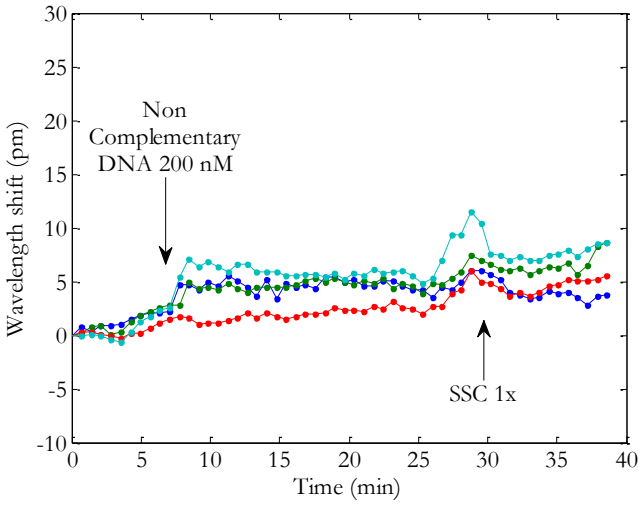

Fig. 4.31: *Time evolution of the response of the RR while flowing non-complementary DNA strands.*

We repeated this DNA sensing experiment with a new sensing chip, but instead of immobilizing the aminated dsDNA probes by spotting and incubated them, this time they were anchored to the isocyanate terminations on the surface by flowing them over the sensor. For this purpose, the surface of the chip was activated with ICPTS identically as performed previously. Afterwards the chip was assembled and mounted on the experimental set-up with the PDMS microchannels, and aminated dsDNA was subsequently flowed during 30 minutes. Finally, ethanol at 80 % in DIW was flowed in order to dehybridized the dsDNA strands and left only the ssDNA probes.

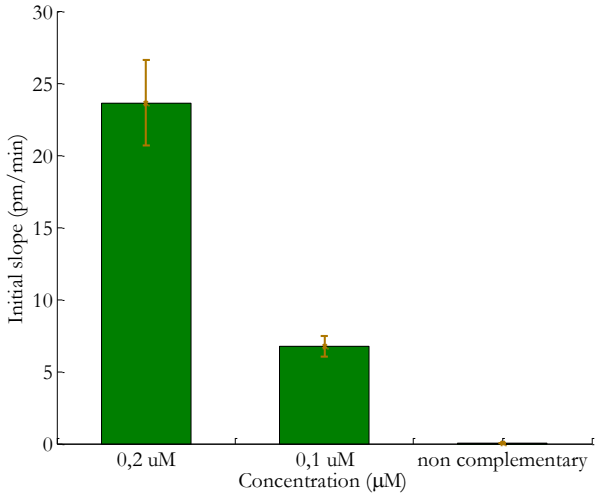

Fig. 4.32: *Comparative study of the initial slope of the hybridization sensing for different DNA concentration after 25 minutes of flow.*

The hybridization experiment consisted on flowing one concentration of complementary ssDNA (200 nM). Fig. 4.33 shows the response of the RR sensors to ssDNA hybridization. Note that in this experiment, the complementary ssDNA was diluted in SSC while the baseline was obtained using PBS, what provokes a bulk refractive index shift when the changes are produced (e.g., at minute 40). This effect may be easily removed by using reference rings. We can observe in the sensors response that the initial slope when the ssDNA reaches the sensors is very high and that all the RRs almost immediately reach a quasi-saturation point indicating that almost all the ssDNA probes are occupied. The higher sensitivity compared with the previous experiment can be attributed to a better surface coverage, which is achieved by flowing on-line the dsDNA probes instead of incubating them off-line.

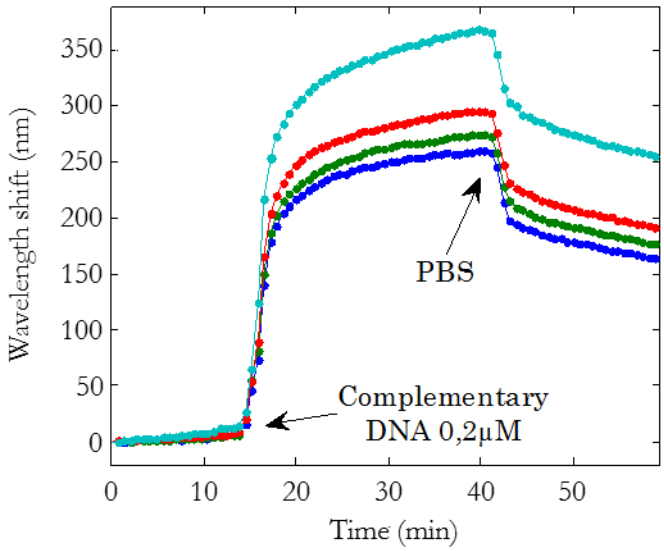

Fig. 4.33: *Response of the four RR sensors to the complementary ssDNA with a concentration of 200 nM. In this case, the dsDNA probes were immobilized by flowing them over the chip. Note that the complementary ssDNA was diluted in SSC, while the baseline was obtained using PBS.*

4.6.2.3 Other experimental issues

As previously mentioned, during the implementation of an experimental protocol, numerous situations where the experiments do not provide the expected results or several unexpected problems that ruin the investigation can appear. In this section, we will discuss some of the most common issues that we have observed during the realization of the experiments and how they influenced in the result. Some of them have an easier explanation than others, which need to be further studied.

Stabilization time

One of the first situations that need to be faced is to determine when the experimental protocol can be started. Clearly, one advantage of photonic sensors against other technologies is their ability to perform a fast detection due to their high sensitivity and the possibility to perform a label-free detection. However, when we start an experiment with functionalized chips that are not completely hydrophilic, the first thing that we needed to do is to start flowing the liquid over the sensing structures. The change in the medium surrounding the sensing structures from air to liquid take some time until the liquid completely fills all the corners and nooks and completely follows the shape of the structures due to the superficial tension between the liquid and the structure. Therefore, the signal will not reach a stable position immediately, but it will take a certain time depending on how the liquid fills the channel and covers the surface of the chip. Fig. 4.34 shows the wavelength shift response of several RRs for two different chips immediately after the initial

pump of the buffer in the channels, where a significant initial drift is observed even after 150 minutes of experiment due to the progressive coverage of the surface.

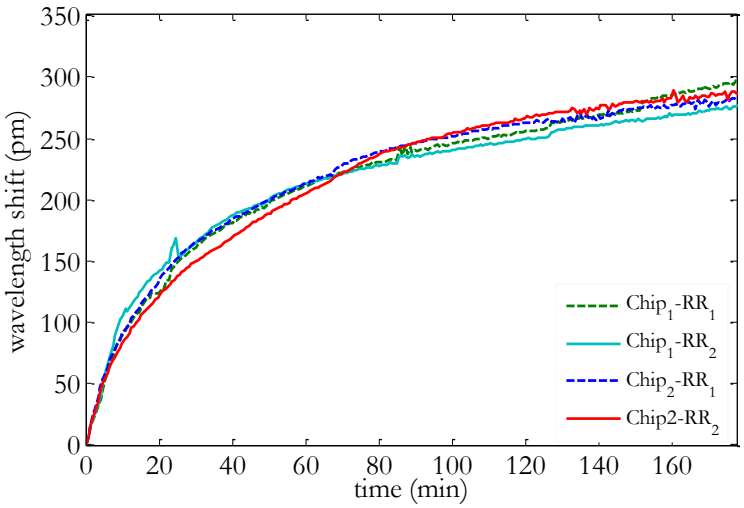

Fig. 4.34: *Time evolution of the resonance shift of RR sensing structures immediately after starting the pump of the SSC over them. The shift evolution for two RRs from two different chips is depicted.*

As previously commented, this effect is probably induced by the kinetic coverage of the liquid over the sensing surfaces and how it fills the channels. By water contact angle analysis, we determined that the surfaces exhibited a certain level of hydrophobicity after the functionalization process, what difficult to fill up with the liquid all the small bends and corners of the photonic structure. To tackle this issue we worked in two alternatives. The first solution was to begin the experiment flowing a solvent that does not cause the biolayer denaturalization during a brief lapse of time. In such way, it is possible to reduce the superficial tension provoked by the cohesive forces, thus favouring the spread of the aqueous sample over the structures. However, in cases where no solvents can be employed in order to keep the biological functionality, the solution was to flow the initial buffer with an increased flow rate until a stable signal was observed. Although any of these alternatives is feasible, the resonances position must be monitored in order to know when the signal is stable in order to start with the experimental protocol.

Signal drift

Other issue that we have usually observed during the experiments was a drift of the resonances even when a homogeneous solution was continuously flowing. Among all the experiments that have been carried out during these years, we have both observed positive and negative drifts. Several causes may provoke these drifts in the response of the photonic sensing structures; among them, the most usual are mass coverage variations and temperature fluctuations.

One of the main reasons of the drift in the sensors response is probably the deposition of matter over the structures. Generally, the buffers that are used to carry out sensing experiments contain a significant amount salts (e.g., PBS 1x contains among other ingredients 8 g of salt per litre), therefore sedimentation of salts can easily occur. Fig. 4.35 shows a SEM picture of a RR in which numerous particles with regular sizes that may be salt crystals can be observed. Therefore, an increment of the matter being deposited over the photonic structures will lead to a positive drift of the sensors response. On the other hand, a negative drift will correspond to the removal of this previously deposited matter from the structure of the RR.

Fig. 4.35: *SEM picture of a RR after an assay where PBS and SSC buffers were employed. The deposition of salt particles on the chip surface provokes a variation of the position of the resonances.*

In order to reduce the drift caused by matter deposition, we determined that higher flow rates might be used and that the liquid flow should not be stopped at any time of the experiment in order to prevent the "landing" of the particles over the photonic sensors. Moreover, it is also desirable to employ buffers with lower salt concentration, such as PBS 0.1x instead PBS 1x, to reduce the salt deposition on the sensing structures.

Concerning temperature influence, a temperature increment will induce a positive drift whereas a decrement will cause a negative drift. A thorough study about the influence of temperature on the sensors response will be introduced in the next section.

Temperature variation

Several properties of the materials may change with the temperature, and refractive index is one of them. For instance the silicon thermo-optic coefficient is 1.8×10^{-4}/K at 1550 nm, and that for the silicon oxide is $1.2 \cdot 10^{-5}$/K [KOM12]. On the other hand, the temperature of the aqueous solution also influences the RR response. However, the thermo-optic coefficient for water has the opposite sign, being $-0.8 \cdot 10^{-4}$/K ; therefore, it will partly compensate the silicon and the silicon oxide variations [KIM12].

In order to study how temperature variations affect to the signal, we placed a Peltier element in contact with the metallic holder of the chip, what allowed us to modify the temperature of the sensor while monitoring the position of the resonances simultaneously. Fig. 4.36a shows the time evolution of the spectral shift of the resonance versus the Peltier temperature, while DIW at room temperature was continuously flowed over the sensors. The temperature sensitivity curve of the sensors is represented in Fig. 4.36b. We calculated the sensor temperature sensitivity obtaining 69.8 pm/Cº. Taking into account the noise level that we obtained for the refractive index experiments (1.2 pm), can estimate that temperature variations simply above 0.017ºC will have an influence over the experiment.

Therefore, temperature variations may influence the response of the sensing structures. However, it is worth to note that significant temperature-related variations were not observed in our sensing system despite not using any temperature compensation mechanism. However, the performance of the sensing system could be improved by implementing mainly two temperature compensation strategies. The first one is based on the use of a Peltier-based temperature control system in the holder of the chip in order to maintain the temperature constant along the whole experiment. The second strategy is based on including reference structures in the photonic chips so that they are isolated from the target sample and allow to compensate the non-sensing related spectral shifts provoked by temperature variations. Therefore, future improvements of our photonic sensing systems will consider the implementation of these two temperature compensation strategies.

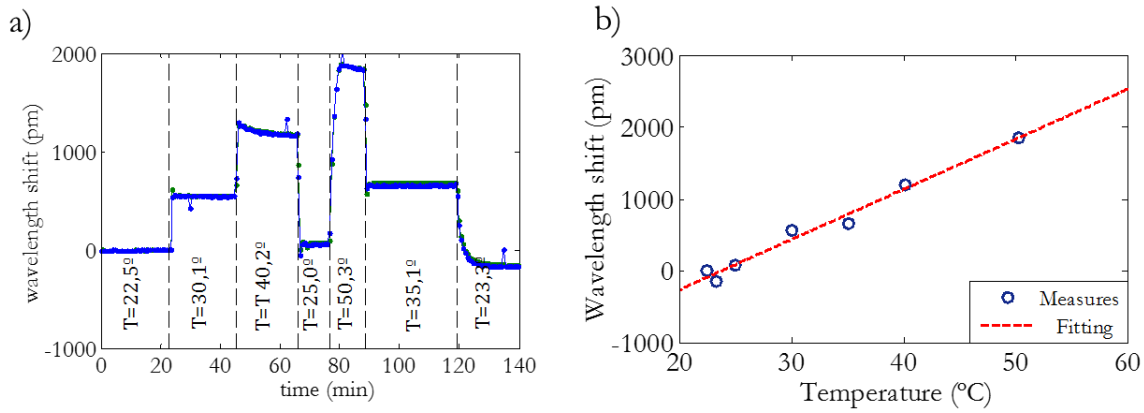

***Fig. 4.36**: a) Time evolution of the spectral shift of the RRs resonances when different temperatures are applied to the chip holder. b) Temperature sensitivity curve of the chip, where the slope of the line is 69.8 pm/Cº.*

Appearance of microbubbles in the channels

Probably, one of the main enemies during the development of any type of sensor for the analysis of liquid samples is the appearance of bubbles during the experiment realization. Unlike the signal drift or temperature issues, this problem has a higher degree of randomness, so it is not straightforward to compensate its effects.

As previously described, the evanescent field of the optical RRs is highly sensitive to local refractive index variations. Therefore, any tiny air bubble that passes nearby the structures or that is adhered to them will produce a strong perturbation of the optical wave that may significantly alter the sensor response. Unfortunately, the formation and accumulation of microbubbles in PDMS-based microfluidic devices is a frequent phenomenon, which is usually related to the connections between the tubes and the PDMS flowcell. A non-completely perfect sealing of the PDMS flowcell and the photonic chip, or any slight entrance of air during the change between the liquid samples may cause the entrance of bubbles.

Fig. 4.37 shows the evolution of the resonance position of four RRs in an experiment where issues related with the appearance of bubbles in the microfluidic system were significant. Despite the signal trend of the RRs is quite stable (with a slight drift that may be easily removed), a sudden change in the resonances position was measured at certain instants of the measurement. These sudden jumps are provoked by the attachment or the release of air microbubbles from the RR surface. Note that these jumps have random magnitudes. However, they use to be significantly larger than the shifts induced by molecular binding interactions, what makes them easy to identify and remove if they are punctual and isolated. In the case when many sudden jumps produced by air microbubbles are observed, real sensing information might be very difficult to be extracted, thus preventing from a successful development of the experiment.

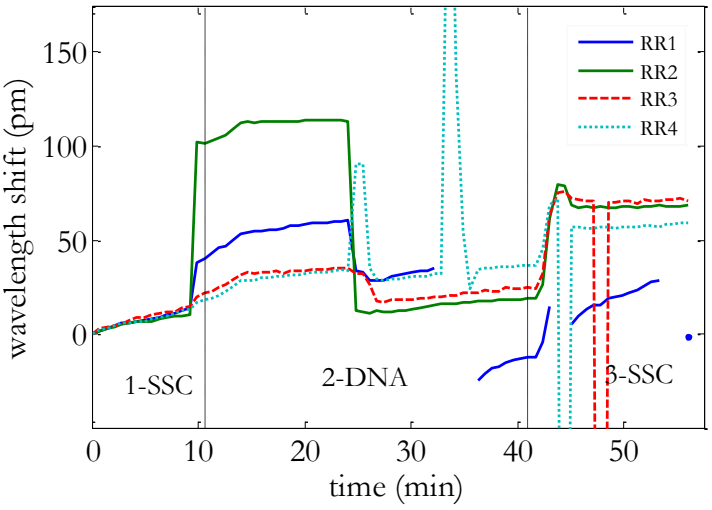

Fig. 4.37: *Example of sensing experiment where several air microbubbles interfered in the measurement. It is observed how the bubbles produce several sudden jumps and variations, significantly difficulting the analysis of the response of the RRs.*

In order to prevent from bubbles formation and reduce their non-desirable effects during the assays, several strategies can be adopted. First, it is important to have a completely hermetic fluidic system in order to avoid the bubble entrance from the interfaces. This can be achieved either by tightly clamping the PDMS flowcell to the chip, as we have done in our experiments, or by using oxygen plasma to stick the PDMS flowcell to the silicon surface of the chip, what has the drawback of the preventing from a further reuse of the sensing chip or for its physical characterization. Another important aspect to be taken into account is the need to degas the liquids before using them in the sensing system. Using this method, bubbles were drastically removed and smoother signals were obtained (although bubbles were not 100% completely removed). To our knowledge, there are other more complex solutions based on elements such as PDMS-based bubbling traps; however, since our work was focused on the development of the photonic sensors themselves as well as the experimental protocols, we did not work in the implementation of this kind of solutions due to their high complexity [LOC12].

4.6.3 GOPTS-based functionalization experiments

Although we have validated the feasibility of the ICPTS chemistry for the development of photonic biosensors that are able to detect antibodies or DNA, many problems arisen for that approach. As described in chapter 2, the isocyanate end of the ICPTS is highly reactive toward nucleophiles and loses its activity in aqueous media, what in many cases has prevented from achieving a successful functionalization of the sensing structures. For this reason, we have studied

other functionalization approach based on GOPTS organosilane, where its terminal epoxy groups are more resistant to the water than the isocyanate groups from ICPTS, thus obtaining a functionalization procedure that is more robust even in humid environments. Furthermore, the covalent coupling between the organosilane and the chip surface for this functionalization strategy can be assisted by UV light exposure, what allows a high spatial selectivity and faster times than traditional immobilization methods based on incubation procedures. In addition, the use of this UV light assisted method to attach the receptors to the sensing structures is characterized for being clean and it exhibited remarkable results, as we will present in this section.

Hereafter, we will introduce the most remarkable results that we have obtained using this UV light assisted GOPTS-based functionalization approach. These experiments have been only focused on the development of a sensing platform for specific detection of ssDNA since it was the objective of the project where the work was framed. Firstly, we will briefly describe the chip functionalization process, which was adapted from chapter 2.

4.6.3.1 Functionalization process

Although the generic GOPTS-based functionalization procedure was already described in chapter 2, herein we will comment the variations that were introduced for the functionalization of the integrated RR-based photonic sensing structures. These variations are mainly related to the incubation times or the reagents concentration.

Firstly, the silicon photonic chips were cleaned in piranha solution during 30 minutes at 50 ºC in order to remove any biological substance from the surface. After that, they were rinsed with DIW and dried under air stream. Subsequently, the chips were completely immersed in a GOPTS solution in toluene at a concentration of 2% in volume during 2 hours to attach the silane molecules to the hydroxyl groups on the surface. The GOPTS molecules that were not attached to the surface were removed by cleaning the chip with 2-propanol and then air-dried. The probes attachment to the RRs was then carried out by spotting a drop of the thiolated ssDNA probe on the silanized surface and then illuminating directly with UV light. Due to the high power of the UV lamp of the lithography equipment that was employed in the optimization for planar structures, the drop with the DNA probes was dried and a non-homogenous coating was obtained, what is not valid for the development of an integrated photonic sensor. For that reason, we carried out the UV light exposure by placing the chips in a humid chamber (created with plastic Petri dishes) and then illuminating with a UV portable lamp at 371 nm that was placed ~ 2 cm above the chip, as shown in Fig. 4.38. The fact of providing less UV light power makes the exposition time longer, being of around 2 hours instead of 10 minutes when using the photolithography equipment. For the development of a multiplexed sensing device, we have the possibility to spot different DNA probes in each of the four RR sensing structures that we can measure in parallel. After the immobilization

of the DNA probes to the GOPTS layer, the chip was rinsed again with PBS-T. In order to block the remaining active epoxy moieties on the surface, 2-mercaptoethanol 0.1 M in PBS was spotted on the chip and illuminated again during 1 hour. Finally, the chip was rinsed to remove the molecules that were not bound to the surface.

Fig. 4.38: *Picture of the UV light exposure during the functionalization of the chip with GOPTS organosilane. Four chips were incubated at the same time to avoid variations in the conditions. The chips were kept in a box to maintain the humidity and the temperature.*

Once the chips were functionalized, they were assembled with the PDMS microchannels following the same procedure that was previously described for the ICPTS-based experiments. Assembled chips were placed on the holder of the experimental set-up in order to carry out the measurements.

4.6.3.2 DNA sensing

Our first objective was to demonstrate the proof-of-principle to perform DNA sensing experiments using the RR photonic sensors with GOPTS-based functionalization. In this first experiment, the chip was functionalized with the procedure mentioned above, where all the RRs were spotted with the same DNA probe.

For this experiment, SSC 1x was used as a buffer and an ethanol solution at 80% was flowed during 5 minutes at the beginning of the experiment in order to increase the surface wettability and reduce the signal stabilization time, as we suggested in the previous section. Then, a stable baseline was obtained for each RR sensor during the flow of SSC 1x buffer, complementary ssDNA with a concentration of 100 nM in SSC 1x was streamed in the system, provoking a shift in the RR response due to the DNA hybridization as shown in Fig. 4.39. However, the variation of the resonances of each RR was remarkably different. This difference in the sensitivity, which was

also observed in previous antibody or DNA sensing experiments, indicates that there is a non-homogeneous coating of the surface with the capture probes after the functionalization process. This effect is probably due to the spotting step, where a single drop is placed on top of the chip coating all the sensors. The use of a single larger drop probably makes that the probes concentration is not well controlled and becomes different depending on the sensor position inside the drop, thus leading to different density coverage.

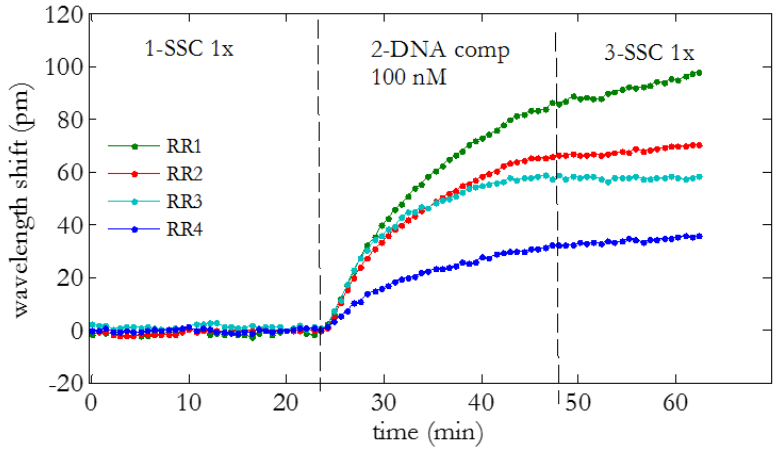

Fig. 4.39: *Hybridization detection of the complementary ssDNA with the probes attached to the surface of the RRs, leading to a permanent shift.*

In order to regenerate the chip, we carried out a dehybridization step by flowing ethanol at 80% during 5 minutes to remove the complementary DNA strands that were previously hybridized. After waiting again for a stable baseline during the SSC 1x flow, non-complementary ssDNA was pumped in the fluidic system. Fig. 4.40 shows the time evolution of the RR resonances during the flow of the non-complementary ssDNA. A sharp peak is observed when the non-complementary ssDNA reaches the sensors, which rapidly returns to the prior position. This sharp peak might be caused by pressure changes in the flowcell during the automatic switch between the liquids to be flowed. Then, during the non-complementary ssDNA stream, no significant shift was observed, thus confirming the specificity of the sensor since no hybridization between the DNA strands was produced. Finally, SSC was pumped again to obtain the net variation which was negligible, only a slight sharp backshift was observed due to the change in the refractive index after changing the flow to the SSC 1x buffer.

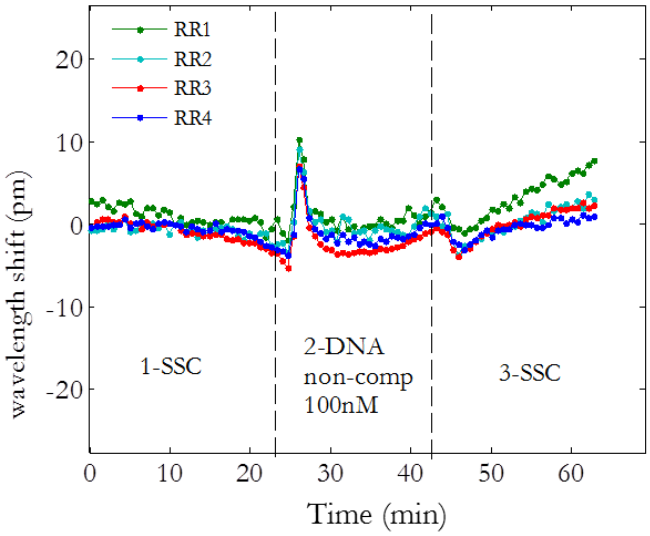

Fig. 4.40: *Response of the RR sensors to non-complementary ssDNA.*

Once the proof-of-principle of DNA sensing using GOPTS functionalized RR sensors was demonstrated in this experiment, we developed a new experimental procedure where a photonic chip with two sensing RRs and one reference RRs was used. In order to achieve this, after the GOPTS activation of the chip surface, only two RRs were spotted with the DNA probes (i.e., a smaller drop was used this time) while the other RR was left uncoated in order to be subsequently blocked with 2-mercaptoethanol. Then, the chip was exposed to UV light for 2 hours and finally all the surface was blocked with 2-mercaptoethanol during 60 minutes.

Fig. 4.41 shows the response of the RRs for different concentrations of complementary ssDNA. After obtaining a stable baseline with SSC, we injected a concentration of 100 nM of the complementary ssDNA. The hybridization with the DNA capture probes caused a change in the refractive index of the surface of the sensors and thus induced a resonance shift of the sensing RRs. It is worth noting that the sensitivity of both sensing RRs was rather similar this time. This was mainly determined by the use of smaller drops for the functionalization of the RRs, what allowed a better control the probes density over the sensors, thus leading to a more homogenous surface coverage of the structures. In addition, when the SSC 1x buffer is flowed again after minute ~63, we observe that the resonances shift is permanent, what means that the hybridization was properly done and unspecific binding or adsorption were practically negligible. On the other hand, the reference ring that was blocked with 2-mercaptoethanol did not exhibit any shift (simply a slight shift due to the refractive index change between the SSC buffer and the ssDNA dilution), thus demonstrating the suitability of the blocking with 2-mercaptoethanol.

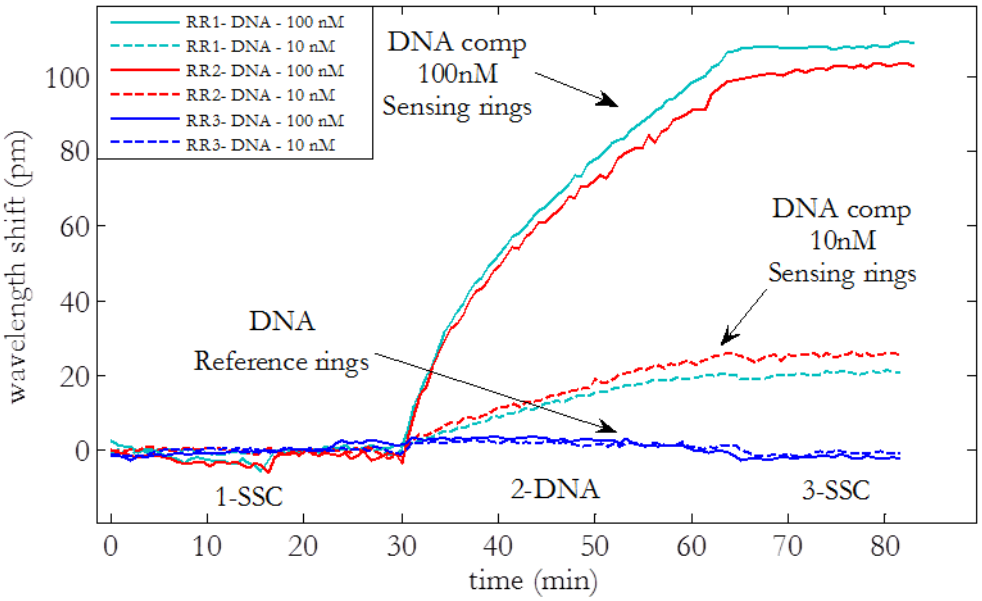

Fig. 4.41: *Specific detection of two ssDNA concentrations. The dehybridization step was carried out employing ethanol 80% in DIW. Each reference ring curve corresponds to a different concentration.*

After the verification of the DNA hybridization using complementary ssDNA 100 nM, the chip was regenerated by dehybridizing with ethanol 80% in DIW, and a second concentration of complementary DNA (10 nM) was flowed over the chip in order to determine the response variation of the sensor for different concentrations of complementary ssDNA. Fig. 4.41 clearly shows this variation in the sensor response when the concentration of complementary ssDNA was changed, exhibiting a lower initial slope and a smaller total shift than for the concentration of 100 nM. Regarding the reference sensor, we can observe that again it did not show any shift (except for a slight refractive index induced shift).

The next and final step was focused on demonstrating again the specificity of the DNA sensors by flowing a non-complementary ssDNA sequence (the chip was first regenerated using ethanol 80%). Fig. 4.42 shows the evolution of the resonances of the three RRs (two sensing RRs + one reference RR). As expected, the position of the resonances remained stable as there was no hybridization of the flowed ssDNA with the capture probes on the surface of the chip. This fact corroborates the specificity of the hybridization detected in the previous experiments. We also note the remarkable stability of the sensing system despite of the lack of a temperature control system in our set-up.

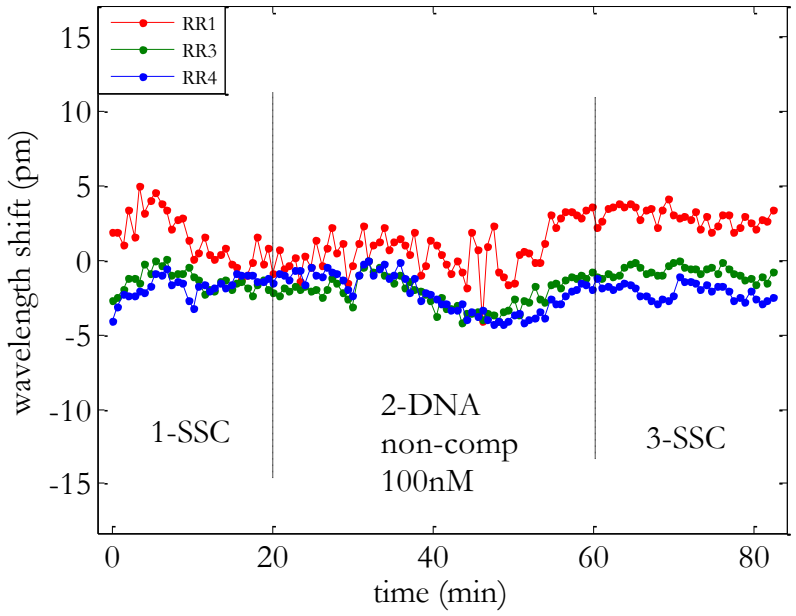

Fig. 4.42: *Response of the sensing and the reference RRs during the flow of non-complementary ssDNA.*

Therefore, with these experiments we were able to demonstrate the feasibility of ssDNA sensing using our photonic sensors functionalized them using GOPTS-based chemistry. We have also demonstrated that this platform provides a specific detection (no response was observed for non-complementary ssDNA), with different response to different complementary ssDNA concentration, and where reference RRs are available to compensate possible temperature or bulk refractive variations.

4.6.3.3 Chip blocking

Despite the good results shown in the previous experiments, we decided to investigate further the blocking procedure used to prevent non-specific adsorption. To this aim, we prepared a set of experiments where the sensing structures were not functionalized with the DNA probes, only silanized with GOPTS and just blocked following different strategies, and then we flowed different concentrations of complementary ssDNA.

The first chip was blocked following the procedure described in the previous section, where after the silanization of the chip by immersion in 2% GOPTS in toluene, the rings were covered with 2-mercaptoethanol 0.1 M in order to block the epoxy moieties of the GOPTS. Then, we irradiated the chip with UV light for 120 minutes in order to promote the blocking of the moieties. Finally, the chip was rinsed, dried and ready to be assembled and measured.

After obtaining the baseline for the flow of SSC buffer, several concentrations of the target ssDNA ranging from 1 nM to 100 nM were flowed over the sensors to observe their response. Fig. 4.42 depicts the shift of the ring resonances for this experiment. We did not appreciate a significant shift of the sensor response for any of the ssDNA concentrations flowed, and thus no non-specific binding was observed. We only observed a slight change in the slope while flowing the DNA, what might be probably due to changes in the composition of the flowed substance and thus of the refractive index. Several spikes were also observed in the sensors response, which might be produced by microbubbles interfering with the sensing structures, as we exposed previously in section 4.6.2.3. Finally, we observed a drift that might be due to a slight temperature variation.

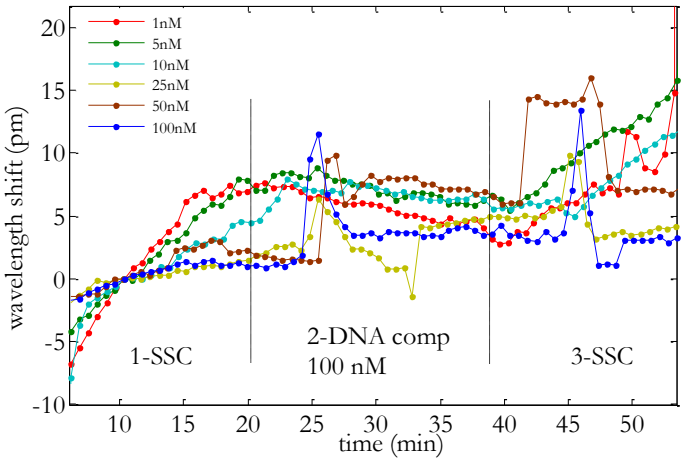

Fig. 4.42: *Sensors response for different ssDNA concentrations when the chip is functionalized with a layer of GOPTS and blocked with 2-mercaptoethanol.*

For the second chip, we simply silanized it by immersion in 2% of GOPTS in toluene, but neither DNA probes nor 2-mercaptoethanol were then spotted on the chip. With this experiment, we wanted to confirm that the epoxy groups from the GOPTS layer already act as a blocking layer for the ssDNA to be flowed in the experiments.

Fig. 4.43 shows the response of the RR sensing structures for all the flowed DNA concentrations. As it happened for the case of blocking with 2-mercaptoethanol, we did not note any non-specific binding of the DNA and all the rings had the same trend (also with a slight drift, some peaks due probably due to microbubbles, etc.). Therefore, this experiment indicated that the GOPTS layer can directly act as blocking layer for reference sensors, since it prevents from the specific adsorption of ssDNA.

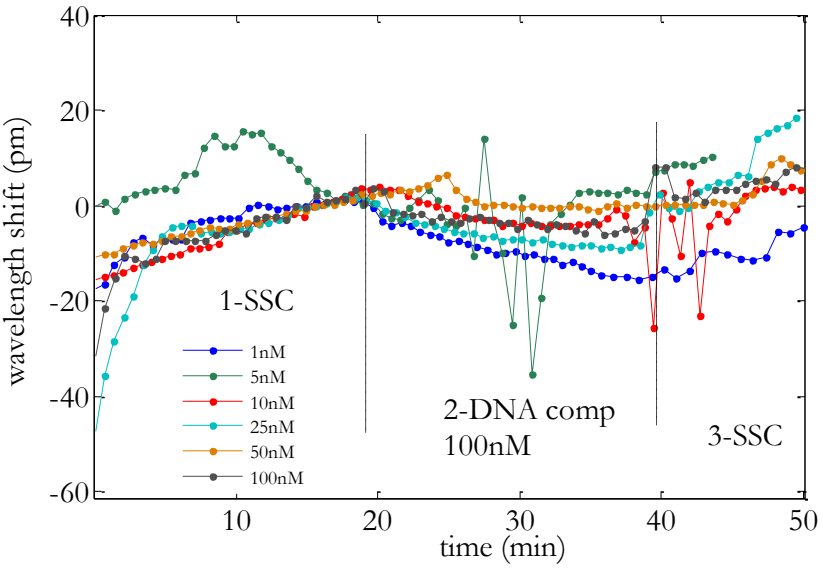

Fig. 4.43: *Sensors response for different ssDNA concentrations when the chip is only functionalized with a layer of GOPTS.*

As conclusion, we investigated the sensor response to non-specific adsorption when the GOPTS layer is blocked with 2-mercaptoethanol and when no other layer is created over the epoxy termination of the organosilane. These tests have shown that no significant binding was detected when the DNA was flowed over the sensors for the two approaches, which did not show a remarkable difference between them. Therefore, for the next experiments, we decided to avoid the blocking step with 2-mercaptoethanol, thus reducing the time required for the chip functionalization.

4.6.3.4 Automated spotting

The intrinsic sensitivity of the RR sensing structures in the same chip is, in principle, identical. However, when the sensors are functionalized and we carry sensing experiments out, we observe that the sensitivity towards a certain target analyte is usually different for the each sensing structure within the chip. These variations are mainly caused by the lack of homogeneity of the biological coating deposited over the sensors.

One of the factors that affect to this lack of homogeneity is the size of the drops that are used in the spotting step. For example, we can see a significant difference in the variation between sensors response for the ssDNA sensing experiments presented in section 4.6.3.2: the first ssDNA sensing experiment exhibited a variation between sensors of ~50 pm (see Fig. 4.39), while the second ssDNA sensing experiment showed a variation between sensors below 10 pm (see Fig. 4.41). The main difference in the functionalization step that was carried out in each case was the

amount of liquid spotted over the sensing structures: while in the first case a large drop was used to cover the four RR sensing structures, in the second case we used a smaller drop in order to only cover two of the four RRs.

In this experiment, we used an automated spotting equipment (BioDot) to deposit the reagents used in the functionalization. Biodot is a microarray-spotting machine that is able to spot drops as small as of 20 nl with a spatial accuracy of 20 μm. The fact of employing such small amount of liquid leads to three advantages related to the functionalization of the RR-based sensor. The first one is the higher spatial resolution in the spotting process, which allows us to spot independently each sensor with a different probe. The second advantage is that by using smaller drops we are reducing the contact area of this drop with the chip, what allows obtaining an increment in the density and the homogeneity of the coating, thus leading to higher sensitivity. And finally, the third benefit is the reduction of the amount of reagent required for the functionalization, what leads to a significant cost saving for the development of the final device. Fig. 4.45 shows two pictures of spotted drops during the functionalization process when manual and automated spotting is used, where the different in sizes can be clearly seen.

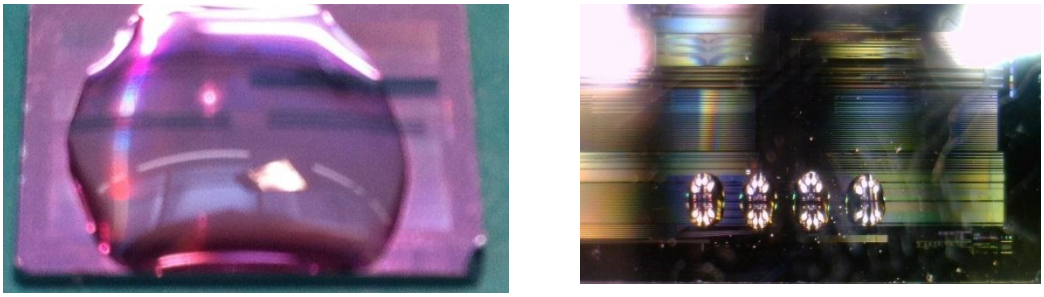

Fig. 4.45: *Comparison of drops deposited in the functionalization process when the spotting is carried out manually and with the automated BioDot equipment. The amount of reactive is ~10 times lower using the latter method.*

In order to corroborate the influence of the drop size in the RR sensitivity, we planned an experiment to measure a significantly low concentration of complementary ssDNA. The functionalization procedure followed the same steps as previously described, but now the spotting of the aminated DNA probes was done using the BioDot equipment; a 40 nl drop of aminated DNA probe was spotted in three of the four RRs of the sensing structure, leaving the fourth RR as a reference structure. Then the chip was irradiated with UV light, cleaned and assembled with the PDMS flowcell.

As done in previous experiments, a short cycle of ethanol was initially flowed over the chip in order to increase the structure wettability. After that, we obtained the sensors baseline by flowing

SSC at a rate of 15 µl/min. Then, we injected the complementary ssDNA with a concentration of only 5 nM. Fig. 4.46 shows the time evolution of the resonances position when the complementary DNA is flowed over the sensors. We can see that the 3 DNA-functionalized sensors clearly respond to the very low concentration of complementary ssDNA that was flowed over the chip, showing a permanent shift of 10 pm for the RRs with lower sensitivity and 16 pm for the RR that exhibits the higher sensitivity. This good response to such low concentration indicated the proper coverage of the surface with the DNA probes when the automated spotting equipment is used. The step signal showed by the reference RR indicates the difference in the refractive index of the SSC buffer and the dilution of the buffer with the complementary ssDNA. This signal can be used to subtract the bulk refractive index effect from the response of the sensing structures, thus obtaining only the sensors response due to the hybridization of the complementary ssDNA on the surface of the chip.

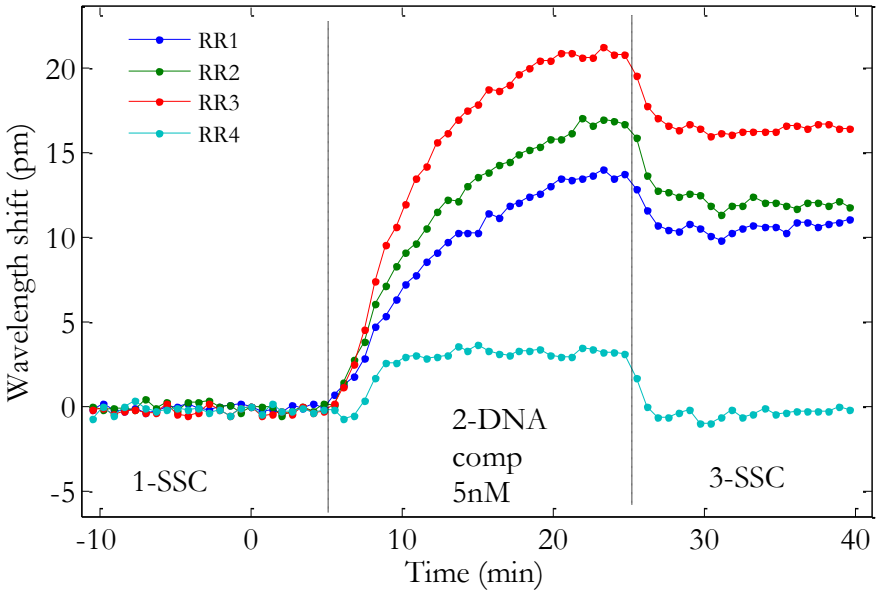

Fig. 4.46: *Specific detection of the DNA hybridization for a concentration of 5 nM. A bulk refractive index variation of the medium is observed for the reference RR and also at the end of the flow of the DNA for the sensing RRs.*

To sum up, after using the BioDot to automatically spot low volumes of the DNA probes on the surface of the chip, we were able to detect a very small ssDNA concentration (only 5 nM) using the RR-based sensors. In addition, the small intrachip variation of the response of the sensors (only ~6 pm) demonstrates the higher homogeneity of the reagents coating that is obtained by spotting tiny drops (only 40 nl) in each sensing structure. Finally, remark also the higher stability of the signal that is obtained during the experiments.

4.6.3.5 Study of different DNA concentrations

Once the functionalization procedure was optimized and proper times, concentrations and volumes were selected, we carried out an assay aimed at obtaining the sensitivity curve of the sensor, where several DNA concentrations ranging from 10 nM to 100 nM were flowed. Fig. 4.47 shows the evolution of the resonances for each concentration, where we can see that the sensors responded with different trend depending on the DNA concentration. Note that the response of RR1 is not depicted for the concentrations of 50 nM and 25 nM, due to multiple jumps that made the signal unusable. For the concentrations of 50 nM, 25 nM and 10 nM, we can observe a small spike when the DNA reaches the sensors, which is due to the change of the automatic valve and it was also observed in other experiments (e.g., see Fig. 4.40). We are further investigating on how to reduce the effect of this problem.

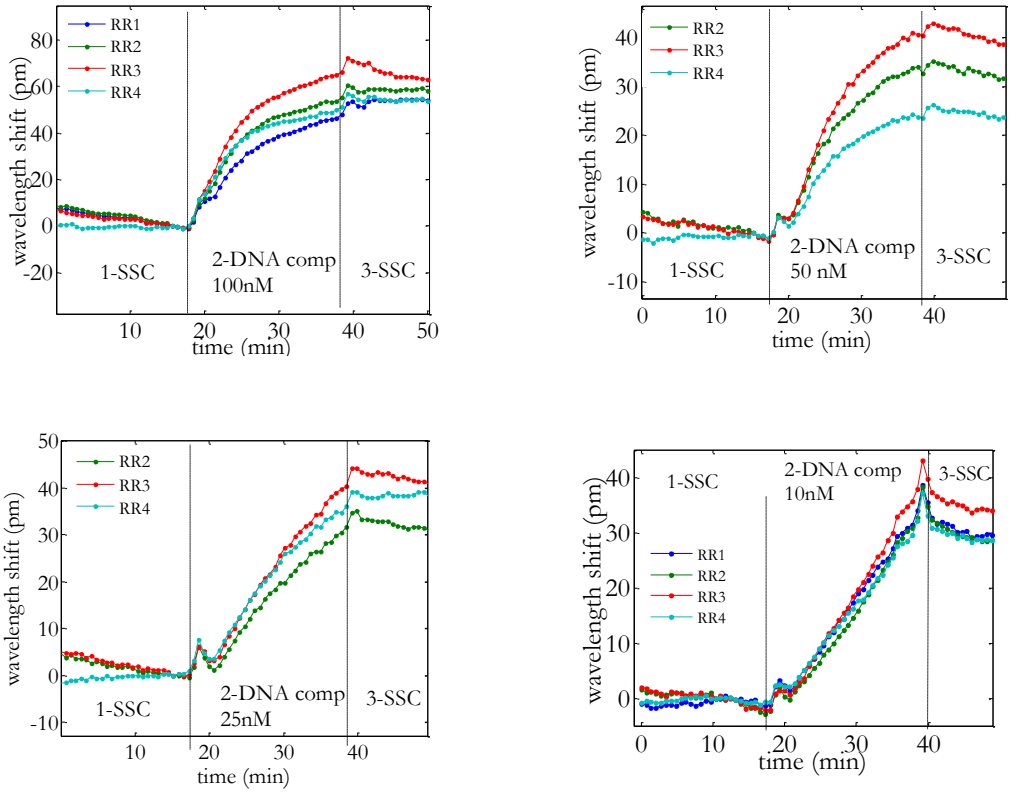

Fig. 4.47: *Time evolution ring resonance's position for different DNA concentrations.*

As we can observe in the graphs, except for the signal of 100 nM, the response of all the sensors is shifted around 30 pm after 20 minutes of flowing the complementary DNA at different concentrations. Therefore, it is extremely difficult to obtain a correlation between the concentration and the final shift of the sensors response. However, we can try to correlate the initial slope of the response with the analyte concentration Fig. 4.48 represents the initial slope of each RR for each

DNA concentration, where the initial slope is obtained by fitting the signal to an exponential function. In this graph, we can observe a clear correlation between concentration and initial slope provided by the sensor, where the higher the concentration, the larger the initial slope. The use of the sensor initial slope to determine the concentration of the target analyte has another significant advantage: the reduction of the time analysis. Since we do not need to flow the analyte over the sensors until the response reaches the saturation point, but only a shorter time until we are able to determine the initial slope of the response.

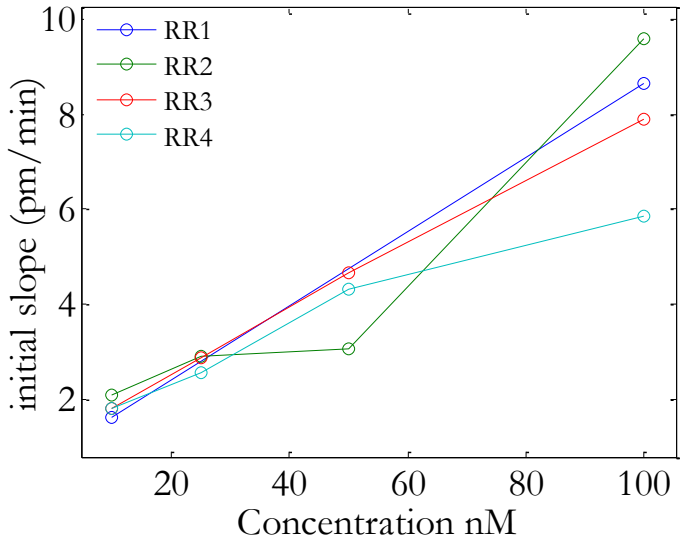

Fig. 4.48: *Sensitivity curve for DNA detection for the four RR sensors on the chip. The curve depicts the initial slope of the response of each RR for different concentrations of complementary DNA.*

4.6.3.6 Study of multiple regenerations

Finally, since we have been reusing the sensing structures by regenerating them with an ethanol flow, in this last assay we studied the sensitivity variation of the sensor after several dehybridization steps. To this aim, the chip was identically functionalized as previously described (i.e., deposition of GOPTS layer, spotting of DNA probes over the four RRs with the BioDot, and without GOPTS blocking), and then several cycles where complementary DNA with a concentration of 50 nM were flowed and then dehybridized were carried out. Fig. 4.49 shows the response of each sensor for each of the DNA sensing cycle, where we can clearly observe a degradation of the sensor response after each regeneration. This degradation may be due for two reasons. The first reason is that the dehybridization step was not removing all the hybridized DNA strands from the surface of the chip, and therefore there were less probes available to be hybridized when the DNA was flowed again. The second reason is related with the probe removal or deactivation; despite the probes are attached to the surface by a covalent bonding, it is possible that

some DNA probes are removed or that their biological activity is lost, thus leading to a lower sensitivity.

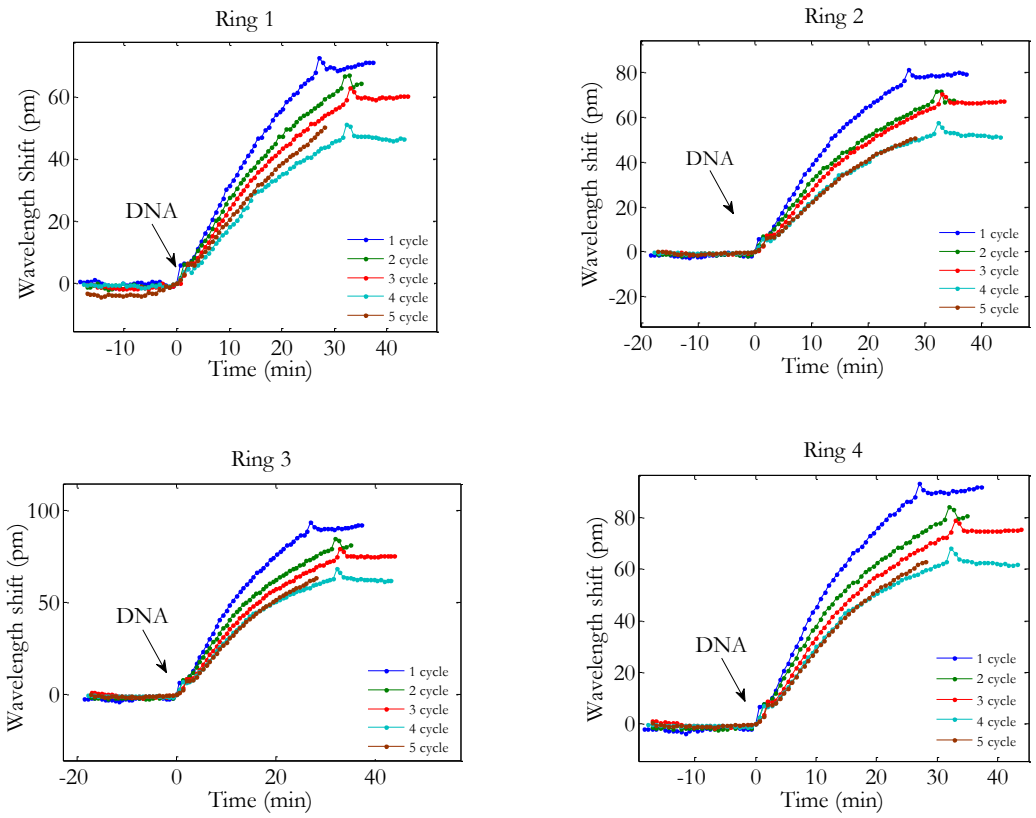

Fig. 4.49: *Evolution of the hybridization curves after each regeneration cycle for each RR sensor. After each regeneration step, the sensitivity decreases.*

Fig. 4.50 represents the variation of initial slope of each ring after each regeneration/sensing cycle. We can see that, after 5 regeneration/sensing cycles, the initial slope is reduced around 30% in average. However, this slight variation between two regeneration/sensing cycles is not a major drawback, but it would necessary to perform a proper calibration of the sensing device and relate it to the regeneration cycle prior to perform any assay in order to obtain a proper correlation between the concentration and the resonance shift for a determined number of regenerations. Finally, note the difference of the sensitivity among sensors in the same chip (e.g., in the first cycle, RR3 exhibits an initial slope ~1.5 times a higher than RR1).

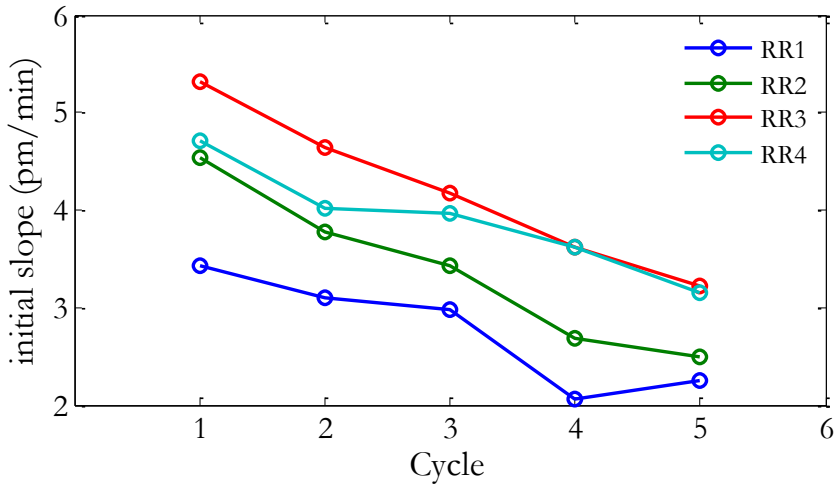

Fig. 4.50: *Evolution of the initial slope of the RRs after five hybridization assays. The trend of the initial slope of the sensor response is constantly decreasing.*

4.7 Conclusions

This chapter was focused on the use of RR structures for their use as sensing elements. We began describing the fundamentals of the RR and its main parameters. There, we determined that it will be desirable to work in an add-drop configuration, since it eases obtaining the critical coupling condition in order to have sharper resonances with higher Q values. Then, we also reviewed the state-of-the-art in the field of RR-based sensors. We observed that a wire cross-section is probably the most appropriate for sensing purposes due to its balance between fabrication simplicity and optical losses (despite configurations like the slot waveguide can provide higher sensitivities), that SOI technology is the most used platform because its CMOS compatibility (although other platforms based in polymer materials might also be interesting), and that several different multiplexing approaches are currently being used. According to all these factors, the RR structures to be used as sensing structures within this PhD work were designed and fabricated (in collaboration with Gent University in the frame of the FP7-INTOPSENS project).

Then, we presented the automated measurement set-up that was used for the experimental characterization of the RR-based sensing structures. Several enhancements were included respect to that previously described in chapter 3 for the characterization of PhC-based sensors, such as the use of an OSA to obtain the spectra instead of a tunable laser, the use of a switching valve to automatically change between the target samples to be flowed, or a PDMS-based microfluidic flowcell that permitted a more homogeneous and controlled sample delivery.

Regarding the experimental characterization of the sensing structures, we began performing refractive index sensing experiments in order to determine the bulk sensitivity of the structure. In these experiments, we obtained a sensitivity value of 82.78 nm/RIU and a detection limit of $1.44 \cdot 10^{-5}$ RIU, what is a common value for this type of sensing technology. Then, we worked in the development of the biosensor for protein and DNA sensing by functionalizing the structures using the ICTPS-based chemistry initially considered. Using this functionalization approach, we were able to successfully demonstrate the detection of low concentrations of antiBSA molecules and ssDNA hybridization. In the case of the DNA sensing, we note that an efficient increment in the hybridization was achieved by functionalizing the chip with dsDNA (and then, dehybridize it), instead of directly attaching the ssDNA probes.

However, several non-desirable effects were observed during the course of these experiments, such as the lack of stability of the response at the beginning of the experiments, signal drift, bubbles into the fluidic system, or temperature variations. Moreover, we also observed many issues related with the use of ICPTS organosilane for the functionalization of the sensors, mainly related with the high reactivity of its isocyanate termination. For these reasons, we decided to work on a second functionalization approach in order to obtain better results (among other reasons).

The second functionalization approach was based in the use of GOPTS organosilane, which has an epoxy termination that reacts towards thiol groups. This reaction between epoxy and thiol groups can be assisted by exposing with UV light, what provides several advantages such as a reduction of the incubation time and a spatial selectivity in the functionalization process that allows to only attach the receptors on those areas that are exposed. Therefore, we used this GOPTS-based functionalization to attach thiolated DNA probes to the sensing RRs. By working in the optimization of this approach for ssDNA sensing we have been able to detect concentrations as low as 5 nM. An interesting fact observed during these experiments was the strong dependence between the drop size during the functionalization process and the surface coverage/efficiency of the sensor, observing that smaller drops provides higher sensitivities and less variation among the sensors. In addition, we carried out a study of the sensitivity evolution after several dehybridization cycles, in order to confirm the possibility of reusing the sensing structures. We obtained that a decrement around 30% of the efficiency was observed after 5 regeneration cycles (i.e., ~5% of loss per regeneration cycle), what confirms that the chips can be reused several times. Therefore, from all the experiments that have been carried out, we can affirm that the RR platform is potentially a good option to develop the next generation of label-free sensors.

References

[ALM04] V. R. Almeida, Q. Xu, C. a Barrios, and M. Lipson, "Guiding and confining light in void nanostructure."Optics letters, vol. 29(11), pp. 1209-11, 2004.

[AND00] J.R. Anderson, D.T. Chiu, R.J Jackman, O. Cherniavskaya, J.C McDonald, H. Wu, S.H Whitesides, G.M Whitesides, "Fabrication of Topologically Complex Three-Dimensional Microfluidic Systems in PDMS by Rapid Prototyping." Analytical Chemistry, vol. 72(14), pp. 3158-3164, 2000.

[BAR07] C. Barrios, K. B. Gylfason, B. Sánchez, A. Griol, H. Sohlström, M. Holgado, and R. Casquel, "Slot-waveguide biochemical sensor."Opticsletters, vol. 32, no. 21, pp. 3080–2, 2007.

[BAR08] C. A. Barrios, M. J. Bañuls, V. González-Pedro, K. B. Gylfason, B. Sánchez, A. Griol, A. Maquieira, H. Sohlström, M. Holgado, and R. Casquel, "Label-free optical biosensing with slot-waveguides."OpticsLetters, vol. 33, no. 7, p. 708, Mar. 2008.

[BAR12] C.A. Barrios, "Integrated micro ring resonator sensor arrays for labs-on-chips." Analytical and bioanalyticalchemistry, vol. 403(6), pp. 1467-75, 2012.

[BOG05] W. Bogaerts, R. Baets, P. Dumon, V. Wiaux, S. Beckx, D. Taillaert, B. Luyssaert, J. Van Campenhout, P. Bienstman, and D. Van Thourhout, "Nanophotonic waveguides in silicon-on-insulator fabricated with CMOS technology," Journal of Lightwave Technology, Vol. 23(1), pp. 401–412, 2005.

[CAR10] C.F. Carlborg, K.B. Gylfason, A. Kaźmierczak, F. Dortu, M.J. Bañuls Polo, A. Maquieira Catala, G.M. Kresbach, H. Sohlström, T. Moh, L. Vivien, J. Popplewell, G. Ronan, C. a Barrios, G. Stemme, and W. van der Wijngaart, "A packaged optical slot-waveguide ring resonator sensor arrayfor multiplex label-free assays in labs-on-chips." Lab on a chip, vol. 10(3), pp. 281–90, 2010.

[CHA06] C.-Y. Chao, W. Fung, and L. J. Guo, "Polymer microring resonators for biochemical sensing applications," IEEE Journal of Selected Topics in Quantum Electronics, vol. 12(1), pp. 134–142, 2006.

[CHE09] Y.K. Cheung, D. Shiovitz, S.K. Sia, K.E. Herold, A. Rasooly, "Microfluidic-based lithography for fabrication of multi-component biocompatible microstructures." Caister Academic Press, Norfolk, UK, p. 115, 2009.

[CLA09] T. Claes, J. G. Molera, K. De Vos, E. Schacht, R. Baets, and P. Bienstman, "Label-Free Biosensing With a Slot-Waveguide-Based Ring Resonator in Silicon on Insulator." IEEE Photonics Journal, vol. 1(3), pp. 197-204, 2009.

[CLA10] T. Claes, W. Bogaerts, and P. Bienstman, "Experimental characterization of a silicon photonic biosensor consisting of two cascaded ring resonators based on the Vernier-effect and introduction of a curve fitting method for animproved detection limit." Optics Express, vol. 18(22), pp. 22747-22761, 2010.

[DUL06] E. Dulkeith, F. Xia, L. Schares, W. M. J. Green, and Y. A. Vlasov, "Group index and group velocity dispersion in silicon-on-insulator photonic wires," Optics Express, vol. 14(9), p. 3853, 2006.

[EPI13] http://www.epixfab.eu/

[FAN08] X. Fan, I. M. White, S. I. Shopova, H. Zhu, J. D. Suter, and Y. Sun, "Sensitive optical biosensors forum labeled targets: a review."Analyticachimica acta, vol. 620(1–2), pp. 8-26,

2008.

[HAL10] J. Halldorsson, N. B. Arnfinnsdottir, A. B. Jonsdottir, B. Agnarsson, and K. Leosson, "High index contrast polymer waveguide platform for integrated biophotonics." Optics express, vol. 18(15), pp. 16217-26, 2010.

[IME13] http://www.imec.be/

[IQB10] M. Iqbal, M. A. Gleeson, B. Spaugh, F. Tybor, W. G. Gunn, M. Hochberg, T. Baehr-Jones, R. C. Bailey, and L. C. Gunn, "Label-Free BiosensorArraysBasedonSilicon Ring Resonators and High-SpeedOpticalScanningInstrumentation"IEEE Journal of SelectedTopics in Quantum Electronics, vol. 16, no. 3, pp. 654–661, 2010.

[KIM08] G.-D. Kim, G. Son, H.-S. Lee, K. Kim, and S. Lee, "Integrated photonic glucose biosensor using a vertically coupled microring resonator in polymers," Optics Communications, vol. 281(18), pp. 4644–4647, 2008.

[KIM12] Y. H. Kim, S. J. Park, S.-W. Jeon, S. Ju, C.-S. Park, W.-T. Han, and B. H. Lee, "Thermo-optic coefficient measurement of liquids based on simultaneous temperature and refractive index sensing capability of a two-mode fiber interferometric probe."Optics Express, vol. 20(21), pp. 23744, 2012.

[KOM12] J. Komma, C. Schwarz, G. Hofmann, D. Heinert, and R. Nawrodt, "Thermo-optic coefficient of silicon at 1550 nm and cryogenic temperaturas."Applied Physics Letters, vol. 101(4), pp. 041905, 2012.

[LAE07] F. Van Laere, G. Roelkens, D.Van Thourhout, T.F Krauss,R. Baets, M. Ayre, J. Schrauwen, D. Taillaert, "Compact and Highly Efficient Grating Couplers Between Optical Fiber and Nanophotonic Waveguides." Journal of Lightwave Technology, vol. 25(1), pp. 151-156, 2007.

[LEE10] S. Lee, S. C. Eom, J. S. Chang, C. Huh, G. Y. Sung, and J. H. Shin, "Label-free optical biosensing using a horizontal air-slot SiN xmicrodiskresonator."Optics Express, vol. 18, no. 20, .p. 20638, 2010.

[LOC12] C. Lochovsky, S. Yasotharan, and A. Günther, "Bubbles no more: in-plane trapping and removal of bubbles in microfluidic devices." Lab on a chip, vol. 12(3), pp. 595-601, 2012.

[LUC10] M. S. Luchansky and R. C. Bailey, "Silicon photonic microring resonators for quantitative cytokine detection and T-cell secretion analysis."Analyticalchemistry, vol. 82(5), pp. 1975-81, 2010.

[LUC11] M.S. Luchansky, A.L. Washburn, M.S. McClellan, and R.C. Bailey, "Sensitive on-chip detection of a protein biomarker in human serum and plasma overan extended dynamic range using silicon photonic micro-ring resonators and sub-micron beads." La bon a chip, vol. 11(12), pp. 2042-4, 2011.

[LUC12] M.S. Luchansky and R.C. Bailey, "High-Q optical sensors for chemical and biological analysis." Analytical chemistry, vol. 84(2), pp. 793-821, 2012.

[MAN12] M. Mancuso, J. M. Goddard, and D. Erickson, "Nanoporouspolymer ring resonatorsfor biosensing."Optics Express, vol. 20(1), pp. 245, 2012.

[PAS07] V. M. N. Passaro, F. Dell'Olio, and F. De Leonardis, "Ammonia Optical Sensing by Microring Resonators." Sensors, vol. 7(11), pp. 2741-2749, 2007.

[PAS13] V. M. N. Passaro, B. Troia, M. L. Notte, and F. D. Leonardis, "Photonic resonant microcavities for chemical and biochemical sensing." RSC Advances, vol. 3(1), pp. 25, 2013.

[QAV10] A. J. Qavi and R. C. Bailey, "Multiplexed detection and label-free quantitation of microRNAs using arrays of silicon photonic microring resonators."Angewandte Chemie (International ed. in English), vol. 49(27), pp. 4608-4611, 2010.

[QAV11] A. J. Qavi, T. M. Mysz, and R. C. Bailey, "Isothermal discrimination of single-nucleotide polymorphisms via real-time kinetic desorption and label-free detection of DNA using silicon photonic microring resonator arrays.," Analytical chemistry, vol. 83(17), pp. 6827–33, 2011.

[RAB07] D.G. Rabus, "Integrated Ring Resonators." Springer Series in Optical Sciences, vol. 127, 2007.

[RAM08] A. Ramachandran, S. Wang, J. Clarke, S. J. Ja, D. Goad, L. Wald, E. M. Flood, E. Knobbe, J. V Hryniewicz, S. T. Chu, D. Gill, W. Chen, O. King, and B. E. Little, "A universal biosensing platform based onoptical micro-ring resonators." Biosensors & bioelectronics, vol. 23(7), pp. 939–44, Feb. 2008.

[SCH12] O. Scheler, J. T. Kindt, A. J. Qavi, L. Kaplinski, B. Glynn, T. Barry, A. Kurg, and R. C. Bailey, "Label-free, multiplexed detection of bacterial tmRNA using silicon photonic microring resonators." Biosensors & bioelectronics, vol. 36(1), pp. 56–61, 2012.

[SU07] H. Su and X. G. Huang, "Fresnel-reflection-based fiber sensor for on-line measurement of solute concentration in solutions," Sensors and Actuators B: Chemical, vol. 126(2), pp. 579–582, 2007.

[SUN09] H. Sun, A. Chen, and L. R. Dalton, "Enhanced Evanescent Confinement in Multiple-Slot Waveguides and Its Application in Biochemical Sensing." IEEE Photonics Journal, vol. 1(1), pp. 48–57, 2009.

[TAI04] D. Taillaert, P. Bienstman, and R. Baets, "Compact efficient broadband grating coupler for silicon-on-insulator waveguides." Optics Letters, vol. 29(23), pp. 2749, 2004.

[VOS07] K. De Vos, I. Bartolozzi, E. Schacht, P. Bienstman, and R. Baets, "Silicon-on-Insulator micro ring resonator for sensitive and label-free biosensing." Optics Express, vol. 15(12), p. 7610, 2007.

[VOS09] K. De Vos, J. Girones, T. Claes, Y. De Koninck, S. Popelka, E. Schacht, R. Baets, and P. Bienstman, "Multiplexed Antibody Detection Withan Array of Silicon-on-Insulator Microring Resonators." IEEE PhotonicsJournal, vol. 1(4), pp. 225–235, 2009.

[WAS09] A. L. Washburn, L. C. Gunn, and R. C. Bailey, "Label-free quantitation of a cancer biomarker in complex media usingsiliconphotonicmicroringresonators."Analyticalchemistry, vol. 81(22), pp. 9499-506, 2009.

[WAS10] A. L. Washburn, M. S. Luchansky, A. L. Bowman, and R. C. Bailey, "Quantitative, label-free detection of five protein biomarkers using multiplexed arrays of silicon photonic micro ring resonators.,"Analytical chemistry, vol. 82(1), pp. 69-72, 2010.

[XU08] D. X. Xu, a Densmore, a Delâge, P. Waldron, R. McKinnon, S. Janz, J. Lapointe, G. Lopinski, T. Mischki, E. Post, P. Cheben, and J. H. Schmid, "Folded cavity SOI micro ring sensors for high sensitivity and real time measurement of biomolecular binding."Optics express, vol. 16(19), pp. 15137–15148, 2008.

[XU10] D.-X. Xu, M. Vachon, a Densmore, R. Ma, a Delâge, S. Janz, J. Lapointe, Y. Li, G. Lopinski, D. Zhang, Q. Y. Liu, P. Cheben, and J. H. Schmid, "Label-free biosensor array based on silicon-on-insulator ring resonators addressed using a WDM approach.," Optics letters, vol. 35(16), pp. 2771–3, 2010.

[YEB12] N. a. Yebo, S. P. Sree, E. Levrau, C. Detavernier, Z. Hens, J. a. Martens, and R. Baets, "Selective and reversible ammonia gas detection with nanoporous film functionalized silicon photonic micro-ring resonator," Optics Express, vol. 20(11), p. 11855, 2012.

[YEN06] W. Fung and L. J. Guo, "Polymer micro ring resonators for biochemical sensing applications."IEEE Journal of Selected Topics in Quantum Electronics, vol. 12(1), pp. 134–142, 2006.

[YEO06] S. Yeon Cho and N. M. Jokerst, "A Polymer Microdisk Photonic Sensor Integrated Onto Silicon." IEEE Photonics Technology Letters, vol. 18(20), pp. 2096-2098, 2006.

[ZHA08] X. Zhang and X. Li, "Design, fabrication and characterization of optical micro ring sensors on metal substrates." Journal of Micromechanics and Microengineering, vol. 18(1), p. 015025, 2008.

5

Low-cost biosensing using 1D photonic bandgap structures

5.1 Introduction

One of the trends in the field of the development of the new sensing devices is focused on the reduction of the cost and the complexity while keeping a high multiplexing level and performance of the photonic sensing structures. Currently, we can find in the market several basic analysis devices such as pregnancy or glucose tests that are commercialized at a very low cost and, moreover, are portable. Therefore, as already introduced in the previous chapters, the aim of the development of high performance photonic biosensors is to develop LOC devices which such level of cost and practicality, but where a more complex analysis is carried out. However, a significant limitation of current sensing approaches based on integrated photonic structures is the high cost of their read-out platform, what really constrain its practical deployment into the market.

As it has been shown in chapters 3 and 4, most photonic sensing techniques are based on continuously acquiring the spectral response of the sensing structures and then monitor the shift of any spectral feature (e.g., PBG or guided band position for PhCs and resonances for RRs), which is dependent on the medium surrounding the sensing structure. Therefore, in order to carry out this type of spectral-based interrogation, it requires performing a spectral sweep of the sensor response by using tunable elements such as a tunable laser or an OSA. This equipment is frequently expensive, heavy and bulky, thus making difficult the development of compact and low-cost analysis devices that might be used for in-situ measurements or POC solutions. For that reason, several research groups have been working since some years ago towards the development of innovative photonic sensing solutions able to provide reliable and high performance results at a reasonable cost. In this PhD work, we propose a novel low-cost interrogation method based on a combination of PBG sensing structures and a limited bandwidth source, where the use of expensive tunable elements (i.e., tunable laser or OSA) is avoided, thus significantly simplifying and reducing the cost of the final sensing platform for biochemical detection. Additionally, this sensing technique also allows us to obtain real-time information of the sensing structure, since the output signal can be continuously monitored.

Before describing the details of our novel sensing technique, we will first present in section 5.2 other currently developed photonic sensing techniques that also look for to reduce the cost of the read-out system. In addition, we will also review in section 5.3 several research works focused on the development of sensing structures based on 1D PhCs, since we have used this type of periodic structures for the experimental demonstration of our sensing technique. In section 5.4 we will provide the operation details of our sensing method, while in sections 5.5 and 5.7 we will provide details related to the design, fabrication and experimental development of the sensing structures and the read-out platform. Finally, in section 5.7 we will show the experimental results obtained using this sensing technique, where we have demonstrated the detection of small amounts of antibodies in real-time confirming that our sensing technique is a completely suitable platform to carry out biological assays for different domain purposes.

5.2 State-of-the-art of non-spectral-based sensing techniques

As previously indicated, a major part of photonic sensors based on planar integrated structures relies on the measurement of the shift of their spectral response, such as in PhCs or RRs. These interrogation techniques require the employment of optical tunable devices that are generally expensive. This drawback encouraged several research groups to work on the development of

different techniques to carry out the detection without using tunable elements. In this section, we present several methods that perform the sensing measurement without sweeping the spectrum.

One of the main examples of this type of development has been reported by researchers from Gent University. They presented a sensing device based in the combination of two cascaded RRs in Vernier configuration and an integrated arrayed waveguide grating (AWG) filter, as it is shown in Fig. 5.1a [CLA11]. Vernier configuration consists on connecting consecutively two RRs with slightly different roundtrips, where the drop port of the first RR is coupled to the input of the second RR. These RRs are designed in such a way that only one resonance out from *n* matches between both RRs obtaining a perfect overlap as depicted in Fig. 5.1b. One of the RRs is completely isolated from the environment (e.g., by depositing a silicon oxide or SU8 upper cladding), whereas the second one is in contact with the sample to be measured. When a change of the refractive index on the surface of the sensing ring is produced, a small shift is induced in its response. However, this shift will be amplified due to the Vernier effect, thus observing a larger shift in the envelope of the combined response of both RRs. This amplification of the shift will be given by the factor $F = \Delta\lambda_r/|\Delta\lambda_s - \Delta\lambda_r|$, where the *r* denotes the reference RR and *s* the sensing RR.

The shift of the output signal may be measured using a typical spectral-based interrogation method however, they take profit of this shift amplification to place an AWG filter at the output, which spatially separates the output spectrum acting as a discrete spectrometer but with a lower resolution. The envelope of the signal of the Vernier sensor is thus obtained by exciting the structure with a broadband source and measuring simultaneously the output ports of the AWG. Then the output signals are fitted by using a square Lorentzian function similarly than in the regular RR, as shown in Fig. 5.1b.

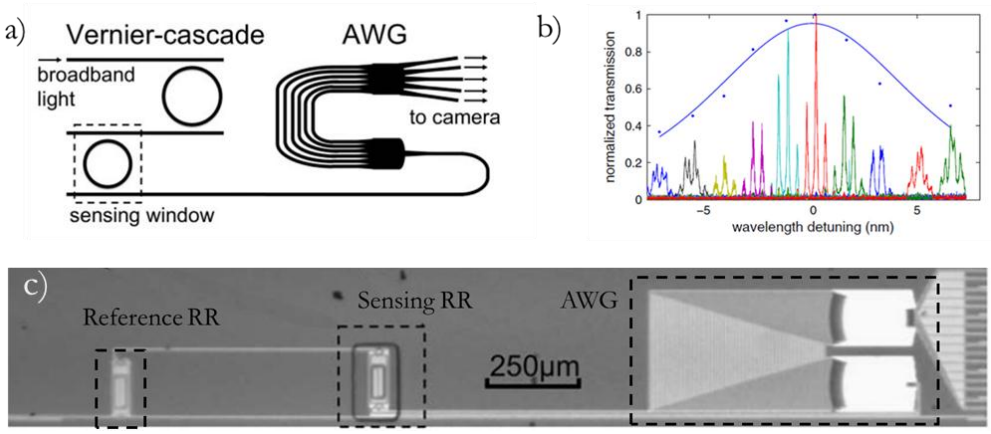

Fig. 5.1: *a) Schematic illustration of the sensing structure proposed in [CLA11] employing two RRs in a Vernier configuration with an AWG filter at the output. b) Transmission spectrum of the structure measured using the output channels of the AWG. c) SEM picture of the fabricated device. The size of the AWG limits the integration level of the structure.*

Employing such configuration, a significant increase of the sensitivity is obtained, reporting a value over 1.000 nm/RIU, what is more than one order of magnitude of typical silicon RR-based sensors. However, although this configuration seems very promising, several issues need to be overcome. The first one is that the "amplification" of the shift of the sensor response does not only provokes an increase of the sensitivity, but also a significant increase of the noise of the system. This fact influences the detection limit of the system, what was reported to be $1.6 \cdot 10^{-5}$ RIU. In order to reduce such noise, a one-minute averaging was applied, leading to a slower measurement and hence preventing from having a real-time measurement. The second drawback of this configuration is the significant increase of the footprint of the sensing device. The area required for the integration of an AWG for each sensor is approximately of 0.25 mm^2, as it can be appreciated in Fig. 5.1c what reduces the integration density in 4 orders of magnitude, thus finishing with the one of the main advantage of planar photonic sensors: their high integration level. Other problem that may be related with the use of an AWG is the significant increase of data that is necessary to acquire and process for the readout of the sensing structure. Since the spectral resolution of the measurement is given by the number of output ports of the AWG, a quite large number of output ports may be required to have a good performance. For instance, in the case of using 16 Vernier-based sensors, each of them with a 16-ports AWG, it would be necessary to analyse simultaneously 256 outputs instead of only 16 for a typical sensor configuration, which would significantly increase the complexity of the system.

A similar configuration was used by a group from Zhejiang University, but in this case, they only measured the intensity of the output of the cascaded RRs by using a simple power meter after exciting the structure with a broadband source [JIN11]. A theoretical sensitivity of $2 \cdot 10^4$ dB/RIU was calculated for this technique; however, that value dropped down to 450 dB/RIU in the reported experiments. This decrement of performance is due to several issues such as variations in the coupling coefficient between the RR and the access waveguide or the intrinsic losses of the structure. Therefore, the performance of the sensing device is quite dependent on fabrication variations, so the robustness of the device is extremely compromised.

A complete new concept of non-spectral-based planar sensing devices is the bimodal waveguide that has been proposed by the group of CSIC CIN2 leaded by Dr. Lechuga. The bimodal waveguide relies on the creation of a 2-level waveguide where two different modes travel simultaneously along it, acting as an interferometer [ZIN11]. The propagating modes have different intensity distribution at the core-cladding interface, what produces a different interaction with the matter on the surface, as depicted in Fig. 5.2. The variation in the output interference pattern is measured by exciting the sensing structure with a monochromatic light and employing a photodiode with two sections placed directly at the output of the waveguide. Since there is no need to implement Y junctions, as it requires other interferometric configurations such as MZI-based

sensors, losses are lower for this device. In addition, since the detection is based on the phase variation of the interferometric signal, the performance of the device is independent of the input light intensity.

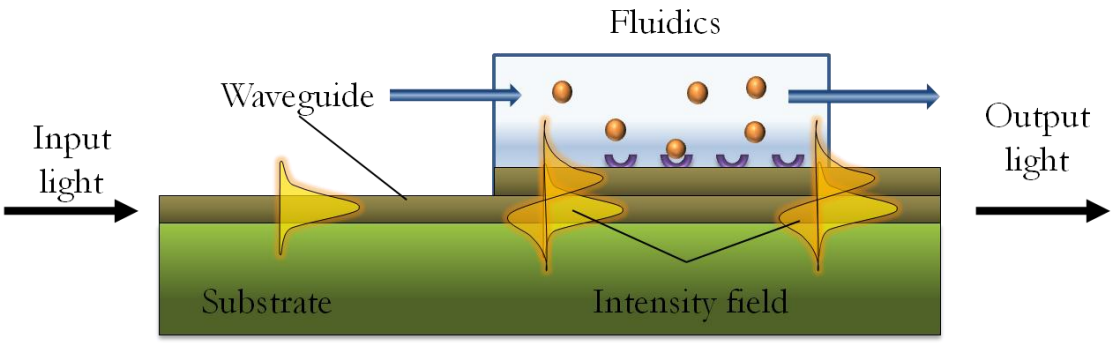

Fig. 5.2: *Principle of operation of the bimodal waveguide sensor. The distribution of the electromagnetic field is different for both propagating modes. Their interaction produces a certain pattern at the output of the structure determined by the interaction of the evanescence wave with the molecules on the surface.*

Using a bimodal waveguide based on a Si_3N_4 ridge waveguide, Dr. Lechuga's group has reported an extremely low detection limit of only $2.5 \cdot 10^{-7}$ RIU for bulk refractive index sensing with a sensitivity as high as $2300 \cdot 2\pi$ rad/RIU. They have also demonstrated its application for label-free biosensing by monitoring the interaction of the couple BSA-antiBSA and the immuno-detection of the human hormone hTSH with a detection limit of 17 ng/ml [DUV12]. However, the main drawback of this configuration is the total length of the bimodal waveguide required to achieve an acceptable sensitivity (e.g., the total length of the bimodal waveguide in the previous work is 25 mm), what significantly reduces the integration level of this photonic sensing approach. In addition, due to the interferometric principle of this sensing structure, the phase of the output signal will be periodic, what can give rise to wrong or ambiguous interpretations. This problem may be solved by implementing a modulation scheme of the laser [DAN12], however, this approach would need to analyse the output signal by using a Fourier transformation, thus increasing the complexity of the interrogation system.

5.3 State-of-the-art of 1D photonic structures for biosensing purposes

As previously mentioned in chapter 3, 1D PhCs are structures consisting in a periodic variation of the refractive index in only one dimension in the direction of the propagation of the

light. In our case, we will focus this section on planar 1D periodic structures since they will be the core of our novel power-based sensing technique. Among these structures, the most popular 1D structures are probably those based on transversal elements (corrugated waveguides), holes in a waveguide and transversal trenches on the structure, all these structures are shown in Fig. 5.3a. This type of structures represent an efficient and intriguing solution for sensing purposes, due to their simpler fabrication and reduced footprint, compared with 2D PhC structures. As it was explained in chapter 3 for 2D PhCs, the periodicity in the propagation direction provokes the opening of a PBG between the guided modes of the structure, as it is shown in Fig. 5.3b. As it was also explained in in chapter 3, the group velocity of the guided modes is reduced at the edge of the Brillouin zone, leading to the slow-light effect. Since the position of the PBG, and therefore the position of the guided modes, depends on the refractive index of the cladding, any refractive index change induced by a molecular recognition event will cause a shift in the spectral response of the structure.

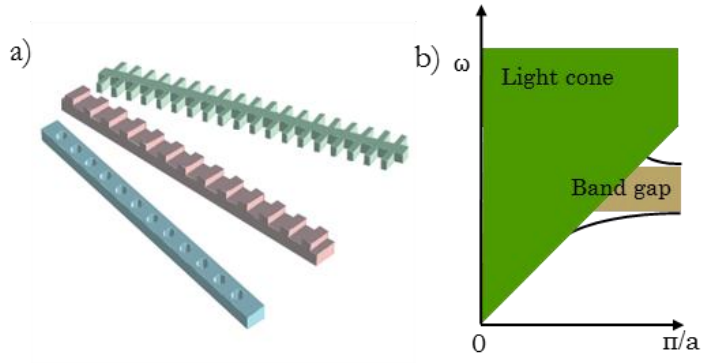

Fig. 5.3: *a) Illustration of different types of planar 1D periodic structures consisting in (from top to bottom) a corrugated waveguide created by inserting transversal elements in a waveguide, a other by inserting transversal trenches in a waveguide, and a1D PhC created by introducing air holes in a single mode waveguide. b) Simplified band structure of a 1D periodic waveguide.*

One of the first theoretical studies of the application of 1D periodic structures for sensing purposes was presented by the Photonics Research Group in Politecnico di Bari by Passaro et al. [PAS08]. In such work, they introduced a mixed numerical approach based on the finite element method and coupled mode theory in order to design a submicrometer integrated optical sensor based on Bragg gratings in SOI technology. The proposed structure consisted of a single mode rib waveguide fabricated in SOI where periodic trenches were etched on the surface. The structure was characterized by its reduced size, which was less than 100 μm^2, thus allowing a high integration density. According to their calculations and assuming a minimum detectable shift of 5 pm, the reported detection limit for bulk refractive index sensing was around 10^{-4} RIU. This value is significantly higher than those achieved for current sensing devices, mainly due to the high

confinement of the electromagnetic field in the lower cladding for the rib architecture waveguide, what reduces the interaction with the target analytes. In addition, one limitation of this structure design is that a second fabrication step is required to create the periodic grooves on the waveguide, since they have a different depth than the regular rib waveguide.

Concerning the experimental demonstration of sensing using 1D periodic structures, Jugessur et al. presented a Nano-Bragg grating sensor fabricated on SOI through e-beam lithography, which is shown in Fig. 5.4 [JUG09]. A PDMS microchannel was used to address the liquid samples to the sensing structures. This PDMS microchannel was sealed on the substrate by instant vacuum. Therefore, it might be peeled off from the chip and, after a proper cleaning procedure, it is possible to reuse both (i.e., the chip and the PDMS microchannel) to carry out more detection experiments. A typical spectral-based interrogation method was employed for the read-out of the sensing structure, obtaining a sensitivity of 180 nm/RIU for bulk refractive index variations.

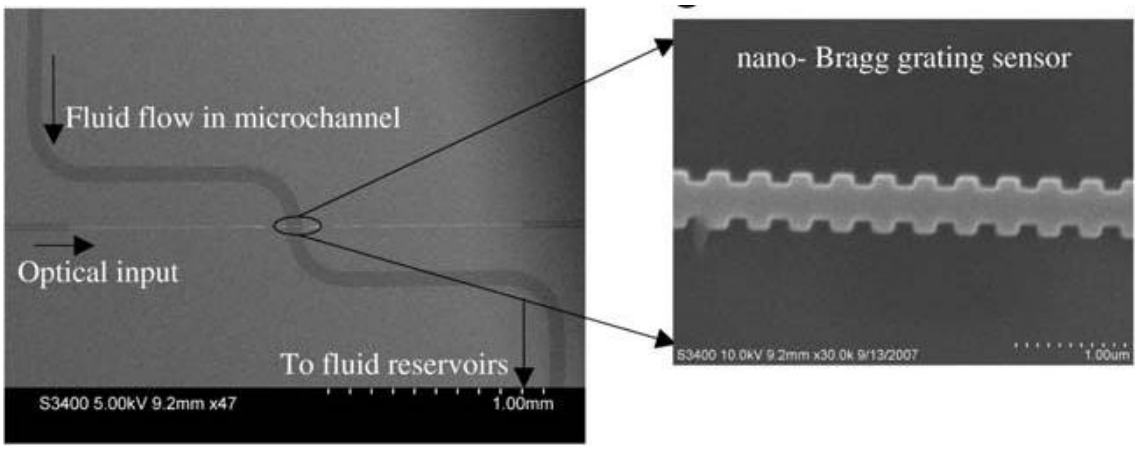

Fig. 5.4: *SEM pictures of the 1D PhC sensing structure with a integrated PDMS microchannel. Close-up view of the nano-Bragg grating sensor. [JUG09].*

In the same context, researchers from the University of Twente also presented a similar 1D periodic sensing structure designed to obtain the bandgap around 1550 nm [KAU09]. The experimental measurements were carried out by spotting a drop of the target sample on top of the chip. By measuring the shift of the bandgap when changing from air to water, they obtained a sensitivity value around 160 nm/RIU. In order to avoid the need of acquiring the spectrum for the interrogation of the sensing structure, what was highly time consuming, they proposed to simply excite the structure at a single wavelength located within the edge of the band edge while continuously measuring the output power. They validated this technique by measuring the power change when a drop of 9% of isopropyl in DIW (v/v) was deposited and while the isopropyl was evaporating. Despite of obtaining good results, one of the main drawbacks of this power-based

monitoring technique is that the band edge of the structure spectrum is not linear, and therefore this non-linearity might affect the response. However, it is possible to perform a calibration of the device in advance. Another limitation is due to the sharp edge of the band used for sensing that will limit the dynamic range of the device (e.g., a maximum shift of 1 nm might be detected in the previous work) and might constrain the applications where it can be used (i.e., those where a large spectral shift is expected). Nevertheless, this is not a dramatic limitation since small spectral shifts are expected for most of the applications targeted by photonic biosensors (e.g., low analyte concentrations, low molecular weights, etc.).

Nevertheless, probably the most advanced sensing results using 1D PhC structures are those reported by Mandal et al. [MAN09]. In this novel optofluidic sensor array (NOSA) configuration, 1D PhC cavity sensors were placed next to a single bus waveguide for their excitation, as shown in Fig. 5.5. The resonant structures consist of a several 1D periodic holes created in a waveguide with a limited length, where the periodicity of the central holes is modified in order to create the cavity. Using this architecture, several cavities with different resonance frequencies can be coupled from a single bus waveguide, thus enabling the possibility to measure several sensing structures simultaneously, as it happened for the "WDM approach" for RRs described in chapter 4. The target sample is delivered to the sensing structures by means of an integrated PDMS-based microfluidic system. With this platform, a total mass detection limit of 63 ag was estimated. Using the couple streptavidin/anti-streptavidin, they characterized the system for a concentration range from 0.01 μg/ml to 100 μg/ml, being able to obtain the kinetic information of the recognition event between the molecules. Furthermore, using this multiplexed architecture, its application for the label-free immunological detection of cancer biomarkers such as interleukins was demonstrated.

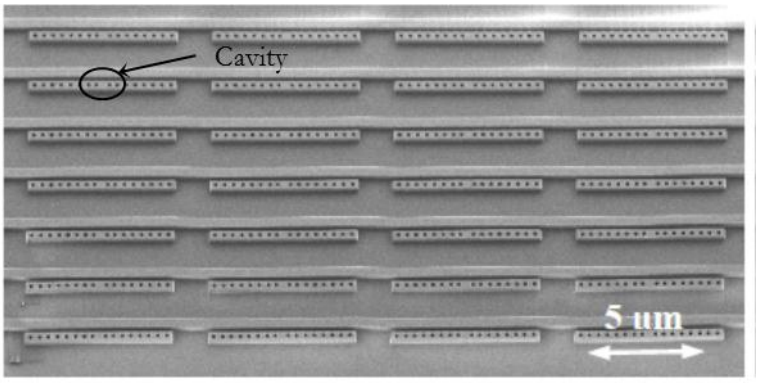

Fig. 5.5: *NOSA architecture in which the central holes of the 1D PhC are shifted to create a cavity [MAN09].*

5.4 Power-based sensing technique using PBG structures

In chapters 3 and 4, we presented our work focused on the development of sensing devices based on 2D PhC and RR structures. However, as previously introduced at the beginning of this chapter, the detection of the presence of the target analyte when using those types of structures is usually based on tracking the spectral position of one or several spectral features, for instance, a PBG or a resonance. Therefore, continuous spectral sweeps are required, as well as the analysis of the spectral response of the structure in order to determine the position of the tracked features. These sensing techniques are well known and there are numerous published works and reviews about them, as it was shown in the sections devoted to the description of the state-of-the-art in chapters 3 and 4. However, although this technique is widely spread among the scientific community, it presents several limitations due to need of either a tunable laser or an OSA to acquire the spectrum. The first restriction is the cost of such equipment, which is expensive, usually being in the range from 20 k€ to 60 k€ depending on the type of equipment (e.g., tunable lasers are usually between 20 k€ and 40 k€, and OSAs use to be above 50 k€) and its performance (i.e., resolution, sweep velocity, possibility to perform continuous sweeps, etc.). Therefore, these costs make difficult obtaining a final commercial system at a competitive price. In addition, such equipment is also bulky and heavy, what makes difficult obtaining a compact and portable device. Furthermore, the spectral sweep of the region of interest can take from seconds to even minutes, thus leading to the impossibility of obtaining a true real-time monitoring of the molecular interactions losing important information. Even though, these times may increase for higher resolution sweeps, which are required to obtain lower detection limits.

In order to overcome all the limitations that we have described above, we have proposed a novel measurement technique simply based on monitoring the output power of a PBG structure that is excited using a filtered broadband source. The working principle of our sensing technique is depicted in Fig. 5.6. Its main objective is to convert the spectral shift of the PBG into power variations, thus being able to determine indirectly the spectral position of the PBG edge. To this aim, a source with a certain bandwidth is used as excitation for the sensing structure, whose PBG edge will be designed to be located within the source bandwidth. At the initial state, a certain amount of power given by the overlap of the source spectrum and the transmission band of the sensing structure is measured at the output of the system. Then, any change in the refractive index produced in the sensing structure either by a molecular recognition event or by bulk refractive index variation will lead to a shift of the PBG position that is translated into a variation of the output power. Hence, by monitoring the output power we can perform an indirect measurement of the PBG position and subsequently to obtain the sensing information.

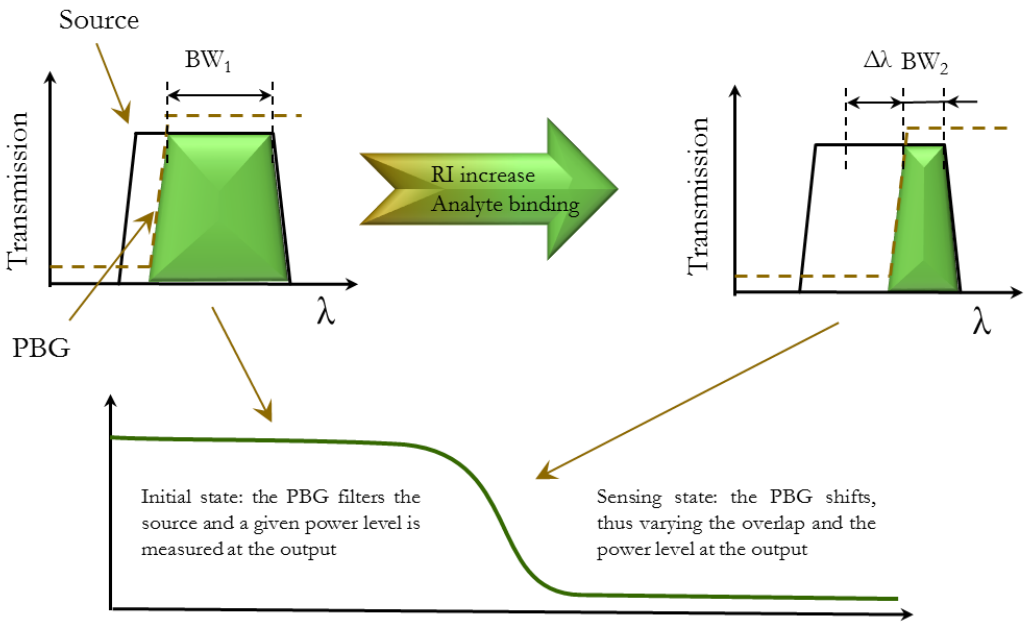

Fig. 5.6: *Schematic representation of the power-based sensing technique. When the PBG edge of the structure is shifted, the amount of optical output power of the device changes. In this manner, the PBG is indirectly measured from the output power variation.*

Therefore, the difference and the main advantage of our proposal compared to typical spectra-based sensing techniques is that there is no necessity to employ any tunable element to continuously acquire the sensor spectrum response and monitor the spectral shift of a feature. As a result, the final sensing system will present the benefits described below:

- **Lower cost read-out system.** Since there is no need to employ a tunable laser or an OSA, the cost of the final system is dramatically reduced. The cost of the equipment required (i.e., broadband source and power meter) will be reduced from several tens of k€ to some k€, which is more than one order of magnitude less.
- **More compact read-out system.** A significant size and weight reduction is also achieved when avoiding the use of a tunable laser or an OSA, what potentially allows the development of portable and even handheld devices for in-situ measurements.
- **True real-time monitoring of the molecular recognition.** As mentioned, spectral-based techniques require obtaining the spectral response of the sensing structure, what can last from some seconds to even few minutes according to the resolution and the velocity of the equipment used (better sweep performances will increment significantly the cost of the equipment and thus of the platform). With our power-based technique, there is no necessity to perform a sweep of the wavelength range of interest, but simply continuously monitoring the output power of the sensing structure. Therefore, we will be able to acquire hundreds or

even thousands data values per second, what allows an instantaneous observation of any binding event that occurs on the surface of the sensing structure.

- **High sensitivity combined with a high information throughput.** The sensitivity of any sensing platform relies on several parameters, which include the intrinsic sensitivity of the transducer, the performance of the functional layer, the noise of the whole system, but also on the interrogation technique. Spectral-based methods require a very high spectral resolution in order to determine the minimum shift detectable, what is translated into longer times to perform each sweep. Therefore, the higher the sensitivity, the slower the measure is. On the other hand, in our power-based read-out technique, wavelength shifts are translated into power variations that are simply measured using a power meter with a short integration time. Normally, the resolution of current photodetectors can easily be in the order of hundredths of dB's, what is sufficient to instantaneously measure very small variations in the refractive index. In addition, a power meter is able to provide hundreds even thousands power values per second, what would permit to perform a simple post processing of the signal in order to reduce the noise and thus enhancing the detection limit even more.
- **Simpler and straightforward system.** Unlike spectral-based techniques, where after the acquisition of the spectral response it is necessary to determine the position of a certain feature, what might not be straightforward, our approach provides the sensing information directly from the output power values without the need of any complex signal analysis or modulations as occur in other techniques [DAN12].
- **Possibility to integrate sources and detectors with the sensing structures.** Since simpler broadband sources and detectors are just needed for the read-out of the sensing structures, they might be directly be integrated within the same chip, thus opening the door of the development of fully-integrated photonic sensor [JAG09, SON13].
- **Insensitive to system losses.** Our method relies in the variation of the output power given by the overlap between the filtered broadband source and the sensing structure. Therefore, the performance of the whole sensing system will be independent of the optical power level of the source and the losses of the system (provided that the output power is enough to be detected by the power meter). However, the sensitivity of the system will be dependent on the initial overlap between the source and the sensor, as it will be described in the next section.

5.4.1 Sensitivity

Unlike spectral techniques where the sensitivity is expressed in terms of nm/RIU, in our power-based measurements the sensitivity will be expressed in terms of dB/RIU, since we measure power variations. Normally, power-based techniques may have the drawback of being dependent on the input power level. However, here we will demonstrate that the performance of our sensing

technique will not depend on the input power level and that the sensitivity will depend on the initial alignment between the source and the sensor. The explanation is schematically depicted in Fig. 5.7. Assuming P_d as the power density of the optical source and BW_1 the initial overlap bandwidth between the source and the sensor, we can obtain the total output power for the initial state, which is the initial overlap. Then, after a certain shift of the bandgap ($\Delta\lambda$) produced either by a bulk refractive index change or by the binding of an analyte, a different output power value will be obtained because of the change of the overlap. From the calculation shown in Fig. 5.7 we can see that the relative output power variation for a given shift will depend only on the initial alignment between the spectral responses of the source and the sensor, thus being independent of the input power level.

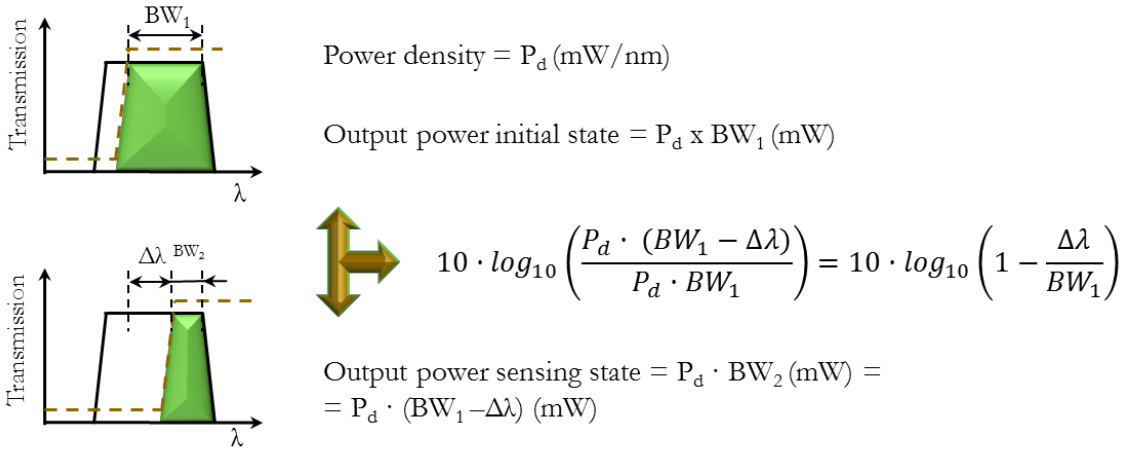

Fig. 5.7: *Schematic explanation of the relative output power variation for a certain initial alignment between the source and the sensor.*

Fig. 5.8 shows the output power evolution of the system according to the expression shown in Fig. 5.7 when wavelength shifts of the sensor's PBG up to 0.2 nm and different initial alignments between the source and the sensor. We can see that the power variation of the system is lower for higher initial overlaps, thus providing a lower sensitivity of the sensing system. However, a linear behavior is observed in this case. On the other hand, as the initial overlap is getting smaller, the sensitivity of the system increases but a more nonlinear behavior is observed. However, this nonlinear behavior might be compensated by performing a proper initial calibration of the sensor. Therefore, a trade-off between sensitivity and linearity is observed for the sensing system, so that we will have to determine the initial overlap depending on the final application of the sensor. Regarding sensitivity values, Table 5.1 shows the simulated sensitivities of the sensing device considering a quasi-linear regime at the initial shift section of the curves shown in Fig. 5.8.

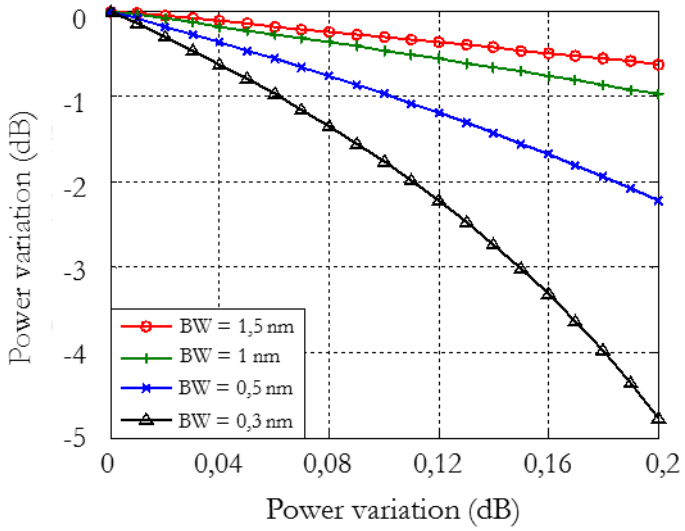

Fig. 5.8: *Power variation vs. wavelength shift for different initial overlaps between the source and the sensor.*

Bandwidth	Sensitivity
1,5 nm	-3dB/nm
1 nm	-4,56dB/nm
0,5 nm	-9,7dB/nm
0,3 nm	-15,8dB/nm

Table 5.1: *Sensitivity values for different initial overlaps between the source and the sensor. The sensitivity value is obtained from the calculations shown in Fig. 5.8 considering a quasi-linear regime at the initial section of the curves.*

5.5 Development of 1D periodic sensing structure

In this section, we will describe the steps followed to determine the 1D periodic structures that were used for the sensing experiments. First, we will indicate the main aspects that need to be taken into account when selecting a 1D periodic structure for sensing purposes. Then, once the configuration of the structure is selected, we will determine its optimal parameters by carrying several simulations out. And finally, the fabrication of the sensing structures will be described.

5.5.1 Selection of the PBG sensing structure

Once we have presented the working principle of our power-based sensing technique, we will focus on the selection of the core photonic sensing structure, which will present a PBG within the bandwidth of the excitation source. As mentioned before, it is possible to employ any structure that presents a sharp PBG within the bandwidth of the optical source; therefore, it would be possible to use any configuration of PhC accomplishing this requirement. However, we initially considered only two main alternatives for the PBG structure in which we have experience: a 1D periodic corrugated waveguide (see Fig. 5.9a) and a holes-on-dielectric 2D PhC (see Fig. 5.9b). Despite some of our previous work was focused on the use of holes-on-silicon PhC waveguides for sensing purposes (as described in chapter 3), we decided to use now 1D corrugated waveguides mainly because of the reasons described below:

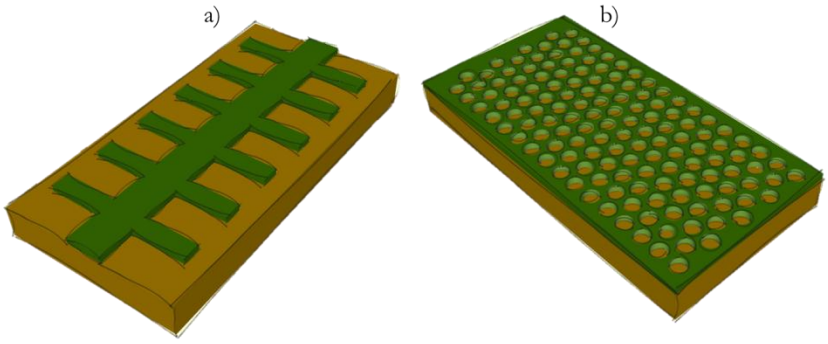

Fig. 5.9: *PhC configurations initially considered for the development of the PBG sensing structures to be employed in our novel power-based sensing technique. a) 1D periodic corrugated waveguide and b) holes-on-dielectric of a 2D PhC structure.*

- **Fabrication complexity**: For the fabrication of photonic structures using e-beam lithography, negative resist and direct writing is preferred for the definition of straight elements, while positive resist and inverse writing is preferred for the definition of networks of holes. For the case of holes-on-dielectric 2D PhCs, which are accessed by means of straight single mode waveguides, positive resist and inverse writing, is used, what is not optimal for the creation of the access structures. Therefore, the fabrication of 1D corrugated waveguides will be simpler, since negative resist and direct writing can be used to create easily the waveguide and the transversal elements on it.
- **Propagation and coupling losses:** Although guided modes of PBG structures are ideally lossless when working below the light line of the substrate, the real implementation of this kind of structures will exhibit propagation losses determined by several mechanisms. Undoubtedly, the most important loss mechanism is related to fabrication imperfections. The non-ideal position of the periodic elements, the variation in their dimensions and sidewall roughness are the main causes of back reflection and scattering of the light, what

will cause the main propagation losses. The higher simplicity of the 1D corrugated waveguide, where simply straight elements are periodically placed in the single mode waveguide, will reduce these effects (as explained in the previous point, the fabrication is simpler). In addition, the transition from guided modes in the access structure to the PBG structure will cause a mode mismatching that will be higher as we get closer to the slow-light regime of the PBG structure. In order to reduce the influence of this non-desirable effect, a tapered transition is introduced between the access waveguide and the PBG structure. For the case of the corrugated waveguide, the taper can be created simply by gradually reducing the width of the periodic transversal elements.

- **Sensor footprint:** SOI platform permits to design structures with a reduced size. In the design of 2D PhC structures it is required to fabricate several periods of holes in the transversal direction in order to obtain the desired PBG effect in that direction, usually leading to transversal sizes above 10 μm. Contrary, 1D periodic structures does not require these long widths in the transversal direction, but simply widths in the order of 1-2 μm, thus providing a footprint reduction of almost one order of magnitude compared to 2D PhC sensing structures.
- **Simulation cost:** From the designer point of view, besides the physical implementation of the sensing structure, it is also necessary to take into account the computational cost required to simulate the structures during the design phase. As we introduced in chapter 3, several simulation tools can be used to design PhC structures; however, in this case we have only used FDTD since we were interested on obtaining the spectral response of the photonic structure and not only the spectral position of the bands and the PBGs. The computational cost of this method is highly dependent on the simulation region, and therefore the use of 1D periodic structures with smaller footprint significantly reduces the calculation time.

To summarize, the selection of the PBG sensing structure is not as straightforward as choosing between a holes-on-dielectric 2D PhC structure or a 1D corrugated waveguide, as we have done in our case. In fact, a variety of PBG periodic structures can be considered to look for an optical configuration. However, we have decided to limit our selection to these two alternatives considering our previous experience in the use of both of them. Regarding the final decision, we have selected the 1D corrugated waveguide because it exhibits a simpler geometry, what is translated into a simpler fabrication process and to lower losses than 2D PhCs, and because its smaller footprint, what leads to a higher integration level and to a lower simulation cost in the design phase. For these reasons, we consider that 1D corrugated waveguides are the most suitable option to demonstrate our power-based sensing technique.

5.5.2 1D periodic structure configuration

Once we decided to use a 1D corrugated waveguide as sensing structure, we continue with the design of its physical parameters. This design process mainly looked at four main requirements: having the edge of the PBG located around 1550 nm, exhibiting a sharp PBG edge, obtaining a high interaction of the optical field with the matter and having a good coupling between the access waveguide and the 1D corrugated waveguide. The 1D corrugated waveguide is defined by a set of physical parameters that are depicted in Fig. 5.10. Namely, the structure consists of a waveguide of a height *h* and width *w*, in which several transversal elements of length w_e and width w_i are inserted along the waveguide with a periodicity *a*. In order to reduce the complexity of the design process, some of these parameters were initially fixed according to different constrains as it will be indicated along the next paragraphs, where the design process is described.

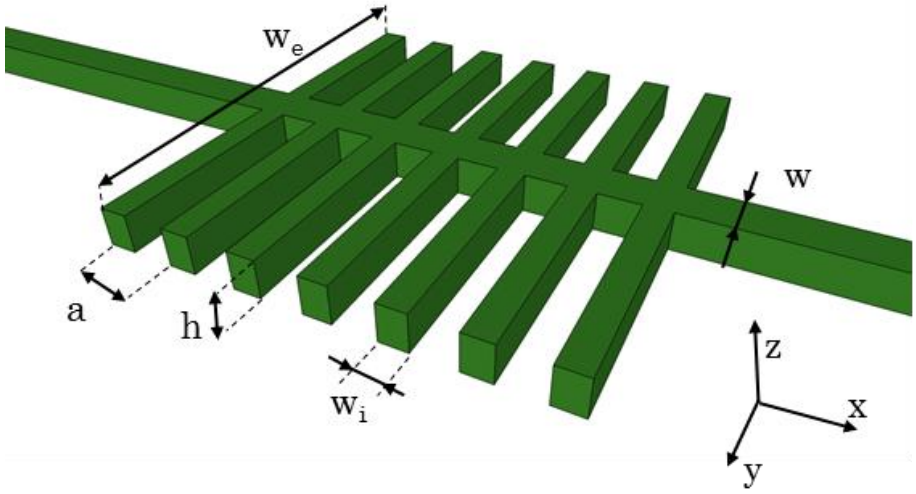

Fig. 5.10: *Schematic illustration of the proposed corrugated waveguide with its main parameters.*

The first aspect to take into account for the design of the corrugated waveguide is to define the refractive index of the materials comprising the structure. In our case, we continued using the SOI platform for the creation of the corrugated sensing structures therefore, we used a refractive index of 3.45 for the silicon, 1.45 for the silicon oxide lower cladding, and of 1.33 for the liquid upper cladding (we considered that the target analytes will be diluted in aqueous solutions with refractive indices in this range).

Regarding the dimensions of the single mode waveguide where the transversal elements will be introduced, we employed a standard waveguide of 220 nm of height (determined by the thickness of the silicon layer of the SOI wafers to be used for the fabrication) and 450 nm of width.

Prior to start with the FDTD simulations of the structure, we theoretically modeled the corrugated waveguide in order to obtain a first approximation for the dimensions of the structure. In this way, we will avoid excessive trial and error simulations that may increase significantly the time employed to design the structure. These calculations have been extracted from A. Brimont's PhD thesis, which was focus on the application of corrugated waveguides for the modulation of optical signals [BRI12].

A 1D periodic structure accomplishes the Bragg condition, where the back and forth reflections provoke the appearance of a PBG, which accomplish the following equation:

$$\mathrm{a} \cdot n_{eff} = \frac{\lambda_{Bragg}}{2} m \tag{5.1}$$

where a is the Bragg period of the structure, n_{eff} is the effective index of the optical mode, m is the order of the mode (in our case it will be 1) and λ_{Bragg} is the wavelength of the PBG. Due to the 1D periodicity of the structure and the changes in the transversal width of the structure, where the effective index of the optical mode will be different, the equation is changed to:

$$\mathrm{d}_1 n_{eff1} + \mathrm{d}_2 n_{eff2} = \frac{\lambda_{Bragg}}{2} m \tag{5.2}$$

where d_1 is the width of the narrow section and d_2 is the width of the wide section (i.e., where the transversal elements are placed, w_i). It is noteworthy that Eq. 5.3 is simply an approximation that will provide us a starting point for the subsequent FDTD simulations. From previous experience, we expect that the optimal duty cycle of the structure is in the order of 33% (i.e., the narrow part of the corrugated waveguide is about 2 times longer than the transversal element). Hence, the equation will be:

$$\mathrm{a} \cdot (0.66 \cdot n_{eff1} + 0.33 \cdot n_{eff2}) = \frac{\lambda_{Bragg}}{2} m \tag{5.3}$$

And finally, by solving the equation for the Bragg period we obtain:

$$\mathrm{a} = \frac{\lambda_{Bragg}}{2 \cdot (0.66 \cdot n_{eff1} + 0.33 \cdot n_{eff2})} m \tag{5.4}$$

In this point, we only need to calculate the effective indices of the propagating wave for both transversal sections of the corrugated waveguide. This calculation has been made using the RSoft's BeamPROP vectorial mode solver. A height of 220 nm has been considered for both sections of the waveguide. A width of 450 nm has been used for the narrow section of the corrugated waveguide. However, we still need to define the width w_e of the transversal elements of the corrugated waveguide. In order to avoid the influence of slight variations in the width of the

transversal elements due to the fabrication, a value significantly larger than that of the width of the single mode waveguide was selected; we chose 2 μm for w_e, which is 4 times larger than the width w of the narrow section, and won't influence in the result. Fig. 5.11 depicts the fundamental mode for each waveguide section. The grid resolution of the simulation was set to 10 nm, what was sufficient to obtain the effective indices of both structures. The result of the calculation of the effective indices are 2.3 and 2.79 for the narrow and the wide sections, respectively. By substituting this values in Eq. 5.4, we estimate a Bragg period of 317.79 nm. This value is a starting point for the design of the corrugated waveguide.

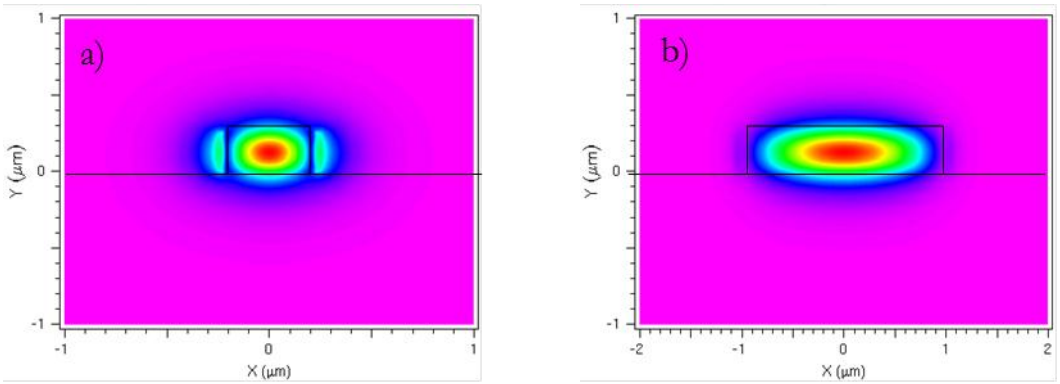

Fig. 5.11: *Cross section of the mode profile propagating through the (a) 450 nm and (b) 2 μm long sections of the corrugated waveguide at 1550 nm. The height of both waveguides is 220 nm. The calculated effective indices for both cross sections are 2.3 and 2.79, respectively.*

At this point, we have already fixed the value for several parameters of the structure, including the height of the structure (h = 220 nm), the width of the waveguide (w = 450 nm) and the width of the transversal elements (w_e = 2 μm). An approximated value has been determined for the period of the structure (a in the range of 320 nm) and a duty cycle of around 30 % has been considered in order to have the PBG around 1550 nm. Now, several 3D FDTD simulations were carried out employing the commercial software RSoft's FullWAVE in order to determine specific values for the period of the structure (a) and the length of the transversal elements (w_i). An initial range for these two parameters was set considering fabrication constrains in order to avoid very small features (w_i > 90 nm was selected) and small separation between the transversal elements to reduce proximity effects ($a - w_i$ > 150 nm). After an initial iteration of coarse simulations for these two parameters, we finally decided to set the parameters range of a = [320 nm – 400 nm] and w_i = [90 nm - 170 nm].

One last parameter of the structure that we need to set for the simulations is the number of elements that conforms the periodic structure. Our idea is to fabricate the structure with 101 transversal elements in order to obtain a good PBG effect and with a sharp edge. However, the 3D FDTD simulation of a structure with this size would lead to a high CPU consumption and require

times of several days or even more. Therefore, in order to perform a reasonable modeling of the corrugated waveguide using 3D FDTD simulations with a prudent complexity and time requirement, we first studied the number of corrugations that are necessary to obtain an acceptable response with a relatively short simulation. Fig. 5.12 shows two simulations of the same corrugated waveguide with 10 and 20 transversal elements. We can see that different PBGs appear in the range 1400-1700 nm, being the first of them (i.e., that around 1500 nm) deeper and with sharper edges. The position of both PBGs is the same for both simulations. However, as expected, the more elements comprising the corrugated waveguide, the deeper the PBGs and the sharper their edges are. The time employed for the 10 elements corrugated waveguide was around 20 hours, while the elapsed time for the 20 elements corrugated waveguide was around 30 hours. Despite the periodic structure with more elements employs significantly more time, the higher accuracy of the obtained spectral response justifies our selection of using corrugated waveguides of 20 elements for the rest of simulations.

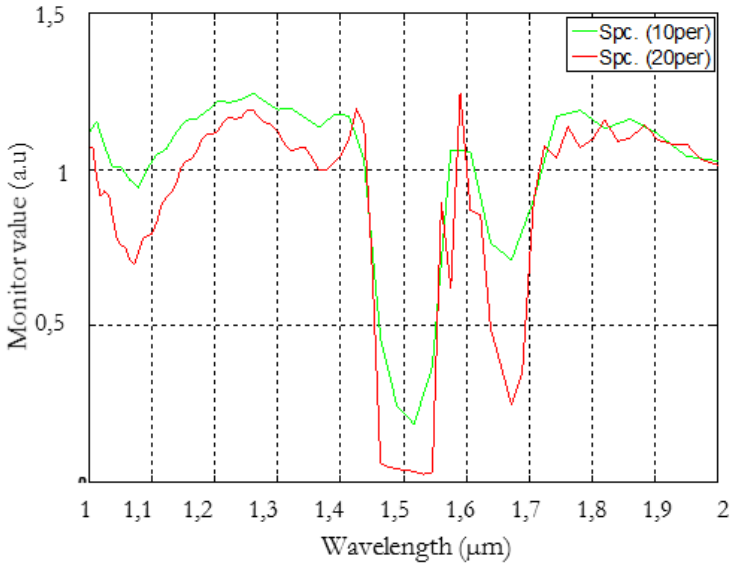

Fig. 5.12: *Comparison of the output spectrum for a corrugated waveguide with two different numbers of transversal elements. The parameters of the simulation were: a = 350 nm, w = 450 nm, h = 220 nm, w_e = 2 μm, w_i = 150 nm.*

The simulation parameters and conditions used for the calculations, which will also be used for the rest of simulations, are:

- 3D calculations were carried out. Despite of 3D simulations have a significantly higher computational cost, the accuracy of their results makes this approach totally worthy to determine the dimensions of the corrugated structure.

- The edges of the simulation window were configured as perfect matching layer (PML) with a width of 500 nm in order to absorb any electromagnetic field and avoid non-desirable reflections that may interfere in the spectral response.
- A non-uniform grid was used, with a different grid size depending on the structural parameters of the structure. The size of the grid in each axis was: $\Delta x = 25$ nm, $\Delta y = 30$ nm and $\Delta z = 20$ nm.
- Since the FDTD software solves the Maxwell's equations along time steps, we need to set sufficient time steps in order to allow the propagation of the optical wave along the whole photonic structure and to collect all the reflections produced during that time. The time step of the simulation was set to $4 \cdot 10^{-7}$ s, what is less than the minimum value recommended by the software for the simulations. A total time of 1500 s in order to obtain a spectral resolution between 0.5 nm and 1 nm in the wavelength region of interest.
- TE response of the structure was calculated.
- The excitation source was configured as a Gaussian pulse centered at 1550 nm.
- Finally, a time monitor was located at the end of the corrugated waveguide in order to measure the output power and perform the Fast Fourier Transform (FFT) of the temporal signal in order to obtain the response in the spectral domain.

In order to reduce the time required to carry out all the simulations initially proposed, we employed a cluster formed by four computers, what allowed us to reduce the simulation time from around 30 hours to less than 15 hours. Due to the great number of simulations carried out, a customized script was developed in order to automatically run the simulations for the different values of the a and w_i parameters using a step of 20 nm. Fig. 5.13 shows an example of the simulated spectral response for a set corrugated waveguides with a corrugation length w_i of 130 nm and different periods. As we can see, the position of the PBGs is shifted to higher wavelengths as the period increases. As previously commented, the PBG appearing at lower wavelengths is deeper and with sharper edges; therefore, we selected this PBG for being used with our power-based sensing technique.

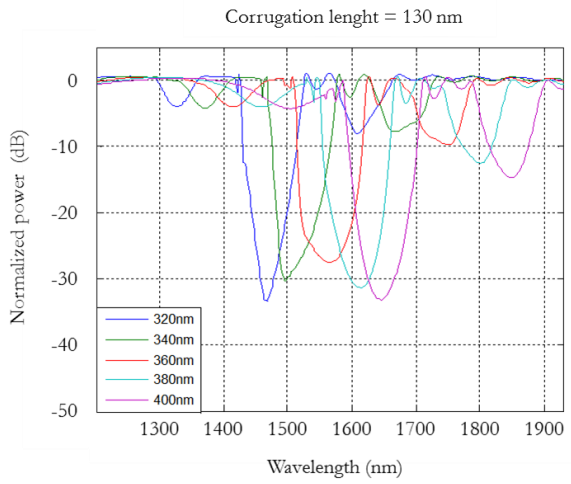

Fig. 5.13: *Simulated transmission spectra of the corrugated waveguide for a length w_i of 130 nm and periods from 320 nm to 400 nm.*

From the two edges of the PBG, we selected to use the upper edge for our power-based sensing technique. In order to determine the configurations of the corrugated waveguide showing their upper PBG edge at 1550 nm we developed a Matlab-based program to analyse the 3D FDTD simulations carried out. Fig. 5.14 represents the position of the upper PBG edge as a function of the period and the w_i parameters for two different upper claddings (n_1 = 1.33 and n_2 = 1.40). The configurations providing an upper PBG edge located around 1550 nm are depicted with a white line.

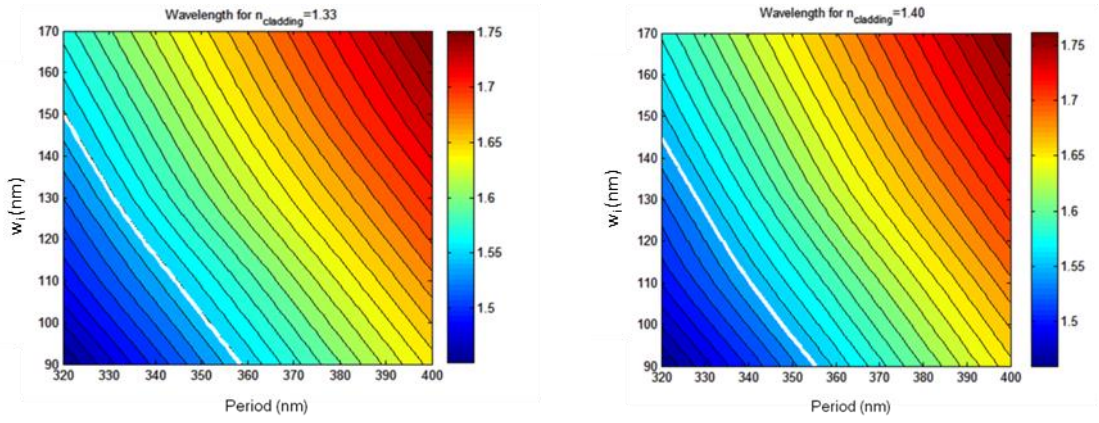

Fig. 5.14: *Contour plot of the upper PBG edge of the corrugated waveguide as a function of the period of the structure and the length of the transversal elements for an uppercladding of a) n = 1.33 and b) n = 1.40.*

The variation of the upper PBG edge when the refractive index of the upper cladding is changed is used to determine the sensitivity of the structure according to the equation:

$$Sensitivity = \frac{\Delta\lambda}{\Delta n_{uppercladding}} \tag{5.5}$$

where $\Delta\lambda$ is the shift of the upper PBG edge and $\Delta n_{upperclading}$ is the refractive index variation of the upper cladding. Fig. 5.15 shows the sensitivity of the corrugated waveguide as a function of the period and the length of the transversal elements. As we can see, the sensitivity is highly dependent of the combination of these parameters, since the specific configuration of the corrugated waveguide will determine the distribution of the optical field that will interact with the upper cladding. Hence, we need to choose wisely the design in order to obtain higher sensitivities. In addition, we also need to take into account the constraint of the wavelength position of the PBG edge in order to be placed around 1550 nm, what has been depicted with a green line.

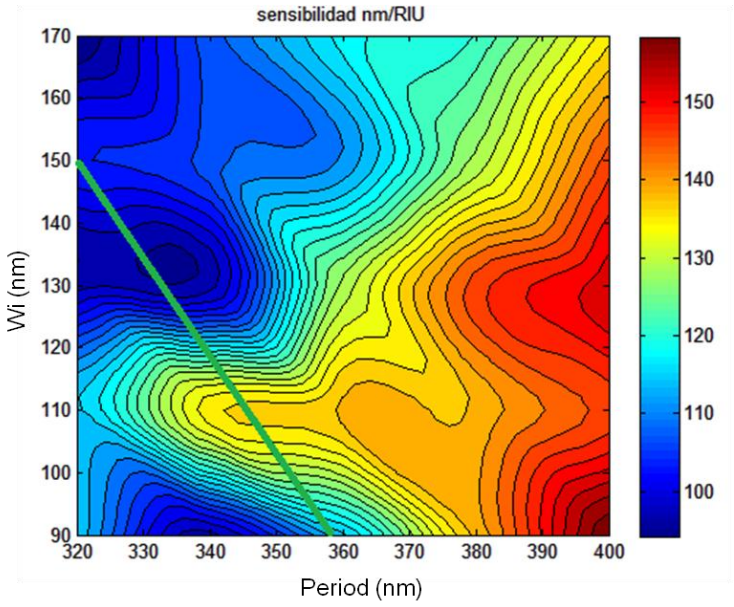

Fig. 5.15: *Calculated sensitivity for the upper PBG edge of the corrugated waveguide. The green line represents the configurations with the upper PBG edge at 1550 nm for an upper cladding of n = 1.33.*

From the previous calculations, we can conclude that the most sensitive configuration of the corrugated waveguide with its upper PBG edge around 1550 is that with a period around a = 340 nm and with an element length around w_i = 110 nm. Although such configuration is potentially the optimal waveguide to fabricate, we finally decided to also include a sweep of the period and the element length in the fabricated corrugated waveguides. Table 5.2 summarizes the parameters selected for the fabrication of the corrugated waveguides.

Parameter	Dimension
w	450 nm
h	220 nm
w_e	2 μm
w_i	110 nm - 170 nm
a	300 nm - 420 nm

Table 5.2: *Summary of the parameters selected for the fabrication of the corrugated waveguides.*

5.5.3 Fabrication of the corrugated waveguides

Once the theoretical response of the sensing structures was determined by means of 3D FDTD simulations, we proceeded with their fabrication. In this case, we decided to use the services of an external CMOS fabrication service that allows the simultaneous fabrication of many repetitions of the design on the same wafer. This factor is important for sensing applications, where the chips are subject of an intensive experimentation, since it allows using a new chip for each experiment. More concretely, we made use of the ePIXfab cost-shared fabrication platform [EPI13], which is co-funded by the EC by means of the FP7 framework. The ePIXfab fabrication platform is participated by IMEC, whose fabrication services were used for the fabrication of the RR sensors used in chapter 4, and by CEA-LETI, whose fabrication services were used in this case for the fabrication of the 1D corrugated waveguides. More information about CEA-LETI can be found in its website [CEA13].

The fabrication process used by CEA-LETI for the fabrication of the photonic structures is schematically illustrated in Fig. 5.16, and it is basically the same procedure that was described for the fabrication by IMEC in chapter 4, therefore here it will be simply summarized. First, a SOI wafer with a silicon thickness of 220 nm on a 2 μm-thick layer of buried silicon oxide is coated using a positive photoresist that will be used to transfer the design of the photonic structures. The resist is baked to obtain the suitable properties for the exposure step. Then, the photomask with the designs to be transferred is placed over the wafer and the area corresponding to the chip is illuminated by UV-light through the mask[3]. The illumination process is repeated over the whole wafer to create the repetitions of the chip. As previously commented in chapter 4, the main benefit of the UV lithographic procedure is the ability to fabricate multiple structures at the same time with a single exposure. However, the minimum resolution of the fabrication process will be limited to ~

[3] The designed mask did not only contain the designs of the 1D corrugated sensing structure, but the area of the chip was shared with other researchers from the NTC in order to include more photonic structures for different purposes.

100 nm due to the optical diffraction during the UV exposure step. After the illumination of the designs over the whole wafer, the development of the resist provides a hardmask on top of the silicon. Then, an etching step is used to transfer the designs to the silicon layer. Finally, the resist mask is removed and the wafer is rinsed to remove any material residue. A second lithography + etching cycle was carried out to fabricate the grating couplers in the waveguides. In this case, a partial etch of the silicon layer was carried out (etch depth of 70 nm). Once the fabrication has finished, a protective layer is deposited over the wafer; this layer can be removed easily employing acetone, isopropyl and DIW.

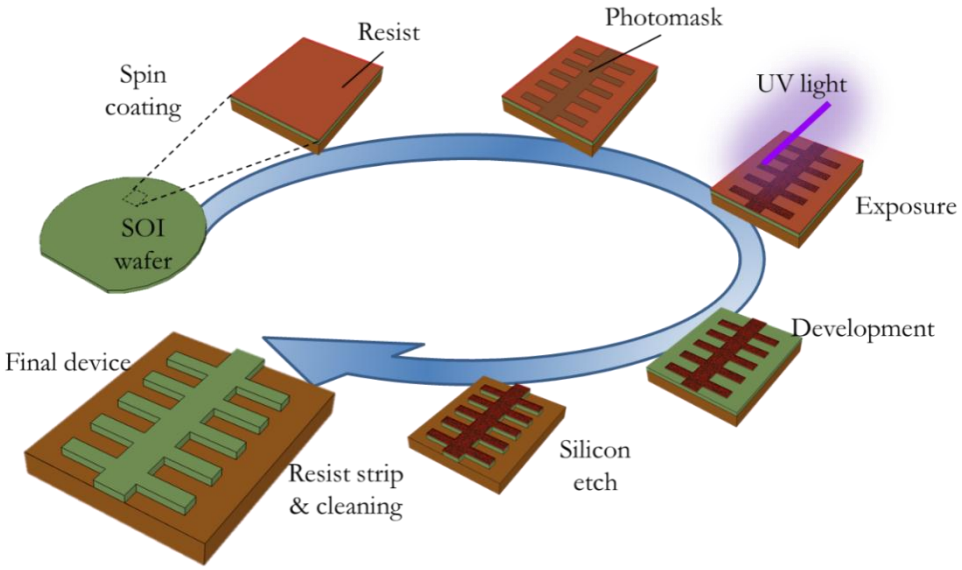

Fig. 5.16: *Schematic representation of the fabrication process used in CEA-LETI to create the photonic structures.*

Two wafers were fabricated using different exposure conditions (mainly changes in the dose were considered) in order to study the effects in the shape of the structures. Fig. 5.17 shows SEM pictures of different corrugated waveguides with the same period and different length w_i of the transversal elements, where different exposure doses were used. We can see that smaller features (e.g., transversal elements) are obtained for higher exposure doses. This is because, since the trenches surrounding the photonic structure are the areas exposed when using a positive photoresist, the size of these areas will increase when increasing the exposure dose, thus leading to smaller features in the silicon. More concretely, we can see in this case that the transversal elements of the corrugated waveguide are totally distorted for a dose of 25 mJ (they have a higher roughness and they even disappear when their theoretical width is 130 nm). On the other hand, the quality of the features is optimal when using a dose of 16 mJ (simply the edges of the transversal elements are slightly rounded due to intrinsic limitations of the fabrication process using UV lithography).

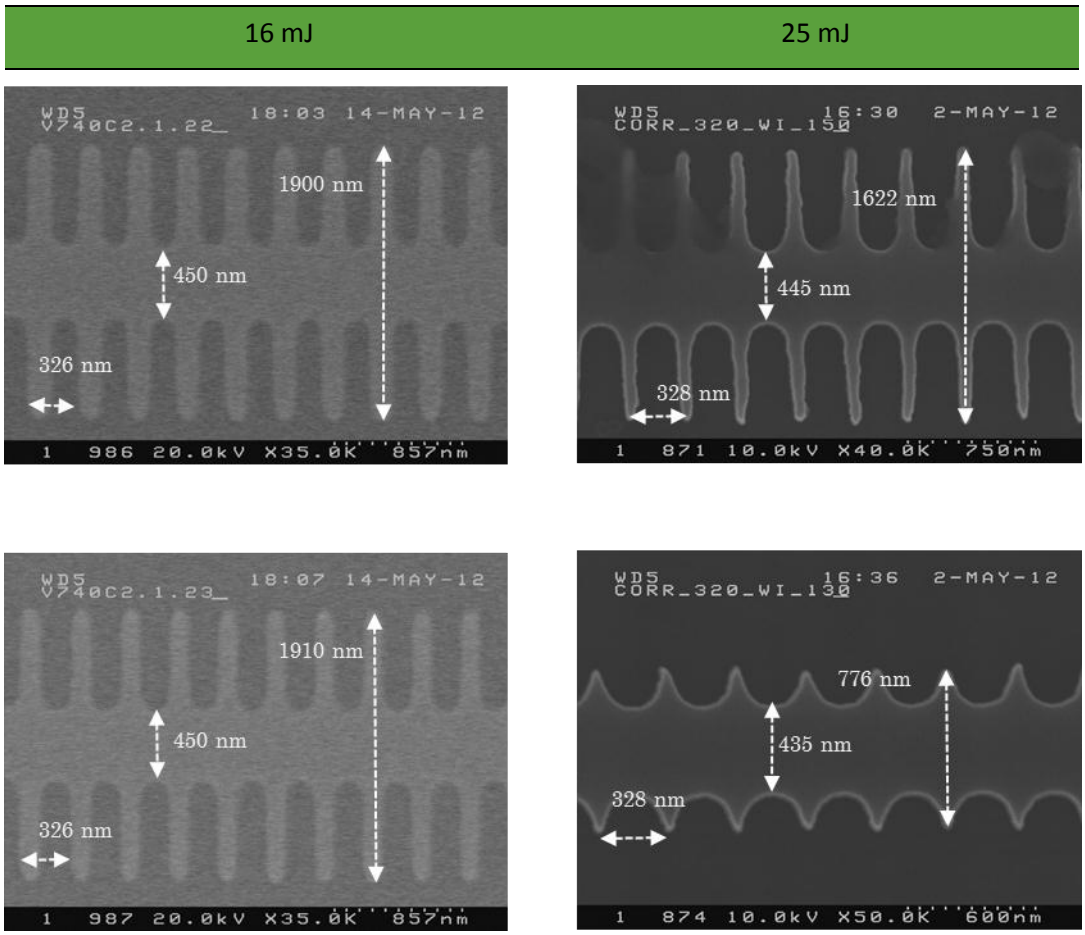

Fig. 5.17: *SEM pictures of corrugated waveguides with different length of the elements and different exposure dose. The left column was fabricated using an exposure dose of 16 mJ whereas in the right column the exposure dose was 25 mJ.*

Regarding the coupling of light to the corrugated waveguides, we included two repetitions of the designs in the chip: one where the corrugated waveguide with the desired dimensions is directly created in the single mode waveguide, and another where a 5-element linear taper was used as a transition between both waveguides, as it is shown in Fig. 5.18 . As we described in chapter 3, non-desired reflections will appear at the interfaces between access waveguide and PhC structures, what will reduce the coupling efficiency between them and will affect to the spectral response of the photonic structure through the appearance of FP ripple. Nevertheless, this effect can be reduced by designing a proper taper at the interface between the access and the corrugated waveguides. The taper that we have created to enhance the coupling between both waveguides simply consists of a linear increment of the width of the transversal elements, as it is shown in Fig. 5.18. It is worth noting the influence of the UV fabrication resolution in those elements located at the edge of the taper, which have a smaller feature size. Fig. 5.19 shows the transmission spectra for two different repetitions of the same configuration of corrugated waveguide, one of them with transition taper and the other without it. We can see that the quality of the spectrum is clearly

improved when using the access taper, since we obtain a lower ripple in the transmission band and a better PBG.

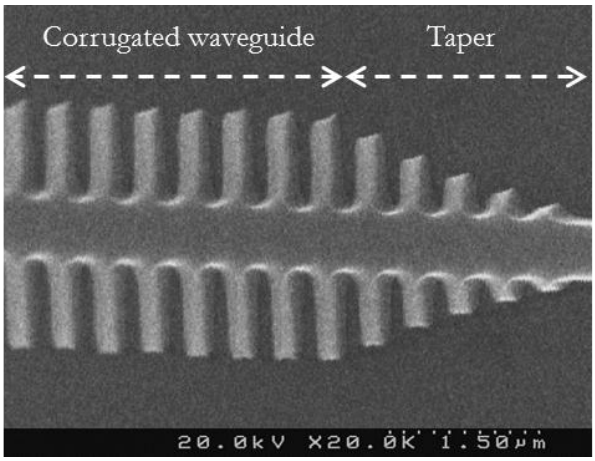

Fig. 5.18: *SEM image of the taper used for enhancing the transition between the single mode waveguide (access waveguide) and the corrugated waveguide.*

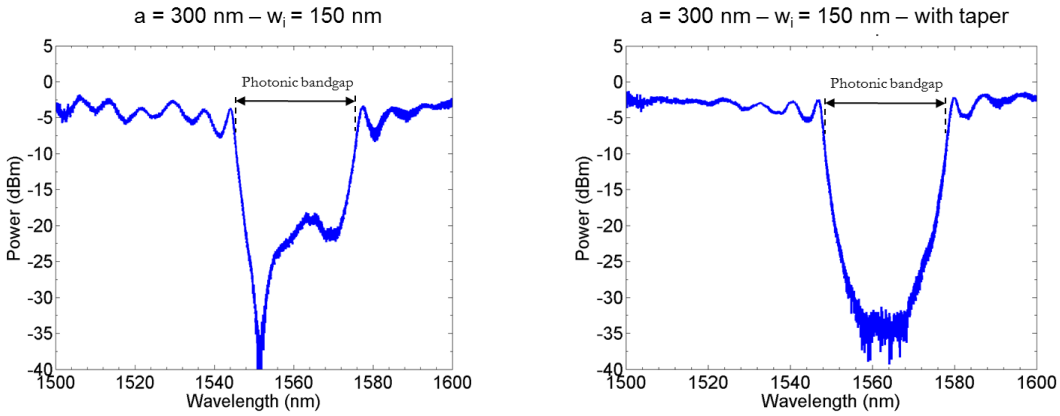

Fig. 5.19: *Transmission spectra of a corrugated waveguide of a = 300 nm and w_i = 150 nm without and with a linear taper of 5 elements.*

Finally, we optically characterized the fabricated corrugated waveguides in order to obtain their spectra. A similar optical set-up to that introduced in chapter 4 was used, where light from an optical broadband source was vertically coupled in/out to the chip using single mode optical fibers, and the spectrum was acquired using an OSA. Since the photonic corrugated waveguides were designed to work in an aqueous environment, we spotted a drop of DIW on top of the structures before acquiring their spectra. The responses of the corrugated waveguides were normalized respect to a single mode reference waveguide in order to remove the spectral response of the grating couplers and the source. Fig. 5.20 shows the transmission spectra for the corrugated waveguides on a given chip for the different dimensions that were considered. The response of structures with the

same period (and different length of the transversal element w_i) are plotted together. As we can see, the position of the PBGs of the corrugated waveguide depends on the w_i parameter as well as the period *a*. For example, for a given period parameter, a shift around 30 nm in the spectral response is observed when a variation of 20 nm in the parameter w_i is produced. Therefore, we have the possibility to select the wavelength range of the corrugated waveguide depending on the parameters of the structure.

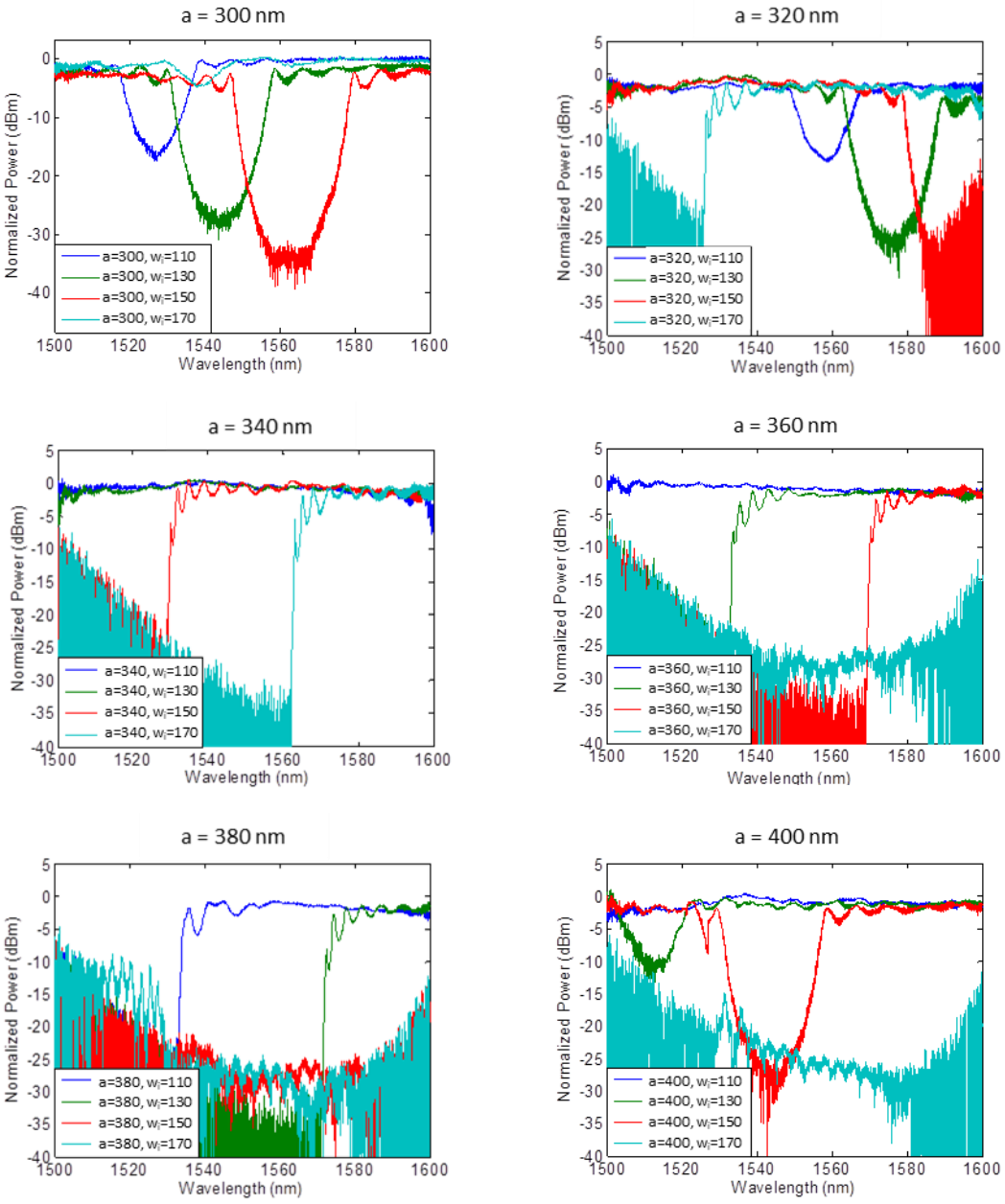

Fig. 5.20: *Transmission spectra for corrugated waveguides with a period from 300 nm to 400 nm, and varying the w_i parameter from 110 nm to 170 nm. All the responses are for tapered structures and with DIW as upper cladding.*

5.6 Experimental set-up

5.6.1 Optical interrogation

The experimental set-up employed for the interrogation of the sensing structures using the proposed power-based technique, which is schematically depicted in Fig. 5.21, was based on the set-up previously introduced in chapter 4 for the interrogation of the RR-based sensors. However, two major differences are introduced now: the use of a broadband source and a broadband detector for the optical interrogation, and the use of a SU8-based microchannel for sample delivery. Since the elements and the operation of the set-up were detailed in chapter 4, herein we will comment only the modifications required to adapt it for the new interrogation technique.

The most relevant difference of this set-up compared to those previously introduced in this PhD thesis is how the optical interrogation is carried out. While a tunable laser and a broadband power meter were used for the interrogation of the PhC-based sensing structures in chapter 3, and a broadband source and an OSA were used for the interrogation of the RR-based sensing structures, here we will simply use a broadband source (the same SLD source used for the interrogation of the RR-based sensors, with a bandwidth of ~60 nm and centered at ~1550 nm) and a power meter (the same power meter used for the interrogation of the PhC-based sensors). Therefore, the use of the tunable elements required for the spectral interrogation in the previous experiments is avoided. Additionally, since for our sensing technique we need to employ a limited-bandwidth optical source, a band-pass filter was used to reduce the bandwidth of the SLD source. As it will be indicated in section 5.7, where the experiments carried out will be described, we have used both a fixed FBG filter and a tunable interference filter from DiCon with a bandwidth of 3.2 nm and a tuning range from 1530 nm to 1560 nm approximately. Filtered input light will be TE-polarized before coupling it into the photonic chip using grating couplers, and it will be collected at the output with a second optical fiber in order to take it to the power meter.

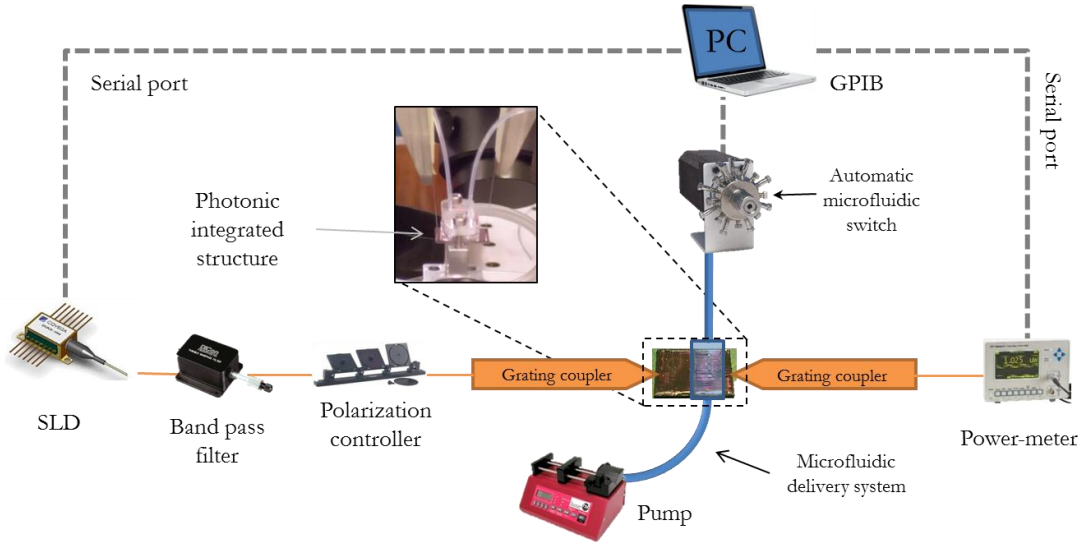

Fig. 5.21: *Schematic representation of the whole experimental set-up employed for the power-based measurements.*

Before starting the experiments, it was necessary to align properly the PBG edge of the sensing structure with the spectral range of the filtered source in order to obtain the overlap required between both responses. For that purpose, we first measured the spectral response of both the filter and the corrugated waveguide separately. For the case of using a fixed FBG filter, we looked for a configuration of the corrugated waveguide that exhibited a PBG edge located within the FBG filter bandwidth. For the case of using the tunable optical filter, we simply tuned it in order to match the position of the PBG edge of the selected corrugated sensing structure, what allowed an easier and more tolerant interrogation procedure.

Once the filtered optical source was aligned with the PBG edge of the sensing structure, the output light received by the power meter was continuously monitored[4] using a custom-made LabVIEW program where the output power was represented as a function of time. Besides the simplification in the equipment required for the interrogation of the photonic sensing structures (i.e., no tunable elements are required), another important advantage of the proposed scheme is that the sensorgram is directly obtained by monitoring the output power without the need to process any spectrum. Therefore, any refractive index change induced either by a bulk variation or by a molecular recognition event will be directly observed without the need of any signal analysis.

5.6.2 Fluidic delivery system based on SU8 and PDMS

Regarding the fluidic sample delivery, the same system to that explained in chapter 4 for the interrogation of the RR-based sensors was used (i.e., a combination of a syringe pump working in withdraw mode and an automatic microfluidic switch to change between the samples to be

[4] Tens of power values per second were usually acquired in the experiments carried out.

flowed). However, instead of using a metallic flowcell (as for the PhC-based sensors) or a PDMS-based microchannel (as for the RR-based sensors), this time we directly created by UV lithography a SU8-based microchannel on top of the photonic sensing structures, as it schematically represented in Fig. 5.22a. Then, the SU8 microchannel was closed using a PDMS lid with two holes in order to inject the fluids in and out. This type of microfluidic approach has several advantages including the higher accuracy in the alignment between the sensing structures and the delivery microchannel, and the fact that the SU8 layer provides a protective layer for the other photonic structures (e.g., waveguides, couplers, junctions). However, it requires an additional fabrication step for the fabrication of this type of microfluidic system.

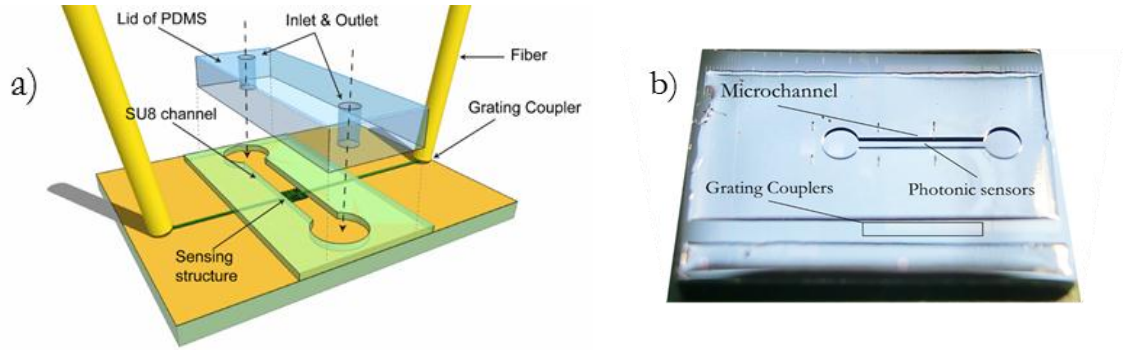

Fig. 5.22: *a)Schematic illustration of the sensing structure with the integrated SU8-based microchannel and a lid of PDMS with two access holes. b) Picture of the photonic chip with the SU8-based microchannel of a width of 400 µm and a height of 50 µm. The resist also offers a protective layer for those structures that must be isolated from the sample.*

A picture of a real SU8-based microchannel is shown in Fig. 5.22b In more detail, the microchannels were fabricated on top of the photonic chip using a variety of SU8 photoresist with a thickness of 50 µm (SU8-2050). After cleaning the chip using acetone and isopropyl alcohol, a layer of SU8 was created onto the chip by spin coating. Then, it was hard baked during 3 minutes at 95ºC. In order to reduce the cost of the fabrication process for the creation of the microchannels, a laser-printed plastic mask was employed for the UV exposure instead of a more expensive chrome and quartz mask. The microfluidic structure was created in order to have the photonic sensors exactly placed in the center of the channel, where the flow of the fluidic sample is completely homogeneous. The channel was then etched vertically using SU8 developer. Two reservoirs were also created in order to facilitate the transition of the stream between the access tubing and the microchannel. The grating couplers were out of the SU8 layer in order to enhance the light coupling between the fibers and the integrated waveguides (it is worth noting that the SU8 is transparent at 1550 nm, so the grating couplers will still work if being covered by the SU8 layer).

5.7 Experimental sensing results using the power-based technique

5.7.1 Bulk refractive index sensing

For the experimental demonstration of our power-based sensing technique, firstly we studied its application for the realization of bulk refractive index sensing experiments by flowing different salt concentrations in DIW, as we previously did for the PhC-based and the RR-based sensing structures described in the previous chapters. This type of experiment will allow us to characterize the bulk performance of this sensing approach and compare it with those approaches based on the spectral-based interrogation of PhC and RR sensing structures measured previously.

For this experiment, we employed a SOI corrugated waveguide as PBG sensing structure in the set-up described in section 5.6, with its upper PBG edge around 1550 nm for a DIW upper cladding. The dimensions of the 1D corrugated structure to achieve such response were w = 450 nm , h = 220 nm, w_e = 2 μm, w_i = 110 nm and a = 380 nm. SEM images of the structure are shown in Fig. 5.23. The fluidic architecture used to deliver the sample to the sensing structures was implemented by a SU8 microchannel closed with a lid of PDMS, as it was described in the previous section.

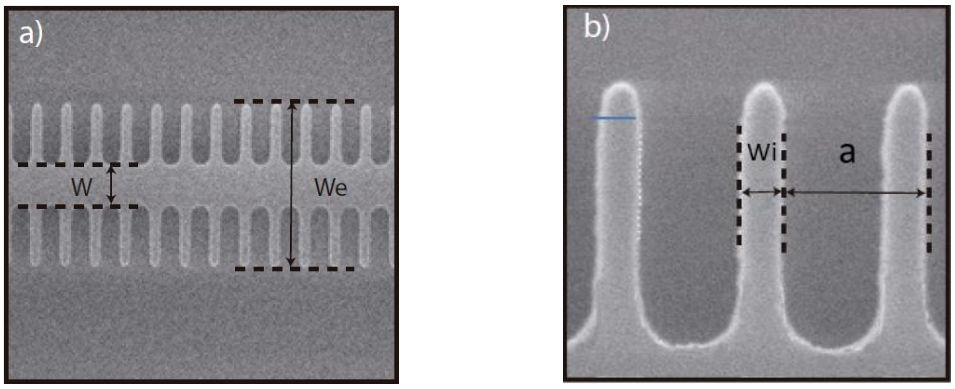

Fig. 5.23: *SEM images of the SOI corrugated waveguide used for the validation of the proposed power-based sensing technique. a) Overview of the corrugated and b) close up view of the transversal elements.*

In order to obtain the limited-bandwidth optical excitation required for the proposed interrogation technique, we filtered our SLD broadband source (with a bandwidth of ~60 nm) using a Chirped Fiber Bragg Grating (CFBG) with a bandwidth of approximately 2 nm and centered in ~1543 nm. The CFBG was developed and fabricated by researchers from the Dpto. de Física Aplicada y Electromagnetismo from Universitat de València. The CFBG was defined by UV

exposure using a uniform phase mask and a proper combination of continuous fiber stretching and UV scanning movements to induce the periodic variation in the refractive index of the fiber [PER08]. The length of the CFBG was 50 mm and it had a reflectance of 95% that makes it suitable for its use as a band pass filter. The normalized responses of the CFBG filter and the corrugated sensing structure with a DIW upper cladding are represented in Fig. 5.24. We can see that the position of the PBG edge of the sensing structure is within the spectrum of the filtered source. Finally, note that since the CFBG worked in reflection mode, we needed to use a circulator to filter the signal from the SLD source with the CFBG.

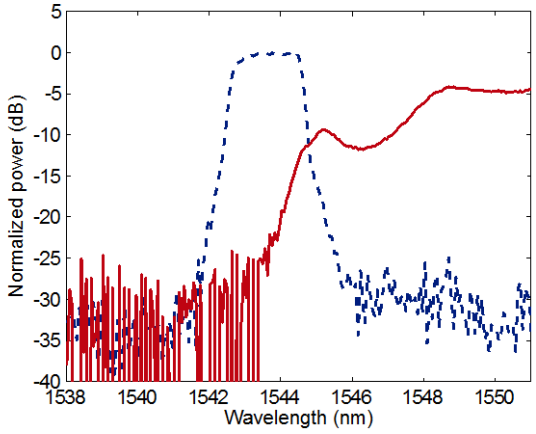

Fig. 5.24: *Normalized transmission spectra of the corrugated waveguide sensor with a DIW upper cladding (solid red line) and the CFBG-filtered optical source (dashed blue line)*

To carry out the refractive index sensing experiments we used several NaCl dilutions in DIW with concentrations ranging from 0.25% to 1% in mass. As it was indicated in chapter 4, the refractive index variation for NaCl-DIW dilutions at room temperature is Δn_{NaCl} = 0.001715 RIU/% for concentrations below 10% at 1550 nm. Fig. 5.25 shows the temporal evolution of the output power of the sensing device when switching among different those dilutions. It can be seen that for the configuration of the power-based read-out technique selected, an output power reduction occurs as the NaCl concentration increases, due to the increase of the refractive index in the upper cladding that leads to a redshift of the PBG edge position, and thus decreasing the overlap. Fig. 5.26 shows the sensitivity curve of the sensing device, where the output power variation is plotted as a function of the refractive index variation. We can see that an extremely high sensitivity value has been obtained, 1786 dB/RIU. Furthermore, although a non-linear behavior was expected from the modeling done in section 5.4.1, in this experiment we observed a good linearity due to the small refractive index changes that we were measuring (in fact, small variations is what we will be interested in measure since our main aim is to detect the presence of small concentrations or analytes).

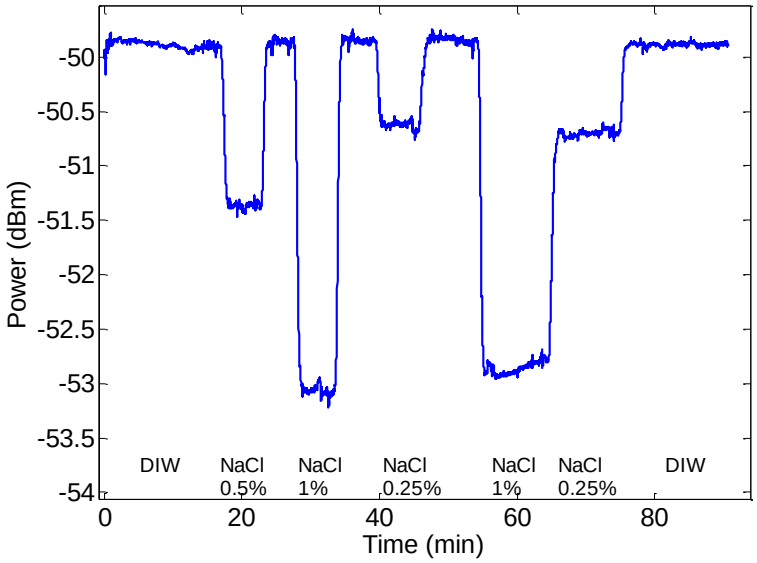

Fig. 5.25: *Time evolution of the output power during the flow of different NaCl concentrations. The increase of the NaCl concentration induce a redshift of the PBG edge that leads to a decrement of the overlap between the source and the sensor responses.*

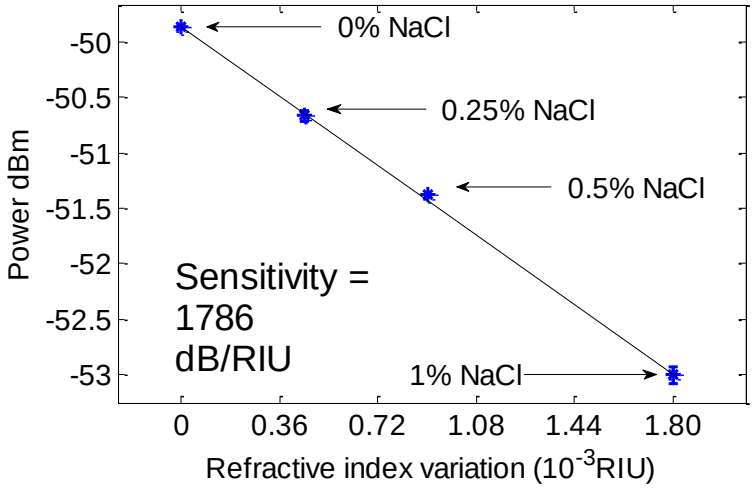

Fig. 5.26: *Sensitivity curve of the sensing device.*

The integration time of the power meter was set to 300 ms. This value is a compromise between the noise and the number of samples per second (the lower the integration time is, the higher the noise of the system is). We also measured the standard deviation of the output signal at different stages of the experiment in order to determine the detection limit at each stage. The values obtained are listed in Table 5.3. We can see that the standard deviation is different for each case, but it is independently related with the output power (e.g., a reduction of the output power does not produce an increment of the system noise). Therefore, the relationship observed between the output power and the noise level is probably determined by the specific experimental conditions at

each moment. For example, the lower noise level is achieved for the pure DIW flow, probably because no particles are diluted on it. On the other hand, the increment on the system noise when NaCl is diluted in DIW is attributed to the non-homogenous distribution of the salt and not to the decrement of the output power. Considering these noise levels for the whole sensing platform (in the range of $\sigma \approx 0.01$ dBm), which include the noise of the source, that of the detector, temperature variations and the power stability, a detection limit of $5.65 \cdot 10^{-6}$ RIU was obtained. However, this value can be further reduced by simply performing an output signal averaging. In the case of averaging 100 points of the raw power values recorded, we can reduce the noise and thus the detection limit to values below $2 \cdot 10^{-6}$ RIU.

Step	Output power	Noise
DIW	-49,85 dBm	σ=0,0085 dBm
0,25 % NaCl	-50,6 dBm	σ=0,0144 dBm
0,5 % NaCl	-51,4 dBm	σ=0,0117 dBm
1 % NaCl	-53,1 dBm	σ=0,0101 dBm

Table 5.3: *Output power and noise values for different NaCl-DIW dilutions flowed in the experiment.*

Finally, we have also characterized the spectral sensitivity of the 1D corrugated waveguide used for the previous experiments. As we have seen, it might be difficult to compare the sensitivity results obtained with our power-based approach with those obtained using typical spectral-based sensing methods, since different units are used (dB/RIU vs. nm/RIU). Fig. 5.27 shows the spectrum of the corrugated sensing structure for different NaCl-DIW dilutions, where we can clearly see how the PBG shifts to larger wavelengths due to the increment of the salt concentration. A maximum shift of ~263 pm is produced when the dilution of 1% of NaCl is flowed over the sensor, what is translated into a spectral sensitivity of the corrugated sensing structure of 153.3 nm/RIU. This sensitivity is slightly lower than the one obtained for the 2D PhC sensors described in chapter 3 (174.8 nm/RIU) and almost twice that for RR sensors described in chapter 4 (82.78 nm/RIU). Therefore, we can see that the higher complexity of PhC-based sensors, together with the slow-light effect occurring on them, allows achieving significantly higher sensitivities compared to RR-based sensors. But, in addition, the use of a spectral-based approach for the interrogation of PBG-based sensing structures significantly limits their performance due to the difficulty of accurately determine the position of the PBG edge. For example, we estimated a detection limit of the order of 10^{-5} RIU for the corrugated waveguide considering the spectra shown in Fig. 5.27, what is one order of magnitude worse than the value obtained using the proposed power-based sensing technique.

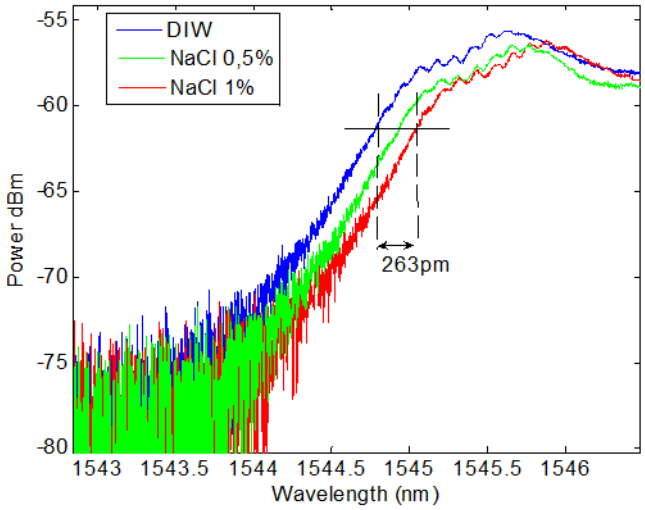

Fig. 5.27: *Shift of the transmission spectra of the corrugated waveguide for different NaCl-DIW concentrations.*

5.7.2 Comparison between power-based and spectral-based interrogation methods

In the previous section, we have demonstrated the ability to detect variations of the refractive index by employing the proposed power-based measurement technique. However, as previously commented, it is difficult to make a comparison between the performance of the power-based and the spectral-based sensing techniques. Therefore, to demonstrate the potential of our new system we studied the detection of several antibody concentrations by employing both interrogation techniques simultaneously in order to directly compare their performances.

First, a slight variation of the configuration of the set-up was needed in order to measure simultaneously the signal using both methods. In this case, the optical filter was not placed right after the broadband source and before the input of the chip, but it was placed at the output of the chip, before the power meter. This configuration is analogous to the one with the filter at the input, but with this configuration, we can measure the transmitted spectra and the overlap at the same time. In this case, we employed a Dicon band pass filter, which can be tuned over several nm, instead of using the CFBG used in the previous experiment. Furthermore, the signal at the output of the chip was divided in two arms using a splitter, so one arm (90%) was taken to an OSA in order to make a spectral-based interrogation and the other signal (10%) was filtered and connected to the power meter in order to make the power-based interrogation. The new configuration of the set-up is depicted in Fig. 5.28.

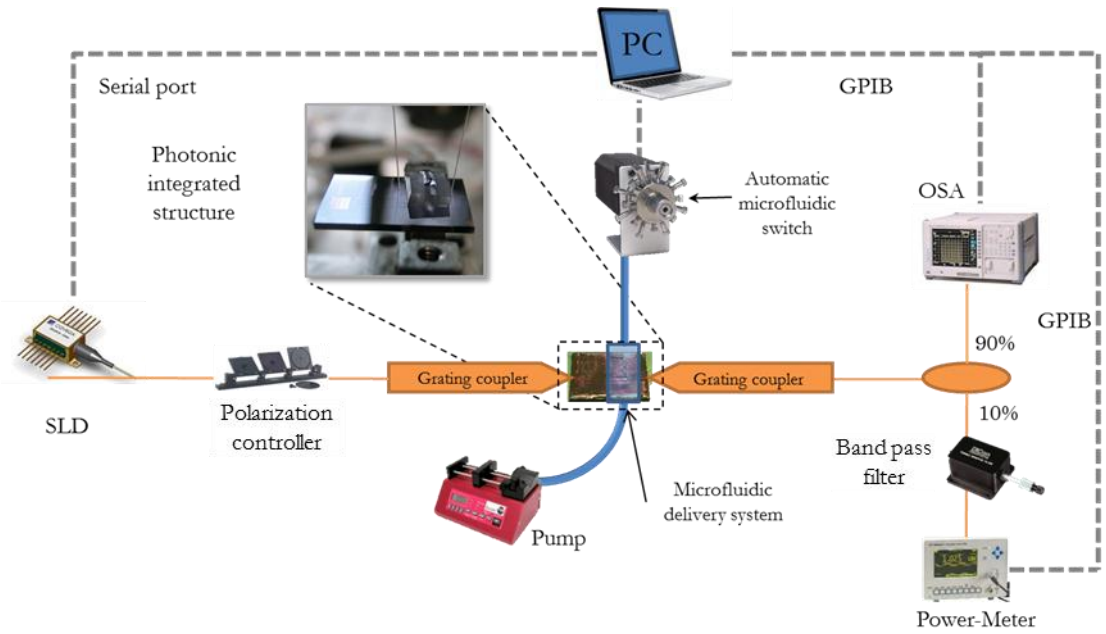

Fig. 5.28: *New configuration of the set-up for carrying out the comparison of the spectral-based and the power-based methods. The main difference is the insertion of the filter at the input of the power meter instead in the output of the source.*

The experiments carried out to perform this comparison between both sensing techniques consisted in the detection of antiBSA antibodies using BSA antigen receptors on the chip surface, as it has been used repeatedly in chapters 3 and 4. For that purpose we employed a corrugated waveguide whose parameters are a = 360 nm and w_i = 120 nm, which exhibits a PBG around 1558 nm. The functionalization procedure was based in the ICPTS chemistry described extensively in chapter 2. Basically, the chip was initially cleaned with piranha solution in order to remove any organic residue and increase the concentration of OH groups in the silicon native oxide of the structure. After the activation of the surface, we carried out the functionalization process in-line (i.e., by flowing the reagents through the SU8 microchannel), which consisted in the silanization of the surface by flowing 5% ICPTS in 2-propanol during 30 minutes, and the flow of a concentration of 10 μg/ml of BSA antigen during 50 minutes. Finally, the chip was rinsed with PBS 1x in order to remove non-bounded molecules and the isocyanate moieties were blocked by flowing a concentration of 0.1 M of ethanolamine in PBS 1x.

Once the surface of the sensor was coated with the BSA probes, two concentrations of antiBSA antibody were flowed in order to perform the detection and study the behavior between both methods. First, PBS 1x was flowed until obtaining a stable baseline, and then we injected the concentration of antiBSA (10 μg/ml first and after regenerating the sensor with NaOH, 100 μg/ml was also injected). Fig. 5.29 shows the sensorgram of the PBG biosensor response for the binding of the antiBSA antibodies to the attached BSA molecules using simultaneously both interrogation

techniques. From the curves shown in Fig. 5.29, we can confirm that the sensor response is equivalent for both read-out techniques. Therefore, it is demonstrated that the power-based interrogation technique allows us to make truthfully an indirect track of the wavelength shift of the sensor PBG edge.

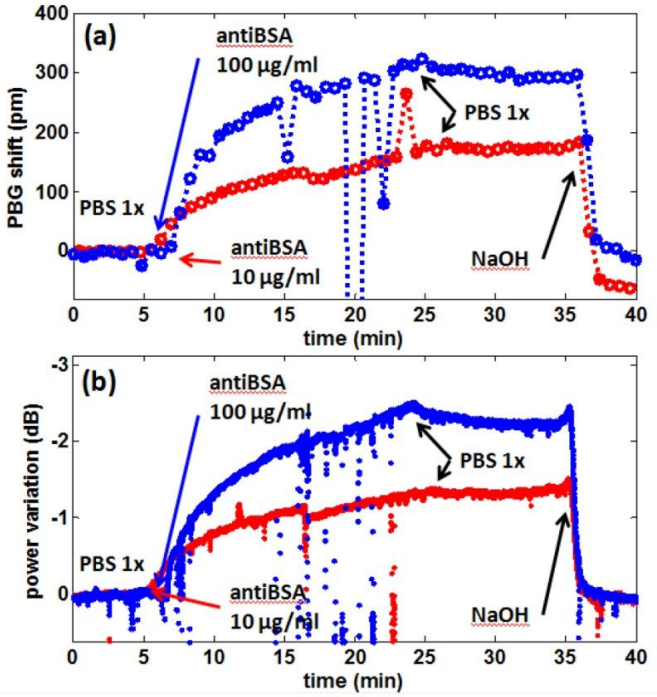

Fig. 5.29: *Time evolution of the PBG biosensor response using (a) a direct spectral-based read-out and (b) our indirect power-based read-out. For both read-out methods, red and blue points depict the output signal for 10 µg/ml and 100 µg/ml of antiBSA, respectively. Arrows indicate the instant of each injection.*

Below, we list several of the main benefits of our power-based sensing technique that can be deduced from the results shown in Fig. 5.29, and which confirms those predicted in section 5.4:

- **Lower cost read-out system:** While the excitation source was the same for both interrogation methods (i.e., a broadband SLD source), the main difference in the equipment between both methods was the detector. The spectral-based interrogation used an OSA with a cost around 50 k€ whereas our power-based interrogation simply used a power meter with a cost below 3 k€ (although other power meters significantly cheaper can be found). Therefore, the cost reduction is significant.
- **More compact read-out system:** The OSA used for the interrogation had a size of 425 (W) x 222 (H) x 450 (D) mm and a weight of 30 kg, while the power meter had a size of 133 (W) x 216 (H) x 308 (D) mm and a weight of 5 kg. Despite the size and weight reduction is not

extremely significant in this case, more compact and lightweight power meters can be found, being even possible to integrate the power detector within the photonic sensing chip.

- **True real-time monitoring of the molecular recognition:** Using the power-based readout technique we can obtain a significantly higher number of sensing data points compared to the case of the spectral read-out. In this specific experiment, the spectral-based method obtains one data point each 42 seconds (i.e., this is the time required to acquire each spectrum with a resolution of 10 pm using the OSA). Whereas the power-based method allows acquiring ~10 points per second, what means an increase of the temporal resolution of more than 100 times when using this lower-cost and simpler approach. This higher temporal resolution enables to perform real-time measurements with a practically instantaneous detection of any event produced in the surroundings of the structure. This is not only useful for the detection of any interaction event between molecules, but also to remove more easily any artifact produced during the experiment without affecting significantly to the sensor performance and perform more complex data analysis. For example, this is the case for the results shown in Fig. 5.27, where several microbubbles have flowed over the sensor and have distorted the measurement (see the response for the antiBSA concentration of 100 μg/ml). For the spectral-based method, we can see abrupt dips in the time positions 17, 20 and 22 minutes; due to the appearance of these "bad" points we are not having sensing information during almost 2 minutes, what is not acceptable. However, for the power-based method, we can observe that the significantly higher temporal resolution allows us to instantaneously recover the position corresponding to the binding curve immediately after the microbubbles have passed through the sensor; therefore, it will be possible to track the signal perfectly without losing any relevant sensing information.
- **High sensitivity combined with a high information throughput:** As we have seen in the previous point, using the power-based read-out technique we will have a higher data throughput (i.e., we have higher temporal resolution) with an optimal performance of the output signal detection (i.e., for the spectral-based readout, a higher spectral resolution always implies longer times to obtain the spectrum). Furthermore, the fact that significantly more data points are recorded at the output using our power-based technique permits to reduce the system noise, and thus the detection limit, by simply temporal averaging.
- **Simpler and straightforward system:** For the spectral-based technique, the position of the PBG edge needs to be determined for each sweep. This determination might not be easy and straightforward and some kind of fitting should be performed. This fact can be seen in Fig. 5.29, the not fully abrupt shape of the PBG edge makes difficult to determine its position with accuracies in the pm range (as required to have low detection limits). On the other

hand, the power-based technique provides directly the sensing signal, so there is no necessity to perform any type analysis of the signal from the sensing structure.

Finally, note that the performance of the sensing structure used in this experiment was not very good (e.g., a shift below 200 pm is observed for an antiBSA concentration of 10 μg/ml, what is relatively high concentration). However, the aim of this experiment was to demonstrate the correlation between both interrogation techniques, compare their practical performance, and show that our interrogation method is a potential competitor for the development of future photonic-based sensing platforms. Nevertheless, better performance will be obtained by properly selecting the photonic sensing structure and its functionalization procedure.

5.7.3 Antibody sensing

Once in the previous section we experimentally demonstrated all the benefits envisaged for the proposed power-based sensing technique, we used this method for the detection of lower antiBSA antibody. As we observed in the previous experiment, the performance of the selected sensing structure was not optimal. Therefore, here we have used another corrugated waveguide to carry out the antibody sensing experiments with other functionalization protocol that provided better results in terms of detection.

In this case, we decided to make the ICPTS-based chemical modification of the chip off-line (i.e., the reagents were not flowed but incubated. Briefly, the SOI sensing structures were first cleaned with piranha solution in order to activate the surface and then the samples were functionalized with pure ICPTS deposited by CVD during two hours at room temperature. Then, the samples were rinsed with 2-propanol, dried with air, and cured in oven during 10 minutes at 150ºC in order to remove the moisture of the chip. A concentration of BSA solution of 25 μg/ml in carbonate buffer (CB) was spotted on the sensing structures and incubated during 2 hours at room temperature in a controlled environment to avoid the evaporation. After the incubation, the chip was rinsed with PBS-T in order to remove all the non-attached BSA molecules and subsequently blocked with ethanolamine. Additionally, the lid of PDMS and the tubes were blocked with OVA before starting the experiments in order to prevent the adsorption of the analytes.

Fig. 5.30 shows the initial spectrum of the filtered source and, the PBG sensing structure, which consisted of a period of a = 320 nm and a length of w_i = 120 nm, whereas the other parameters are identical to the previous experiments. The spectrum was recorded with PBS 1x as upper cladding (it will be the buffer used in the experiments). The signal at the output of the sensing structure, which is given by the overlap of both responses and will this output signal will provide the sensing information, is also depicted.

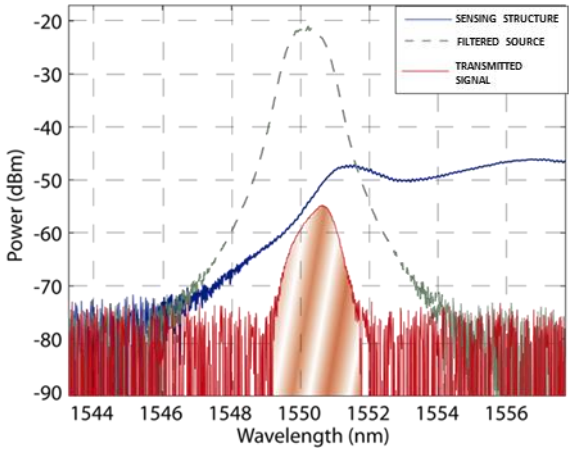

***Fig. 5.30**: Initial spectra of the filtered source (dashed green line), the PBG sensing structure (solid blue line) and the overlap between them at the output of the photonic sensor (shaded area).*

The scope of this experiment was to demonstrate the feasibility of our proposed interrogation method for the detection of several analyte concentrations and performing a regeneration step between each of them. For that purpose, several concentrations ranging from 100 ng/ml to 1000 ng/ml of antiBSA diluted in PBS1x were prepared. Fig. 5.31 shows the temporal evolution of the output power for the antiBSA detection experiment carried out. An output power value was acquired each 20 ms (i.e., 50 data points per second), what is a temporal resolution significantly higher than that used in most sensing results reported in literature (e.g., one data point almost every minute for [SCU11], or one data point every 3 seconds for [VOS10]), what allows a better observation of the binding kinetics in the sub-second scale. The concentrations of antiBSA in PBS 1x were flowed over the chip at a constant rate of 20 µl/min. We can note that a decrement of the output power is produced at each detection cycle due to the binding of the antiBSA molecules to the BSA receptors. This decrement is permanent as it can be seen when the PBS 1x buffer is flowed again. We can also see that the amount and the rate of the output power variation is different for each concentration of antiBSA, having larger changes and initial slopes for higher concentrations of the antibody. After each sensing cycle, the photonic sensor was regenerated by flowing a solution of NaOH at 20 mM during 5 minutes in order to remove the antiBSA bound to the BSA receptors, due to the pH change. We can see that the regeneration step induces a sudden blue-shift of the PBG edge due to release of the antiBSA and the different index, what is translated into an increment of the output power. Then, the baseline is perfectly recovered when the PBS 1x is flowed again over the sensing structure.

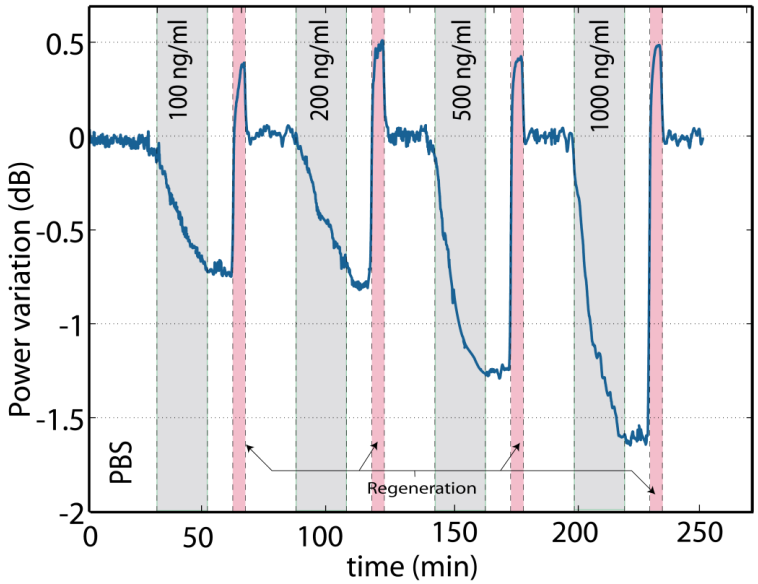

Fig. 5.31: *Temporal evolution of the output power when several concentrations of antiBSA were flowed over the sensor. The regeneration was performed by using NaOH.*

In this experiment, we measured the concentration of the analytes by calculating the initial slope at the moment of the recognition. Fig. 5.32a shows the initial slope of the sensor response for each antiBSA concentration, which have been used to determine the sensitivity curve of the sensor that is shown in Fig. 5.32b. The analysis of the sensor response was carried out using a custom-made Matlab program where the data was fitted to an exponential equation given by the affinity response introduced in chapter 2. The fact that several data points are acquired each second, allows a more adequate fitting of the sensing curve. The initial slope is obtained from the derivative of the fitting curve at the initial point of the detection. As we appreciate from the sensitivity curve in Fig. 5.32b, the sensor exhibits a clearly linear behavior of the initial slope for the range of antiBSA concentrations considered.

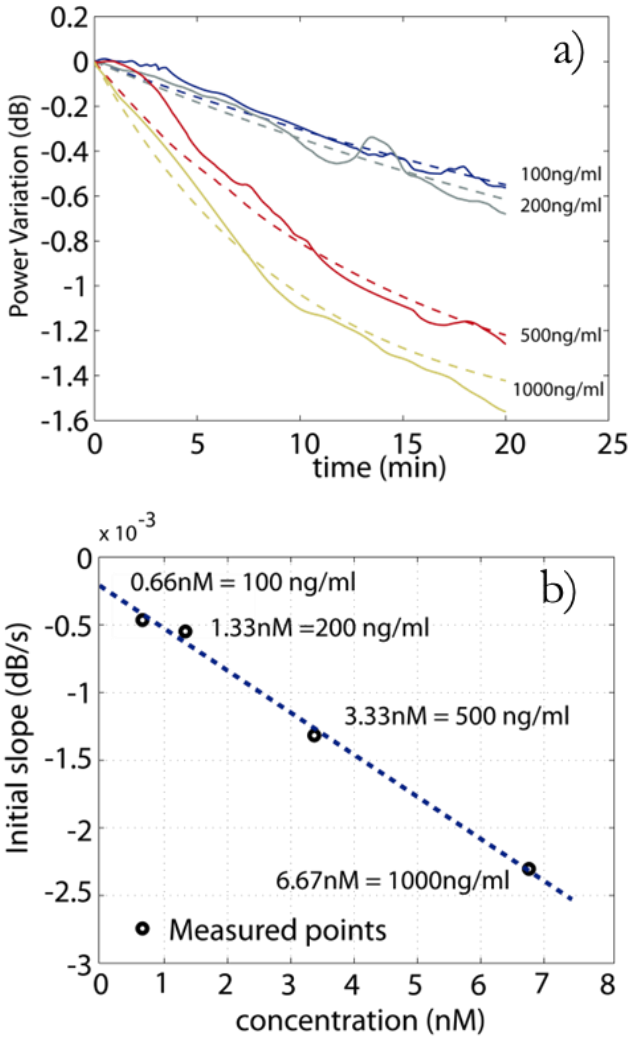

Fig. 5.32: *a) Fitting analysis of the signal. b) Values of the initial slope of the response of the sensor as a function of the antiBSA concentration (in molar).*

Despite the minimum antiBSA concentration experimentally measured was 100 ng/ml, we have also estimated the detection limit from the system noise. A noise level of σ = 0.02 dB was measured during the flow of the buffer solution after the stabilization of the sensor. From this value, we estimated a detection limit of 2 ng/ml. Table 5.4 lists several state-of-the-art values for the detection limit of antigen/antibody/protein sensing experiments of the last years. Although our result is not the best from all of them, it is less than one order of magnitude above that reported in [XU08] (0.4 ng/ml). Besides, we expect that this detection limit value can be further decreased by continuing working on the sensing structures, the functionalization and the readout platform. However, it is worth noting that this detection limit value has been achieved using a power-based interrogation technique that provides many benefits compared to the spectral-based interrogation techniques used to obtain the rest of the results (except for [ZIN11]).

Reference	Model	Structure	min. conc. detected
[XU08]	Streptavidin-Biotin	Folded Ring Resonator	0,4 ng/ml
[ZLA09]	bBSA-antiBiotin	PhC. Microcavity	3,2 µg/ml
[LI10]	BSA-biotin	Ring Resonator	2,4 ng/ml
[SCU11]	Avidin-Biotin	SlottedPhC.	3,6 ng/ml
[ZIN11]	BSA-aBSA	Bimodal Waveguide	0,42ng/mm^2
Our sensor	BSA-antiBSA	Corrugated waveguide	2 ng/ml

Table 5.4: *Comparison of the detection limit reported for other sensors based on planar photonic structures for the detection of antigens/antibodies/proteins.*

With this experiment, we demonstrated that the power-based method that we proposed is suitable for biosensing measurements. Despite not being the most sensitive system according to the state-of-art, we can state that our system provides other very relevant advantages such as real-time measurements, simpler system or lower cost equipment, what makes our system a good candidate for the development of new practical and affordable LOC devices.

5.8 Conclusions

In this chapter, we presented our novel sensing interrogation technique that contributes with several advantages respect to current sensing techniques. Our optical power-based measurement technique exhibits several interesting advantages such as a lower cost of the read-out system, a higher compactness of the system, or the possibility to monitor in real-time the molecular interaction.

For the experimental demonstration of the technique, we decided to use 1D periodic corrugated waveguides as PBG structures, mainly because of their higher simplicity, easier fabrication and good sensitivity. Such characteristics make of that structure, together with the proposed measurement technique, a good candidate for the development of new emerging biosensing applications. We designed the optimal parameters for the sensing structures and fabricated them through the cost-shared ePIXfab fabrication platform using CMOS technology, what permits a large-scale fabrication of the chips and a substantial reduction of the cost per unit.

Then, our experiments began pursuing the demonstration of the ability to perform bulk RI measurements by employing the power-based interrogation technique, for what we detected

different salt concentrations. We obtained a sensitivity as high as 1786 dB/RIU and a detection limit as low as $2 \cdot 10^{-6}$ RIU, what verifies the potential of the proposed technique for sensing purposes. Moreover, note that the larger number of data points that are reorder using this power-based technique also permits to perform an averaging of the output signal to reduce the noise and therefore the detection limit.

Our next experiments targeted to compare the performances of the typical spectral-based readout techniques with our power-based method, by interrogating simultaneously the PBG sensing structure where a detection of antibodies is being carried out. With these experiments, we confirmed that the sensing information that is obtained with both approaches, but that our power-based approach provides several relevant advantages such as the cost, size and weight reduction of the readout system, the possibility to observe the molecular interactions in true real-time, the possibility to have a high resolution with a fast response, etc.

And finally, we carried out several sensing experiments targeting the detection of low concentrations of antibody. In this kind of experiment, we performed multiple regenerations of the sensor surface between detections employing NaOH, thus making possible several assays in a single chip. As a result, we were able to determine a detection limit of 2 ng/ml for the sensing system that we employed.

Therefore, we have been able to experimentally demonstrate all the expected advantages for our novel power-based interrogation technique, thus making it a very valuable approach for the development of future cost-effective, portable, high performance and practical LOC devices.

References

[BRI12] A.Brimont, "Towards Compact and High Speed Silicon Modulators", Universitat Politècnica de València, thesis dissertation, 2012.

[CEA13] Laboratoire d'Electronique des Technologies Informatiques, www.leti.cea.fr, 2013.

[CLA11] T. Claes, W. Bogaerts, and P. Bienstman, "Vernier-cascade label-free biosensor with integrated arrayed waveguide grating for wavelength interrogation with low-cost broadband source." Optics Letters, vol. 36(17, pp. 3320–3322, 2011.

[DAN12] S. Dante, D. Duval, B. Sepúlveda, A. B. González-Guerrero, J. R. Sendra, and L. M. Lechuga, "All-optical phase modulation for integrated interferometric biosensors." Optics Express, vol. 20(7), p. 7195, 2012.

[DUV12] D. Duval, A.B. González-Guerrero, S. Dante, J. Osmond, R. Monge, L.J. Fernández, K.E. Zinoviev, C. Domínguez and L.M. Lechuga, "Nanophotonic lab-on-a-chip platforms including novel bimodal interferometers, microfluidics and grating couplers." Lab on a chip, vol. 12(11), pp. 1987-1994, 2012.

[EPI13] www.epixfab.eu

[JAG09] P. Jaguiro, P. Katsuba, S. Lazarouk, S. Moore, and A. Smirnov, "Si-based optoelectronic couple." Physica E: Low-dimensional Systems and Nanostructures, vol. 41(6), pp. 1094-1096, 2009.

[JIN11] L. Jin, M. Li, and J.-J. He, "Optical waveguide double-ring sensor using intensity interrogation with a low-cost broadband source." Optics Letters, vol. 36(7), pp. 1128-1130, 2011.

[JUG09] A. S. Jugessur, J. Dou, J. S. Aitchison, R. M. D. L. Rue, and M. Gnan, "Microelectronic Engineering A photonic nano-Bragg grating device integrated with microfluidic channels for bio-sensing applications." Microelectronic Engineering, vol. 86(4–6), pp. 1488-1490, 2009.

[KAU09] L. J. Kauppinen, H. J. W. M. Hoekstra, and R. M. de Ridder, "A compact refractometric sensor based on grated silicon photonic wires." Sensors and Actuators B: Chemical, vol. 139(1), pp. 194-198, 2009.

[PAS08] V. M. N. Passaro, R. Loiacono, G. D'Amico, and F. De Leonardis, "Design of Bragg Grating Sensors Based on Submicrometer Optical Rib Waveguides in SOI." IEEE Sensors Journal, vol. 8(9), pp. 1603-1611, 2008.

[LI10] H. Li and X. Fan, "Characterization of sensing capability of optofluidic ring resonator biosensors." Applied Physics Letters, vol. 97(1), p. 11105, 2010.

[PER08] P. Pérez-Millán, S. Torres-Peiró, J. L. Cruz, and M. V. Andrés, "Fabrication of chirped fiber Bragg gratings by simple combination of stretching movements." Optical Fiber Technology, vol. 14(1), pp. 49-53, 2008.

[SCU11] M. G. Scullion, a Di Falco, and T. F. Krauss, "Slotted photonic crystal cavities with integrated microfluidics for biosensing applications." Biosensors & bioelectronics, vol. 27(1), pp. 101-105, 2011.

[SON13] J. Song, X. Luo, J.S. Kee, Jack Sheng K. Han, C. Li, M.K. Park, X. Tu, H. Zhang, Q. Fang, L. Jia, Y.L. Yoon, T.Y. Liow, M. Yu, G.Q. Lo , "Silicon-based optoelectronic integrated circuit for label-free bio/chemical sensor," Optics Express, vol. 21(15), p. 17931, 2013.

[XU08] D. X. Xu, a Densmore, a Delâge, P. Waldron, R. McKinnon, S. Janz, J. Lapointe, G. Lopinski, T. Mischki, E. Post, P. Cheben, and J. H. Schmid, "Folded cavity SOI microring sensors for

high sensitivity and real time measurement of biomolecular binding." Optics Express, vol. 16(19), pp. 15137-15148, 2008.

[ZIN11] K. E. Zinoviev, A. B. Gonzalez-Guerrero, C. Dominguez, and L. M. Lechuga, "Integrated Bimodal Waveguide Interferometric Biosensor for Label-Free Analysis." Journal of Lightwave Technology, vol. 29(13), pp. 1926-1930, 2011.

[ZLA09] S. Zlatanovic, L. W. Mirkarimi, M. M. Sigalas, M. a. Bynum, E. Chow, K. M. Robotti, G. W. Burr, S. Esener, and A. Grot, "Photonic crystal microcavity sensor for ultracompact monitoring of reaction kinetics and protein concentration." Sensors and Actuators B: Chemical, vol. 141(1), pp. 13-19, 2009.

6

Conclusions and future trends

6.1 Conclusions of the work

From the 80's, there has been an increasing interest in develop more efficient and powerful sensing devices that play an important role in diverse fields such as medical diagnosis, environmental control, drug discovery, CBRN detection or food testing. A biosensor is a device that is used to determine the presence of a target analyte, which consists of a transducer, a functional layer for receptors, a fluidic delivery system and the read-out. The main objective is to integrate those biosensors into more complex LOC devices, in which is possible to implement several functionalities in a single chip and carry out several analysis simultaneously. Integrated optical structures are a very promising candidate for the development of this type of sensing devices, especially when using silicon-based and CMOS compatible materials and process. This technology will not only provide a very high sensitivity and low detection limits, but also a very high integration level, low cost, and the possibility to directly integrate complex microfluidic sample preparation and delivery systems.

In this PhD Thesis, we studied several sensing platforms where integrated SOI photonic structures were employed, including PhC-WGs, RRs and corrugated waveguides. In addition, we

proposed a novel power-based interrogation method in order to overcome many of the weaknesses of current photonic sensing techniques based on tracking the spectral shift of the response of the sensing structure. Our method is able to measure indirectly the shift of the PBG position without the need of any tunable element for the interrogation, what is the key of all the advantages that it presents.

One of the first problems that we addressed in this PhD work was determining the procedures required to attach the receptors to the silicon surface of the photonic sensing structures; this process is called bio-functionalization. We decided to work with a chemistry based in the use of organosilanes, which allows creating covalent links with the structure surface. These compounds anchor to inorganic substrates and promote the binding of the receptors through the functional groups at their end. We investigated different kinds of organosilanes and finally we developed successfully two functionalization routes. The first strategy was based on ICPTS organosilane, which provides an isocyanate group at the end that allows the binding of amines. However, we observed many problems during the development of this functionalization strategy because the isocyanate group of the ICPTS hydrolyzes in presence of humidity and loses its functionality. Therefore, we decided to propose a second functionalization approach based on GOPTS organosilane, which has an epoxy termination. One of the particularities of this procedure is that the attachment of thiolated receptors to the epoxy-ended organosilane can be assisted with UV light, leading to a significant reduction of the time required for the immobilization and to a spatial selectivity. As it has been shown throughout this document, in our experiments we confirmed that successful sensing results can be obtained using both methods for planar silicon-based photonic structures.

The first structures that we studied for their use as sensors were PhCs. These structures can present a PBG, a range of wavelengths where the propagation of light through them is not allowed, as well as the so-called slow-light phenomena, which provides a high enhancement of the light-mater interaction in the sensing areas and thus an increase of the sensitivity. We studied different configurations of PhCs and decided to use W1 PhC-WG created in a holes-on-silicon configuration for our experiments. Once we began with the characterization of the PhC-WG sensing structures, we observed the appearance of sharp fringes in the slow-light regime near the edge of the guided band. We modeled the presence of these fringes, which were due to the creation of a Fabry-Perot cavity between the PhC-WG and the access waveguides, and demonstrated the possibility of using them for sensing purposes. The use of these FP fringes ensures us that we are working in the slow-light regime of the structure, and eases the accurate determination of the spectral feature to be tracked. Finally, we successfully carried out several measurements in order to experimentally demonstrate our FP-based approach for refractive index sensing (with a sensitivity of 174,8 nm/RIU and a detection limit of $3 \cdot 10^{-6}$ RIU), antibody detection (with an estimated total mass

detection limit of 0.2 fg), and ssDNA hybridization sensing (reaching an estimated detection limit as low as 19,8 nM). Therefore, these results validate the potential of the PhC-WG for the development of high performance sensing structures for biological purposes.

The second type of structures that we used in this PhD work were RRs. As it can be seen in the literature, RRs are probably the most commonly employed photonic structures for the development of biosensing devices due to their simplicity, versatility and multiplexing potential. RR-based sensing structures provide a high sensitivity determined by their large effective interaction length caused by the circulation of the mode within the RR, making that the photons interact many times with the target analytes. We worked in modify and improve our experimental measurement platform in order to be able to measure the spectral response of the RRs using an OSA (instead a tunable laser), use a PDMS-based microfluidic flowcell to deliver the target samples, change automatically the different samples to be flowed, and monitoring continuously the resonance position. Using this platform, we were able to demonstrate refractive index sensing using RRs, determining an intrinsic sensitivity of the RR of 82,78 nm/RIU and a detection limit $1{,}44 \cdot 10^{-5}$ RIU. Employing RR as a sensing platform, we also worked on biosensing of antibodies and ssDNA. We optimized two functionalization methods, based on ICPTS and in GOPTS organosilanes. With both methods, we were able to sense ssDNA with a high sensitivity and low detection limit (e.g., a concentration as low as 5 nM was detected using the GOPTS-based chemistry). However, the experimental procedures that we developed showed us that the GOPTS-based chemistry exhibits several advantages compared to the ICPTS-based chemistry, such as higher stability, better sensitivities, time reductions, and the possibility to do a spatially-specific functionalization.

Finally, we proposed and experimentally demonstrated a novel technique for the development of PBG-based photonic biosensors. This technique contributes with several advantages compared to current approaches, which are mainly determined by the lack of tunable elements. In this way, the measurements can be performed using low-cost equipment at real-time as well as allowing the possibility of a future direct integration of the sources and the detectors within the photonic sensing device. With this new approach, where we only used a broadband source and a power meter for the experiments, we achieved an outstanding sensitivity of 1786 dB/RIU and a detection limit of only $2 \cdot 10^{-6}$ RIU. In addition, we have shown how the performance of a PBG biosensor is significantly enhanced by simply using our power-based read-out method instead of a typical spectral-based interrogation. We compared simultaneously the sensing response when using both interrogation approaches (i.e., spectral-based method vs. our power-based method) for an antigen-antibody (BSA-antiBSA) analysis experiment, and we observed that the shape of the response is analogous in both cases. However, our power-based approach provides several advantages that are not provided by typical spectral-based approaches, such as a lower detection limit, a higher number of acquired points, an instantaneous observation of any interaction event, or

a significant reduction of the cost, the size and the weight of the readout platform, among others. Finally, we demonstrated a limit of detection of only 2 ng/ml for BSA-antiBSA detection using our sensing approach. Therefore, the experimental results obtained using this novel sensing technique confirms the great potential for sensing purposes predicted when it was theoretically proposed, making it probably one of the most suitable options for the development high performance, portable and low-cost LOC devices based in photonic technology.

In the table 6.1 we can compare the parameters of the different sensing techniques and structuresthat were presented in this thesis.

Interrogation technique	Sensing structure	Source	detector	Sensitivity	Limit of detection
Wavelenght-based	Photonic cristal	Tunable laser	Power-meter	174.8 nm/RIU	$3 \cdot 10^{-6}$ RIU
Wavelength-based	Ring resonator	Broadband source	OSA	82.78 nm/RIU	$1.44 \cdot 10^{-5}$ RIU
Power-based	Corrugated Waveguide	Broadband source.	Power-meter	150 (1786 dB/RIU)	$2 \cdot 10^{-6}$ RIU

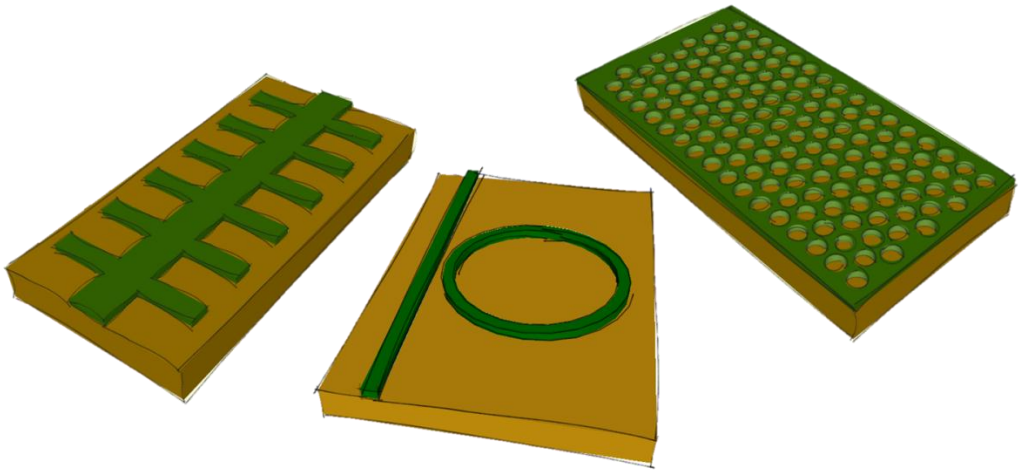

Table 6.1: *Summary table of the different methods employed in the thesi with the obtained results and schematic illustration of the structures: photonic crystal, ring resonator and corrugated waveguide.*

6.2 Future trends

In this PhD Thesis, we have worked in the development of sensing devices based on different type of structures (i.e., 2D PhCs, 1D PhCs and RRs), using different approaches for their functionalization (i.e., ICPTS- and GOPTS-based chemistry), and even of a new low-cost sensing

approach based on PBG structures. However, there still a long path to follow and a lot of work needs to be done before a practical sensing system with real commercial potential can be deployed into the market. Herein, we propose several concepts and ideas that can be considered in the future in order to further enhance the current sensing platform and orient it towards a final device with practical application in the real world:

- Although the estimated detection limit is in the range of the state-of-the-art values, lowering this parameter is always desired. By increasing the sensitivity of the photonic integrated structures we can be able to reduce such parameter. To this aim, current structures may be modified in order to confine the optical field in those areas where the interaction with the matter is stronger. The combination of 1D structures with the slot concept might provide promising results. On the other hand, it would be possible to consider the use of other structures such as the 2D PhCs, as employed in chapter 3.
- Regarding the chemical modification procedure, a significant reduction of the biofunctionalization time was obtained with the novel light assisted technique based on GOPTS. However, that time stills being long. By employing a more powerful UV light or by having a higher directivity, we could reduce the reaction time to few minutes; however, we will need to control the evaporation of the liquid being incubated. It would be also interesting to study the temperature and humidity conditions in order to obtain better coverage efficiencies, thus lowering the detection limit as well.
- One of the issues that we observed during the course of this PhD work was the variability of the surface coverage due to the size of the drops used to attach the receptors. Better performances were observed by reducing the volume of the spot; therefore, a fully automated functionalization procedure using adequate equipment (e.g., the nanodot equipment used within this work) should be developed in order improve the immobilization procedure. In addition, this type of equipment will also allow to attach different probes to different sensing structures.
- Other problem that we observed during the experimental characterization of the photonic sensing structures is that related with the signal drift and its initial stabilization, which influences negatively to the system performance. In order to reduce this problem, we propose diverse routes. First, the implementation of a temperature control system in the optical set-up in order to compensate the temperature variations during the experiments. Other approach is the use of reference structures within the sensing chip in order to compensate any type of non-sensing signal variations. In order to do this, we will need to have an experimental set-up where multiple photonic structures can be interrogated simultaneously. To this aim, we propose the use of flood illumination of several access

structures with a collimator at the input and an IR camera at the output, instead of using a fiber-to-fiber set-up as we have done in this PhD work.

- Regarding the fluidic delivery system, we employed different types of architectures (e.g., metallic flow cell, microfluidic PDMS-based flow cell, and integrated SU8-based microchannels). However, the development of future LOC devices requires of more complex microfluidic systems able to implement sample preparation functions and not only delivering the sample to the sensing structures. Therefore, a possible future work would be the implementation of novel microfluidic architectures with the possibility of bubble trapping, sample filtering, sample mixing, etc. in order to provide more complexity to our final system. In addition, we will also need to look for new fabrication techniques that can reduce the cost of the development of the master molds.
- The fabrication process of the photonic structures should be optimized in order to obtain a higher degree of repeatability of the chips. For that reason, we will need to constantly work in the improvement of the fabrication procedures. Furthermore, we will need to look for implementing in-house UV lithography systems like those used by IMEC and CEA-LETI in the frame of the ePIXfab platform.
- Design better coupling structures to improve the efficiency of the transmitted power between the accesses waveguides and the sensing structures in order to improve the output power in the characterization experiments.
- Regarding the measurement set-up, several aspects can be enhanced. For instance, the data acquisition must be optimized in order to increase the number of power values obtained per second, what will allow a better temporal resolution of the measurement as well as a reduction of the detection limit. Other improvement of the sensing platform might be the implementation of an user-friendly software that allows to easily configure the experiment by any type of non-technical user (e.g., indicating parameters of the assay such as the time for each sample, samples to be analyzed, type of information to be provided, etc.).
- One of the most interesting possibilities that our power-based sensing approach offers, is the possibility to integrate the sources and the detectors directly with the photonic sensing structures. This will allow having a final photonic sensor that is simply electrically accessed, what will allow having an extremely simple, compact, and low-cost electronic platform for the readout.

Author contributions

International Journals

1. J. Escorihuela, M. J. Bañuls, J. García Castelló, V. Toccafondo, J. García-Rupérez, R. Puchades, and Á. Maquieira, "Chemical silicon surface modification and bioreceptor attachment to develop competitive integrated photonic biosensors.," *Analytical and Bioanalytical Chemistry*, Vol. 404, No. 10, pp. 2831-2840, Dec. 2012.

2. J. G. Castelló, V. Toccafondo, J. Escorihuela, M. J. Bañuls, A. Maquieira, and J. García-Rupérez, "Real-time observation of antigen-antibody association using a low-cost biosensing system based on photonic bandgap structures," *Optics Letters*, Vol. 37, No. 17, pp. 3684-3686, Aug. 2012.

3. J. García-Rupérez, J. G. Castelló; V. Toccafondo; J. G. Castelló., "Label-Free biosensing using Photonic crystal waveguides", ISBN 978-953-51-0416-2, *Photonic Crystals - Innovative Systems, Lasers and Waveguides - Chapter 12, Editions InTech*, 2012.

4. J. G. Castelló; V. Toccafondo; P. Pérez-Millán; N. Sánchez; J. L. Cruz; M. V. Andrés; J. García-Rupérez, "Real-Time and Low-Cost Sensing Technique Based on Photonic Bandgap Structures", *Optics Letters*, Vol. 36, No. 14, pp. 2707-2709, Jul. 2011.

5. J. García-Rupérez, V. Toccafondo, M.J. Bañuls, J. G. Castelló, A. Griol, S. Peransi-Llopis, and Á. Maquieira, "Label-free antibody detection using band edge fringes in SOI planar photonic crystal waveguides in the slow-light regime", *Optics Express*, Vol. 18, No 23, pp. 24276-24286, Nov. 2010.

6. V. Toccafondo, J. García-Rupérez, M. J. Bañuls, A. Griol, J. G. Castelló, S. Peransi-Llopis and A.Maquieira, "Single Strand DNA Detection Using a Planar Photonic Crystal Waveguide Based Sensor", *Optics Letters*, Vol. 35, No. 21, pp. 3673-3675, Nov. 2010.

International Conference Proceedings

1. M.J. Bañuls, J. Escorihuela, J.G. Castelló , R. Puchades, J. García-Rupérez, A. Maquieira, "Photoinduced attachment of thiolated oligonucleotides on silicon based surfaces. Application to label-free photonic biosensing", *NanoPT 2013*, February 2013, Oporto, Portugal,

2. J. Garcia-Ruperez, J.G. Castello, J. Escorihuela, M.J. Bañuls, A. Maquieira, "Specific DNA Detection Using Light Assisted Bio-functionalized Ring Resonators", *Nanomeeting 2013*, May 2013, Minsk, Belarus.

3. J.G. Castelló, V.Toccafondo, J. Escorihuela, M.J.Bañuls, A. Maquieira, J. García-Rupérez; "Real-Time Analysis of Antigen-Antibody Association Kinetics using a Low-cost SOI Photonic Biosensor", *Group IV photonics*, August 2012, San Diego, EEUU.

4. J.G. Castelló, V. Toccafondo, M.J. Bañuls, J. Escorihuela, A. Maquieira, J.García-Rupérez, "Label-free antibody detection using a low cost biosensor based on photonic bandgap structures", *Europtrode XI Congress*, 1-4 April 2012, Barcelona, Spain.

5. V. Toccafondo, J.G. Castelló, , M.J. Bañuls, J. Escorihuela, T.Claes, P.Bienstman, A. Maquieira, J.García-Rupérez , "Detection on chip DNA hibridization using Silicon Based microringring resonators", *Europtrode XI Congress*, April 2012, Barcelona, Spain.

6. J.G. Castello, V. Toccafondo, P.Perez-Millan,J.L.Cruz, M.V.Andrés, J.García-Ruperez, "Measurement Technique or Real-time and Low-Cost Biosensing Using Photonic Bandgap Structures", *8th International Conference on Group IV Photonics*, September 2011, London, England.

7. V. Toccafondo, J. García-Rupérez, M.J. Bañuls, A. Griol, J.G. Castelló, S. Peransí-LLopis and Á. Maqueira, "High sensitivity sensors based on SOI photonic crystal waveguides for protein and DNA detection", *VII reunión española de optoelectrónica (OPTOEL* 2011*)*, June 2011, Santander, Spain.

8. J. Garcia-Ruperez, J.G. Castello, V. Toccafondo, A. Brimont, "Sensing Technique for the Development of Real-time and Low-cost Biosensors Using Photonic Bandgap Structures", *OSA Advanced Photonics 2011 Congress*, June 2011, Toronto, Canada.

9. M. Kristensen, A. Krüger, N. Groothoff, J. García-Rupérez, V. Toccafondo, J.G. Castelló, M.J. Bañuls, S. Peransi-Llopis, and A. Maquieira, "Photonic Crystal Biosensor Chip for Label-Free Detection of Bacteria", *OSA Advanced Photonics 2011 Congress*, June 2011, Toronto, Canada.

10. J. García-Rupérez, V. Toccafondo, A. Griol, J. G. Castelló, "Refractive Index Sensing Using Band Edge Fringes In Photonic Crystal Waveguides", *IX International Conference on Photonic and Electromagnetic Crystal Structures (PECS-IX)*, 26-30 September 2010 in Granada, Spain.

11. J. García-Rupérez, V. Toccafondo, M. J. Bañuls, A. Griol, J. G. Castelló, S. Peransi-Llopis and A.Maquieira, "Single Strand DNA Hybridization Sensing Using Photonic Crystal Waveguide Based Sensor", *IEEE 7th International Conference on Group IV Photonics*, September 2010, Beijing, China.

12. V. Toccafondo, J. García-Rupérez, M. J. Bañuls, A. Griol, J. G. Castelló, S. Peransi-Llopis and A. Maquieira, "DNA detection using a photonic crystal waveguide sensor", abstract SWB3, oral communication at the 2010 Sensors Topical Meeting within *Advanced Photonics: OSA Optics & Photonics Congress*, June 2010, Karlsruhe, Germany.

13. V. Toccafondo, J. García-Rupérez, M. J. Bañuls, A. Griol, J. G. Castelló, S. Peransi-Llopis and A. Maquieira, "Photonic crystal waveguide sensor for low concentration DNA detection", *Conferencia española de nanofotónica, CEN-10*, June 2010, Segovia, Spain.

14. D. Hill, V. Toccafondo, J. Garcia-Rupérez, A. Griol, J. Garcia-Castelló, A. C. Krüger, M. Kristensen, T. Claes, J. Gironès-Molera, K. De Vos, E. Schacht, R. Baets and P. Bienstman, "A highly integrated optical sensor for point of care label free indentification of pathogenic bacteria strains and their antibiotic resistance", *Conferencia española de nanofotónica, CEN-10*, June 2010, Segovia, Spain.

15. Javier. G. Castelló, Jaime García, Amadeu Griol, Juan Hurtado, Laurent Belliers, José Ayucar, Javier Martí, "*Sensor óptico integrado basado en anillos resonantes en Silicio*", *VI reunión española de optoelectrónica (*OPTOEL *2009)*, June 2009, Málaga, Spain.

16. J.G. Castelló, J. García, A. Griol. J. Hurtado, L. Belliers, J. Ayucar, J. Martí, "Integrated optical sensor using silicon ring resonators", *Trends in Nanotechnology (TNT2009)*, September 2009, Barcelona, Spain.

List of figures

List of tables

ANNEX A

Author's specific contribution to the presented work

The development of a photonic biosensing platform generally covers different scientific fields such as photonics, biochemistry, or microfluidics. Achieving a complete synergy among these fields is an ambitious challenge. For that reason, this kind of projects are carried out by multidisciplinary teams with highly qualified researchers who work together towards a successful result. Namely, the work described in this thesis has been framed within several research projects in which the participation of the different partners has been fundamental to achieve the defined objectives. For this reason, the author has attempted to explain not only the work mainly done by himself, but also the work that has been done in direct collaboration with other partners and researchers. Obviously, the author did not contribute equally in all the steps of the developments presented in this thesis, but his involvement in all the stages has been significant in different levels. In fact, it is difficult to isolate the work carried out by the author during the thesis. In this annex, we specify the role of the author in the research work that has been included in this thesis.

Starting in chapter 2, where the chemical modification of the structure's surfaces is studied, this task was mainly carried out by the "Centro de Reconocimiento Molecular y Desarrollo Tecnológico" of the UPV led by Prof. Ángel Maquieira, as already mentioned in the introduction of the chapter, Prof. Maquieira's group, which also participated as a partner in the FP7-INTOPSENS project, has an enormous expertise in the field of biofunctionalization and molecular recognition. Despite the background of the author was not related with the chemistry field, he actively participated in the optimization of the modification process for the planar photonic structures,

where his contributions were substantial in order to obtain the final protocols. Furthermore, we considered that it was necessary to include this chapter in order to give an overview of the chemical modification protocols employed in the forthcoming chapters.

The work described in chapter 3, which deals with PhC-based sensing structures, was developed at the initial stage of the author's PhD studies. Therefore, the focus of the author's work within this period was to acquire the knowledge and skills related with the development of photonic sensing structures, being the research work mainly led by Dr. Jaime García-Rupérez and Dra. Veronica Toccafondo. As mentioned in chapter 3, the initial PhC-WG structure was proposed by Dr. Kristensen's group from Aarhus University in the frame of the FP7-INTOPSENS project. However, the author also worked in modelling and optimizing the structure by means of 2D and 3D FDTD simulations. These simulations were also used to confirm the possibility of employing the Fabry-Perot fringes appearing at the edge of the transmission band for sensing purposes, what was proposed by Dr. Jaime García-Rupérez. Regarding the experimental development of the PhC-based sensors, the author collaborated in the assembly of the set-up, designed the metallic flow cell used for delivering the liquids to the photonic sensing structure, and worked in the automatization of the set-up by means of a LabVIEW application. Finally, the author also participated in the experimental characterization of the PhC-based sensors; however, since he was in the initial stage of his PhD studies, he worked together with other experienced researchers and had an "assistant-like" role.

Regarding the work described in chapter 4, in which RR-based sensors were studied, three stages can be considered. In the first stage, the author spent several months in the Photonics Research Group of the Gent University working in Dr. Peter Biestman's group. This research stay was carried out in the frame of the FP7-INTOPSENS project. In this period, the author studied the RR structure for sensing purposes as well as vertical coupling mechanisms based on surface gratings. Despite the author did not directly contribute to the final design of the RRs employed in this thesis work (it was carried out by the group of Gent University in the frame of the FP7-INTOPSENS project), the author also learnt how to model and simulate the behaviour of these structures, as described in the initial sections of chapter 4 for the sake of clarity and coherence. In addition, during this research stay he also learnt how to fabricate and use PDMS-based microfluidic delivery systems, which were later used in the NTC group. The second stage was developed in the UPV, where the author started to deploy all the acquired knowledge. He contributed in the adaptation of the new measurement set-up based on grating couplers and where PDMS-based microfluidic sample delivery systems were used, taking profit of his recent experience in Gent University. Regarding the experimental development of the RR-based sensors using ICPTS chemistry, it was carried out in close collaboration with Dra. Veronica Toccafondo, having both the same level of responsibility. Finally, the last period consisted in the development of the RR-based sensors using GOPTS-based chemistry, where the author had a prominent and leading role. He did

not only carry out the biosensing experiments and the analysis of the obtained results, but he also participated actively in the development of the photofunctionalization procedures in an intense collaboration with Prof. Maquiera's group.

Finally, in chapter 5, the author was the main contributor to the experimental development of the proposed novel power-based sensing technique. That sensing technique was previously theoretically proposed by Dr. Jaime García-Rupérez, but is has been the author who has experimentally demonstrated its practical potential for the development of compact, low-cost and real-time sensing systems. In summary, the author was in charge of carrying out the simulations to determine the optimal parameters of the 1D periodic sensing structures to be used, the implementation of the set-up for the interrogation of the sensing structures using the proposed sensing technique, and the realization of all the experiments required to demonstrate the performance of the proposed sensing technique. Furthermore, the author produced several scientific articles for their submission to peer review journals and conferences.

Summarizing, the author has actively participated in all the steps required for the whole development of the sensing platforms presented in this PhD work. Of course, the involvent has been different depending of the research field and the stage of his PhD studies, but his implication in the developed work has been absolute and he has contributed to the achievement of the scientific objectives defined in the research project where the work has been enframed.